Measurement of Top quark properties and
Search for the Standard Model Higgs Boson
in proton anti-proton collisions at √s=1.96TeV

重心系エネルギー1.96TeV の陽子・反陽子衝突実験における
トップクォーク精密測定と標準模型ヒッグス粒子探索

March 2011

Koji Ebina

# Abstract

We present a measurement of the top quark mass and of the top-antitop ($t\bar{t}$) pair production cross section and a search for the Standard Model Higgs boson with CDF II Detector in $p\bar{p}$ collisions at $\sqrt{\hat{s}} = 1.96 TeV$.

The integrated luminosity of $2.9 fb^{-1}$ is used for top-antitop pair production cross section and top quark mass measurement. We adopt a neural-network algorithm to select candidate events from six or more jets. At least one of these jets should be required to be $b$ jet, as identified by the reconstruction of a secondary vertex inside the jet. The mass measurement is based on a likelihood fit incorporating reconstructed mass distributions representative of signal and background, where the absolute jet energy scale (JES) is measured simultaneously with the top quark mass. The measurement yields a value of $174.8 \pm 2.4$ (stat + JES) $^{+1.2}_{-1.0}$ (syst) $GeV/c^2$, where the uncertainty from the absolute jet energy scale is evaluated together with the statistical uncertainty. The procedure also measures the amount of signal from which we derive a cross section, $\sigma_{t\bar{t}} = 7.2 \pm 0.5$ (stat) $\pm 1.0$(syst) $\pm 0.4$ (lum) $pb$, for the measured values of top quark mass and JES.

Top quark mass and W boson mass constrain the mass of the Standard Model Higgs boson, indirectly. This prediction implies $M_H = 89^{+35}_{-26} GeV/c^2$ (68% confidence level) as of July 2010.

Therefore, we concentrate on the Standard Model Higgs mass search region with $\leq 135 GeV/c^2$. Then, we search for the Standard Model Higgs boson associated with vector boson using the decay modes consisting of leptons only: Signal processes are $WH \to l\nu + \tau\tau$ and $ZH \to ll + \tau\tau$. We simply select 3 or 4 lepton including hadronic $\tau$ to pick candidate events out. To improve search sensitivity, we adopt Support Vector Machine to discriminate signals from backgrounds.

Using about $6.2 fb^{-1}$ data, there was no clear discrepancy between data and our background estimation. Therefore, we extract cross section upper limit of the Standard Model Higgs production at 95% confidence level. The observed upper limit on assumption of $M_H = 115 GeV/c^2$ is $25.1 \times \sigma^{SM}$ at 95% confidence level while the expectation is $17.3 \times \sigma^{SM}$ at 95%.

In Dedicated to the memory of my friend, Homare Asano.

# Acknowledgement

It is regrettable that the Tevatron II will shutdown on September, 2011, too early.

I left physics five years ago, then I had worked for a company as programmer, for three years. I came back as a researcher on April, 2009.

So, I would like to show my gratitude to Professor Kunitaka Kondo first, who used to be my supervisor. He had considered about me even after I left physics. I appreciate his gratifying when I came back to be as a researcher.

Kohei Yorita, who used to be one of students of Kunitaka Kondo as same as I and is an associate professor in Waseda University, gave me second chance to live in physics, hired me as an assistant researcher. Without a given situation, I would have wandered around. I am indebt to him whose comments made enormous contribution to my work.

Nobu Oshima who retired and had worked for DZero experiments took me everywhere when I stayed at Fermilab; Asian store, restaurants, EAA AirVenture Oshkosh, Ravinia Festival and so on. When he sometimes taught me how to face physics, I felt as if the scales had fallen from my eyes.

I visited many times at Fermilab. For the first time, it was September, 1999. Moreover, I had stayed in Fermilab for two years (2002-2004) as a guest scientist when I was a graduate student of doctor course. During my staying at Fermilab, Goddess let me have a fateful encounter with many people, there. They are my best friends, masters of life and ... I am not able to express my pleasure completely even if I use any words. We met them at User's Center in Fermilab, where people working at Fermilab come to have meals and drinks. When I met her for the first time, I was a senior in the Department of Science and Engineering at Waseda University. Her name is Chivas Makaroplos who is a bartender of User's Center. She made me meet incredible and energetic people; Arden A. Warner who works for Accelerator Division, Superconducting Radiofrequency beam test facility department, David Vander Meulen who works for Accelerator Division, Antiproton Source Department, Debora Koolbeck who was a school teacher at that time, Gianni Tasotto who works for Accelerator Division, Engineering, Instruments Department, Kiyomi Seiya who works for Accelerator Division, Main Injector Department, Rene Padilla who is an engineer and works for Accelerator Division, Engineering, RF Department, Rich Cantal who already retired and had worked for DZero Experiments, Selda Esen who is a postdoctoral research associate of Brown University and so many people. They taught me how to live in the US and how to enjoy my life.

At the end, I would like to loudly say that I have been so happy that I belong to the CDF Collaboration and work for it.

# Contents

# List of Figures

# List of Tables

# Chapter 1

# Introduction

We already have known many things about nature, and the facts stimulate us study more and more about it. On the one hand, we are unhappy that we can not prevent ourselves from studying it because of the spilit of inquiry. On the other hand, we are so happy that we can have many things to understand the nature, forever. In any case, one of our challenges and our ancestor's since an ancient period is to elucidate what the source of matter is. This world consists of particles and interactions between them. We know a matter consists of atoms, the atom does of nuclei and electrons, the nucleus does of nucleons (proton and neutron), the nucleon does of quarks. All we know or believe now is that leptons and quarks (Fig.1.1) are the end, not dividable particles. The current picture of particle physics are these particle properties and its interactions. Particles which constitute the matter are quarks and leptons. Their interactions can be classified into four major ones; electromagnetic, weak, strong and gravitational interaction.

We completed particles at the end of past century, 2000 ([1]).



Figure 1.1: List of quarks and leptons. Figure are showing three generations of matter (Fermions).

These particles have resemble feature, but have different masses. The up-type

1

quarks (u, c, t) have $+\frac{2}{3}e$ charge and spin $\frac{1}{2}$. The down-type quarks (d, s, b) have $-\frac{1}{3}e$ charge and spin $\frac{1}{2}$. The charged leptons ($e$, $\mu$, $\tau$) have $-1e$ charge and spin $\frac{1}{2}$. The neutral leptons ($\nu_e$, $\nu_\mu$, $\nu_\tau$) have no charge and spin $\frac{1}{2}$.

The interactions between particles are performed by exchanging particle; the photon $\gamma$ for the electromagnetic interaction, the charged weak boson $W^\pm$ and the neutral weak boson $Z$ for the weak interaction and the gluon $g$ for the strong interaction.

All particles introduced as above are performers that has been on the stage, the Standard Model of particle physics. Only Higgs boson which plays the role of giving mass other performers is not yet on the stage.

This paper is one of challenges for the Standard Model Higgs boson search.

## 1.1 The Standard Model of Particle Physics

The Standard Model of particle physics describes observed phenomena of particle properties and their interactions. This theory consists of quantum chromodynamics (QCD) [3][4] and Electroweak theory, which is the Glashow-Salam-Weinberg (GSW) theory [5][6], which describe the interactions between particles (6 quarks and 6 leptons), and of Higgs mechanism. Electroweak interaction in the Standard Model requests $SU(2)_L \times U(1)_Y$ gage invariant. This means that the field of $SU(2)$ and the field of $U(1)$ are mixed. The mixing angle $\theta_W$ (Weinberg Angle) are not predicted by the Standard Model, so it should be measured by experiments. The mixing angle $\theta_W$ can be extracted by coupling constants of electromagnetic interaction ($g$) and weak interaction ($g_W$); $g_W/g = \tan(\theta_W)$. The gage invariance requires these should be no mass term in the basic Lagrangian. In order for particles to get mass, there is the Higgs Field has been proposed in the Standard Model, which is invariant for $SU(2) \times U(1)$. This cause that one of gauge boson (photon) does not have mass ($m_\gamma = 0$) and three of them (charged weak boson, neutral weak boson and the SM Higgs) have mass. The Higgs Field and the Weinberg Angle can extract mass of charged weak boson ($W^\pm$) and neutral weak boson ($Z$). These mass are precisely measured and good agreement with experimental results. The Standard Model has been verified by many experiments and has been successful to describe particle interactions. But only one particle in the Standard Model is not discovered yet, that is the Higgs boson which should have mass. The Higgs boson shoulders responsibility for the Higgs field which gives particles mass.

The Standard Model has succeeded in describing interactions between particles introduced above. The particles of the matter and gauge bosons have been discovered experimentally. And it also has confirmed many of the predicted properties of these particles.

The Standard Model is not enough theory of describing everything of particles and its interactions because it does not incorporate the general theory of relativity, such as gravitation, dark energy, the number of generations and so on. The theory does not take correctly account for neutrino oscillations, their non-zero masses. It also does not reveal about the dark energy and matter problems which is deduced from observational

| | particle | | | | anti-particle | | | |
|---|---|---|---|---|---|---|---|---|
| | quarks | | leptons | | quarks | | leptons | |
| Symbol | $u$ | $d$ | $e^-$ | $\nu_e$ | $\bar{u}$ | $\bar{d}$ | $e^+$ | $\bar{\nu}_e$ |
| Charge | $+\frac{2}{3}e$ | $-\frac{1}{3}e$ | $-1e$ | $0$ | $-\frac{2}{3}e$ | $+\frac{1}{3}e$ | $+1e$ | $0$ |
| Isospin | $+\frac{1}{2}e$ | $-\frac{1}{2}e$ | $-\frac{1}{2}e$ | $+\frac{1}{2}e$ | $-\frac{1}{2}e$ | $+\frac{1}{2}e$ | $+\frac{1}{2}e$ | $-\frac{1}{2}e$ |
| Color | $3$ | $3$ | $1$ | $1$ | $3$ | $3$ | $1$ | $1$ |
| Mass | $\sim 3$ | $\sim 6$ | $\sim 0.511$ | $< 2$ | $\sim 3$ | $\sim 6$ | $\sim 0.511$ | $< 2$ |
| $(GeV/c^2)$ | $\times 10^{-3}$ | $\times 10^{-3}$ | $\times 10^{-3}$ | $\times 10^{-9}$ | $\times 10^{-3}$ | $\times 10^{-3}$ | $\times 10^{-3}$ | $\times 10^{-9}$ |

Table 1.1: The properties of First Generation particles.

| | particle | | | | anti-particle | | | |
|---|---|---|---|---|---|---|---|---|
| | quarks | | leptons | | quarks | | leptons | |
| Symbol | $c$ | $s$ | $\mu^-$ | $\nu_\mu$ | $\bar{c}$ | $\bar{s}$ | $\mu^+$ | $\bar{\nu}_\mu$ |
| Charge | $+\frac{2}{3}e$ | $-\frac{1}{3}e$ | $-1e$ | $0$ | $-\frac{2}{3}e$ | $+\frac{1}{3}e$ | $+1e$ | $0$ |
| Isospin | $+\frac{1}{2}e$ | $-\frac{1}{2}e$ | $-\frac{1}{2}e$ | $+\frac{1}{2}e$ | $-\frac{1}{2}e$ | $+\frac{1}{2}e$ | $+\frac{1}{2}e$ | $-\frac{1}{2}e$ |
| Color | $3$ | $3$ | $1$ | $1$ | $3$ | $3$ | $1$ | $1$ |
| Mass | $\sim 1.3$ | $\sim 0.1$ | $\sim 0.106$ | $< 2$ | $\sim 1.3$ | $\sim 0.1$ | $\sim 0.106$ | $< 2$ |
| $(GeV/c^2)$ | | | | $\times 10^{-9}$ | | | | $\times 10^{-9}$ |

Table 1.2: The properties of Second Generation particles.

| | particle | | | | anti-particle | | | |
|---|---|---|---|---|---|---|---|---|
| | quarks | | leptons | | quarks | | leptons | |
| Symbol | $t$ | $b$ | $\tau^-$ | $\nu_\tau$ | $\bar{t}$ | $\bar{b}$ | $\tau^+$ | $\bar{\nu}_\tau$ |
| Charge | $+\frac{2}{3}e$ | $-\frac{1}{3}e$ | $-1e$ | $0$ | $-\frac{2}{3}e$ | $+\frac{1}{3}e$ | $+1e$ | $0$ |
| Isospin | $+\frac{1}{2}e$ | $-\frac{1}{2}e$ | $-\frac{1}{2}e$ | $+\frac{1}{2}e$ | $-\frac{1}{2}e$ | $+\frac{1}{2}e$ | $+\frac{1}{2}e$ | $-\frac{1}{2}e$ |
| Color | $3$ | $3$ | $1$ | $1$ | $3$ | $3$ | $1$ | $1$ |
| Mass | $\sim 173$ | $\sim 4.2$ | $\sim 1.78$ | $< 2$ | $\sim 173$ | $\sim 4.2$ | $\sim 1.78$ | $< 2$ |
| $(GeV/c^2)$ | | | | $\times 10^{-9}$ | | | | $\times 10^{-9}$ |

Table 1.3: The properties of Third Generation particles.

cosmology. There are some unpleasant results for the Standard Model. Understanding results that is not explained by the Standard Model is the most important things to open the gate of new physics.

One of the most fundamental problems in particle physics is to understand the mechanism that breaks electroweak symmetry and gives the masses to all known elementary particles. This problem is mainly discussed in this paper.

## 1.2 The Standard Model Higgs Boson

Higgs boson in the Standard Model is only one undiscovered particle. At first, theoretical views of the Standard Model Higgs boson are discussed. After that, experimental views of one are discussed in this section.

### 1.2.1 Theoretical Backgrounds

If particles follow $SU(3) \times SU(2) \times U(1)$, particles are not capable of having its mass. In order to give mass to particles, the Higgs mechanism [2] are advocated. In Higgs mechanism, the $SU(2)_L \times U(1)_Y$ gauge invariant field (Higgs field) is prepared.

Higgs mechanism in the Standard Model succeeded giving mass particles but the Standard Model does not predict the mass of particles and the magnitude of coupling. These are all parameters in the Standard Model (Fig. 1.3).
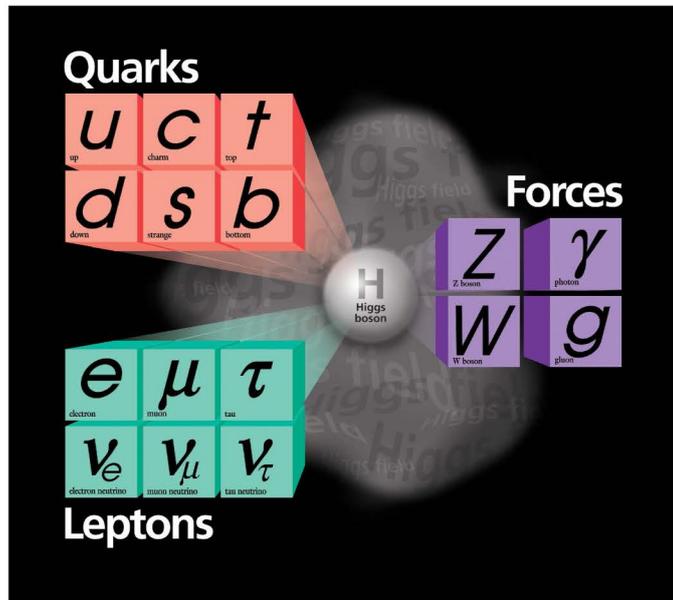


Figure 1.2: Higgs Boson and Particles.

### 1.2.2 Experimental Backgrounds

The Higgs mechanism and Weinberg-Angle predict the masses of charged weak bosons $(W^{\pm})$ and neutral weak boson $(Z^0)$. The Weinberg-Angle $\theta_W$ decides the mixing degree between electromagnetic force and weak force, has to be measured experimentally. Then, $W$ and $Z$ bosons are discovered in 1983 by UA1 and UA2 collaborations, which masses were close to predicted ones.
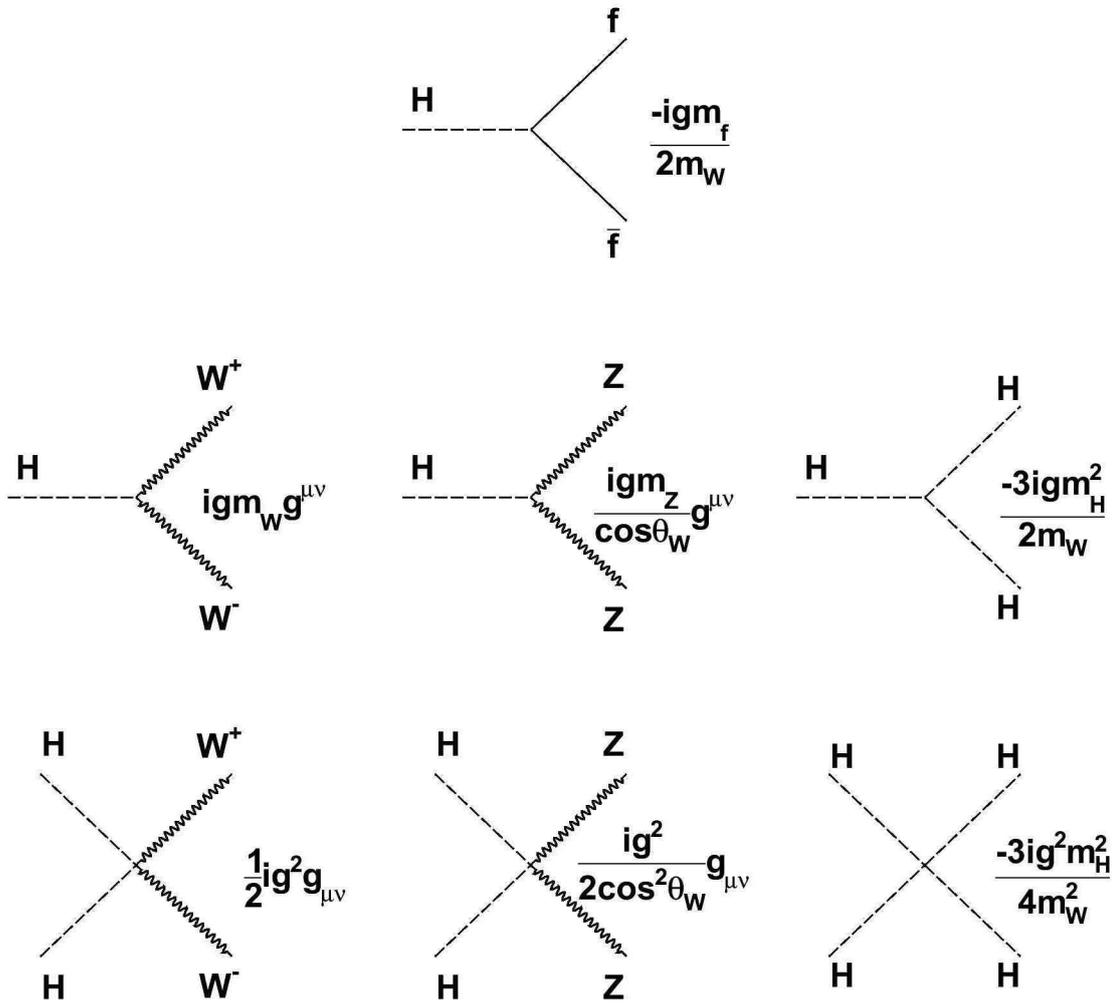
Figure 1.3:  Feynman diagrams and coupling for the Standard Model Higgs boson.

Based on the Standard Model, the masses of particles are parameters and Higgs mass itself is also one of parameters, which have to be measured experimentally. So many parameters are around the Standard Model Higgs boson and undecided.

From the view of experimental side, LEP-2 experiment in CERN directly exclude the region of Higgs mass $M_H < 114.4 GeV/c^2$ at 95 % confidence level in 2002. Tevatron/CDF&DZERO experiments exclude the mass range $158 GeV/c^2 < M_H < 175 GeV/c^2$ at 95 % confidence level in July 2010 (Fig. 1.5).

Production cross section of the Standard Model Higgs boson in Tevatron II is shown in Figure 1.4. The process which has the highest cross section is the process of Higgs production by gluon fusion. The processes of Higgs boson production associated with

vector boson follow gluon fusion production at Tevatron II.
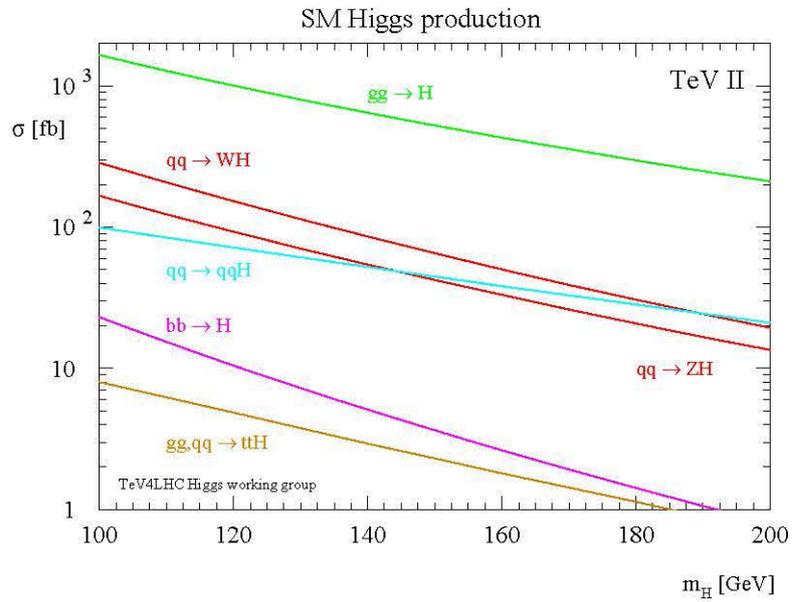


Figure 1.4:   Production Cross Section of Higgs boson in Tevatron II.
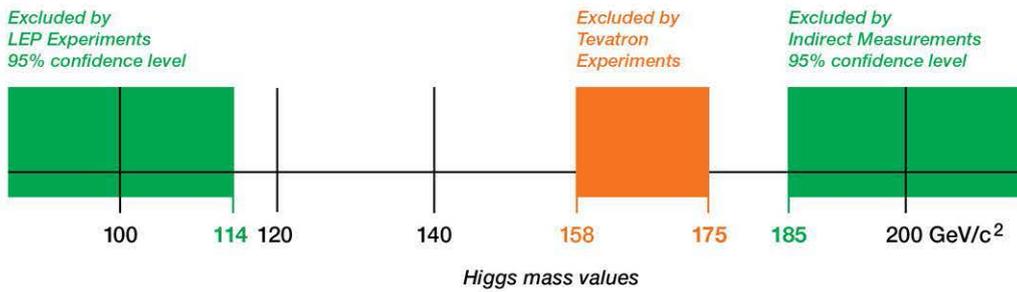


Figure 1.5:   The Standard Model Higgs Boson Mass Exclusion as of July 2010.

# Chapter 2

# Experimental Apparatus and Physical Objects

## 2.1 Fermi National Accelerator Laboratory

Fermi National Accelerator Laboratory (Fermilab) is located in Batavia, Illinois, which is close to Chicago. The laboratory was founded as the National Accelerator Laboratory (NAL) in 1967. It changed the name "NAL" to "Fermi National Accelerator Laboratory" in 1974 because of being reverence for Enrico Fermi. Its first beam of hight-energy particles was produced in 1972. Since then, hundreds of experiments have used the accelerator (Tevatron) to research on particles, which are component of matter at smaller scales.

Fermilab have obtained so many important achievements so far; Discovery of the top quark, Discovery of the bottom quark and subsequent studies of its properties, Determination of top quark and W boson masses to high precision, Observation of direct CP violation in kaon decays, Precise measurement of the lifetimes of charm particles, First direct evidence for the tau neutrino and so on.

Here, Fermilab's accelerator chain are described in next section.

## 2.2 Fermilab's Accelerator Chain

Accelerator of Fermilab is producing and accelerating protons and anti-protons beam. There are some accelerating stages. To use proton and anti-proton collisions has some advantages for technical and physics side. For technical side, an anti-proton and proton collider can be built with one accelerator ring of magnets because protons and anti-protons have equal and opposite electric charge, and they can fly in opposite directions through the magnets. For physics side, collision energy up to $\sqrt{s} = 3TeV$ is a borderline of production cross section of some processes between $\bar{p}p$ collisions and $pp$ collisions.

## FERMILAB'S ACCELERATOR CHAIN
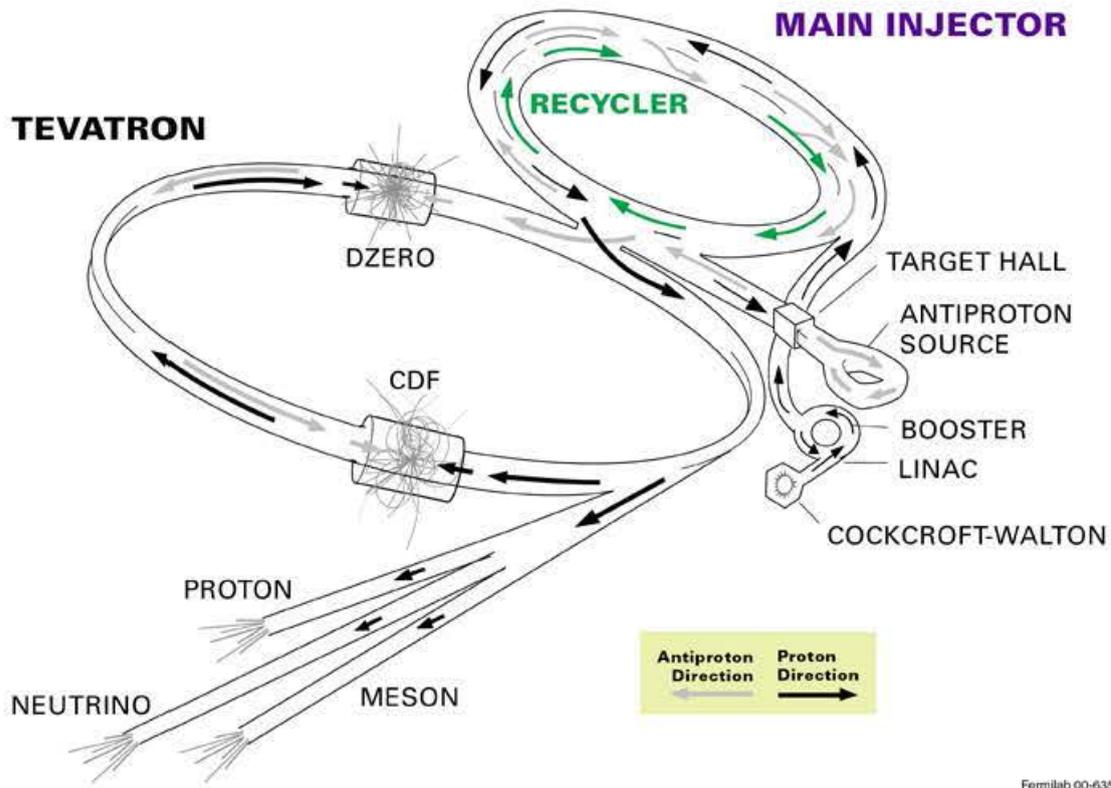


Figure 2.1: Fermilab's Accelerator Chain.

### 2.2.1   Proton Source

Protons are accelerated to 8 GeV kinetic energy in 3 steps, which are Cockroft-Walton pre-accelerator, Linear Accelerator and Booster Accelerator.

#### Cockcroft-Walton Accelerator

The Cockcroft-Walton Accelerator is a 750 kV DC voltage source. This accelerator is based on Cockcroft-Walton multiplier. This pre-accelerator is the first step of proton acceleration. Inside this apparatus, hydrogen gas is ionized to be negative ions $H^-$, which components are two electron and one proton. Then, ions are accelerated by positive voltage to 750 keV. The maximum voltage is limited by how much the air can "stand off" before sparking.

Figure 2.2: The Cockcroft-Walton Accelerator. This is the first step of Fermilab accelerator chain.

### Linac (Linear Accelerator)

After the first stage acceleration, negative hydrogen ions go to the linear accelerator. The length of tunnel is about 150 meter. In Linac, oscillating electric fields accelerate ions to 400 MeV. Before entering the third step (Booster), negative hydrogen ions are taken off two electrons, leaving only positive charged proton.

### Booster (Rapid Cycling Booster Accelerator)

The Booster is accelerating proton in circle pipe. To accelerate in circle, it uses magnets to bend the beam of protons. The protons are flying in the Booster about 20,000 times so that they repeatedly experience electric fields. With each revolution, the protons
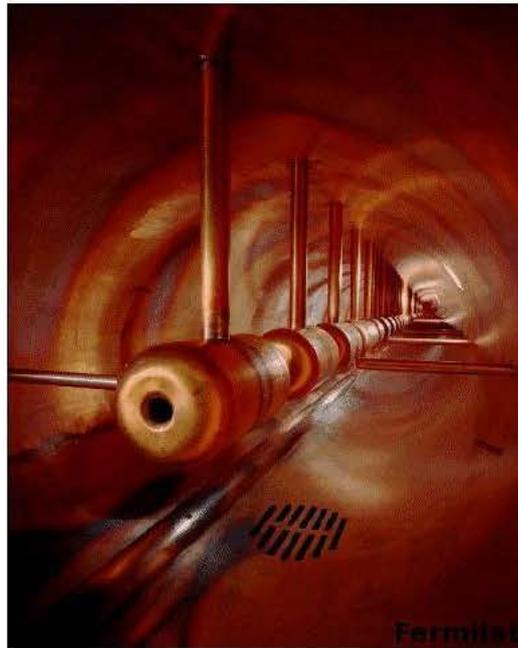
Figure 2.3:   The Linac Accelerator. This is the second step of Fermilab accelerator chain.

increase more energy, then, leave the Booster with 8 GeV.

## 2.2.2   Anti-proton Source

The anti-proton source apparatus (Figure 2.5) have three main components, which is the Target Station, the Debuncher and the Accumulator.

To produce anti-proton, 120 GeV proton beam from the main injector is sent to the Anti-proton Source, which is nickel target. The protons collide with a nickel target, then many secondary particles are produced, which particles are including many anti-protons. The anti-protons are bunched because of 120 GeV proton beam being bunched. Bunched anti-protons are debunched to transform from the large energy spread and narrow time spread, into a narrow energy spread and large time spread. Then, these are gathered, focused and then stored in the Accumulator ring.

## 2.2.3   Recycler

The aim of the Recycler is to increase the luminosity. The Recycler keep beam with a fixed 8 GeV kinetic energy in storage ring. It is placed in the Main Injector tunnel above the Main Injector pipe (beamline), which is close to the ceiling.

It was planned to 3 roles for the Recycler. The first part is to act as high reliability storage ring for anti protons. The second is to act like a post-Accumulator ring. The
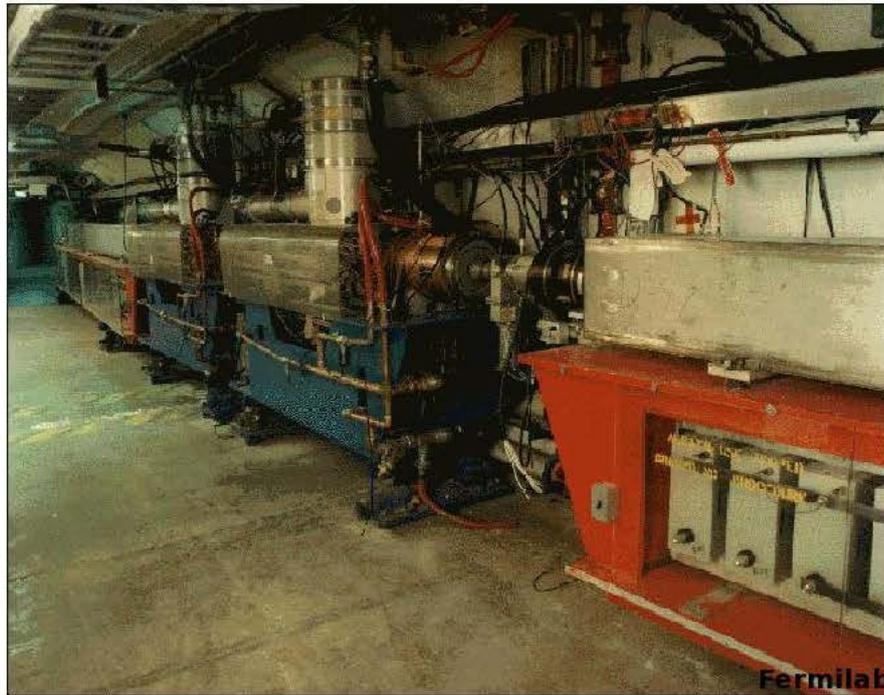
Figure 2.4: The Booster Accelerator.

third is to act as a receptacle for anti protons left over at the end of Tevatron stores. But third one has not worked so far.

### 2.2.4   Main Injector

The Main Injector has 4 roles for acceleration. The first role is to accelerate protons, which come from the Booster, from 8 GeV to 150 GeV. The second is to accelerate proton up to 120 GeV, which is used for anti-proton productions. The third is to accelerate anti-protons, which comes from Anti-proton Source apparatus, from 8 GeV to 150 GeV. The forth is to inject protons and anti-protons to the Tevatron.

### 2.2.5   Tevatron

The protons and anti proton with 150 GeV enter to the Tevatron from the Main Injector. The Tevatron accelerates protons and anti proton up to 980 GeV beam. The circumference of the Tevatron is about 6 km. The protons and anti protons circle the Tevatron ring in opposite directions, then cross each other at centers of CDF (Sec.2.3) and DZero detectors, which are located in the tunnel of the Tevatron. All dipole, quadrapole, and correction element magnets are superconducting magnets, cooled to about 4.6 Kelvin with liquid Helium. The separators around the ring separate the proton bunches from the anti-protons except at the collision regions. There are three

Figure 2.5: The Pbar Ring and The Pbar Souce Tunnel.

trains of 12 bunches and an abort gap between the trains in the Tevatron.

In the collider mode the Tevatron can store beams for hours once they are injected. The collision rate of proton-antiproton interactions is given by

$$R = \sigma_{int} L, \tag{2.1}$$

where $L$ is the instantaneous luminosity. It depends on the revolution frequency $f$ and the area $A$ that the beam occupies. If $N_p$ and $N_{\bar{p}}$ are the number of particles in each

Figure 2.6: The Main Injector and the Tevatron. The lower part of overlook picture is the Main Injector ring and the upper part is the Tevatron.

bunch and $n$ is the number of bunches in either beam, then the luminosity $L$ can be expressed by

$$L = \frac{fnN_pN_{\bar{p}}}{A} \tag{2.2}$$

This stable situation of 1960 GeV proton anti-proton collisions is called a store. The peak luminosity at the beginning of the stores in 2010 was $402.4(1/microbarn/sec)$, which is the maximum one (Figure 2.7). The store luminosity continually decreases from its initial values as protons and anti-protons are consumed through interactions and as the bunch emittance increases with time. The effect at the beginning of a store is largely dominated by emittance growth due to intrabeam scattering, while after several hours of running the effect of antiproton loss becomes more important and the luminosity falls off exponentially. In about 20 hours the luminosity drops too low, then the store is ended and the Tevatron prepare for new beam. This sequence of the stores continues 24 hours a day except for some short periods of time allocated for maintenance.

The integrated luminosity $\int L dt$ is the measure of the number of collisions during a time period (Figure 2.8).
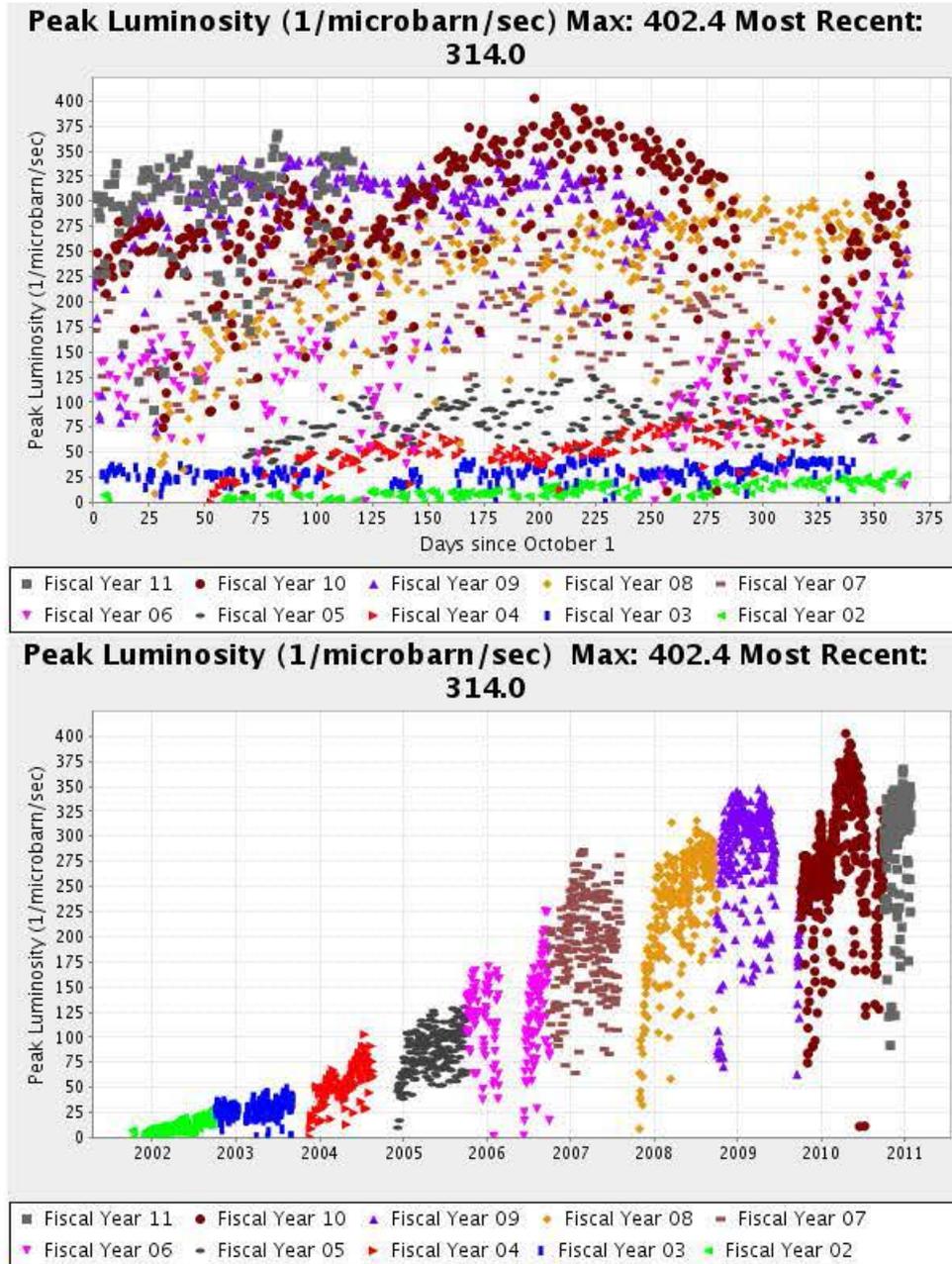
Figure 2.7:  Peak Luminosity
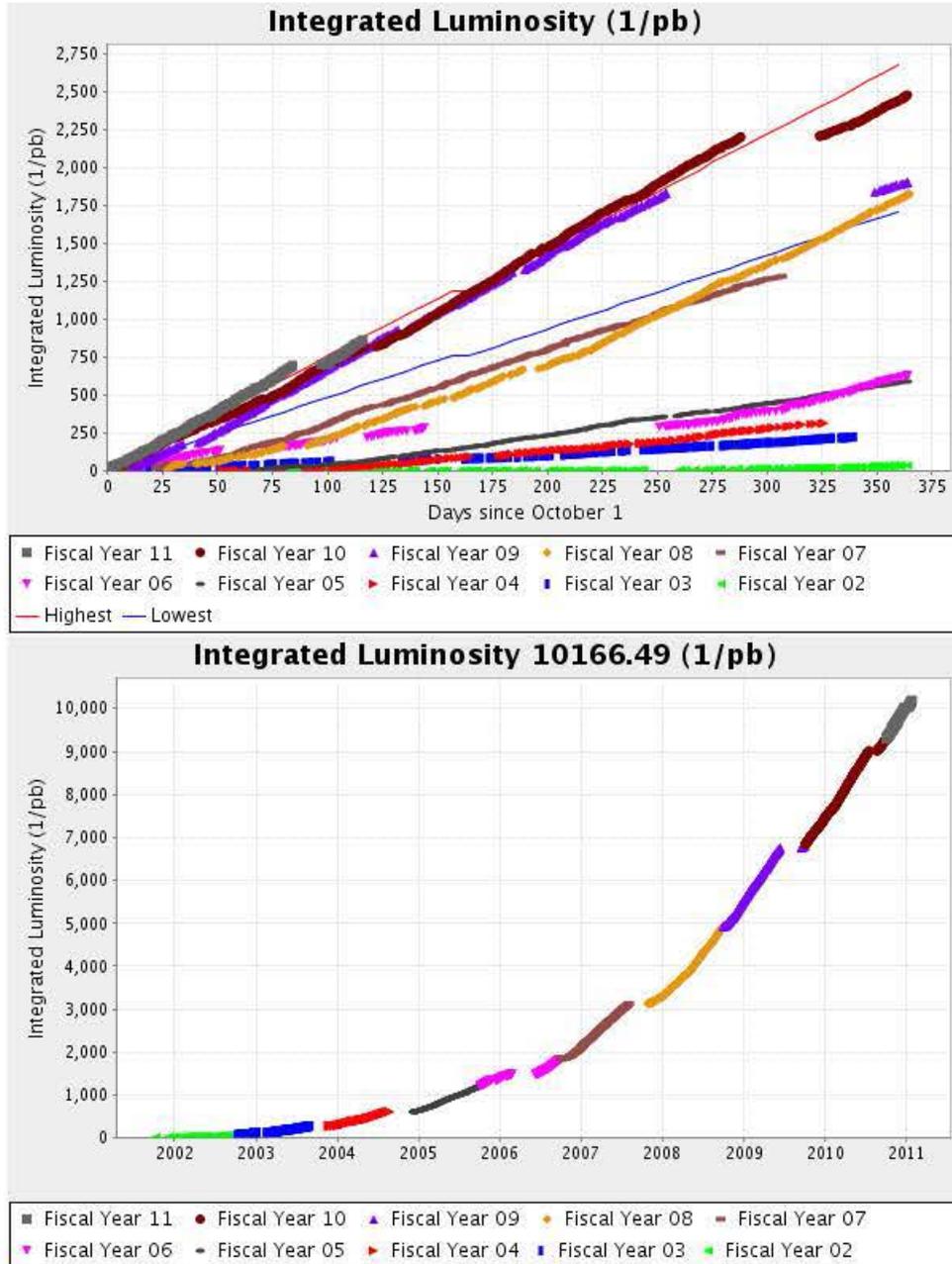
Figure 2.8:  Integrated Luminosity

## 2.3 Collider Detector at Fermilab (CDF)

CDF Run II detector (Fig. 2.9) had been improved since Run Ib experiment (1994-1995) was done. CDF detector is a compound detector, which are Silicon tracking detector, Central Outer Tracker, Electromagnetic Calorimeters, Hadron Calorimeters and Muon Detectors, ordered by innermost detector.
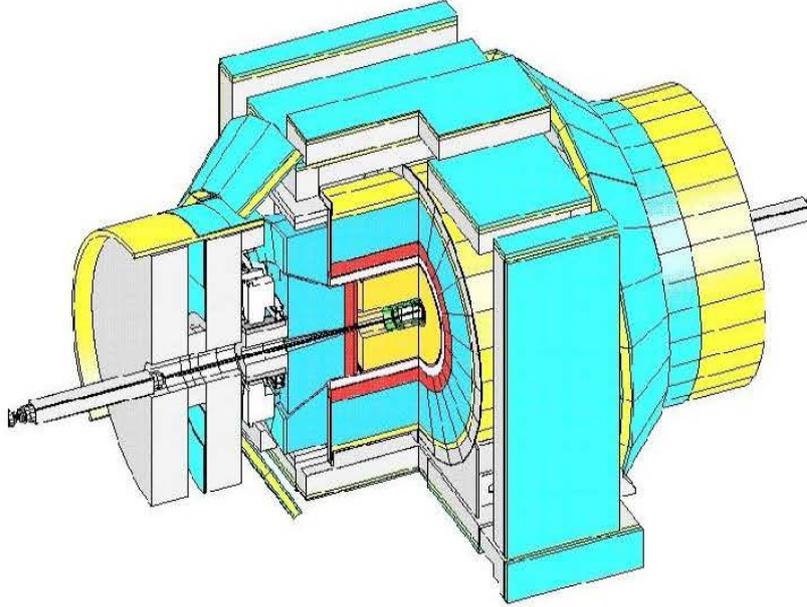


**Collider Detector at Fermilab**

Figure 2.9: Isometric Cartoon of Collider Detector at Fermilab.

The CDF in operation since 2001 is azimuthally and forward-backward symmetry apparatus about the transverse plane passing through the interaction point. It is useful coordinate to identify locations of particles in $\phi - \eta$ plane, where $\phi$ is the azimuthal angle and $\eta$ is the pseudo-rapidity represented in terms of the polar angle $\theta$ as

$$\eta = -ln(\tan\frac{\theta}{2}) \tag{2.3}$$

In detail, $\theta$ is the angle between the particle momentum $\vec{p}$ and the beam axis.

In terms of the momentum, the pseudo-rapidity can be written as below.

$$\eta = \frac{1}{2}ln(\frac{|\vec{p}| + p_L}{|\vec{p}| - p_L}), \tag{2.4}$$

where $p_L$ is the component of the momentum along the beam axis. It approximately represents,

$$\eta = \frac{1}{2}ln(\frac{E + p_L}{E - p_L}), \tag{2.5}$$

which is under assumption that particles velocity are close to the speed of light or the mass of the particle is nearly zero. The difference from Equation 2.4 is in order $\epsilon^2 = (\frac{m}{p_T})^2$. This value is often used in experimental particle physics because particles production is almost constant as a function of rapidity.
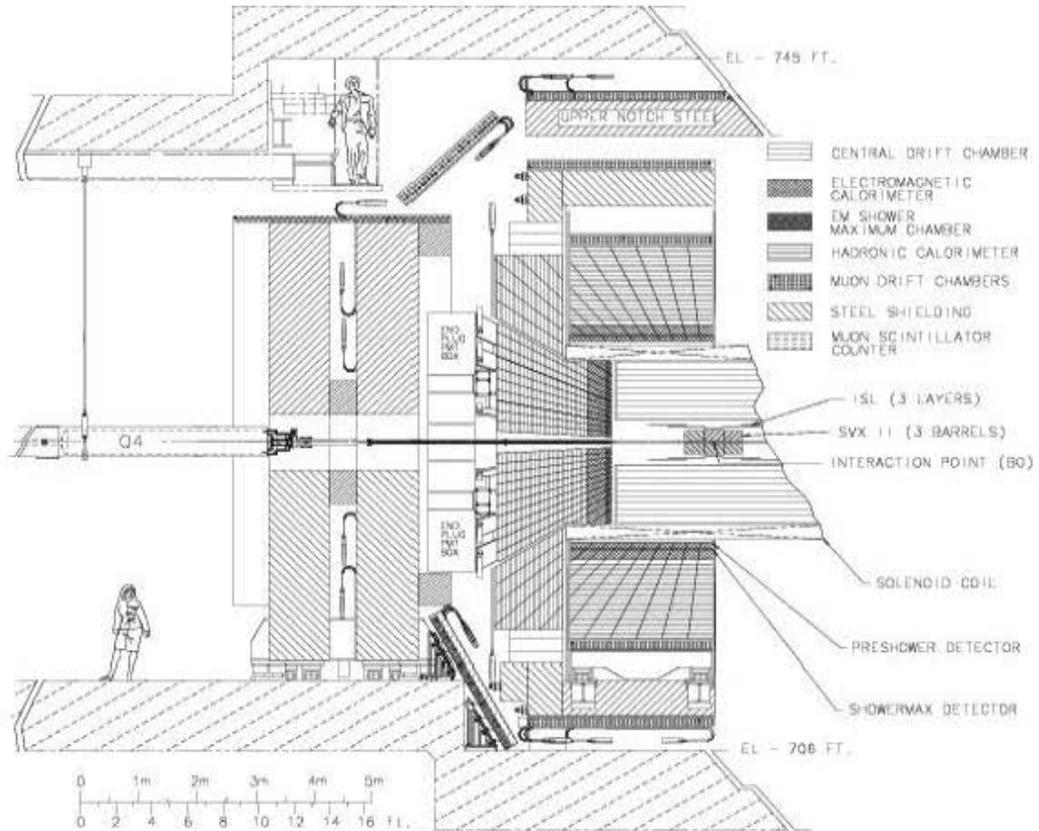


Figure 2.10: Elevation view of CDF detector.

## 2.3.1   Cherenkov Luminosity Monitor

The beam luminosity measurement is crucial part for the entire experiment. It is determined from the rate of inelastic $p\bar{p}$ interactions, called minimum bias events. The beam luminosity is determined by using gas Cherenkov counters located in $3.7 < |\eta| < 4.7$ region which measure the average number of inelastic $p\bar{p}$ collisions per bunch crossing [8].

## 2.3.2   Silicon Tracking System

Silicon Tracking System (Figure 2.11) is important detector to detect secondary vertices from heavy flavor, like bottom and charm quarks, weak decays. It is useful and excellent

tool for b-tagging and for b-physics.

## CDF  Tracking  Volume
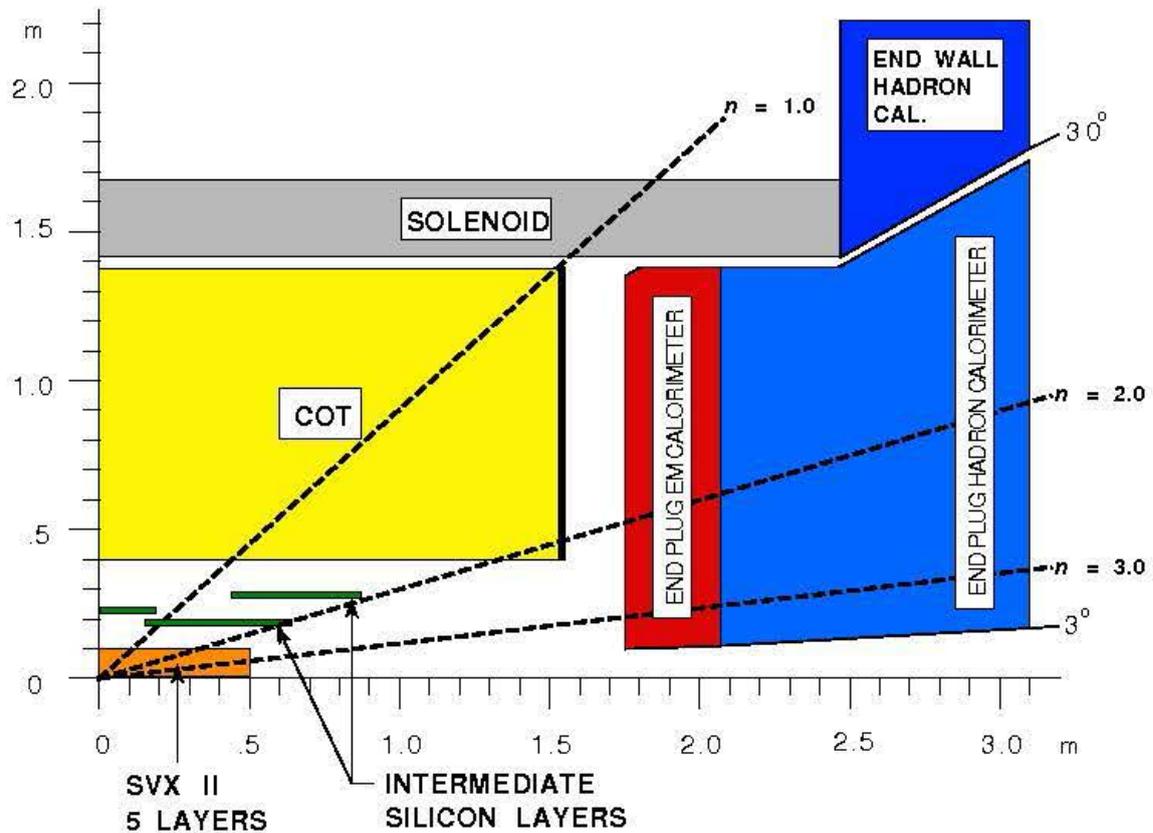


Figure 2.11:  Longitudinal View of the CDF II Tracking System.

In this paper, Silicon Tracking System is used for increasing quality of tracks for physical objects with high $\eta$ in particular.

## 2.3.3   Central Outer Tracker (COT)

The Central Outer Tracker (COT) is located outside the Silicon Tracking Detectors within a 1.4 T solenoidal magnetic field (Figure 2.11). It is designed to find charged tracks in the central region $|\eta| < 1.0$ with transverse momentum $p_T$ as low as $0.4 GeV$, and link tracks to hits in the inner silicon detectors. The COT is 3.1 m long cylindrical drift chamber [12] that covers the radial range from $40cm$ to $137cm$ and provides 96 measurement layers, organized into alternating axial and $\pm 2°$ stereo superlayers.

## 2.3.4 Calorimeter

Segmented electromagnetic and hadronic sampling calorimeters surround the tracking system and outside of solenoid. These cover the pseudo-rapidity range $|\eta| < 3.64$. These calorimeters are geometrically distinguished into two regions; the one is central region, the other is plug region.

These measure the energy flow of interacting particles which are neutral particles, and are charged particles with $p_T > 350 MeV$. Charged particles needs the energy more than $350 MeV$ to escape the magnetic field.

Basically, in particles traversing through the absorber, they lose energy and produce cascades of secondary particles, called showers, which then interact in the scintillators. The showers penetrate through many layers, and are sampled by the scintillators until they are completely absorbed. The scintillator's light is collected through acrylic light guides attached to phototube, which are located at the rear end of each wedge.

### Central Calorimeter

The central calorimeters cover the pseudo-rapidity region $|\eta| < 1.1$. In including the endwall hadronic calorimeters, they cover the pseudo-rapidity region $|\eta| < 1.3$. The central calorimeters are divided azimuthally into 24 wedges, so each wedge cover an azimuthal angle of 15° and extending about 250 cm along the beam axis on either side of $z = 0$.

**Electromagnetic Shower Counter**  The Central Electromagnetic Shower counter (CES), which is a proportional strip and wire chamber, is embedded in each tower of the central calorimeter at location where maximal average electromagnetic shower deposition occurs, to measure precisely the transverse energy. The CES has cathode strips running in the azimuthal direction, which provide $r - \phi$ information.

**Electromagnetic Calorimeter**  The central electromagnetic calorimeter (CEM) uses lead sheets interspersed with polystyrene scintillator as the active medium and adopts phototube readout. Its energy resolution is $13.5\%/\sqrt{E_T} \oplus 2\%$.

**Hadronic Calorimeter**  The endwall hadronic calorimeter cover the pseudo-rapidity range $|\eta| < 1.3$. The central hadronic calorimeter (CHA) uses steel absorber interspersed with acrylic scintillator as the active medium. Its energy resolution is $75\%/\sqrt{E_T} \oplus 3\%$.

### Plug Calorimeter

The Plug Calorimeters cover the pseudo-rapidity region $1.1 < |\eta| < 3.64$ (([13])). These are sampling calorimeters which are read out with plastic fibers and phototubes. The geometry of plug calorimeters is shown in Figure 2.12.
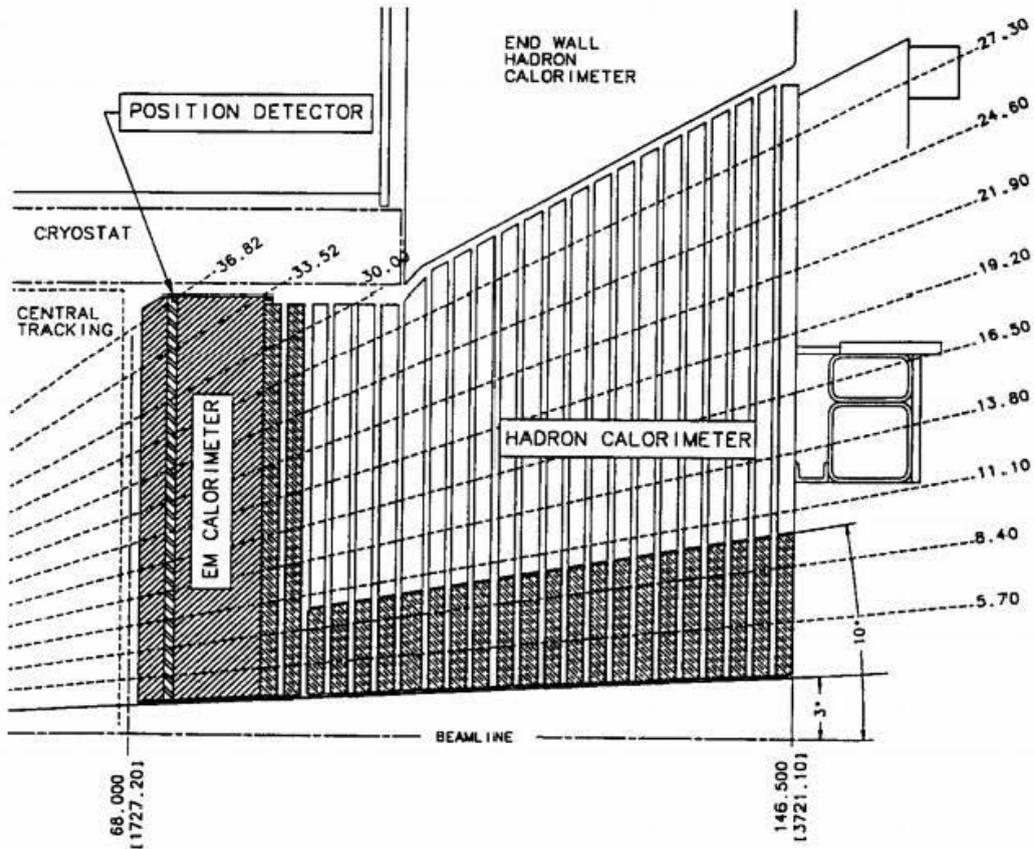
Figure 2.12:  Cross section of upper part of new end plug calorimeter.

**Electromagnetic Calorimeter**    The energy resolution of the plug electromagnetic calorimeter is $16\%/\sqrt{E_T} \oplus 1\%$.

**Hadron Calorimeter**    The energy resolution of the plug hadronic calorimeter is $74\%/\sqrt{E_T} \oplus 4\%$.

## 2.3.5  Muon Detectors

Muon Detector System are made up of four different regions, which are Central Muon Detector (CMU), Central Muon Upgrade (CMP), Central Muon Extension (CMX) and Intermediate Muon Detector (IMU). Muon Detector System also resides outside of calorimeter because muon are characterized by their penetrating ability.

All Muon Detectors coverage are shown in Figure 2.13 by $\eta - \phi$ plane.
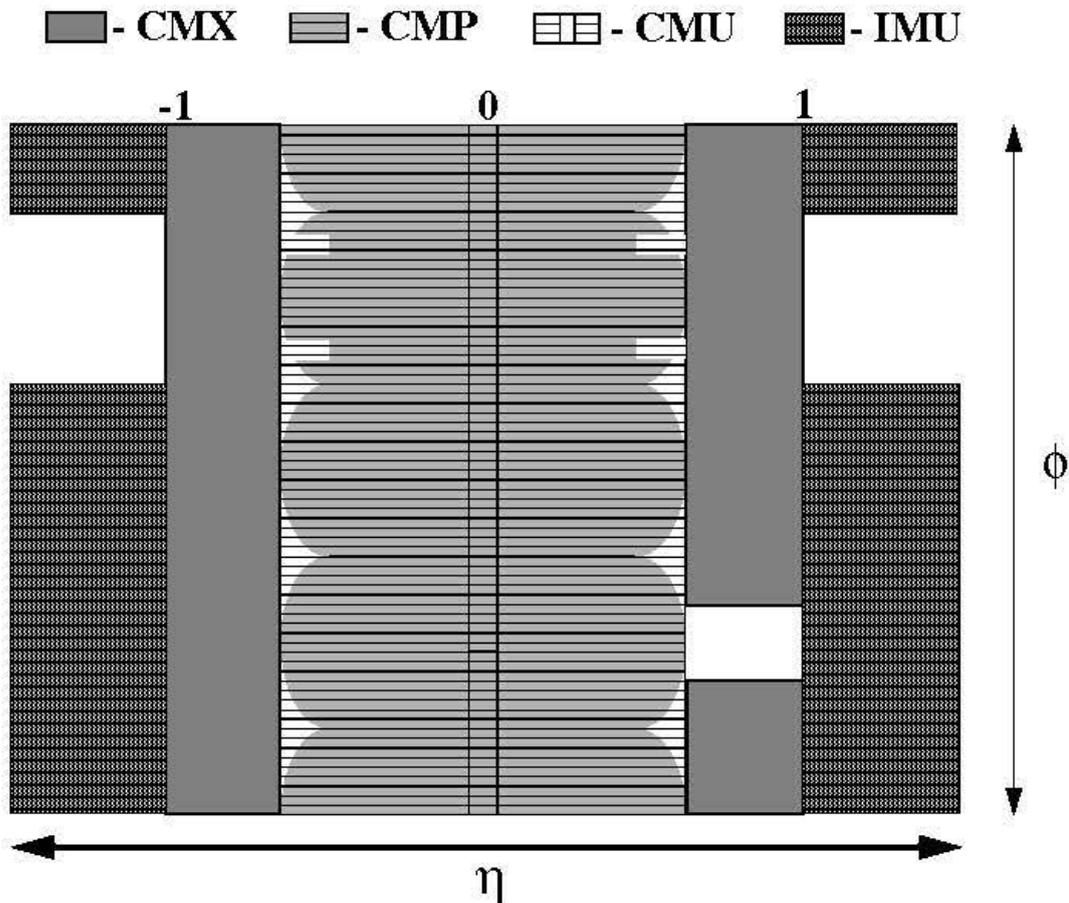
Figure 2.13: Muon Detector Coverage.

## CMU

CMU that have four layers of planar drift chambers detect muons with $p_T > 1.4 GeV/c$ which penetrate the five absorption lengths of calorimeter steel ($\sim 5.5\lambda$). The set of muon chambers consists of 144 modules with 16 rectangular cells per module, which cell is $6.35 \times 2.68 \times 226$ cm in size and has $50\mu m$ stainless steel wire in the center. The 16 cells in a module are stacked four deep in the radial direction, with a small $\phi$ offset between the first and third and second and fourth layers. More information about the CMU detector is described in [21].

## CMP/CSP

CMP, that have additional four layers of planar drift chambers and have $0.6m$ of steel outside the magnet return yoke, detect muons with $p_T > 2.0 GeV/c$. A layer of scintillation counters (the CSP) is installed on outside surface of the CMP chambers.

The counters are rectangular in shape: 2.5 cm $\times$ 15 cm $\times$ 320 cm. The total number of scintillation counters is 216. These counters are read out by single phototubes which are located at the center of the array. The scintillation light comes from scintillator and wave length shifting fibers, which is glued on side of scintillator (2.5 cm $\times$ 320 cm) [22]. Then, the CMU and CMP cover $|\eta| < 0.6$.
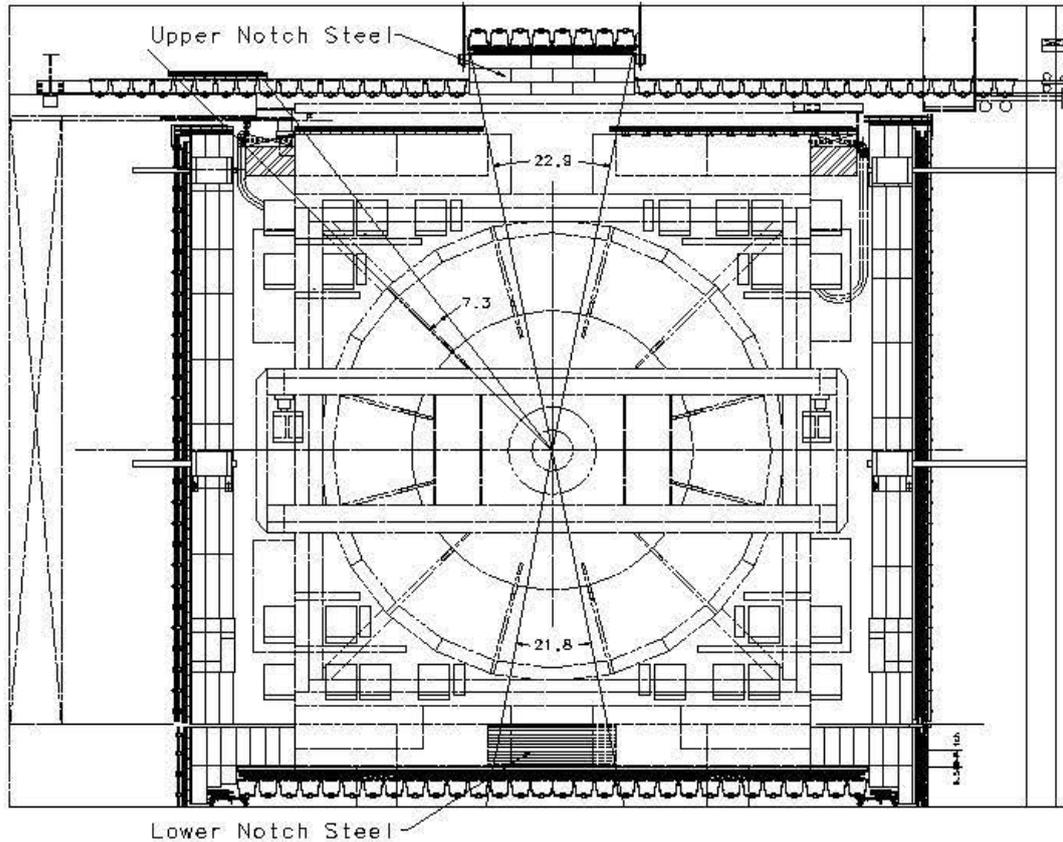


Figure 2.14: Configuration of the Central Muon Upgrade (CMP), Central Upgrade Scintillator (CSP) and steel absorber in Run II.

## CMX/CSX

The CMX (Central Muon Extension) muon chamber extended muon detector coverage and the CSX (Central Scintillator Extension) is located at each end of the central detector and extending in polar angle from $\sim 0.6 < |\eta| < \sim 1.0$.

## IMU(BMU/BSU&TSU)

The IMU (Intermediate Muon Detector) covers the region $1.0 < |\eta| < 1.5$ and consists of the Barrel Muon Detector (BMU), the Barrel Scintillator Upgrade (BSU) and the Toroid Scintillator Upgrade (TSU).
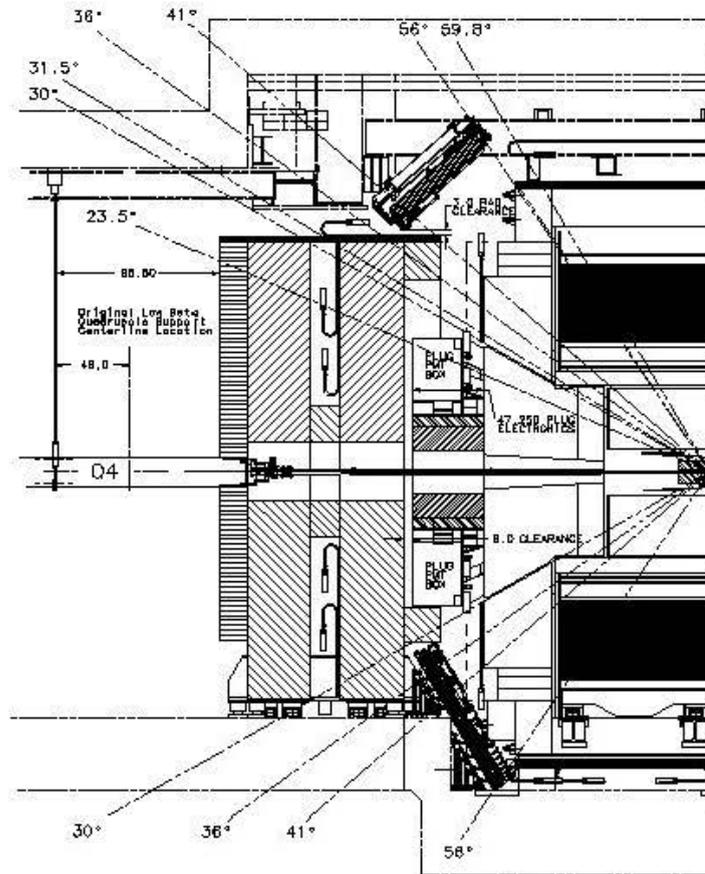
Figure 2.15: Side view showing the placement of chambers to complete the CMX coverage and the IMU barrel chambers (BMU) and scintillator (BSU), toroid scintillator (TSU) and the endwall counters are also shown.
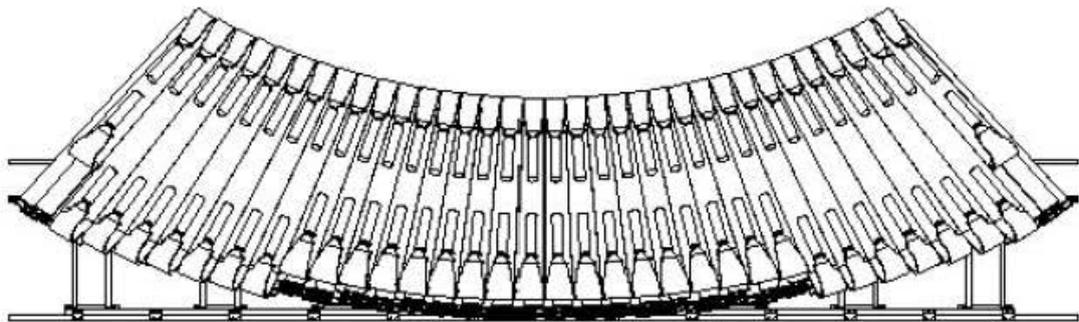


Figure 2.16: Lower chambers for the Central Muon Extension and Scintillators.
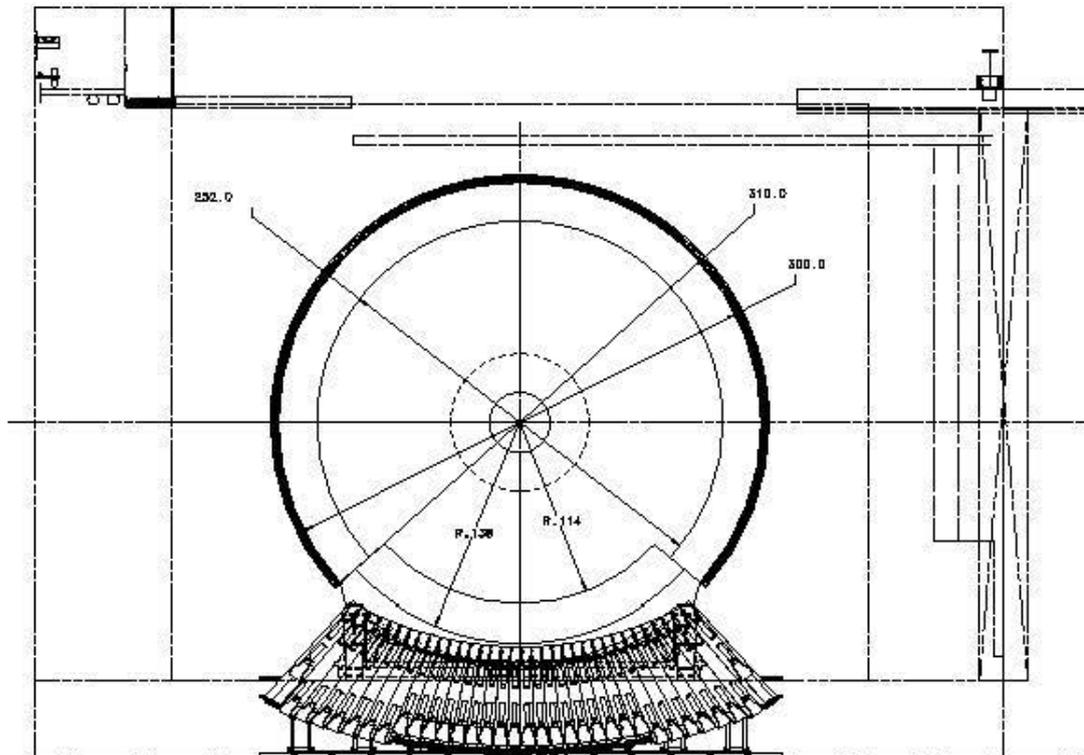
Figure 2.17: Elevation view of the IMU Barrel. The IMU chamber and scintillator are installed at the outer circle around the toroids. The CMX lower 90° section is also shown.

## 2.3.6 Trigger and Data Acquisition System

The trigger and data acquisition systems (Figure 2.18) are designed to accommodate the high rates and large data come from upgraded Tevatron, Run II. To accommodate a 132 nsec bunch-crossing time and a 5.5 $\mu$sec decision time for the first trigger level, all front-end electronics are fully pipelined, with on-board buffering for 42 beam crossings.
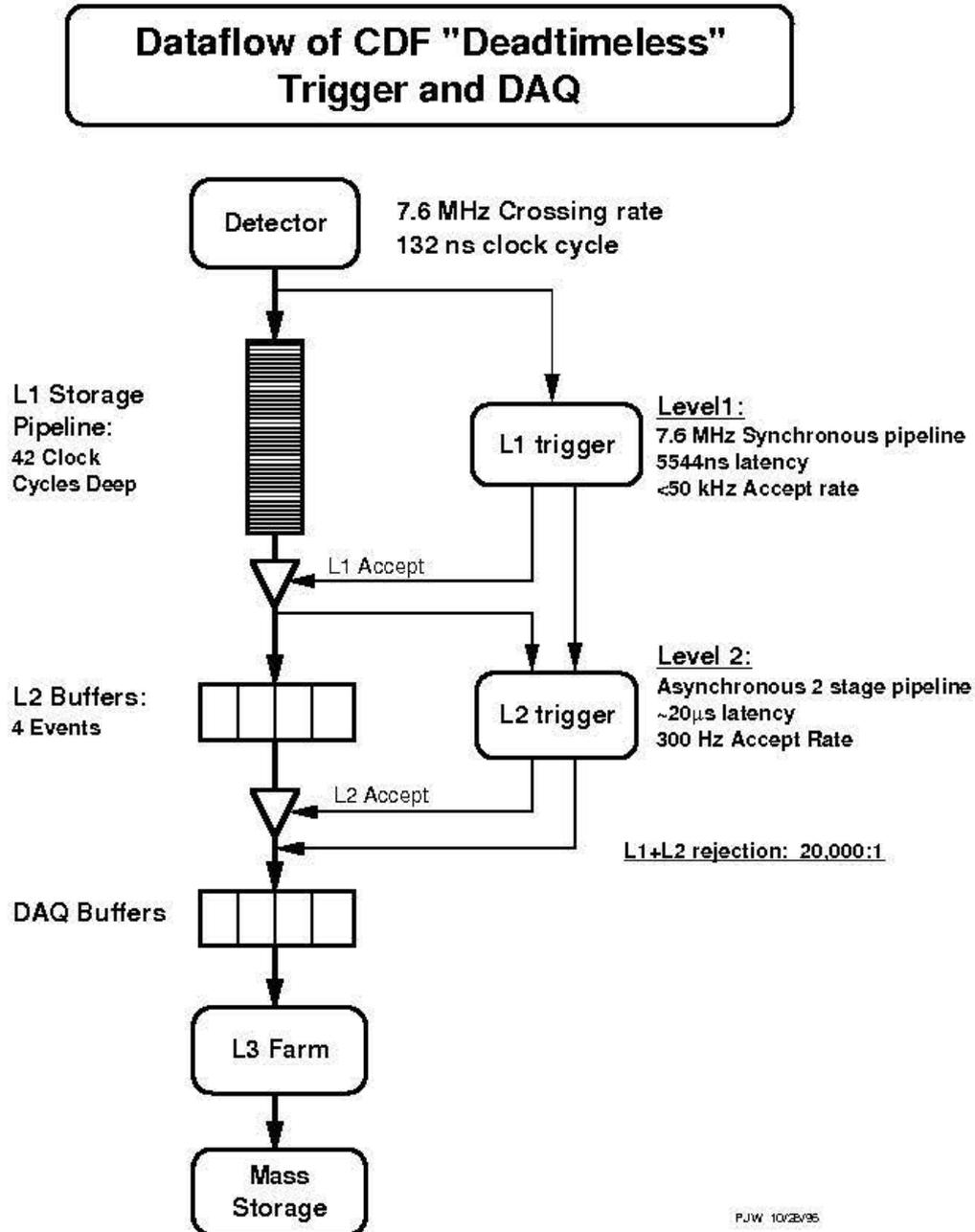


Figure 2.18: Functional block diagram of the CDF II data flow.

## 2.4 Physical Objects in Experiments

Physical objects are reconstructed from detector responses as in Figure 2.19. Photons might be detected as object that does not have any track and has the most of imprints in electromagnetic calorimeters. Electrons might be detected as object that has a single track and has energy deposit like as photon. Because muons penetrate strongly, it is detected as a single track and a minimum ionizing particle.
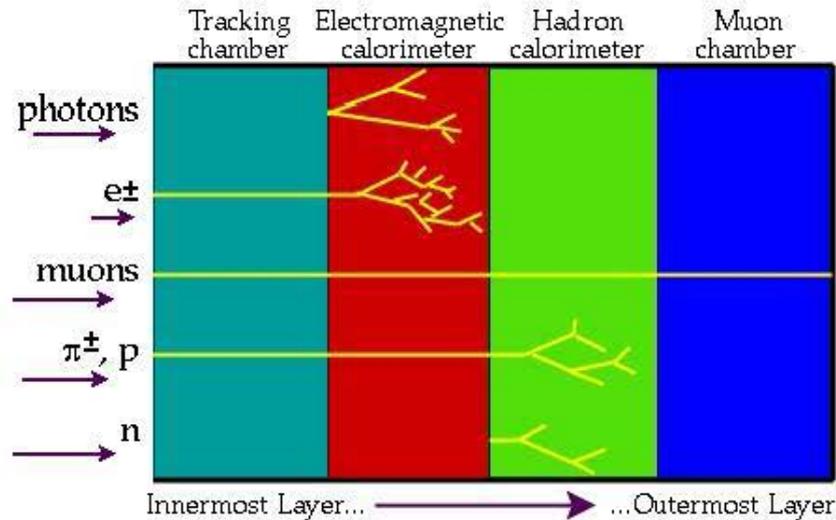


Figure 2.19: Particle Detection Cartoon. In CDF case, "Tracking chambers" are silicon tracking detector & COT, "Electromagnetic calorimeters" are CEM & PEM, "Hadronic calorimeters" are CHA & PHA, "Muon chambers" are CMU & CMP & CMX & BMU.

## 2.4.1 Electron Identification

Electrons are categorized to 3 types; tight **TCE** central electrons, loose **LCE** central electrons and **PHX** plug electrons.

Electron candidates deposit the most of their energies in the CEM calorimeters, moreover a single electromagnetic calorimeter tower.

| | TCE |
|---|---|
| Region | Central |
| Fiducial | Track Fiducial to CES |
| Track $p_T$ | $\geq 10(5$ if $E_T < 20)$ |
| Track $|z_0|$ | $\leq 60cm$ |
| #Ax Super Layer (5hits) | $\geq 3$ |
| #St Super Layer (5hits) | $\geq 2$ |
| Conversion | Excluded |
| Had/Em | $\leq 0.055 + 0.00045E$ |
| Iso/$E_T$ | $\leq 0.1$ |
| Lshr | $\leq 0.2$ |
| E/P | $< 2.5 + 0.015E_T$ |
| Signed CES $\Delta X$ | $-3cm \leq q\Delta X \leq 1.5cm$ |
| CES $|\Delta Z|$ | $< 3cm$ |
| Tracks | beam constrained track |

Table 2.1: Tight CEM Electron Identification Cuts.

| | LCE |
|---|---|
| Region | Central |
| Fiducial | Track Fiducial to CES |
| Track $p_T$ | $\geq 10(5$ if $E_T < 20)$ |
| Track $|z_0|$ | $\leq 60cm$ |
| #Ax Super Layer (5hits) | $\geq 3$ |
| #St Super Layer (5hits) | $\geq 2$ |
| Conversion | Excluded |
| Had/Em | $\leq 0.055 + 0.00045E$ |
| Iso/$E_T$ | $\leq 0.1$ |
| Tracks | beam constrained track |

Table 2.2: Loose CEM Electron Identification Cuts.

| | PHX |
|---|---|
| Region | Plug |
| PES to Detector $\eta$ | $1.2 < |\eta| < 2.0$ |
| PEM 3x3 Fit Tower | true |
| PEM 3x3 $|\chi^2|$ | $\leq 10$ |
| PES 5x9 U | $\geq 0.65$ |
| PES 5x9 V | $\geq 0.65$ |
| Iso$/E_T$ | $\leq 0.1$ |
| $\Delta R$(PES, PEM) | $\leq 3.0$ |
| # Si Hits | $\geq 3$ |
| Track $|Z_0|$ | $\leq 60cm$ |

Table 2.3: Phoenix Electron Identification Cuts.
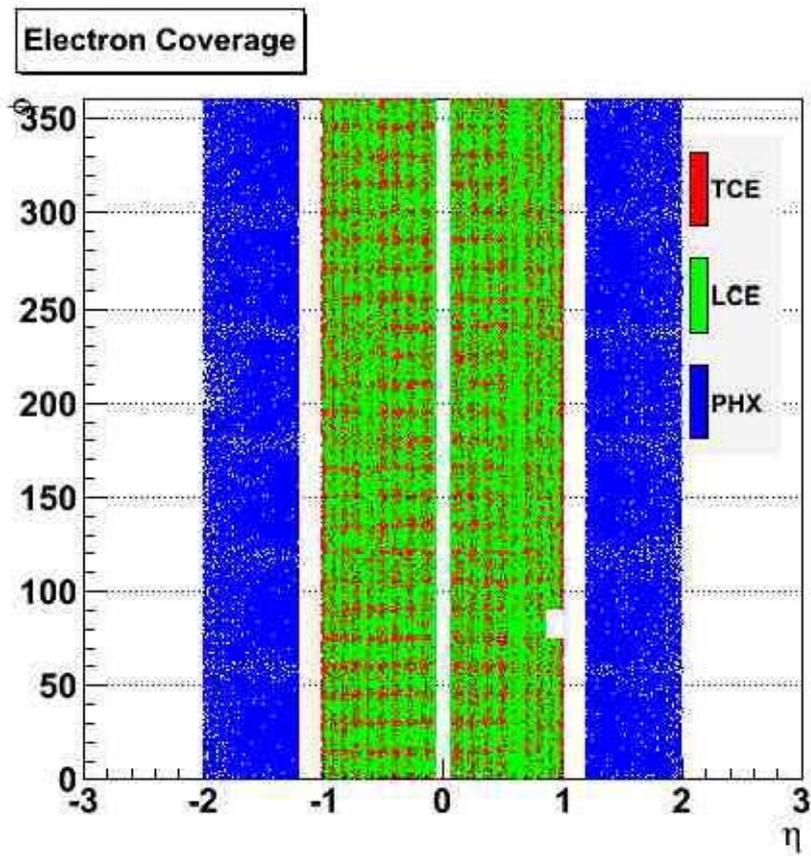


Figure 2.20: Electron Coverage.

## 2.4.2 Muon Identification

Muons are categorized to 7 types; **CMUP** muons, **CMX** muons, **CMU-only**, **CMP-only**, **CMIOCES**, **CMIOPES** and **BMU**.

The first two categories (**CMUP/CMX**) are triggered objects in this paper. The **CMUP** muons are reconstructed in both the CMU and CMP chambers. The **CMX** muons are detected by CMX detector.

| | CMUP/CMX |
|---|---|
| CMU Fiducial | x-fid $< 0cm$, z-fid $< 0cm$ |
| CMP Fiducial | x-fid $< 0cm$, z-fid $< -3cm$ |
| CMX Fiducial | x-fid $< 0cm$, z-fid $< -3cm$ |
| $E_{em}$ | $\leq 2 + \max(0, (p - 100) \times 0.0115)GeV$ |
| $E_{had}$ | $\leq 6 + \max(0, (p - 100) \times 0.028)GeV$ |
| Iso/$P_T$ | $\leq 0.1$ |
| #Ax Super Layer (5 hits) | $\geq 3$ |
| #St Super Layer (5 hits) | $\geq 2$ |
| Track $|Z_0|$ | $\leq 60cm$ |
| Track $|d_0|$ | $\leq 0.2cm$ ($0.02cm$ if #SiHits$> 0$) |
| $\chi^2/ndf$ | $\leq 3$ (4 if run $\leq 186598$) |
| $|\Delta x_{CMU}|$ | $\leq 7$ cm |
| $|\Delta x_{CMP}|$ | $\leq 5$ cm |
| $|\Delta x_{CMX}|$ | $\leq 6$ cm |
| $\rho_{exit}$ | $> 140$ cm if CMX |
| CMP veto | No Bluebeam in CMP for run $< 154449$ |
| CMX veto | No CMX for run $< 150144$, No Miniskirt, No Keystone |
| Arches | Arches only for all run range |
| | Arches removing wedge 14 on West Side for run $> 190697$ |

Table 2.4: CMUP and CMX Muon Identification Cuts.

The **CMU(CMP)** muons are fiducial to the **CMU(CMP)** detectors but not to the **CMP(CMU)** detectors. Further, the **CMU** muons are required not to be fiducial to the **CMX** detectors, because there is a small overlap between these detectors. The **CMP** muons also have an additional $\pm 2°$ cut around the gaps. Identification cuts for the **CMU/CMP** muons are listed in Table 2.5.

The **BMU** muons cover pseudo-rapidity region $1.0 < |\eta| < 1.5$, are detected by using the Intermediate Muon detector. The **BMU** muons increase the purity of the current stubless forward muon category (**CMIOPES**). The **BMU** muons are required its track is fiducial to the PES detector. This restriction makes the available coverage of the chamber be like small, so the **BMU** muons are defined as a subset of the **CMIOPES** stubless muons. Identification cuts are listed in Table 2.6.

The **CMIOCES/CMIOPES** stubless muons are the minimum ionizing tracks

| CMU/CMP | |
|---|---|
| $E_{em}$ | $\leq 2 + \max(0, (p - 100) \times 0.0115) GeV$ |
| $E_{had}$ | $\leq 6 + \max(0, (p - 100) \times 0.028) GeV$ |
| Iso/$P_T$ | $\leq 0.1$ |
| #Ax Super Layer (5 hits) | $\geq 3$ |
| #St Super Layer (5 hits) | $\geq 2$ |
| Track $|Z_0|$ | $\leq 60cm$ |
| Track $|d_0|$ | $\leq 0.2cm$ (0.02cm if #SiHits$> 0$) |
| $\chi^2/ndf$ | $\leq 3$ (4 if run $\leq 186598$) |
| CMU | |
| CMU Fiducial | x-fid $< 0cm$, z-fid $< 0cm$ |
| $\Delta x_{CMU}$ | $\leq 7cm$ |
| CMP veto | Not in CMP Fiducial |
| CMX veto | Not in CMX Fiducial |
| CMP | |
| CMP Fiducial | x-fid $< 0cm$, z-fid $< -3cm$ |
| $\Delta x_{CMU}$ | $\leq \max(6.0, 150.0/p_T)cm$ |
| $\phi$-gaps | $\phi$ mod $15° \leq 2$ or $\phi$ mod $15° \geq 13$ |
| CMU veto | Not in CMU Fiducial |
| | No Bluebeam for run $\leq 154449$ |
| Tracks are beam constrained track | |

Table 2.5: CMU and CMP Muon Identification Cuts.

| BMU | |
|---|---|
| Fiducial | PES Fiducial |
| | BMU Fiducial |
| $E_{em}$ | $\leq 2 + \max(0, (p - 100) \times 0.0115) GeV$ |
| $E_{had}$ | $\leq 6 + \max(0, (p - 100) \times 0.028) GeV$ |
| $E_{em} + E_{had}$ | $> 0.1$ GeV |
| Iso/$P_T$ | $\leq 0.1$ |
| Track $|Z_0|$ | $\leq 60cm$ |
| Track $|d_0|$ | $\leq 0.2cm$ (0.02cm if #SiHits$> 0$) |
| #Ax Super Layer (5 hits) | $\geq 1$ for $\eta_{det} < 1.25$, $\geq 1$ for $\eta_{det} \geq 1.25$ |
| #St Super Layer (5 hits) | $\geq 2$ for $\eta_{det} < 1.25$, $\geq 1$ for $\eta_{det} \geq 1.25$ |
| $\Delta x_{BMU}$ | $< 9cm$ |

Table 2.6: BMU Muon Identification Cuts.

which point into the fiducial volume of the CES/PES. Identification cuts are listed in Table 2.7. These are inside-out tracks which COT track is with no muon stubs. The

**CMIOCES** stubless muons are required not to be identified **CMUP, CMX, CMU-only** and **CMP-only**. The **CMIOPES** stubless muons are required not to be **BMU** muons.

| CMIOCES/CMIOPES | |
|---|---|
| $E_{em}$ | $\leq 2 + \max(0, (p - 100) \times 0.0115)GeV$ |
| $E_{had}$ | $\leq 6 + \max(0, (p - 100) \times 0.028)GeV$ |
| Iso/$P_T$ | $\leq 0.1$ |
| Uniqueness | Not a CMUP or CMX muon |
| Track $|Z_0|$ | $\leq 60cm$ |
| Track $|d_0|$ | $\leq 0.2cm$ (0.02cm if #SiHits> 0) |
| $E_{em} + E_{had}$ | $> 0.1$ GeV |
| CMIOCES | |
| Track Fiducial | Tracks in CES Fiducial |
| #Ax Super Layer (5 hits) | $\geq 3$ |
| #St Super Layer (5 hits) | $\geq 3$ |
| $\chi^2/ndf$ | $\leq 3$ |
| | Tracks are beam constrained track |
| CMIOPES | |
| Track Fiducial | Tracks in PES Fiducial |
| Cot Hit Fraction | $> 0.6$ |
| | No beam constraint on IO tracks |

Table 2.7:  CMIOCES and CMIOPES Stubless Muon Identification Cuts.
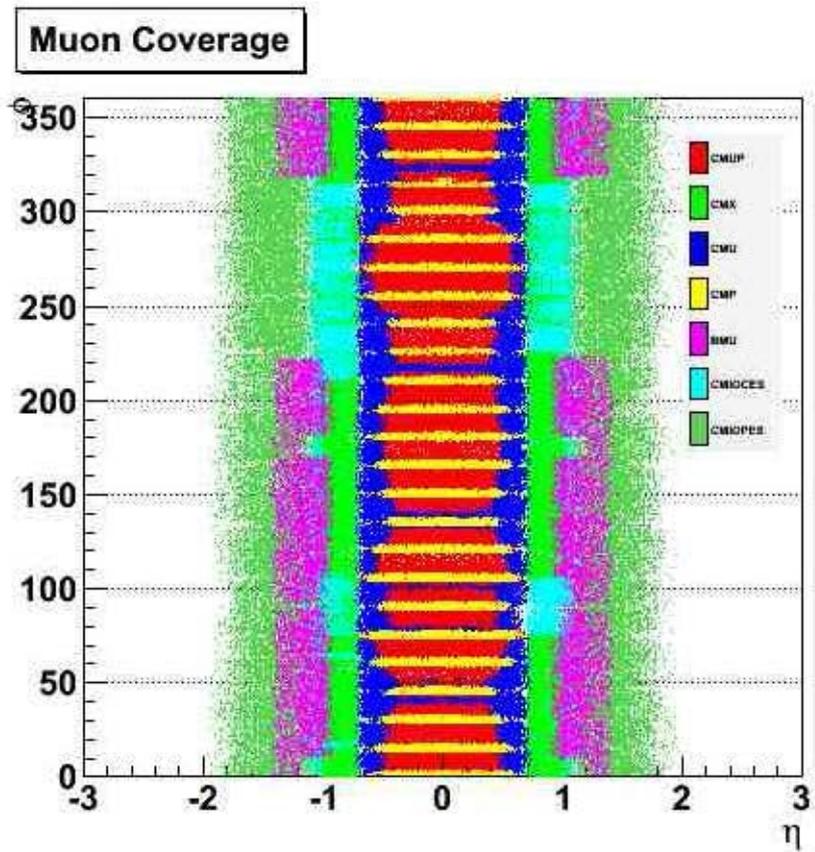
Figure 2.21: Muon Categories and Coverage.

### 2.4.3 Crack Track Identification

For tracks going into cracks of CDF detector, this category of lepton are called the **CrkTrk**. The **CrkTrk** is similar to the **CMIOCES** stubless muon category except for no minimum ionizing calorimeter requirements and the tracks being required not to be in the fiducial volume of the CES or PES. These try to fill in the cracks between the CEM wedges , the wedge edges which are not CES fiducial, $\eta = 0$ and $|\eta| = 1$. The **CrkTrk** category might be electron, muon or 1-prong hadronic tau. The problem is to define the calorimeter isolation variable. The calculation of isolation for muons excludes the towers into which the muon candidate projects, but for electromagnetic calorimeter objects the isolation excludes all the towers in the electromagnetic calorimeter cluster. The isolation on the basis of the nearest electromagnetic calorimeter object within $\Delta R < 0.05$ or as a muon only excluding the high towers. Identification cuts are listed in Table 2.9.

In calculating $\not{E}_T$, the **CrkTrk** is treated as a muon, but the energy of the nearest electromagnetic calorimeter cluster is removed if it is within $\Delta R < 0.05$.

| | CrkTrk |
|---|---|
| Iso/$P_T$ | $\leq 0.1$ using CDF Muon or |
| | $\leq 0.1$ using nearest CDF EMObj with $\Delta R < 0.05$ |
| Track $|Z_0|$ | $\leq 60cm$ |
| Track $|d_0|$ | $\leq 0.2cm$ ($0.02cm$ if #SiHits$> 0$) |
| $\chi^2/ndf$ | $\leq 3$ |
| | Tracks are beam constrained track |
| #Ax Super Layer (5 hits) | $\geq 3$ |
| #St Super Layer (5 hits) | $\geq 3$ |
| Uniqueness | Not a CMUP or CMX muon |
| Track Fiducial | Not in CES or PES Fiducial |
| Conversion | Excluded |

Table 2.8: Crack Track Identification Cuts.
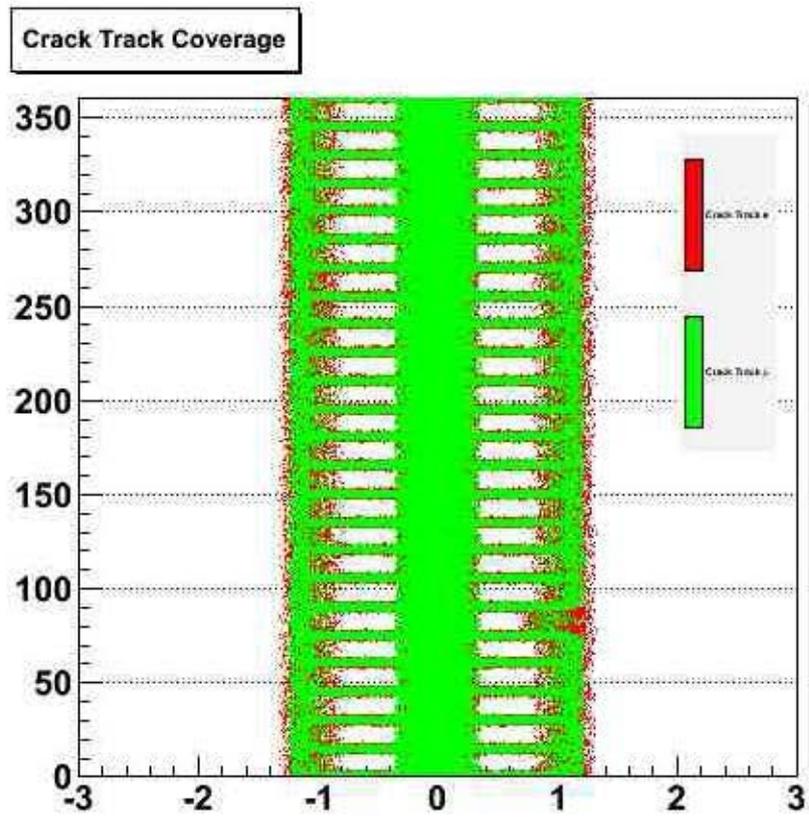
Figure 2.22: Crack Track Coverage.

## 2.4.4 Hadronic Tau Identification

Tau lepton identification is characterized to 2 types (2.23) by the way to decay; one is leptonic decay, the other is hadonic decay. When tau decays to electron or muon: $\tau \rightarrow l\nu_l\nu_\tau$, this case is identified by electron or muon. When tau decays to hadrons: $\tau \rightarrow X_h\nu_\tau$, it can be characterized by a narrow bundle of hadrons (2.24). $X_h$ can be a $\pi^\pm/K^\pm$, or some short-lived intermediate resonance that decays directly to final states containing $\pi^{\pm,0}$, $K^{\pm,0}$.
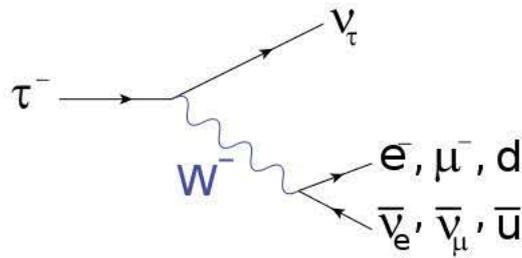


Figure 2.23: Tau Decay.
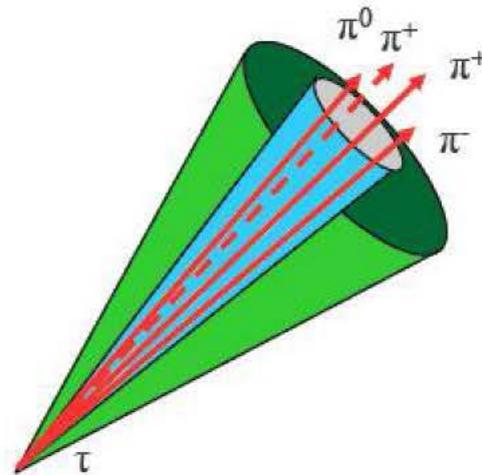


Figure 2.24: Tau Cone Definition Cartoon for identification.

| Tau | |
|---|---|
| | Calorimeter |
| Seed Tower $E_T$ | $> 6 GeV$ |
| Shared Tower $E_T$ | $> 1 GeV$ |
| $N^{twr}$ | $\leq 6$ |
| | Track |
| Seed Track $P_T$ | $> 6 GeV/c$ |
| Shared Track $P_T$ | $> 1 GeV/c$ |
| Track $|Z_0|$ | $\leq 60 cm$ |
| Track $|d_0|$ | $\leq 0.2 cm$ ($0.02 cm$ if #SiHits$> 0$) |
| Seed Track Fiducial | $9.0 cm < |z_{CES}^{seedtrk}| < 230.0 cm$ |
| # Ax Super Layer (5 hits) | $\geq 3$ |
| # St Super Layer (5 hits) | $\geq 2$ |
| $\theta_{sig}$ | $\min(0.17, \frac{5.0 rad/GeV}{E^{\tau cl}})$ |
| $\theta_{iso}$ | $0.52 rad$ |
| Track Charge Sum | $|\sum Q^{trk}| = 1$ |
| $\Delta z^{shtrk}$ | $< 5 cm$ |
| track in signal cone | $N_{sig}^{trk} = 1, 3$ |
| Visible $P_T$ | $> 15 GeV$ for 1-prong, $> 20 GeV$ for 3-prong |
| visible mass | $< 1.8 GeV/c^2$ |
| track in isolation cone | $\sum p_{T trk}^{iso} < 2 GeV$, no tracks with $p_T > 1.5 GeV$ |
| $\pi^0$ in isolation cone | $\sum E_{T \pi^0}^{iso} < 1 GeV$ |
| electron removal | $\xi' > 0.1$ |

Table 2.9: Tau Identification Cuts.
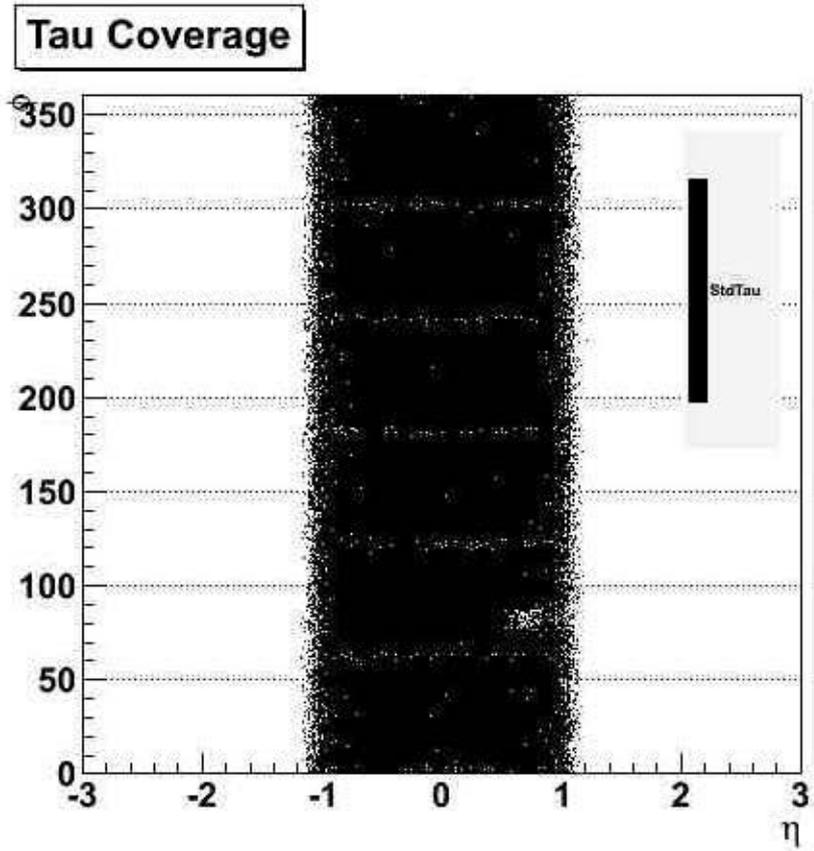
Figure 2.25: Hadronic Tau Coverage.

## 2.4.5  Jet Reconstruction

Almost all the quarks except for top quark tend to be observed as jet phenomena, which is bundle of hadrons.

The jets are observed as cluster of energy located in adjacent detector towers in calorimeters. A jet contains neutral or charged hadrons, which are mostly pions, fewer kaons and light baryons such as protons and neutrons.

The energy of the initial parton can be approximated by summing the tower energies within a cone of specified size. This algorithm is called as "Jet Clustering". The cone size is chosen to encompass most of the jet energy without allowing a significant contribution from other event activity. It is defined in $\eta - \phi$ plane by its radius, $R = \sqrt{\Delta\phi^2 + \Delta\eta^2}$, and is centered at the largest calorimeter energy tower serving as a seed tower of the jet cluster. In this paper, $\Delta R = 0.4$ is used in this analysis.

After applying this algorithm, the location of the jet is determined by using the $E_T$ weighted centroid of the cluster as below.

$$\eta_{centroid} = \frac{\sum_{i=1}^{N} E_T^i \eta^i}{\sum_{i=1}^{N} E_T^i}, \phi_{centroid} = \frac{\sum_{i=1}^{N} E_T^i \phi^i}{\sum_{i=1}^{N} E_T^i},$$

where the sums are carried out over all calorimeter towers in the cluster. It defined the centroid tower and a new cone drawn around this position. This process is iterated until the cluster remains unchanged in two consecutive paths. In some cases two clusters can overlap and then they are either merged into one, if the sum of the energies in shared towers exceed 75% of the energy of the smaller cluster, or left intact.

The jet for-momentum $(E^{raw}, p_x^{raw}, p_y^{raw}, p_z^{raw})$ is then determined by the following sums over the cluster towers:

$$E^{raw} = \sum_{i=0}^{N} E_i \tag{2.6}$$

$$p_x^{raw} = \sum_{i=0}^{N} E_i \sin\theta_i \cos\phi_i \tag{2.7}$$

$$p_y^{raw} = \sum_{i=0}^{N} E_i \sin\theta_i \sin\phi_i \tag{2.8}$$

$$p_z^{raw} = \sum_{i=0}^{N} E_i \cos\theta_i \tag{2.9}$$

These quantities are referred to as raw, since they are affected by mismeasurements for a variety of reasons in order to both to physics and to detector effects and are different from the true energies of the partons which initiated jets. Therefore proper corrections need to be applied to reconstruct true momentums of partons.

**Jet Energy Corrections**

The measured four-vector of jets generally differs from the energies of the initial partons. This is the result from both instrumental and physical effects such as low energy non-linearities, $\eta$ crack energy losses, underlying events, and clustering. Some of the corrections are decided by the measurable quantities independent of the theory, while some of them depend on the theory prediction. Thus the raw jet energies measured in the calorimeter must be corrected for detector effects at first before they can be compared to physics predictions/models. The correction strategy is as below.

- Relative Corrections
  The first step in jet energy corrections is to correct the jets for any variation in the response with detector $\eta$. For this correction, dijet event samples are used. Since the transverse energy of the two jets in a $2 \to 2$ process should be equal, the energies of jets in the plug and forward calorimeters are scaled to give the energy of an equivalent jet in the central calorimeter. One well-measured central jet $(0.2 < |\eta| < 0.6)$ is required and a scale factor is derived from the dijet balance to the second jet. The central calorimeters CEM/CHA are the best understood calorimeters in CDF and the selected region is far away from the cracks. The gain variation depending on the time (run range) in the plug calorimeters is also taken into account. The corrections for the Monte Carlo (MC) samples and data are determined separately since some discrepancy between data and MC simulation can be seen to a lack of the materials in the detector simulation.

- Multiple Interaction Corrections
  The multiple interaction affects the measured jet energy when the energy from these minimum bias events falls into the jet clustering cone. The transverse energy in a random cone is measured in minimum bias data and parameterized as a function of the number of vertices in the event. This transverse energy is subtracted from each jet to account for multiple interaction in the same bunch crossing as a function of the number of vertices in the event. This correction factor is a linear function of the number of reconstructed vertices in the event. Only vertices associated with at least 2 COT tracks in minimum bias events are used to decide this correction factor.

- Absolute Corrections
  The jet energy measured by the calorimeters must be corrected for any non-linearity and energy loss in the un-instrumented regions of each calorimeter. The absolute jet corrections account for the response to particle-level energy in the central calorimeter. This correction depends on the jet fragmentation properties. The calibration point is derived using a 50 GeV pion from test beam data. For the non-linearity response, the tuned MC samples are used for the charged and neutral particles. After fragmentation, the events are processed with a full CDF detector simulation. Each simulated event is compared to the total $p_T$ of all

generated particles lying in a cone centered about the measured jet axis. A quadratic spline fit is used to parameterize the mean jet response as a function of $E_T$ for the each cone size.

- Underlying Event Corrections
  The underlying event contains all the soft interactions except for the hard one. The underlying event energies must be subtracted from the measured jet energy when these particles fall into the clustering cone. The correction procedure is the same as the multiple interaction correction. Events with only one vertex are used to determine the underlying event correction.

- Out-of-Cone Corrections
  The jet clustering may not include all the energy from the initiating parton. Some of the partons generated during fragmentation may fall outside the cone chosen for clustering algorithm. Out-of-Cone corrections are applied in order to correct the particle-level jet energy to the parton energy as much as theoretically allowed. These corrections are completely independent of detector/calorimeter performance and depend on the parton fragmentation functions. The correction factor is parameterized as function of jet $p_T$. Jet tends to become narrower at large energies, and the fractional energy deposited outside the cone decreases.

Thus, the jet energy is corrected by

$$p_T(R) = [p_T^{raw}(R) \times f_{rel} - UEM(R)] \times f_{ABS}(R) - UE(R) + OC(R), \qquad (2.10)$$

where R denotes the clustering cone size, $p_T$ and $p_T^{raw}$ are the corrected and raw transverse momenta of jet, $f_{rel}$ is the relative jet energy correction, UEM(R) is the multiple interactions correction, $f_{abs}(R)$ is the absolute jet energy correction, UE(R) is the underlying event correction, and OC(R) is the Out-of-Cone correction.

## 2.4.6  Missing Energy

Neutrinos interact only through weak interactions and therefore cannot be directly detected as they traverse the detector material. Production of neutrinos in an event can be spotted by the existence of the large imbalance in the calorimeter energy. The longitudinal component of the colliding partons is not known, but the transverse component is subject to conservation, and the sum of the transverse components of the neutrino momenta can be measured. This quantity is called missing transverse energy $\vec{\not{E}}_T$. The missing transverse energy is two-component vector $(\not{E}_{Tx}, \not{E}_{Ty})$ The raw value of $\vec{\not{E}}_T$ is defined by the negative vector sum of the transverse energy of all calorimeter towers;

$$\vec{\not{E}}_T^{\,raw} = -\sum_{tower} (E_i \sin\theta_i)\vec{n_i}, \tag{2.11}$$

where $E_i$ is the energy of the $i$-th tower, $\vec{n_i}$ is a transverse unit vector pointing to the center of the tower and $\theta_i$ is the polar angle of the line pointing from $z_0$, $z$-coordinate of the event vertex, to the $i$-th tower. This sum extends to $|\eta_{detector}| < 3.6$.

The value of $\vec{\not{E}}_T^{\,raw}$ should be further corrected for escaping muons and jet energy mismeasurements. Muons do not deposit substantial energy in the calorimeter, but may carry out significant amount of the energy. The sum of transverse momenta of escaping muons $\sum \vec{P}_T(\mu)$ measured in the COT has to be added to the $\vec{\not{E}}_T^{\,raw}$ with a negative sign and the energy deposited by muons in the calorimeters $\sum \vec{E}_T(\mu)$ has to be subtracted from that sum, as it has been already counted in the $\vec{\not{E}}_T^{\,raw}$.

Only raw values of jet energies contribute to the $\vec{\not{E}}_T^{\,raw}$ and these values have to be replaced in the sum by the corrected ones. The corrected value of $\vec{\not{E}}_T^{\,corr}$ is therefore given by the following relation:

$$\vec{\not{E}}_T^{\,corr} = \vec{\not{E}}_T^{\,raw} - (\sum \vec{P}_T - \sum \vec{E}_T) - (\sum \vec{E}_T^{\,corr}) - \sum \vec{E}_T^{\,raw})) \tag{2.12}$$

Uncertainties in $\vec{\not{E}}_T^{\,corr}$ are dominated by uncertainties in jet energies. Mismeasurements of $\vec{\not{E}}_T$ result from jets traversing through poorly instrumented regions of detectors, e.g. cracks, dead zones, and beam halo effects. They may also result from cosmic rays, muon misidentification and mismeasurements in muon track momenta.

The resolution of the $\not{E}_T$ generally depends on the response of the calorimeter to the total energy deposited int the event. It is parameterized in terms of the total scalar transverse energy $\sum \not{E}_T$, which is defined as

$$\sum \not{E}_T = \sum_{towers} E_i \sin\theta_i \tag{2.13}$$

The $\not{E}_T$ resolution in the data is measured with minimum bias events, dominated by inelastic $p\bar{p}$ collisions. In minimum bias events the $x$ and $y$ components of $\vec{\not{E}}_T$ are

distributed as Gaussian around zero with $\sigma_x = \sigma_y = \sigma$:

$$\frac{N}{d\not{E}_{Tx}} \approx \exp(-\frac{\not{E}_{Tx}^{2}}{2\sigma^2}) \tag{2.14}$$

The missing transverse energy resolution $\Delta = \langle \not{E}_T^{2} \rangle$ is then given by $\Delta = \sqrt{2}\sigma_{x,y}$. It is expected to scale as a square root of the total transverse energy in the event, $\sum E_T$, is determined to be $\Delta \approx 0.64\sqrt{\sum E_T}$ from minimum bias studies.

# Chapter 3

# Measurement of Top Properties

Following the discovery of the bottom ($b$) quark in 1977 at Fermilab, the existence of its doublet partner, the top ($t$) quark was strongly expected for several reasons. The evidence of the top quark production was reported by the Tevatron/CDF collaboration in 1994. In the next year, the discovery of the top quark was established with more statistics of data by both the CDF and DZERO collaborations [29], [30]. Using $\sim 100pb^{-1}$ data of Run I (1992-1996 Collider Run), combined datasets from both experiments provided the top quark mass $M_{top} = 178.0 \pm 4.3 GeV/c^2$ [31]. After the discovery of top quarks, experimenters has kept testing the Standard Model on top quark properties by the different view of features because of its large mass, its peculiar decay process and so on.
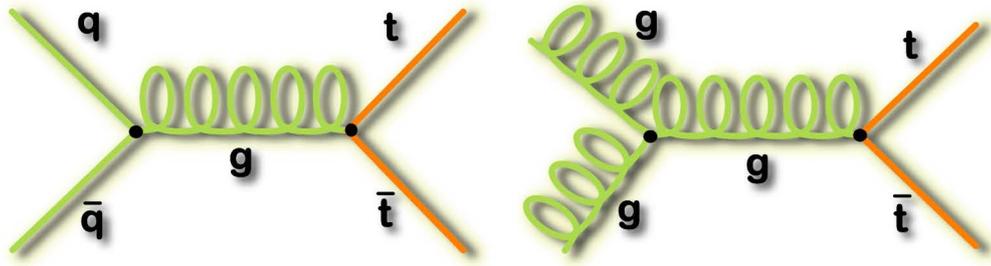


Figure 3.1: Top Pair Production Process. Left figure shows production process via quark anti-quark annihilation. Right figure shows production process via gluon fusion.

At hadron colliders like as Tevatron, the top quarks are produced in pair through the strong interaction as same as quark pair productions. In other words, top pair production based on the Standard Model is via the quark anti-quark annihilation and gluon fusion as shown in Figure 3.1. Both top pair production processes are produced by gluon exchange, which a effective virtual mass of intermediate gluon is typically more than $2M_{top}$.

The top quark has a peculiarity in decay process. The pair production of lighter

43
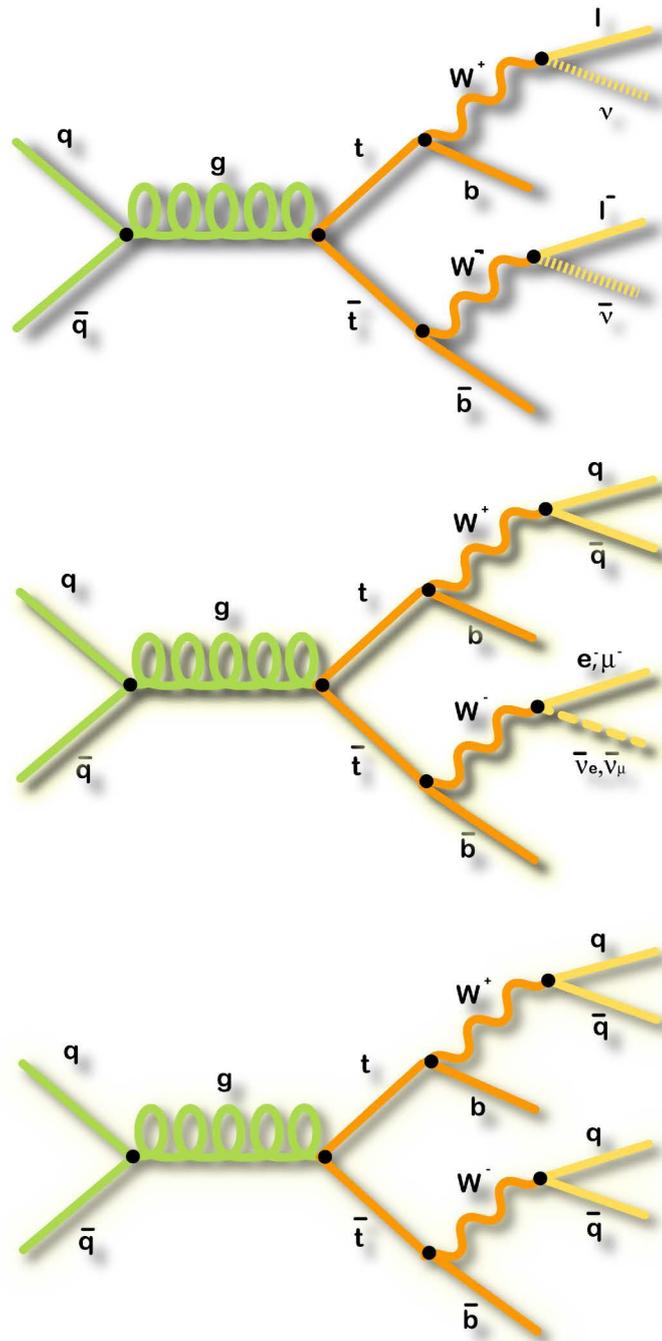
Figure 3.2:   Final States of Top Pair Decay Process.  Three characteristic final states are shown.  Upper figure shows decay process including two leptons and 2 *b*-jets, which is called "dilepton channel".  Middle figure shows decay process including one lepton, two $W$ jets and two *b*-jets, which is called "lepton plus jets channel".  Lower figure shows decay process that two $W$ boson decay hadronically, which has 6 jets including 2 *b*-jets and is called "all hadronic channel".

quark is observed by dijet events because lighter quarks does not have its mass with $> M_W \sim 80 GeV/c^2$, whereas the top quark mostly decay via electroweak process ($t \to Wb$), instead of forming bound states. Because its large mass make it decay with a mean lifetime of $\tau_{top} \approx 10^{-24} sec$ which lifetime is shorter than the time scale required for quarks to form bound states. In its decay process, the $b$-quark decays proceed to form bound states, and then observed as a feature jet. The $W$ boson rapidly decays into either a pair of quarks ($q\bar{q'}$) or a pair of charged lepton and a neutrino ($l\nu_l$). Therefore, its decay process in which six particles are included is roughly categorized to 3 types as shown in Figure 3.2. The decay of $W$ boson defines the decay channel of $t\bar{t}$ system.

**Dilepton Channel**, where both $W$ bosons decay to leptons with high momentum leptons, two jets and large missing energy associated with two neutrinos. When only electron and muon in the final state are considered, this channel carries a branching ratio of 4 %. From the view of experiments, its case of final states include electron and muon from tau lepton decay. The feature of this channel is negatively less statistics and is positively less background events.

**Lepton plus Jets Channel**, where one $W$ decays to the pair of lepton and neutrino, and the other to quarks. In an experimental signature, one high momentum lepton, four jets and a missing energy associated with neutrino are observed. When only electron and muon in the final state are also considered, this channel carries a branching ratio of 30 %.

**All-Hadronic Channel**, where both $W$ bosons decay to the pair of quarks. This channel is observed as a 6 jets event with no energetic leptons. This decay channel carries the largest branching ratio of 46 %. This channel suffers from the largest amount of QCD background.

In this chapter, measurement of top mass and top pair production cross section using all-hadronic channel is discussed. As mentioned above, the major challenge of this channel is the large background from QCD multijet production, which dominates the signal by 3 orders of magnitude after the application of a specific online event selection. To increase the purity of the candidate sample, requirements based on the kinematical and topological characteristics of SM $t\bar{t}$ events are expressed in terms of an artificial neural network and applied to the data. Further improvement is then obtained from the requirement of at least one jet identified as originating from a $b$ quark using a secondary vertex $b$-tagging algorithm. Simulations predict that a clear $t\bar{t}$ signal will thus become visible over background in the selected data sample, and the measurement of the top quark mass and the $t\bar{t}$ cross section is made possible in spite of the overwhelming QCD multijet production.

A reconstructed top quark mass is determined by fitting the kinematics of the six leading jets in the event to a $t\bar{t}$ final state. This variable, denoted as $m_t^{rec}$, does not strictly represent a measurement of $M_{top}$, but its distribution obtained by a sample of $t\bar{t}$ events is sensitive to $M_{top}$ itself. The jet energy scale (JES) is a factor representing the set of corrections needed to obtain a better estimate of the energy of a parton starting from a jet reconstructed by clusters in the calorimeter. The default JES used in simulated events is obtained by a tuning to the data, but possible discrepancies between

data and simulation lead to an uncertainty on this value. The strong correlation existing between the $m_t^{rec}$ distribution and the JES implies therefore a corresponding uncertainty on $M_{top}$. However, the JES can be calibrated using the selected samples of $t\bar{t}$ candidate events, where a second variable, $m_W^{rec}$, is reconstructed by the four-momenta of the jets assigned to the W bosons. This variable is related to the well-known value of the W boson mass, and the $m_W^{rec}$ distributions for simulated events match the observed data. The inclusion of this procedure, usually referred to as *in situ* calibration, enables a significant reduction of the systematic uncertainty associated with the inaccurate knowledge of the JES, and represents an important improvement of the work described in this paper with respect to the previous CDF analysis by similar method [33].

The $m_t^{rec}$ and $m_W^{rec}$ distributions are reconstructed in two separate samples of selected data events, defined by the presence of exactly one and two or more $b$-tagged jets, respectively. The data are then compared to corresponding distributions expected from background and $t\bar{t}$ events simulated with various values of the top quark mass and of the JES to fit for these parameters. In addition, the fitted signal yields are used to derive a measurement of the $t\bar{t}$ production cross section.

Top quark mass and cross section of $t\bar{t}$ pair production are measured by using $2.9fb^{-1}$ data.

## 3.1 Neural-network-based Kinematical Event Selection

For signal events, $t\bar{t}$ Monte Carlo events are generated by PYTHIA v 6.2 [28] with $M_{top}$ values ranging from 160 to $190GeV/c^2$ in $10GeV/c^2$ steps. As for the background, mostly QCD, data-driven modeling is used. This is based on the tag rate parametrization of jets. All data and MC events have to pass some prerequisites;

1. good run condition

2. good quality of primary vertex

3. no tight lepton identified in the event

Then, the event has tight jets ($E_T > 15GeV$, $|\eta| < 2$) from 6 to 8, that is $6 \leq N_{tightjets} \leq 8$. Those jets are required with a minimum distance ($\min \Delta R(jet, jet) > 0.5$) in $\eta - \phi$ plane. In addition, the absence of significant missing transverse energy ($\frac{\not{E}_T}{\sum E_T}$) is required.

In this analysis, the neural network (NN) chosen here is the Multilayer perceptron (MLP), a simple feed-forward network. The number of input nodes which are kinematic variables reconstructed using tight jets is 13, with inclusion of jet shape variables. The 13 inputs are:

1. Sum of the jet $E_T$;

2. Sum of the three subleading jet $E_T$, that is except the two highest-$E_T$ jets;

3. Centrality;

4. Aplanarity;

5. Minimum of the invariant mass of dijet system;

6. Maximum of the invariant mass of dijet system;

7. Minimum of the invariant mass of trijet system;

8. Maximum of the invariant mass of trijet system;

9. $E_T^{1,*} = $ leading jet $E_T \sin^2(\theta^*)$;

10. $E_T^{2,*} = $ next-to-leading jet $E_T \sin^2(\theta^*)$;

11. $\langle E_T^* \rangle$ (geometric average over the 3rd-4th...Nth jets);

12. $\langle M_\eta^s \rangle$, geometric average of the light quark jet $\eta$ momenta in the calorimeter;

13. $\langle M_\phi^s \rangle$, geometric average of the light quark jet $\phi$ momenta in the calorimeter;

Then, the tagged jets among the six leading jets is required. Events are categorized to 2 types. One of types is event with exactly one tagged jet. The other is event with 2 more tagged jets. Finally, events are selected if the output value from the neural network, $N_{out}$, is larger than 0.90 for 1 tagged jet events, 0.88 for 2 more tagged jets events.

Figure 3.3, 3.4 and 3.5 respectively show reconstructed $W$ mass, top mass and neural-network output distribution in control region which is background dominant and is not for analysis use.

In order to extract one set of $m_{top}^{rec}$ and $m_W^{rec}$ values from an event, $\chi^2$ is defined as below.

$$\chi^2 = \frac{(m_{jj}^{(1)} - M_W)^2}{\Gamma_W^2} + \frac{(m_{jj}^{(2)} - M_W)^2}{\Gamma_W^2} + \frac{(m_{jjb}^{(1)} - M_t^{rec})^2}{\Gamma_t^2} + \frac{(m_{jjb}^{(2)} - M_t^{rec})^2}{\Gamma_t^2} + \sum_{i=1}^{6} \frac{(p_{T,i}^{fit} - p_{T,i}^{meas})^2}{\sigma_i^2}$$

(3.1)

After the event selection as in Table 3.1, the number of events is shown in Table 3.2.
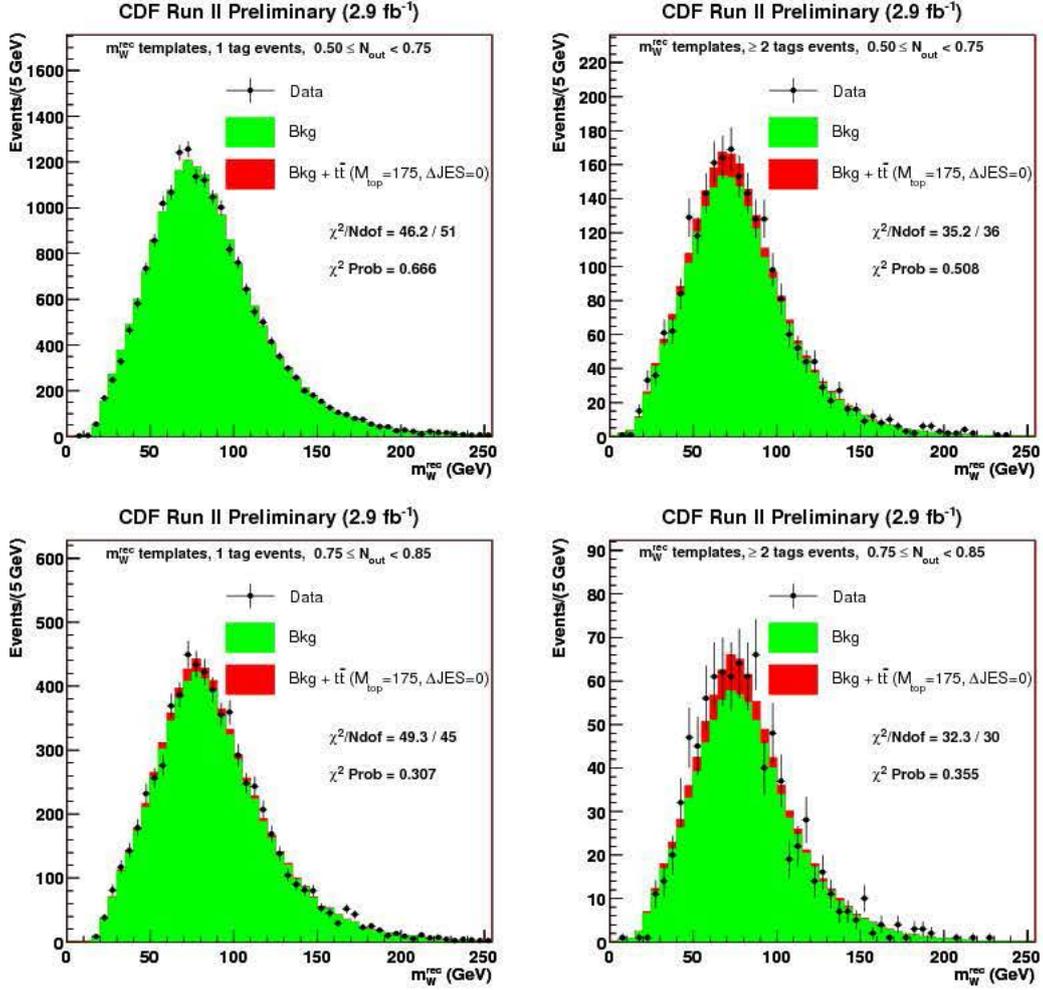
Figure 3.3: Reconstructed W boson mass distribution for exact 1 tagged events (left), and for $\geq 2$ tagged events (right) in a control region defined by $0.50 \leq N_{out} < 0.75$ (upper) and $0.75 \leq N_{out} < 0.85$ (lower).

| Event sample | $b$ tags | $N_{out}$ | $m_t^{rec}$ fit $\chi^2$ |
|:---:|:---:|:---:|:---:|
| 1 tag | $\equiv 1$ | $\geq 0.90$ | $\leq 6$ |
| $\geq 2 tags$ | 2 or 3 | $\geq 0.88$ | $\leq 5$ |

Table 3.1: Final definition and requirements for selected event samples.
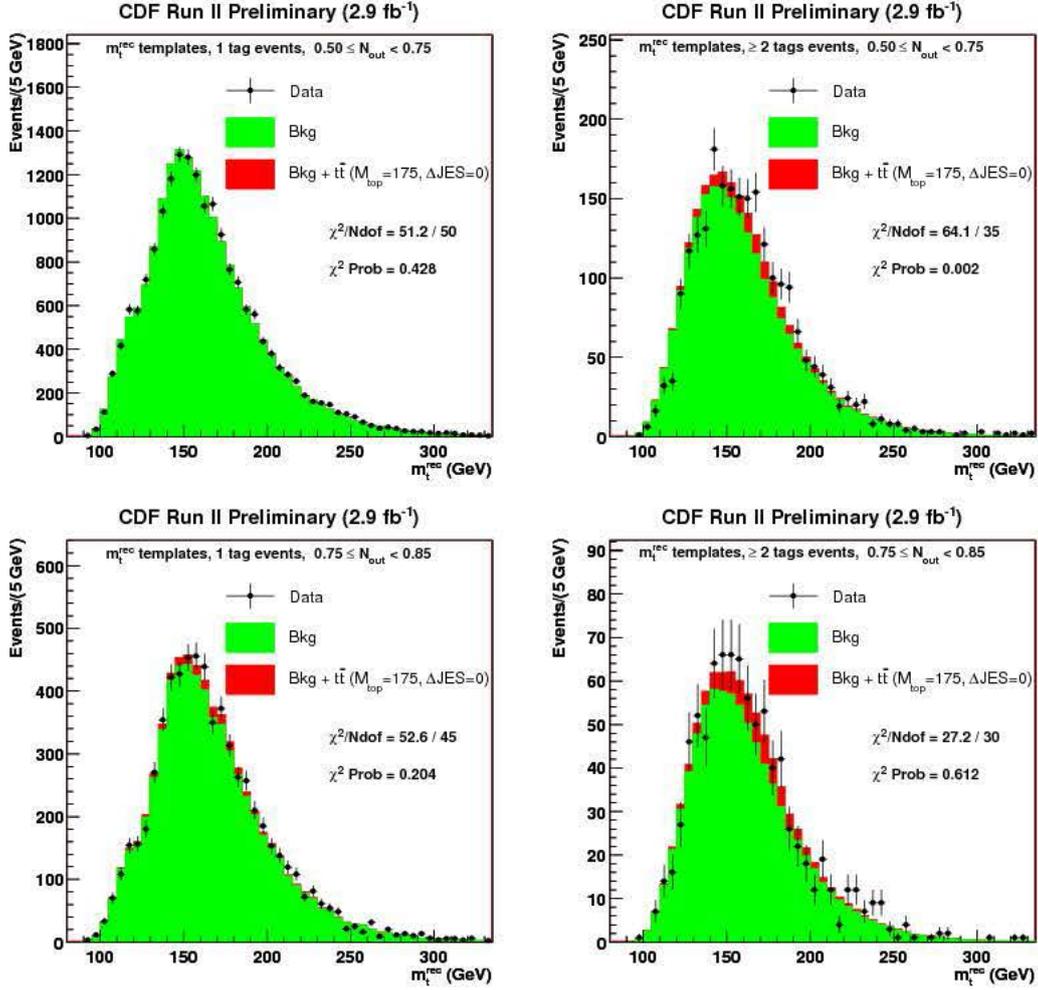
Figure 3.4: Reconstructed top quark mass distribution for exact 1 tagged events (left), and for $\geq 2$ tagged events (right) in a control region defined by $0.50 \leq N_{out} < 0.75$ (upper) and $0.75 \leq N_{out} < 0.85$ (lower).

| Event sample | Observed | Background | $t\bar{t}$ |
|---|---|---|---|
| 1 tag | 3452 | $2785 \pm 83$ | 693 |
| $\geq 2 tags$ | 442 | $201 \pm 29$ | 193 |

Table 3.2: Number of events observed in the selected data samples and corresponding expected numbers of background and $t\bar{t}$ events. The signal contribution is evaluated for $M_{top} = 175 GeV/c^2$, $\Delta JES = 0$, and $\sigma_{t\bar{t}} = 6.7 pb$.
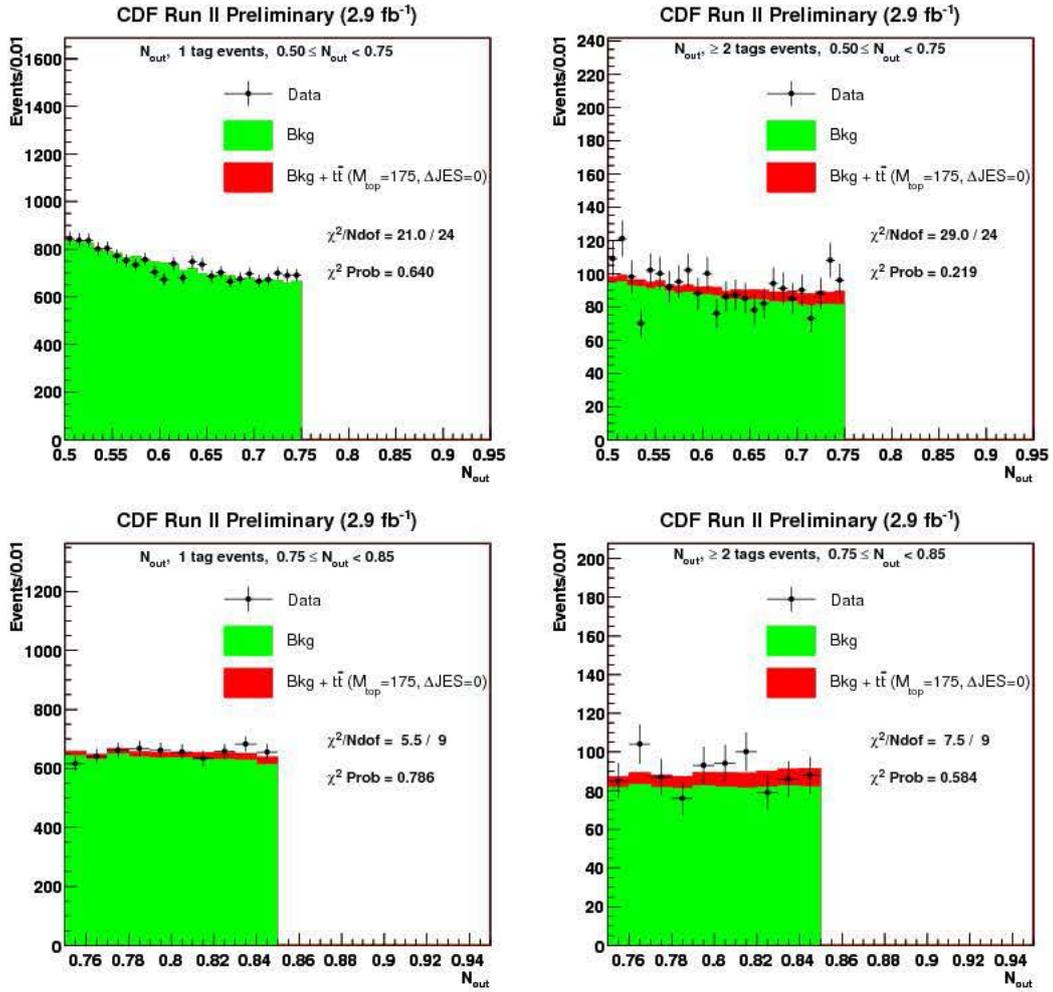
Figure 3.5: $N_{out}$ distribution for exact 1 tagged events (left), and for $\geq 2$ tagged events (right) in a control region defined by $0.50 \leq N_{out} < 0.75$ (upper) and $0.75 \leq N_{out} < 0.85$ (lower).
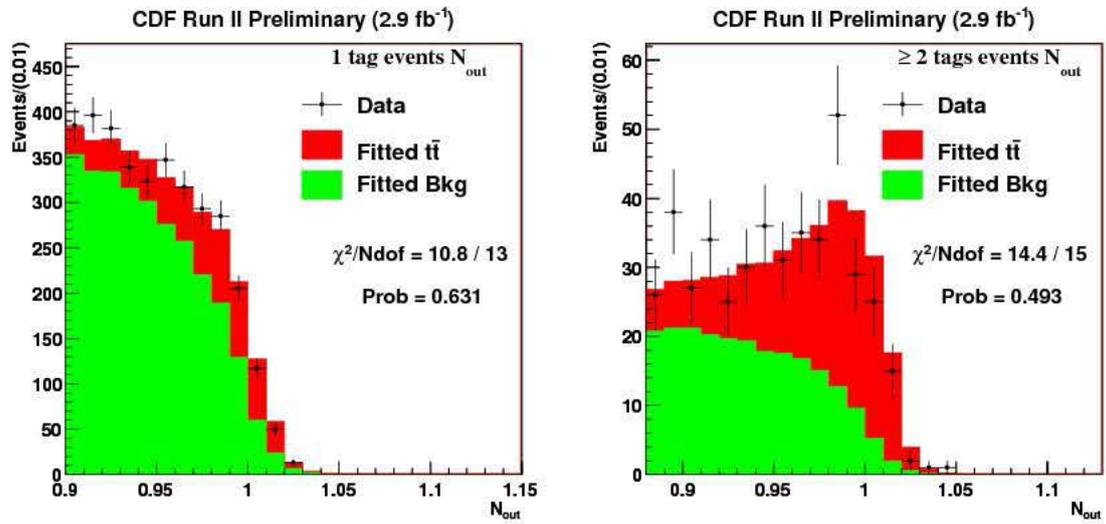
Figure 3.6: $N_{out}$ Distribution for signal region. Left figure shows distribution for exact 1 tagged events. Right figure shows distribution for $\geq 2$ tagged events.

## 3.2   Measurement of Top Mass

To measure the top quark mass simultaneously with the JES, a fit is performed where an unbinned likelihood function is maximized to find the values of $M_{top}$, $\Delta JES$, and the number of signal ($n_s$) and background ($n_b$) events for each tagging category which give the probability density functions best describing the data.

Signal templates for 1 tagged events is shown in Figure 3.7.  Signal templates for $\geq 2$ tagged events is shown in Figure 3.8.  Background templates is shown in Figure 3.9.

The likelihood function $L$ is divided into three main parts and can be written as below.

$$L = L_{1tag} \times L_{\geq 2tags} \times L_{\Delta JES_{constr}} \tag{3.2}$$

The $L_{1tag}$ and $L_{\geq 2tags}$ terms further consist of other factors.

$$L_{1tag,\geq 2tags} = L_{M_{top}} \times L_{JES} \times L_{posisson} \times L_{N_{constr}^{bkg}}, \tag{3.3}$$

where the four terms on the right side assume, respectively, the following form [the superscripts referring to the tag sample are omitted and $f_s \equiv n_s/(n_s+n_b)$, $f_b \equiv 1-f_s$]:

$$\prod_{i=1}^{N_{obs}} f_s \cdot P_{sig}^{m_t^{rec}}(m_{t,i}|M_{top},\Delta JES) + f_b \cdot P_{bkg}^{m_t^{rec}}(m_{t,i}), \tag{3.4}$$

$$\prod_{i=1}^{N_{obs}} f_s \cdot P_{sig}^{m_W^{rec}}(m_{W,i}|M_W,\Delta JES) + f_b \cdot P_{bkg}^{m_W^{rec}}(m_{W,i}), \tag{3.5}$$

In the first expression, the probability to observe the set $m_{t,i}, (i = 1, \ldots, N_{obs})$ of $m_t^{rec}$ values reconstructed in the data is calculated by using the total probability density function resulting from the combination of the parameterized signal and background probability density functions, $P_{sig}^{m_t^{rec}}$ and $P_{bkg}^{m_t^{rec}}$, respectively, as a function of the free parameters of the fit. In second term, the same is done for the set of the observed W masses, $m_{W,i}, (i = 1, \ldots, N_{obs})$, and the $m_W^{rec}$ probability density function.

$$L_{poisson} = \frac{e^{-(n_s+n_b)} \cdot (n_s + n_b)^{N_{obs}}}{N_{obs}!}, \tag{3.6}$$

where $L_{poisson}$ gives the probability to observe the number of events selected in the data, given the average number of signal($n_s$) and background ($n_b$) events expected in the sample, as assumed at each step of the likelihood fit.

$$L_{N_{constr}^{bkg}} = \exp[-\frac{(n_b - n_{(b,exp)})^2}{2\sigma_{n_{(b,exp)}}^2}], \tag{3.7}$$

where the parameter $n_b$ is constrained by a Gaussian to the *a priori* background estimate; for instance, $n_{(b,exp)} = 2785 \pm 83$ for 1-tag events and $n_{(b,exp)} = 201 \pm 29$ for $\geq$ 2-tag events as in Table 3.2.

The final term $L_{\Delta JES_{constr}}$ is a Gaussian term constraining $\Delta JES$ to its *a priori* value:

$$L_{\Delta JES_{constr}} = \exp\left[-\frac{(\Delta JES - \Delta JES_{constr})^2}{2}\right] \qquad (3.8)$$

When the measurement is performed on data, the JES can be constrained to the value independently measured in [34].
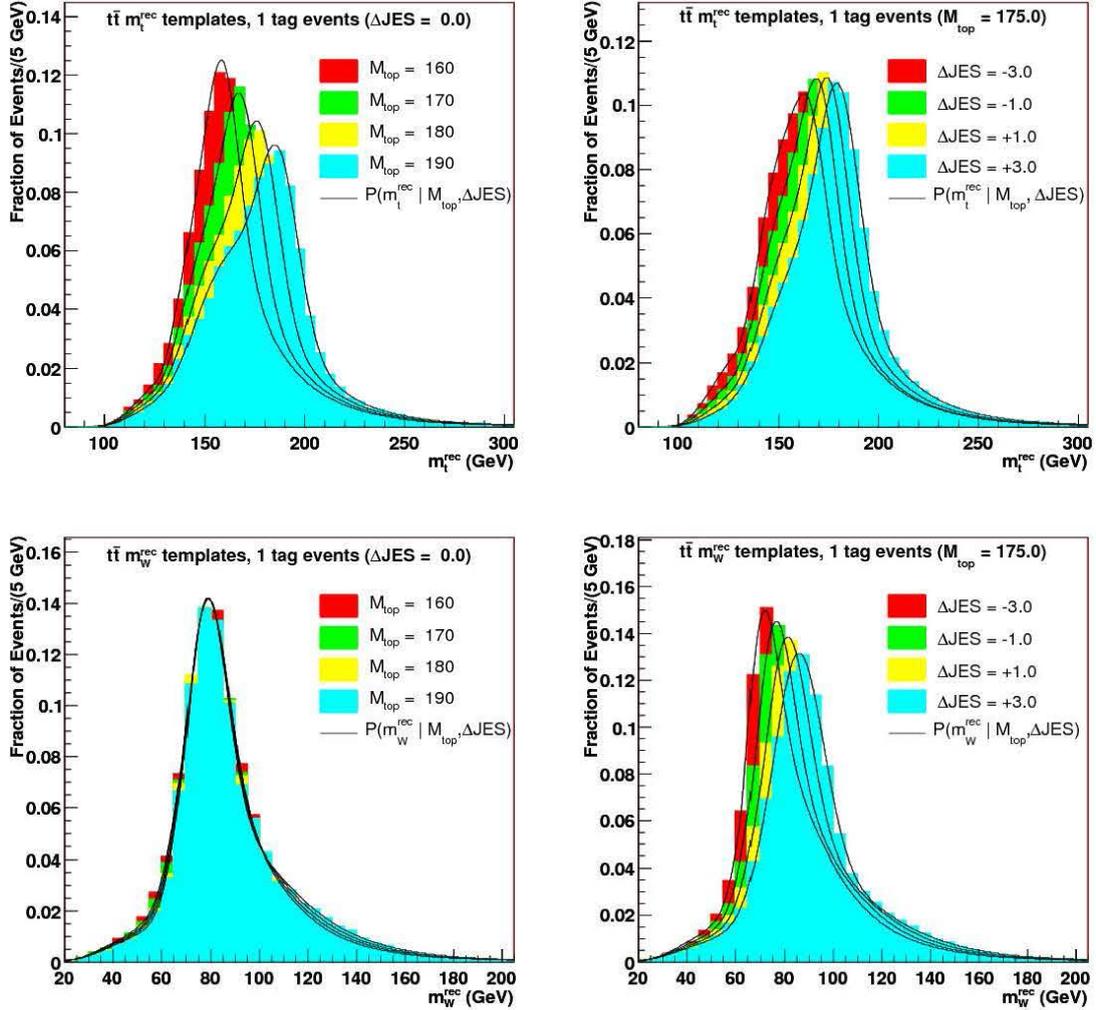


Figure 3.7:  Signal Templates for top quark mass and W boson mass. Various mass points and jet energy scale are shown in a plot. These plots are for exact 1 tagged events.

Summarizing, the measured values for the top quark mass and the jet energy scale are

$$M_{top} = 174.8 \pm 2.4(stat + JES)^{+1.2}_{-1.0}(syst)GeV/c^2 \qquad (3.9)$$
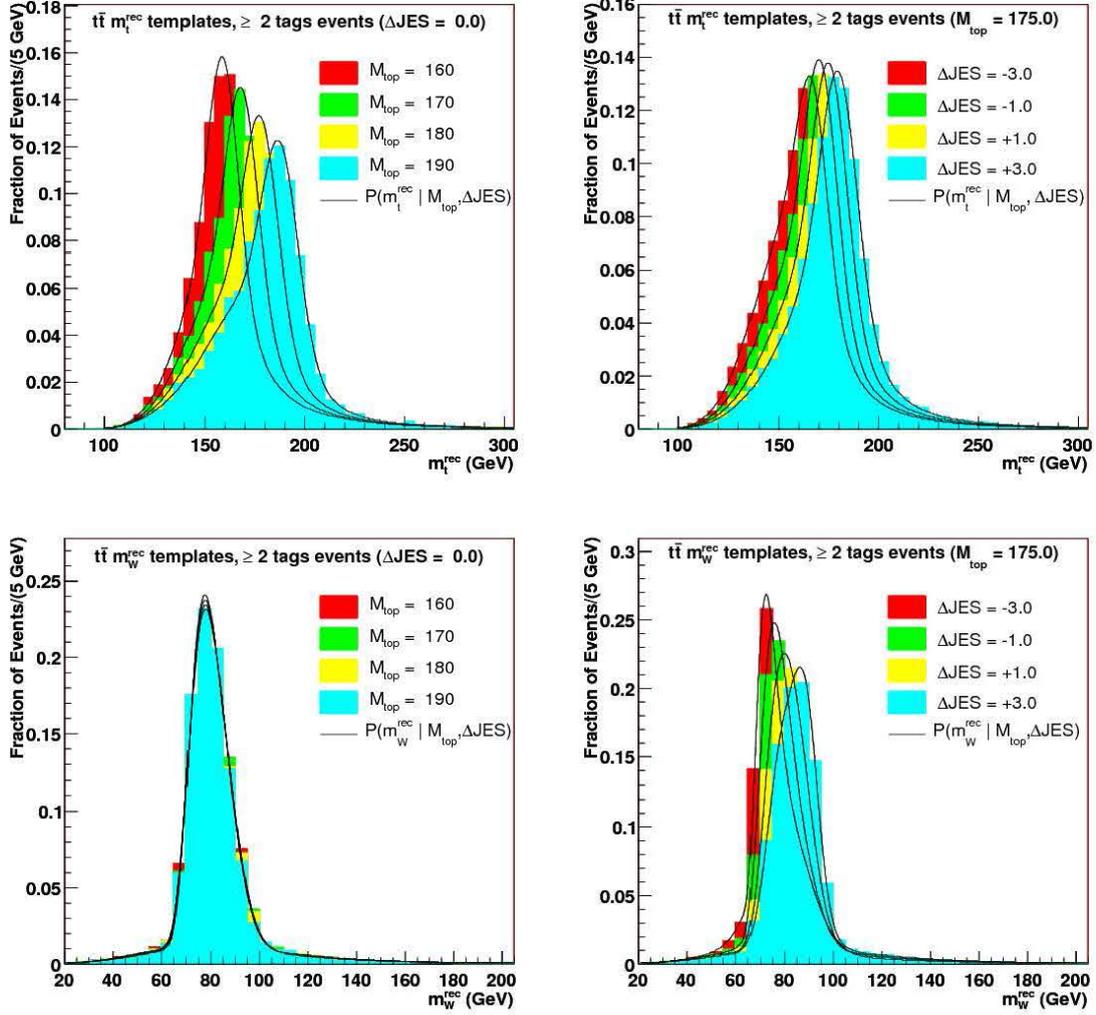
Figure 3.8: Signal Templates for top quark mass and W boson mass. Various mass points and jet energy scale are shown in a plot. These plots are for 2 more tagged events.

,

$$\Delta JES = -0.30 \pm 0.35 (stat + M_{top})^{+0.34}_{-0.37}(syst),  \tag{3.10}$$

which, isolating the purely statistical contributions and adding the uncertainties from JES and $M_{top}$ to the respective systematic uncertainties, can also be written as

$$M_{top} = 174.8 \pm 1.7 (stat)^{+2.0}_{-1.9}(syst) GeV/c^2  \tag{3.11}$$

,

$$\Delta JES = -0.30 \pm 0.35 (stat)^{+0.49}_{-0.47}(syst),  \tag{3.12}$$
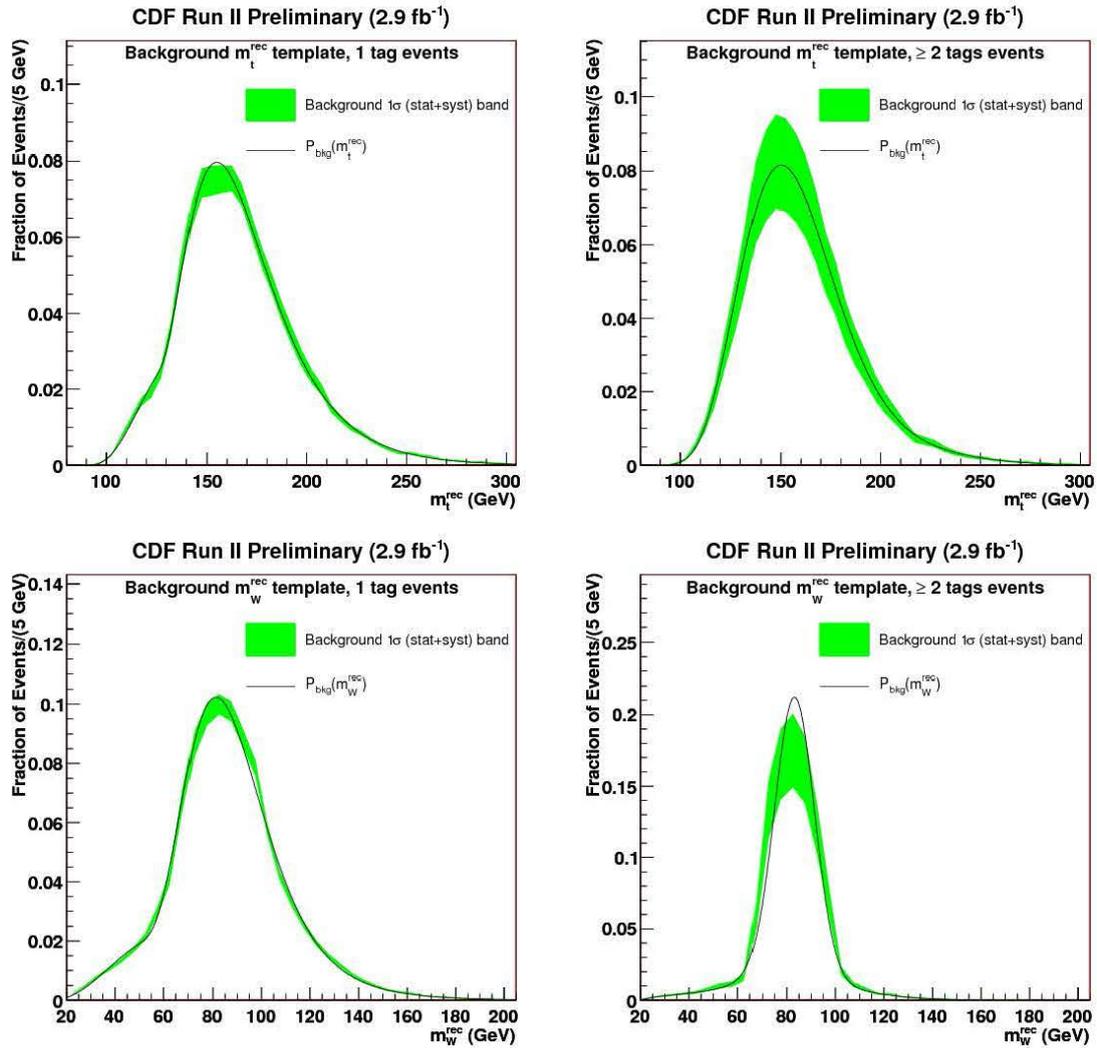
Figure 3.9: Background Templates for top quark mass and W boson mass. Various mass points and jet energy scale are shown in a plot. These plots are for exact 1 tagged events (left) and 2 more tagged events (right).
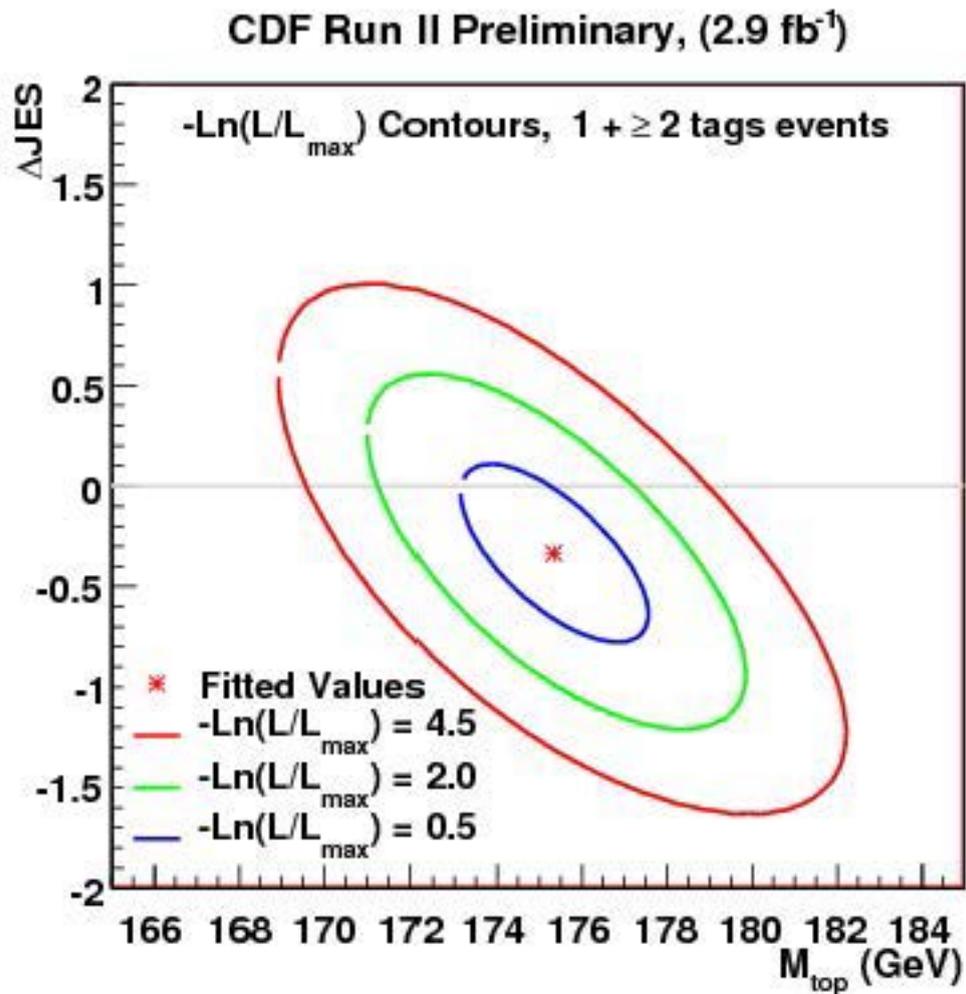
Figure 3.10: Negative log-likelihood contours for the likelihood fit performed for the $M_{top}$ and $\Delta$JES measurements.
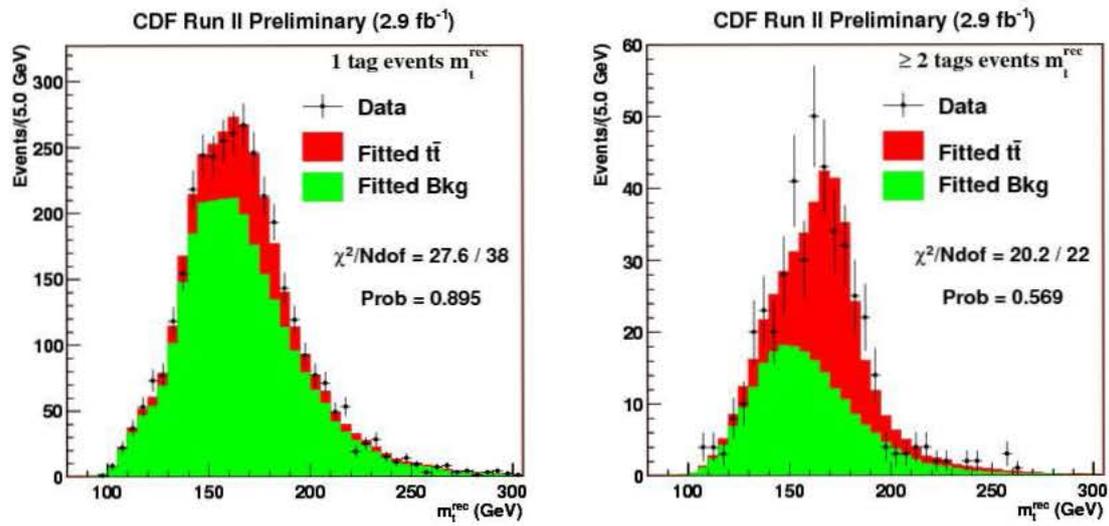
Figure 3.11:  Reconstructed top mass for 1 tagged events and $\geq 2$ tagged events.

## 3.3 Measurement of $t\bar{t}$ Production Cross Section

The procedure used to measure the top quark mass also returns the average number of signal events expected given the selected data samples. These results can be turned into a measurement of the $t\bar{t}$ cross section, as follow.

From the number of signal events, $n_s^{1tag}$ and $n_s^{\geq 2tags}$, as obtained from the mass likelihood fit, we derive a measurement of the $t\bar{t}$ production cross section considering the efficiency for selecting a $t\bar{t}$ event in the two tagging categories.

The cross section measurement is performed by maximizing a likelihood function which can be divided into two parts:

$$L = L_{1tag} \times L_{\geq 2tags}, \tag{3.13}$$

where each term can be expressed as

$$L_{1tag, \geq 2tags} = L_{\sigma_{t\bar{t}}} \times L_\epsilon, \tag{3.14}$$

where

$$L_{\sigma_{t\bar{t}}} = \exp\left(-\frac{(\sigma_{t\bar{t}} \cdot \epsilon \cdot \int \mathcal{L}dt - n_s)^2}{2\sigma_{n_s}^2}\right) \tag{3.15}$$

contains all the parameters of the fit, i.e. the production cross section $\sigma_{t\bar{t}}$, the integrated luminosity $\int \mathcal{L}dt$, the signal efficiency $\epsilon$, and the signal yield $n_s \pm \sigma_{n_s}$, as given by the mass measurement, while $L_{epsilon}$ is a Gaussian term constraining the efficiency within its statistical uncertainty.

The efficiencies are evaluated using a sample of about $4 \times 10^6 t\bar{t}$ events generated with $M_{top} = 175 GeV/c^2$ and assuming $\Delta JES = -0.3$, i.e. the value we measured by the mass likelihood fit, and are summarized along with signal yields and other parameters in Table 3.3.

| variable | Input value |
|---|---|
| Signal yield, exact 1 tag | $643 \pm 59 \pm 54$ |
| Signal yield, $\geq 2$ tags | $216 \pm 21 \pm 14$ |
| Efficiency, exact 1 tag | $(2.55 \pm 0.01)\%$ |
| Efficiency, $\geq 2$ tags | $(1.00 \pm 0.01)\%$ |
| Integrated Luminosity | $2874 \pm 172 pb^{-1}$ |

Table 3.3: Input variables to the cross section evaluation. For the signal yields, the first uncertainty is the purely statistical one.

While studying the performance of the procedure, using pseudo-experiments produced assuming a given input cross section, we observe the need to introduce a small correction. The outcome of the fit needs to be multiplied by a factor $k_\sigma = 0.982 \pm 0.008$ in order to obtain an unbiased measurement of the cross section.

From the maximization of the likelihood, we obtain a central value for the $t\bar{t}$ production cross section

$$\sigma_{t\bar{t}} = 7.2 \pm 0.5(stat) \pm 0.4(lum)pb, \tag{3.16}$$

evaluated assuming $M_{top} = 175GeV/c^2$ and $\Delta JES = -0.3$, close to the values measured in Section 3.2. The first uncertainty is the statistical one, while the second one derives from the 6% uncertainty on the integrated luminosity. As the signal efficiencies depend strongly on the assumed values for $M_{top}$ and $\Delta JES$, the measured $t\bar{t}$ cross section also has the same dependence. For reference we report in Table 3.4 the cross sections corresponding to other $(M_{top}, \Delta JES)$ points with a top quark mass near the current CDF average. In this case we assume $\Delta JES = 0$, and the systematic uncertainty on JES is increased from 6.1.% to 9.2%, corresponding to changing the $\Delta JES$ by $\pm 1$ rather than by $\pm 0.6$ units, that is, the sum in quadrature of the uncertainties on the measured jet energy scale, Section 3.2.

| $M_{top}(GeV/c^2)$ | $\Delta JES$ | $\sigma_{t\bar{t}}(pb)$ |
|---|---|---|
| 175.0 | -0.3 | 7.24 |
| 175.0 | 0.0 | 7.00 |
| 172.5 | 0.0 | 7.21 |
| 170.0 | 0.0 | 7.29 |

Table 3.4:  Cross section as evaluated assuming different values for $M_{top}$ and $\Delta JES$.

Most of the sources of systematic uncertainties affecting the measurement of $\sigma_{t\bar{t}}$ are the same as the ones discussed for the measurement of the top quark mass. We just need to evaluate their effects both on the signal yields and on the signal efficiencies in order to derive the effects on the cross section. There are few other sources of systematic uncertainty specific to a cross section measurement. These include the uncertainty on the calibration constant, $k_\sigma$ , on the $W \rightarrow$ hadrons branching ratio (BR) [32], on the trigger simulation, and on the distribution of the primary vertex $z$ coordinate. As for the effect of the JES uncertainty on the efficiency, we have evaluated it by changing the $\Delta JES$ by $\pm 0.6$ units with respect to the measured value $\Delta JES = -0.4$. Residual effects due to individual levels of corrections have been accounted for, too. The total relative uncertainties $\Delta\sigma_{t\bar{t}}/\sigma_{t\bar{t}}$ is 13.7%. The $\sigma_{t\bar{t}}$ production cross section amounts to

$$\sigma_{t\bar{t}} = 7.2 \pm 0.5(stat) \pm 1.0(syst) \pm 0.4(lum)pb, \tag{3.17}$$

assuming $M_{top} = 175GeV/c^2$ and $\Delta JES = -0.3$.

## 3.4 Appendix: Measurements of Top Properties

### 3.4.1 Centrality

The centrality is defined as

$$C = \sum E_T / \sqrt{\hat{s}},$$

where $\sqrt{\hat{s}}$ stands for jets system.

### 3.4.2 Aplanarity

The sphericity tensor is defined as

$$S^{\alpha\beta} = \frac{\sum_i p_i^\alpha p_i^\beta}{\sum_i |\vec{p_i}|^2},$$

where $\alpha, \beta = 1, 2, 3$ corresponds to the $x$, $y$ and $z$ components. By standard diagonalization of $S^{\alpha\beta}$ one may find three eigenvalues $\lambda_1 \geq \lambda_2 \geq \lambda_3$, with $\lambda_1 + \lambda_2 + \lambda_3 = 1$. The sphericity of the event is then defined as

$$S = \frac{3}{2} \left( \lambda_2 + \lambda_3 \right),$$

so that $0 \leq S \leq 1$. Sphericity is essentially a measure of the summed $p_\perp^2$ with respect to the event axis; a 2-jet event corresponds to $S \approx 0$ and an isotropic event to $S \approx 1$.

The aplanarity $A$, with definition $A = \frac{3}{2}\lambda_3$, is constrained to the range $0 \leq A \leq \frac{1}{2}$. It measures the transverse momentum component out of the event plane: a planar event has $A \approx 0$ and an isotropic one $A \approx \frac{1}{2}$.

### 3.4.3 $\eta$ moments ($M_\eta$) and $\phi$ moments ($M_\phi$) of a jet

A good discrimination between quark-initiated and gluon-initiated jets can be accomplished with $\eta$ moments ($M_\eta$) and $\phi$ moments ($M_\phi$) of a jet, which are defined as

$$M_\eta = \sqrt{[\sum_{tow} \frac{E_T^{tow}}{E_T} \eta_{tow}^2] - \eta^2}$$

and

$$M_\phi = \sqrt{[\sum_{tow} \frac{E_T^{tow}}{E_T} \phi_{tow}^2] - \phi^2},$$

where $E_T$, $\eta$ and $\phi$ are, respectively, the transverse energy, the pseudo-rapidity, and the azimuthal angle of the jet.

To remove possible biases coming from $E_T$ distributions, which might differ in signal and background events, by deconvoluting the $E_T$ dependence through a rescaling of all moments to a common reference value of $E_T = 50$ GeV. Scaled moments are

$$M_\eta^S = M_\eta \frac{f_q^\eta(50 GeV)}{f_q^\eta(E_T)}$$

and

$$M_\phi^S = M_\phi \frac{f_q^\phi(50 GeV)}{f_q^\phi(E_T)},$$

where $f_q^\eta(E_T)$ and $f_q^\phi(E_T)$ are the functions that fit the profiles of $m_\eta$ vs $E_T$ and of $M_\phi$ vs $E_T$ in quark-initiated jets from simulated $t\bar{t}$ events.

## 3.5 Prospect for the Standard Model Higgs

The top quark mass is a fundamental parameter in the Standard Model. Moreover, its mass is quite large, $\sim 175 GeV/c^2$ and is about 35 times larger than next-large-mass quark, bottom quark $\sim 5 GeV/c^2$. Actually, the world average of top quark mass is shown in Figure 3.12 as of July 2010.

### Mass of the Top Quark

| July 2010 | | (* preliminary) |
|---|---|---|
| CDF-I dilepton | | $167.4 \pm 11.4$ (±10.3 ± 4.9) |
| DØ-I dilepton | | $168.4 \pm 12.8$ (±12.3 ± 3.6) |
| CDF-II dilepton * | | $170.6 \pm 3.8$ (± 2.2 ± 3.1) |
| DØ-II dilepton * | | $174.7 \pm 3.8$ (± 2.9 ± 2.4) |
| CDF-I lepton+jets | | $176.1 \pm 7.4$ (± 5.1 ± 5.3) |
| DØ-I lepton+jets | | $180.1 \pm 5.3$ (± 3.9 ± 3.6) |
| CDF-II lepton+jets * | | $173.0 \pm 1.2$ (± 0.7 ± 1.1) |
| DØ-II lepton+jets * | | $173.7 \pm 1.8$ (± 0.8 ± 1.6) |
| CDF-I alljets | | $186.0 \pm 11.5$ (±10.0 ± 5.7) |
| CDF-II alljets | | $174.8 \pm 2.5$ (± 1.7 ± 1.9) |
| CDF-II track | | $175.3 \pm 6.9$ (± 6.2 ± 3.0) |
| Tevatron combination * | | $173.3 \pm 1.1$ (± 0.6 ± 0.9) |
| | | (± stat ± syst) |
| | | $\chi^2$/dof = 6.1/10 (81%) |

$m_{top}$ (GeV/c$^2$)

Figure 3.12: Summary of Top Mass in FNAL as of July, 2010.

Top quark properties contributes to higher order corrections to electroweak processes. It also helps to constrain the mass of Higgs boson via the radiative correction to the mass of the W boson. The precise electroweak measurements elicit the mass of the Standard Model Higgs boson is less than $158 GeV/c^2$ at 95% confidence level. This upper limit derived from $\Delta\chi^2 = 2.7$ for the blue band in left side of Figure 3.13. In addition, indirect bounds on the mass of the Standard Model Higgs boson are extracted by precision measurements of the top quark and W boson masses as in Figure 3.14, as these quantities are sensitive to $ln(M_H)$ through radiative corrections. Using current results of the top quark mass and W boson mass [36], the constraints are as below.

$$M_H = 89^{+35}_{-26} GeV/c^2 (68\% C.L.) \tag{3.18}$$
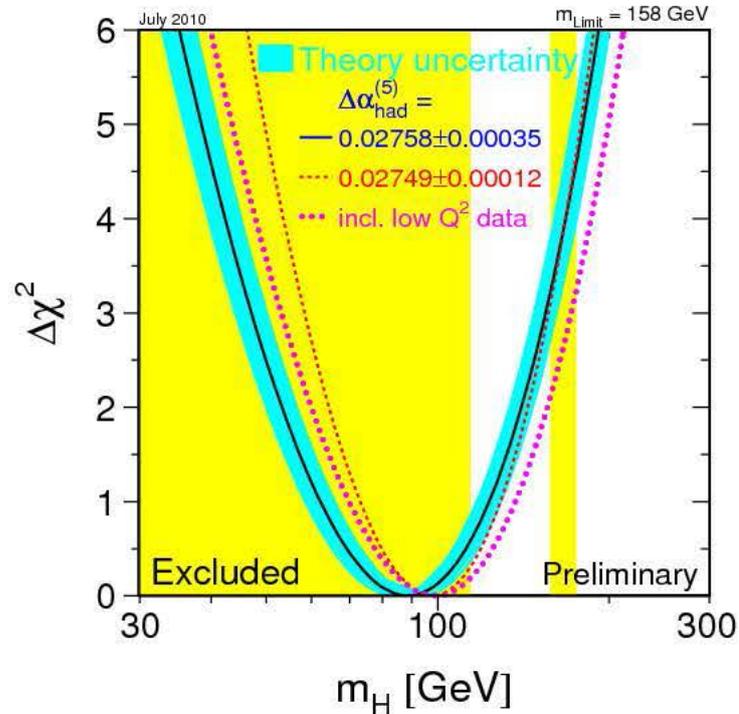


Figure 3.13:  Constraints on the Standard Model Higgs Boson.

Direct searches for the Standard Model Higgs boson at the CERN Large Electron Positron (LEP) collider exclude the mass region of $M_H < 114.4 GeV/c^2$ at 95% confidence level [35]. One at Tevatron also exclude the mass region of $158 GeV/c^2 < M_H < 175 GeV/c^2$ at 95% confidence level as of July 2010.

The most probable range in which the Standard Model Higgs boson lay down is
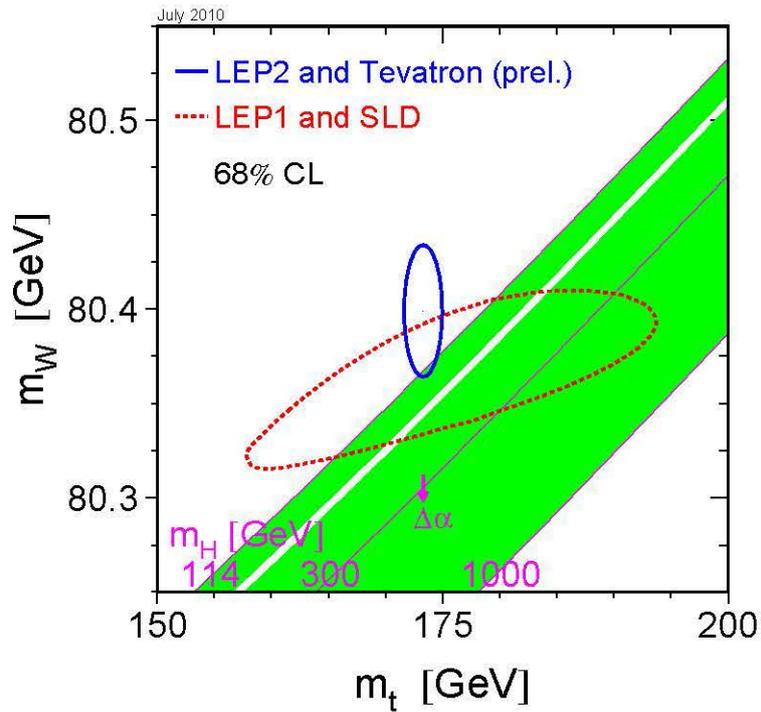
Figure 3.14: Constraints on the Standard Model Higgs Boson from the view of top quark mass and W boson mass.

$114.4 GeV/c^2 < M_H < 158 GeV/c^2$ from the view of theoretical and experimental results.

# Chapter 4

# The Standard Model Higgs Search

As stated in Chapter 3.5, it is higher probability that the Standard Model Higgs boson might be lying down in mass region with $< 150 GeV/c^2$.

In this mass region, the Standard Model Higgs boson decays to b quark pair dominantly and to $\tau$ pair having about 7% branching ratio (Fig. 4.1).

CDF group has searched in its mass region using $H \rightarrow b\bar{b}$ decay mode. We need to think about analysis using $H \rightarrow \tau^+\tau^-$ under considering things after its discovery.

## 4.1 Target Process

CDF group has searched using $XH \rightarrow X + b\bar{b}$ channel and also has done the Higgs boson search using $jj + \tau\tau$ final state using data of $2.3 fb^{-1}$, which is corresponding to $VBF^1 \rightarrow jj + \tau\tau$, $H \rightarrow jj + \tau\tau$, $WH \rightarrow jj + \tau\tau$ and $ZH \rightarrow jj + \tau\tau$.

We newly add the search channel for the Standard Model Higgs using $VH^2$ decaying to all leptonic decay channel (Fig. 4.2) in low mass region ($M_H < 135 GeV/c^2$).

So, the expected number of produced events considering $\sigma(VH)BR(W \rightarrow l\nu/Z \rightarrow ll)BR(H \rightarrow \tau\tau)$, is smaller than other channels. It is quite small compared to b quark pair. But we can expect to have clean events (and less backgrounds) for all leptonic decay channel compared with other channels.

Table 4.1 shows expected number of produced events ($M_H = 115 GeV/c^2$) at $\int Ldt = 6 fb^{-1}$ and $\int Ldt = 16 fb^{-1}$, which we concerned final states.

---

[1]Vector Boson Fusion

[2]"V" stands for Vector boson: $W^\pm$ or $Z$
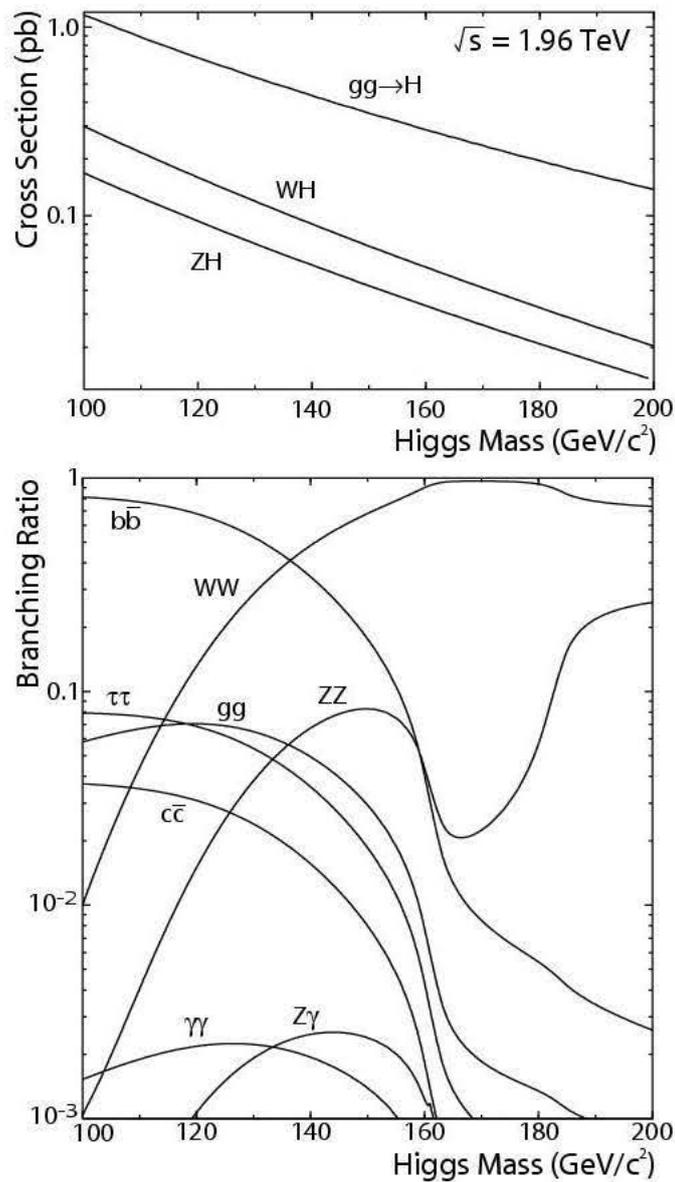
Figure 4.1: Higgs Production cross section at Tevatron and branching ratio of Higgs decay.

## 4.2 Trigger and Luminosity

## 4.3 Event Selection

Our targets of physical processes have 3 or 4 leptons including hadronic $\tau$. Then, our strategy of event selection cuts is to suppress the Drell-Yan events, especially $ee$ and $\mu\mu$, and to keep events including tau as many as possible for $VH$ process. Because
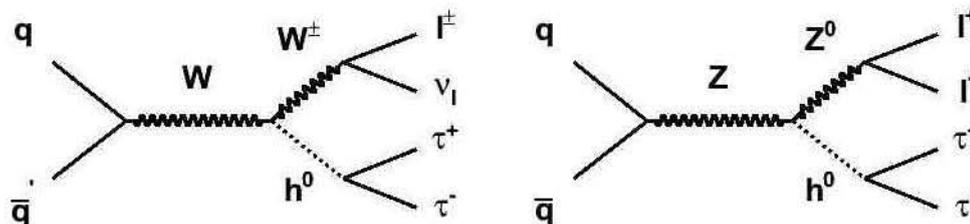
Figure 4.2:  Feynman diagram for the SM Higgs production associated with vector boson. Left figure shows $WH \to l\nu + \tau\tau$. Right figure shows $ZH \to ll + \tau\tau$.

| Process | Nev @ $\int Ldt = 6fb^{-1}$ | Nev @ $\int Ldt = 16fb^{-1}$ |
|---|---|---|
| $WH \to L\nu + \tau\tau$ | $\sim 25$ events | $\sim 66$ events |
| $ZH \to LL + \tau\tau$ | $\sim 5$ events | $\sim 14$ events |

Table 4.1: Expected number of produced events at $M_H = 115 GeV/c^2$.

we are also planning to use multivariate technique to discriminate target process from backgrounds, which would maximize sensitivity.

### 4.3.1   Trigger Requirements

To satisfy with trigger requirement for Monte Carlo samples, we require one isolated lepton, which is CEM electron or CMUP/CMX muon, and isolated track with seed track $P_T > 10 GeV/c$. These 2 objects satisfy with $\Delta R(lep, trk) > 0.175$.

Our lepton categories are summarized in Table 4.2.

### 4.3.2   Event Selection Cuts

We require event quality, topological condition and kinematical condition. At first, we require vertex quality as same as other CDF analysis do. To avoid identifying 2 lepton object as 1 lepton object and avoid taking lepton from different process, we require enough distance between leptons in $\eta - \phi$ plane and leptons come from same $z$-vertex position. Topological condition requirements are the number of leptons in an event, which indicate all leptonic decay channel of $WH$ should have 3 lepton including hadronic tau in an event and such channel of $ZH$ should have 4 lepton. We also require the sum charge of leptons must be $\pm 1$ for $WH$ case and be 0 for $ZH$ case. About kinematical condition requirement, we require $\not{E}_T$ significance just to clean up events,

| Trig Req. | | 3rd&4th lep |
| --- | --- | --- |
| $e$ or $\mu$ | track | |
| TCEM | TCEM | TCEM |
| CMUP | LCEM | LCEM |
| CMX | CMUP | PHX |
| | CMX | CMUP |
| | CMU | CMX |
| | CMP | CMU |
| | CMIOCES | CMP |
| | HadTau | CMIOCES |
| | CrkTrk $e$ | BMU |
| | CrkTrk $\mu$ | CMIOPES |
| | | HadTau |
| | | CrkTrk $e$ |
| | | CrkTrk $\mu$ |

Table 4.2: Possible lepton composition in candidate events categorized by detector region.

especially Drell-Yan process, QCD process and so on.

Summarized event selection cuts are listed as below:

- Vertex quality

  - good quality vertex
  - $|\Delta z(vertex)| < 60.0 cm$

- $NL = 3$ or $NL = 4$, which include hadronic tau

  - $|\Delta z(vertex, lepton)| < 4.0 cm$
  - $|\Delta z(lepton, lepton)| < 4.0 cm$
  - $\Delta R(lepton, lepton) > 0.2$

- $|\Sigma Q_{lep}| = 1$ for $N_{Lep} = 3$ or $|\Sigma Q_{lep}| = 0$ for $N_{Lep} = 4$

- $\not{E}_T/\sqrt{\Sigma E_T} > 1$.

### 4.3.3 Expected Number of Events

**Corrections to the Monte Carlo samples**

Luminosity scaling and some efficiencies are applied to the Monte Carlo samples separately for each lepton combination (lepton type, lepton detector region and so on). We evaluate the weight ($w_i$) for $i$ th event of a MC sample as below.

$$w_i = \frac{\sigma \times B \times L_i \times \epsilon_i^{vetex} \times \epsilon_i^{trigger} \times s_i^{leptonID} \times s_i^{conv}}{N^{gen}} \quad (4.1)$$

$\sigma$ The cross section of each MC process. It is multiplied by K-factor if it needs.

$B$ The branching fraction for each MC process if it needs.

$N^{gen}$ The number of observable MC events ($|Z_0| < 60cm$), which is denominator for acceptance.

$L_i$ The integrated luminosity that depends on which leptons are included in an event. To get the integrated luminosity, data with good quality is only account.

$\epsilon_i^{vertex}$ The efficiency of the $z$-vertex position requirement.

$\epsilon_i^{trigger}$ The trigger efficiency depends on trigger lepton type and the prong number of isolated track. $\epsilon_{CEM}$ for CEM electron, $\epsilon_{CMUP/CMX}$ for CMUP/CMX muon, $\epsilon_{n-prong}$ for isolated track, We apply trigger efficiency for all Monte Carlo process as below.

$$\epsilon_i^{lep-trigger} = 1. - (1. - \epsilon_{CEM})^{N_{CEM}} (1. - \epsilon_{CMUP})^{N_{CMUP}} (1. - \epsilon_{CMX})^{N_{CMX}}$$

$$\epsilon_i^{trk-trigger} = 1. - (1. - \epsilon_{1-prong})^{N_{1-prong}} (1. - \epsilon_{2-prong})^{N_{2-prong}} (1. - \epsilon_{3-prong})^{N_{3-prong}}$$

$$\epsilon_i^{trigger} = \epsilon_i^{lep-trigger} \times \epsilon_i^{trk-trigger},$$

where we assign $\epsilon_{CEM} = 0$ if $N_{CEM} = 0$, the same way to other efficiency $\epsilon$.

$s_i^{leptonID}$ We use common scale factors (data/MC) for electron/muon/crack track/hadronic tau identification because we need to absorb the difference lepton identification efficiencies between data and MC. Then, the effective lepton id scale factor $s_i^{leptonID}$ for an event is

$$s_i^{leptonID} = \prod_k^{N_i^{lep}} s_k,$$

where $s_k$ has different value for each lepton type. Lepton type we use were described in Section 2.4. $N_i^{lep}$ note the number of leptons in an event.

$s_i^{conv}$ The scale factor of photon conversion removal efficiency to absorb the difference efficiency between data and MC samples.

Then, we evaluate the expected number of events ($N^{BGMC}$),

$$N^{BGMC} = \sum_i^{N^{pass}} w_i,$$

where $N^{pass}$ is the number of events which pass event selection cuts.

To confirm the modeling of scale factors and so on, we checked invariant mass distribution in exact 2 lepton case. In this region, we can neglect signals and can use it as control region. Invariant mass distributions are given by different lepton combinations (See Figure 4.3 and 4.4).
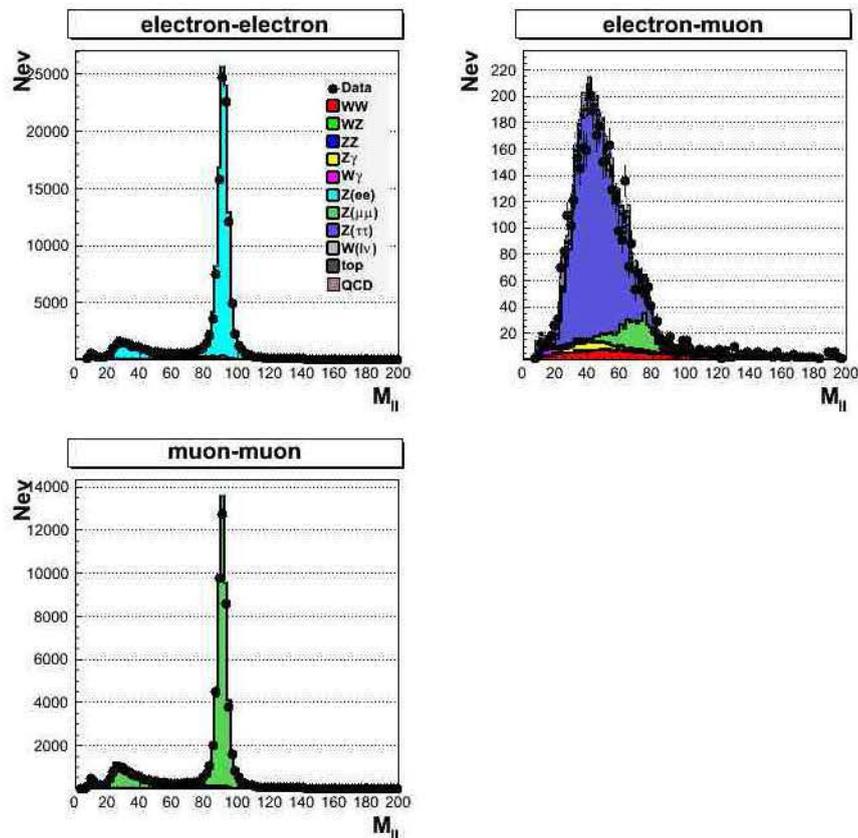
Figure 4.3: Invariant mass distribution in exact 2 lepton case (Control Region), Part I

**Backgrounds Estimation**

After applying our baseline cuts, the expected number of events is shown in Table 4.3. Dominant background process for entire categories is Drell-Yan process, which event include 2 real lepton and jets fake leptons. Shown errors in Table 4.3 include all systematic uncertainties, which is described in next section 4.5.

The way to estimate QCD backgrounds and systematic uncertainties for it is described in next section.

## 4.3.4 Expected Signal Events

We describe the expected number of signal events here. Table 4.4 shows the expected number of $WH \rightarrow All + \tau\tau$ events for different mass sample. About $LLLL$ case in this table, some events can be assigned but the number is less than 1% comparing with other lepton categories of the same mass. Table 4.5 shows the expected number of $ZH \rightarrow All + \tau\tau$ events for different mass sample. We also got the expected number of $VBF$ and $H$ but these expected events are less than 0.1 events for entire lepton
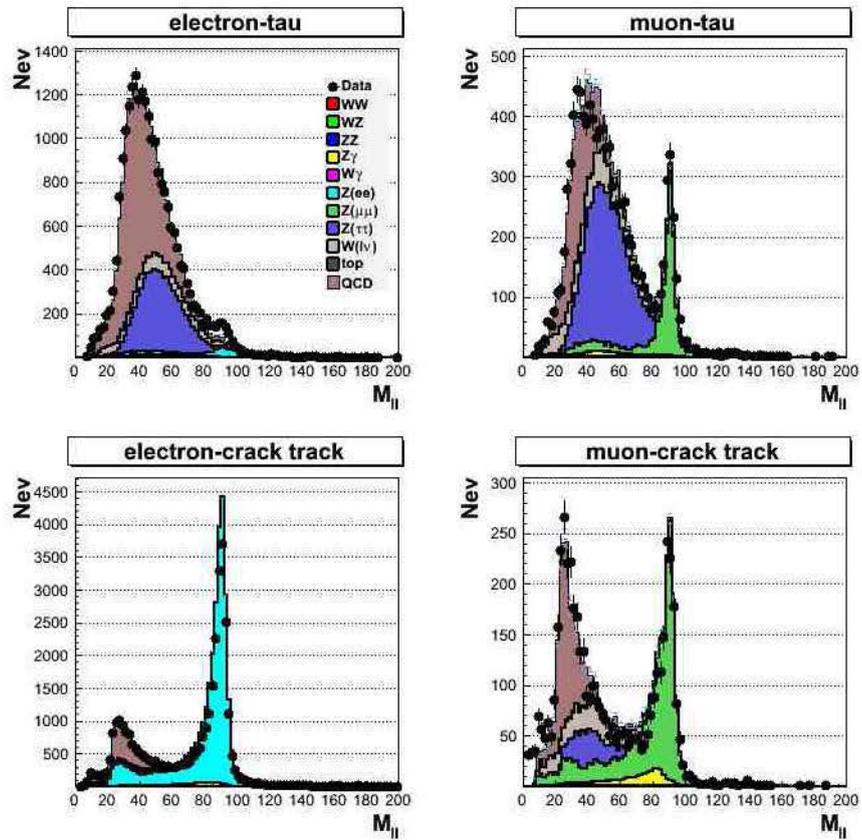
Figure 4.4: Invariant mass distribution in exact 2 lepton case (Control Region), Part II

categories. We do not summarize these here in table but Figure 4.5 include these.

| | 3L | | | | 4L |
|---|---|---|---|---|---|
| | *lll* | *llτ* | *eμτ* | *lττ* | *LLLL* |
| *ZZ* | $6.84 \pm 0.92$ | $2.32 \pm 0.32$ | $0.19 \pm 0.04$ | $0.22 \pm 0.04$ | $0.93 \pm 0.13$ |
| *WZ* | $24.00 \pm 3.17$ | $3.75 \pm 0.51$ | $0.61 \pm 0.09$ | $0.51 \pm 0.08$ | $0.08 \pm 0.02$ |
| *WW* | $1.88 \pm 0.76$ | $1.80 \pm 0.73$ | $0.24 \pm 0.11$ | $0.38 \pm 0.17$ | $0.01 \pm 0.01$ |
| *DY(ee)* | $158.90 \pm 61.04$ | $78.35 \pm 30.25$ | $0.01 \pm 0.01$ | $0.44 \pm 0.19$ | $0.72 \pm 0.39$ |
| *DY(μμ)* | $67.80 \pm 26.09$ | $49.32 \pm 19.14$ | $0.51 \pm 0.21$ | $0.88 \pm 0.35$ | $0.38 \pm 0.21$ |
| *DY(ττ)* | $13.89 \pm 5.35$ | $24.96 \pm 9.61$ | $2.19 \pm 0.75$ | $6.52 \pm 2.53$ | $0.06 \pm 0.04$ |
| *Zγ* | $12.75 \pm 1.87$ | $4.28 \pm 0.67$ | $0.69 \pm 0.12$ | $0.48 \pm 0.09$ | $0.07 \pm 0.02$ |
| $t\bar{t}$ | $21.54 \pm 5.97$ | $6.82 \pm 1.91$ | $0.39 \pm 0.12$ | $0.30 \pm 0.10$ | $0.35 \pm 0.13$ |
| *Wγ* | $0.27 \pm 0.06$ | $0.26 \pm 0.06$ | $0.10 \pm 0.04$ | $0.03 \pm 0.02$ | $0.00 \pm 0.00$ |
| *W + Jets* | $13.05 \pm 7.00$ | $16.40 \pm 8.79$ | $0.33 \pm 0.20$ | $4.49 \pm 2.43$ | $0.00 \pm 0.00$ |
| *QCD* | $9.48^{+10.29}_{-9.48}$ | $26.06 \pm 12.16$ | $0.00 + 1.29$ | $6.19 \pm 5.48$ | $0.82^{+1.05}_{-0.82}$ |
| total | $330.40^{+68.13}_{-68.01}$ | $214.32 \pm 40.05$ | $5.26^{+1.59}_{-0.93}$ | $20.44 \pm 6.53$ | $3.43^{+1.16}_{-0.95}$ |
| Data | 284 | 203 | 8 | 16 | 6 |

Table 4.3: Expected Number of Events for each lepton combination categories. The notation of "*l*" in the above table means electrons, muons and crack tracks. The notation of "*L*", any charged leptons including hadronic tau. Errors in table are all systematic uncertainties included.

| | 3L | | | | 4L |
|---|---|---|---|---|---|
| | *lll* | *llτ* | *eμτ* | *lττ* | *LLLL* |
| 100 | $0.24 \pm 0.02$ | $0.36 \pm 0.03$ | $0.17 \pm 0.01$ | $0.20 \pm 0.02$ | $0.0032 \pm 0.0006$ |
| 105 | $0.21 \pm 0.02$ | $0.31 \pm 0.03$ | $0.15 \pm 0.01$ | $0.18 \pm 0.02$ | $0.0024 \pm 0.0004$ |
| 110 | $0.19 \pm 0.02$ | $0.29 \pm 0.02$ | $0.13 \pm 0.01$ | $0.16 \pm 0.01$ | $0.0017 \pm 0.0003$ |
| 115 | $0.16 \pm 0.01$ | $0.24 \pm 0.02$ | $0.11 \pm 0.01$ | $0.13 \pm 0.01$ | $0.0019 \pm 0.0003$ |
| 120 | $0.14 \pm 0.01$ | $0.20 \pm 0.02$ | $0.093 \pm 0.008$ | $0.11 \pm 0.01$ | $0.0018 \pm 0.0003$ |
| 125 | $0.112 \pm 0.009$ | $0.17 \pm 0.01$ | $0.077 \pm 0.007$ | $0.089 \pm 0.008$ | $0.0015 \pm 0.0003$ |
| 130 | $0.089 \pm 0.007$ | $0.13 \pm 0.01$ | $0.058 \pm 0.005$ | $0.070 \pm 0.006$ | $0.0010 \pm 0.0002$ |
| 135 | $0.067 \pm 0.006$ | $0.097 \pm 0.008$ | $0.045 \pm 0.004$ | $0.051 \pm 0.004$ | $0.0008 \pm 0.0001$ |
| 140 | $0.048 \pm 0.004$ | $0.070 \pm 0.006$ | $0.035 \pm 0.003$ | $0.037 \pm 0.003$ | $0.00055 \pm 0.00009$ |
| 145 | $0.032 \pm 0.003$ | $0.046 \pm 0.004$ | $0.022 \pm 0.002$ | $0.025 \pm 0.002$ | $0.00032 \pm 0.00005$ |
| 150 | $0.020 \pm 0.002$ | $0.030 \pm 0.003$ | $0.013 \pm 0.001$ | $0.015 \pm 0.001$ | $0.00018 \pm 0.00003$ |

Table 4.4: Expected number of events for $WH \rightarrow all + \tau\tau$

| | 3L | | | | 4L |
|---|---|---|---|---|---|
| | *lll* | *llτ* | *eμτ* | *lττ* | *LLLL* |
| 100 | $0.23 \pm 0.02$ | $0.26 \pm 0.02$ | $0.028 \pm 0.003$ | $0.039\pm$ | $0.091 \pm 0.008$ |
| 105 | $0.21 \pm 0.02$ | $0.23 \pm 0.02$ | $0.025 \pm 0.002$ | $0.038\pm$ | $0.081 \pm 0.007$ |
| 110 | $0.18 \pm 0.01$ | $0.20 \pm 0.02$ | $0.025 \pm 0.002$ | $0.032\pm$ | $0.072 \pm 0.006$ |
| 115 | $0.16 \pm 0.01$ | $0.17 \pm 0.01$ | $0.019 \pm 0.002$ | $0.027\pm$ | $0.063 \pm 0.005$ |
| 120 | $0.13 \pm 0.01$ | $0.14 \pm 0.01$ | $0.017 \pm 0.002$ | $0.025\pm$ | $0.056 \pm 0.005$ |
| 125 | $0.100 \pm 0.008$ | $0.12 \pm 0.01$ | $0.014 \pm 0.001$ | $0.020\pm$ | $0.046 \pm 0.004$ |
| 130 | $0.082 \pm 0.007$ | $0.089 \pm 0.008$ | $0.012 \pm 0.001$ | $0.015\pm$ | $0.036 \pm 0.003$ |
| 135 | $0.061 \pm 0.005$ | $0.068 \pm 0.006$ | $0.0087 \pm 0.0008$ | $0.012\pm$ | $0.026 \pm 0.002$ |
| 140 | $0.043 \pm 0.004$ | $0.048 \pm 0.004$ | $0.0064 \pm 0.0006$ | $0.008\pm$ | $0.019 \pm 0.002$ |
| 145 | $0.029 \pm 0.002$ | $0.031 \pm 0.003$ | $0.0040 \pm 0.0004$ | $0.006\pm$ | $0.013 \pm 0.001$ |
| 150 | $0.018 \pm 0.001$ | $0.020 \pm 0.002$ | $0.0025 \pm 0.0002$ | $0.004\pm$ | $0.0084 \pm 0.0007$ |

Table 4.5: Expected number of events for $ZH \rightarrow all + \tau\tau$
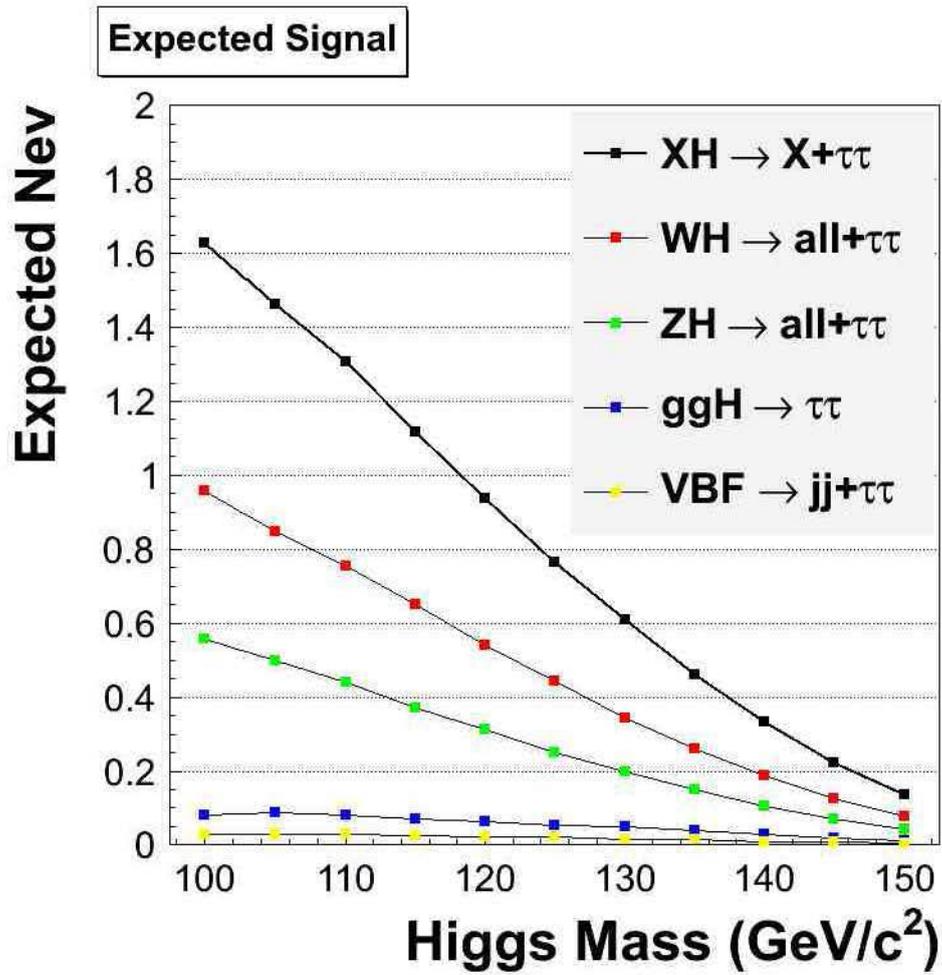
Figure 4.5: The expected number of $H \rightarrow \tau\tau$ events for different Higgs mass.

# 4.4 Signal and Background Discrimination

To discriminate signals from backgrounds, we use a multivariate technique. In this section, we introduce our method and strategy, first. Then, we describe input variables, training & test results of classifiers and how to create convoluted response.

## 4.4.1 Support Vector Machine

Machine learning can distinguish 2 categories. One is supervised learning, the other is unsupervised learning. Support Vector Machine (SVM) is a kind of supervised learning method. Basic concept of simple SVM is classifying given data into 2 categories in a hyperspace having dimension with the order of the number of input variables. This concept of SVM might be naturally and/or simply extending "cut base analysis".

Given data is supervised, for example, one have class:$c_i = +1$, the others have class:$c_i = -1$. SVM put given supervised data into a hyperspace and separate data using hyperplane. There are many hyperplanes satisfying with the condition. Any hyperplane can satisfy with $\mathbf{w} \cdot \mathbf{x} - b = 0$, where $\mathbf{x}$ is a set of input variables and the vector $\mathbf{w}$ is a normal vector of hyperplane. The parameter $frac{b}{\mathbf{w}}$ is the offset of the hyperplane from the origin along the normal vector $\mathbf{w}$. Then, $\mathbf{w} \cdot \mathbf{x}_i - b \geq 1$ for points of $c_i = +1$ and $\mathbf{w} \cdot \mathbf{x}_i - b \leq 1$ for points of $c_i = -1$. These 2 equation can be unified to $c_i(\mathbf{w} \cdot \mathbf{x}_i - b) \geq 1$.

Meaning of training related to SVM is to look for the hyperplane which maximize margin between 2 categories under a condition. This condition is different by using different SVM algorithm. Here, we use the soft margin method of SVM ([38]) that modified the maximum margin method that allow mislabel to given data. This method looks for a hyperplane separate given data as cleanly as possible. The equation changes to $c_i(\mathbf{w} \cdot \mathbf{x}_i - b) \geq 1 - \xi_i$, where $\xi_i$ is the slack variables. The optimization problem changes from $\min_{\mathbf{w}}\{\frac{1}{2}||\mathbf{w}||^2\}$ to $\min_{\mathbf{w},\xi_i}\{\frac{1}{2}||\mathbf{w}||^2 + C\sum_{i=1}^{n}\xi_i\}$, which $C$ is called penalty constant and should be optimized.

To deal with non-linear classification, the kernel function is applied to hyperplanes (kernel trick) ([39],[40]). The algorithm transforms input variable space to high dimensional space, then the kernel function may fit the maximum-margin hyperplane in a transformed feature space (Bottom of Figure 4.6). Here, Gaussian kernel for which feature space corresponds to Hilbert space:

$$K(\mathbf{x}_i \cdot \mathbf{x}_j) = exp(-\gamma||\mathbf{x}_i - \mathbf{x}_j||^2), \gamma > 0$$

So, optimization parameters penalty parameter $C$ which comes from soft-margin way, and kernel parameter $\gamma$ which comes from kernel trick.

By the way, we simply use support vector machine in the TMVA tool kit [37].
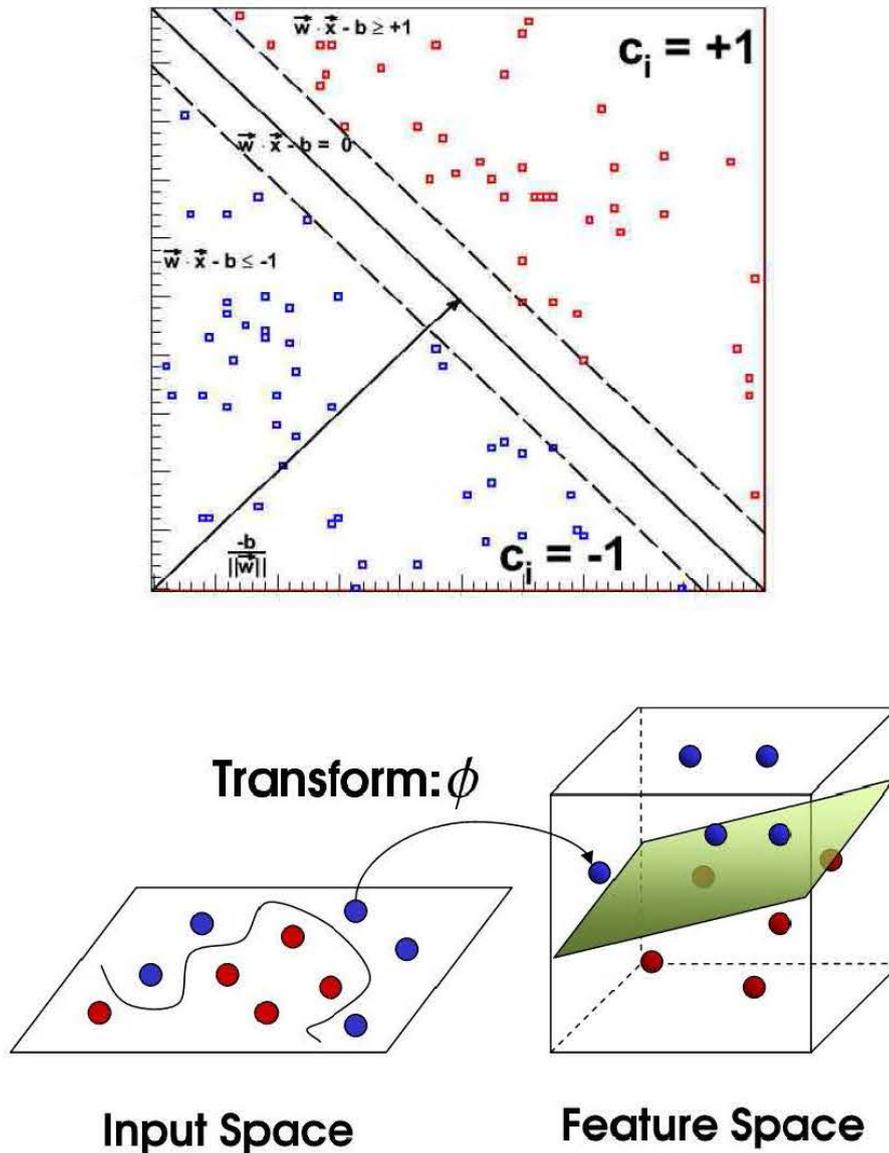
Figure 4.6:   Top figure shows rough sketch of Support Vector Machine.  Given data belong to class $+1$ or class $-1$ in hyperspace. For example, blue boxes belong to class $-1$ and red boxes belong to class $+1$. The maximum margin hyperplane is defined by $\vec{w} \cdot \vec{x} - b = 0$. Support vector is points on hyperplane defined by $\vec{w} \cdot \vec{x} - b = \pm 1$, which does not care blue or red.  Bottom figure shows the transformation of input space. Kernel function shoulders the transformation.

### 4.4.2   Strategy for Training and Unifying Response

We prepare for 8 trained classifiers to discriminate signal from backgrounds. Our training strategy is to discriminate plenty, different kinematics and similar kinematics backgrounds separately/simultaneously.

In $lll$ and $ll\tau$ cases, we have large contribution from Drell-Yan process ($ee,\mu\mu$) as shown in Table 4.3. These cases include Drell-Yan plus one fake lepton, which is mostly making a fake of electron or hadronic tau. In $e\mu\tau$ and $l\tau\tau$ cases, there are smaller statistics than $lll$ and $ll\tau$ cases, and we also have smaller MC statistics. These cases indicate such events that Z boson decays to $\tau\tau$ and jet makes a fake of hadronic tau. In 4 lepton case, $WH$ signal process does not fall into much.

For $lll$ and $ll\tau$ cases, we train 3 classifiers for each case, that is "$VH$ vs $WZ/ZZ$", "$VH$ vs Drell-Yan($ee,\mu\mu$)" and "$VH$ vs $t\bar{t}$". For $e\mu\tau$ and $l\tau\tau$ cases, we train 1 classifier. For 4 lepton case, we also train 1 classifier, which is trained using $ZH$ Monte Carlo sample and all background Monte Carlo samples. About signal process $WH/ZH$, $WH \rightarrow L\nu + \tau\tau$ ($M_H = 120 GeV/c^2$) and $ZH \rightarrow LL + \tau\tau$ ($M_H = 120 GeV/c^2$) Monte Carlo samples are used to train. In whole, we train 8 classifiers for analysis as in Table 4.6.

| | 3L | | | 4L |
|---|---|---|---|---|
| $lll$ | $ll\tau$ | $e\mu\tau, l\tau\tau$ | | $LLLL$ |
| $VH$ vs DY($ee,\mu\mu$) ($f^{DY0}$) 6500 : 6500 | $VH$ vs DY($ee,\mu\mu$) ($f^{DY1}$) 2500 : 2500 | $VH$ vs All Bkg ($f^{AL0}$) 850 : 850 | | $ZH$ vs All Bkg ($f^{AL1}$) 650 : 650 |
| $VH$ vs $t\bar{t}$ ($f^{TT0}$) 1800 : 1800 | $VH$ vs $t\bar{t}$ ($f^{TT1}$) 600 : 600 | - | | - |
| $VH$ vs $WZ/ZZ$ ($f^{DB0}$) 4550 : 4550 | $VH$ vs $WZ/ZZ$ ($f^{DB1}$) 1050 : 1050 | - | | - |

Table 4.6: Training Categories. "$V$" stands for vector boson, "$W/Z$". DY stands for Drell-Yan. "All Bkg" means that all kind of background Monte Carlo samples are used for training. The number in table is showing the number of training sample (SG:BG).

Each classifier $f$ returns a response for $i$ th input variables $\mathbf{x}_i$. For example, a classifier $f^{DY0}$ which was trained by "$VH$ vs Drell-Yan ($ee,\mu\mu$)" in $lll$ case returns a response $r^{DY0}$ as below.

$$r_i^{DY0} = f^{DY0}(\mathbf{x}_i)$$

We prepare for 3 classifiers for $lll$ and $ll\tau$, resulted in 3 responses from 3 classifiers for an event. So, we convolute 3 responses into 1 response using a simple function below.

$$g(x_1, x_2, x_3) = (x_1 \cdot x_2 + x_2 \cdot x_3 + x_3 \cdot x_1)/3.$$

Then, we get a response for $i$ th event as below.

$$r_i = g(r_i^{DY0}, r_i^{TT0}, r_i^{DB0})$$

We finally have 5 responses for 5 lepton combination categories.

## 4.4.3 Input Variables

Each classifier for each lepton category uses a different set of input variables because backgrounds are different. The lists and ranks of input variables are shown in Table 4.7 for 3 lepton case and Table 4.8 for 4 lepton case.

In the tables, the cell filled by number is used for each classifier. The numbers show the ranking of the separation gain for each input variable. We list notations related to input variables in Table 4.7 and Table 4.8 as below.

**LCOMB:** It represents lepton combination. For example in *lll* case, we respectively give numbers to *eee*, *eeμ*, *eμμ* and so on. Lepton types we distinguish are $e$, $\mu$, crack track and $\tau$. Further more examples, the process of $Z\gamma \to ee + \gamma$ pretends to be *eee*.

**# of Jets:** This shows the number of jets with level 5 corrected $E_T > 15GeV$ and $|\eta| < 2.5$.

**$H_T$:** We define that scalar sum of lepton $P_T$ and $\not{E}_T$.

**$L1$:** It represents 1st leading lepton. Here, we do not distinguish lepton type.

**$L2$:** It represents 2nd leading lepton. Here, we do not distinguish lepton type.

**$L3$:** It represents 3rd leading lepton. Here, we do not distinguish lepton type.

**$L4$:** It represents 4th leading lepton if exists. Here, we do not distinguish lepton type.

**$\sum_{sig} P_T^{trk}$:** The scalar sum of $P_T$ in signal cone hadronic tau.

**$\sum_{iso} P_T^{trk}$:** The scalar sum of $P_T$ in isolation cone for hadronic tau.

**$\sum_{sig} \Delta R^{trk}$:** The sum of $\Delta R$ between seed track and tracks in signal cone.

**$\sum_{iso} \Delta R^{trk}$:** The sum of $\Delta R$ between seed track and tracks in isolation cone.

| Input Variable | $lll$ | | | $ll\tau$ | | | $e\mu\tau, l\tau\tau$ |
|---|---|---|---|---|---|---|---|
| | $f^{DY0}$ | $f^{TT0}$ | $f^{DB0}$ | $f^{DY1}$ | $f^{TT1}$ | $f^{DB1}$ | $f^{AL0}$ |
| LCOMB | 1 | 1 | 14 | - | 2 | - | - |
| # of Jets | - | 2 | - | - | 1 | - | - |
| $H_T$ | 8 | - | 11 | 7 | - | 6 | - |
| $\not{E}_T$ | 3 | - | - | 1 | 14 | 9 | 10 |
| $P_T(L1)$ | - | - | 7 | 13 | - | - | 7 |
| $P_T(L2)$ | - | - | 6 | 15 | 8 | 11 | 4 |
| $P_T(L3)$ | 7 | 3 | 3 | - | 3 | - | - |
| $\Delta\phi(L1, \not{E}_T)$ | 9 | 5 | 12 | - | 11 | 12 | - |
| $\Delta\phi(L2, \not{E}_T)$ | - | - | 13 | - | - | - | - |
| $\Delta\phi(L3, \not{E}_T)$ | - | 9 | 4 | - | 9 | - | - |
| $\Delta R(L2, L3)$ | - | - | - | - | - | - | - |
| $\Delta R(L1, L2)$ | - | - | 16 | 16 | 15 | 10 | - |
| $\Delta R(L1, L3)$ | - | - | - | - | - | - | - |
| $M_T(L1, \not{E}_T)$ | 11 | - | 15 | 4 | - | - | - |
| $M_T(L2, \not{E}_T)$ | 4 | - | - | 3 | - | 7 | - |
| $M_T(L3, \not{E}_T)$ | 2 | - | - | 2 | - | 13 | 8 |
| $M_T(Leps + \not{E}_T)$ | 6 | - | 9 | 8 | - | 15 | 2 |
| $M(Leps + \not{E}_T)$ | 5 | - | 8 | 9 | - | 16 | 1 |
| $M(Leps)$ | - | 6 | 1 | - | 5 | - | 3 |
| $M(L2, L3)$ | 10 | 4 | 10 | - | 4 | - | 9 |
| $M(L1, L2)$ | 12 | 8 | 2 | - | 12 | 3 | 6 |
| $M(L1, L3)$ | - | 7 | 5 | - | 6 | 14 | 11 |
| Visible $E_T$ | N/A | N/A | N/A | 11 | 16 | 1 | 5 |
| Visible $M$ | N/A | N/A | N/A | 10 | 10 | 8 | 12 |
| $\sum_{sig} P_T^{trk}$ | N/A | N/A | N/A | 14 | - | 5 | - |
| $\sum_{iso} P_T^{trk}$ | N/A | N/A | N/A | 12 | - | 4 | - |
| $\sum_{sig} \Delta R^{trk}$ | N/A | N/A | N/A | 6 | 13 | 2 | - |
| $\sum_{iso} \Delta R^{trk}$ | N/A | N/A | N/A | 5 | 7 | - | - |
| total # of input variables | 12 | 9 | 16 | 16 | 16 | 16 | 12 |
| Figure # | 4.7 | 4.8 | 4.9, 4.10 | 4.11, 4.12 | 4.13, 4.14 | 4.15, 4.16 | 4.17 |

Table 4.7:  List of input variables in 3 lepton case. The notation of "N/A" means "can not be for use". 6 input variables from bottom are related to hadronic tau.

| Input Variable | $LLLL$ |
|---|---|
| | $f^{AL1}$ |
| # of crack track | 1 |
| # of hadronic tau | 12 |
| $H_T$ | 13 |
| $P_T(L1)$ | - |
| $P_T(L2)$ | 5 |
| $P_T(L3)$ | 6 |
| $P_T(L4)$ | 4 |
| $\phi(L1, \not{E}_T)$ | 17 |
| $\phi(L2, \not{E}_T)$ | - |
| $\phi(L3, \not{E}_T)$ | - |
| $\phi(L4, \not{E}_T)$ | 20 |
| $M_T(L1, \not{E}_T)$ | - |
| $M_T(L2, \not{E}_T)$ | 11 |
| $M_T(L3, \not{E}_T)$ | 10 |
| $M_T(L4, \not{E}_T)$ | 16 |
| $M_T(Leps + \not{E}_T)$ | 14 |
| $M(Leps + \not{E}_T)$ | 2 |
| $M(Leps)$ | 3 |
| $M(L2, L3)$ | 7 |
| $M(L1, L2)$ | 19 |
| $M(L1, L3)$ | 18 |
| $M(L1, L4)$ | 15 |
| $M(L2, L4)$ | 8 |
| $M(L3, L4)$ | 9 |
| total # of input variables | 20 |
| Figure # | 4.18,4.19 |

Table 4.8: List of input variables in 4 lepton case.
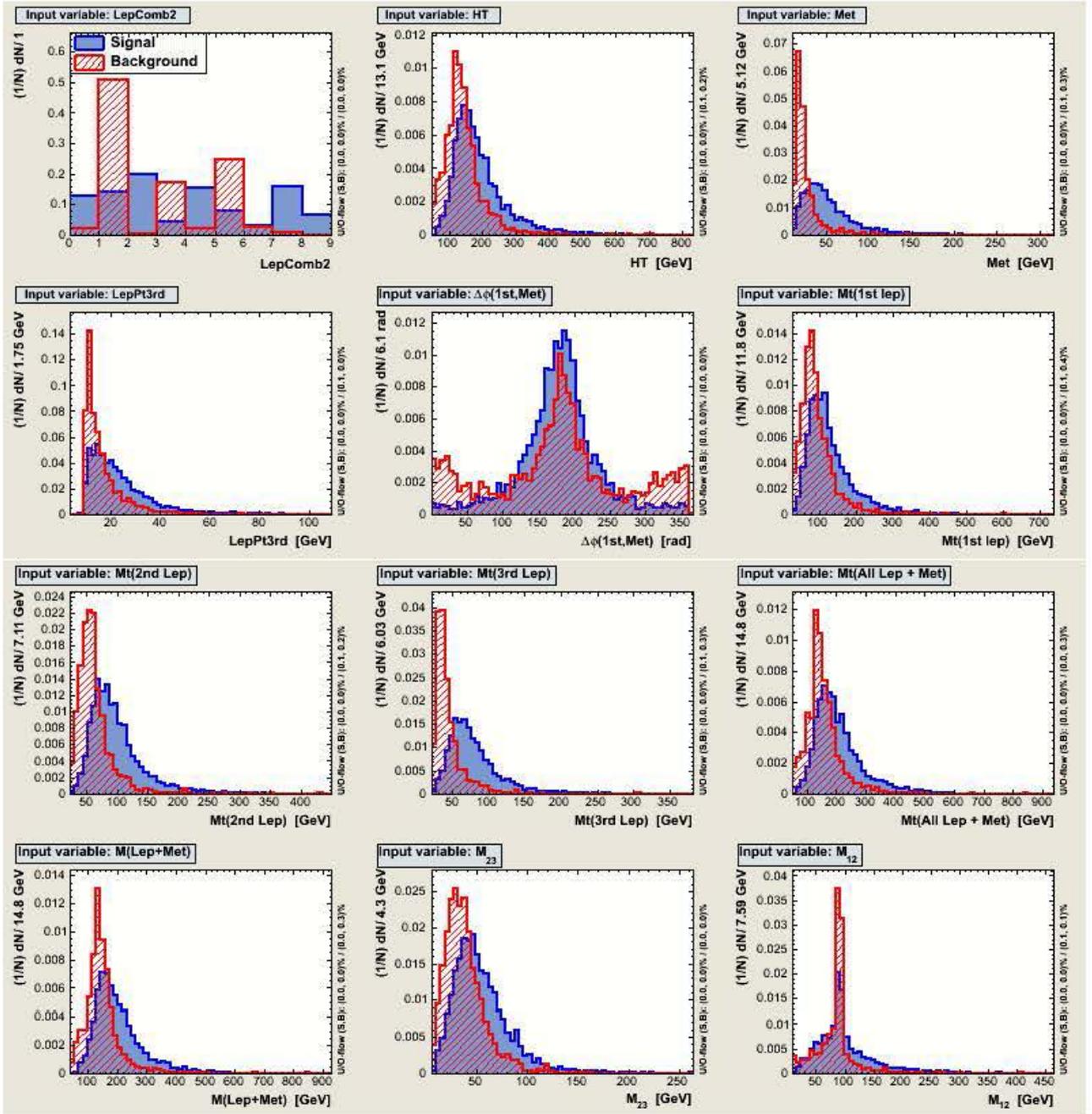
Figure 4.7: Input Variable Distributions for $f^{DY0}$.
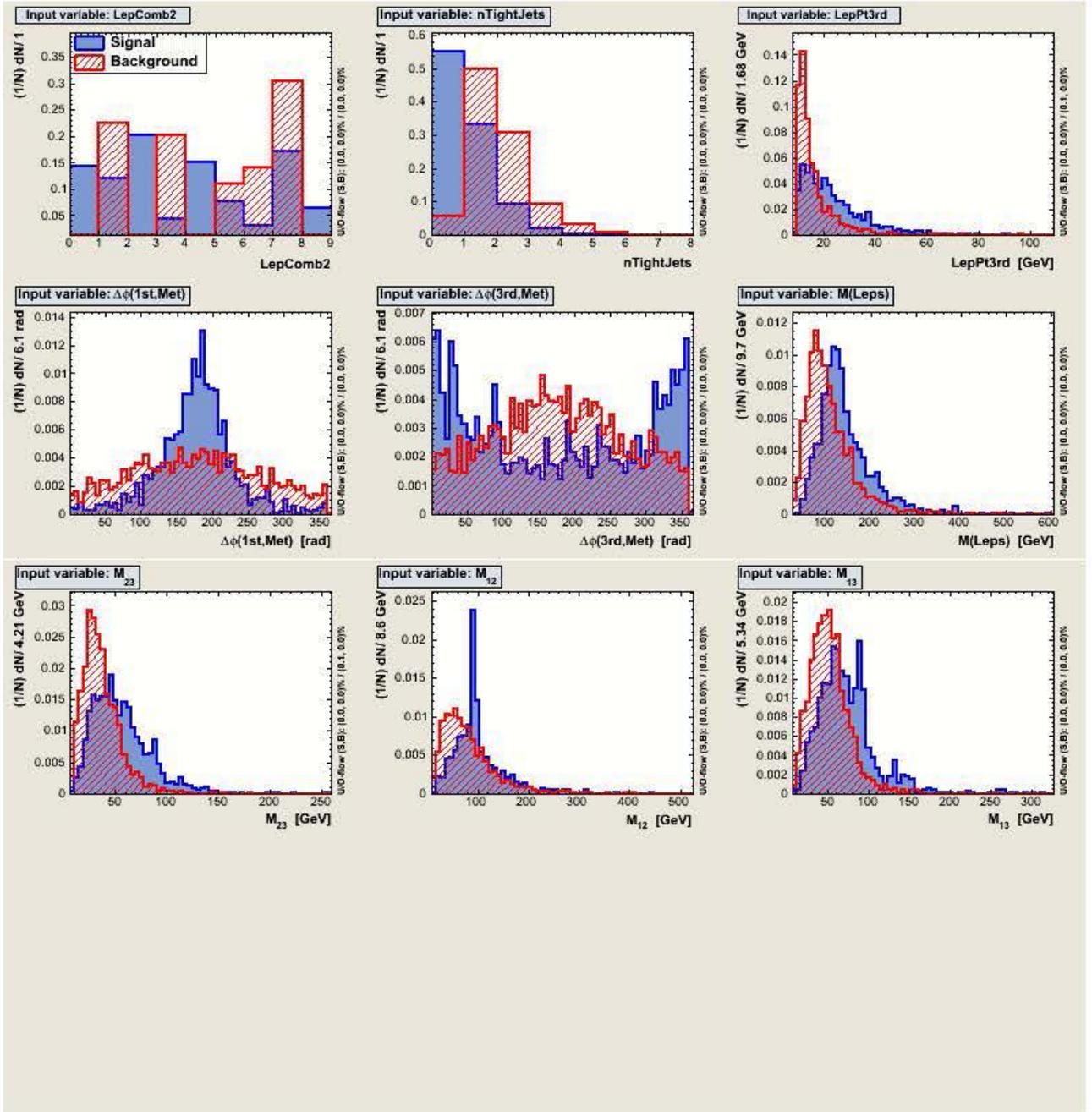
Figure 4.8: Input Variable Distributions for $f^{TT0}$.
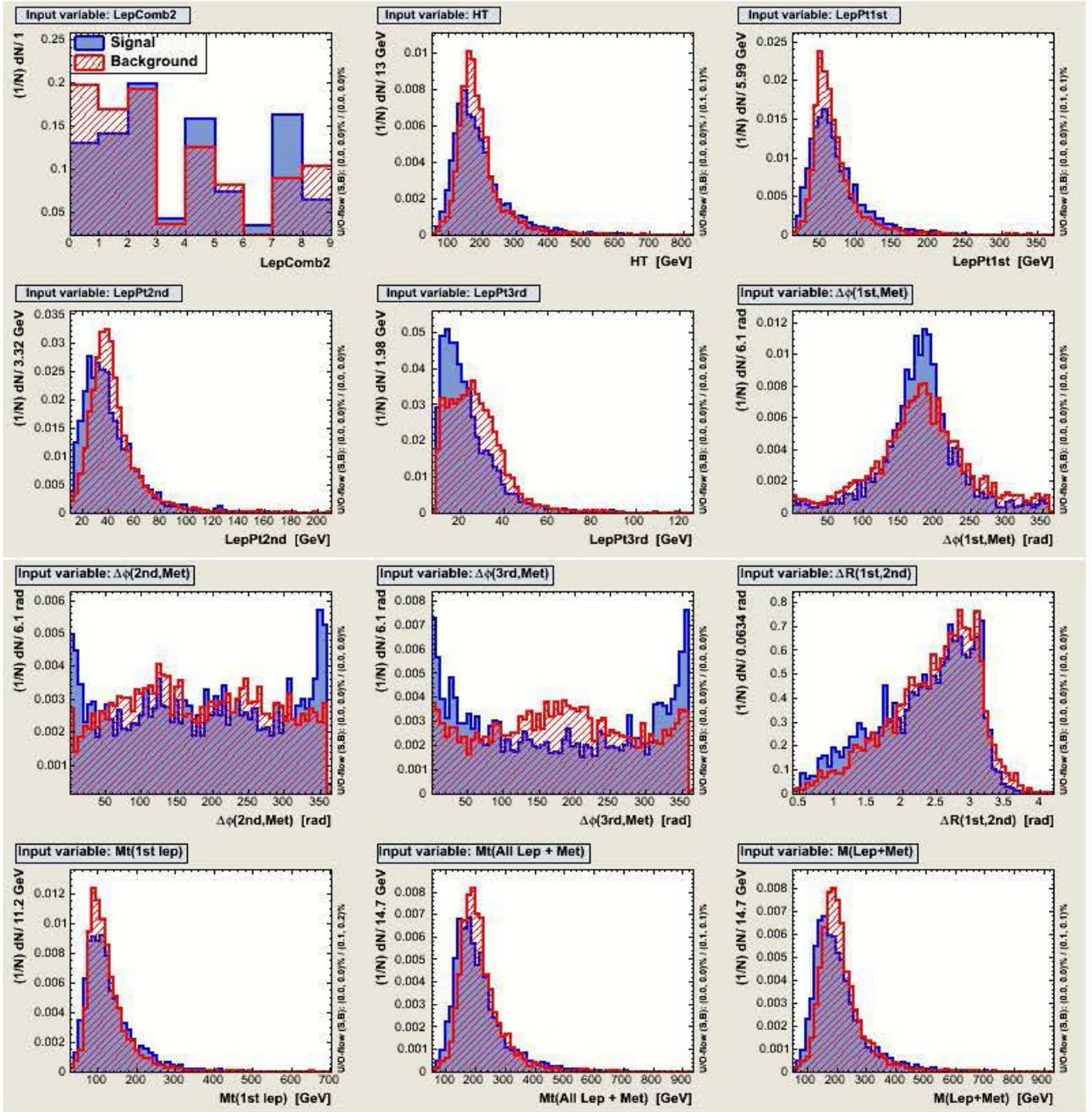
Figure 4.9: Input Variable Distributions for $f^{DB0}$ (PART 1).
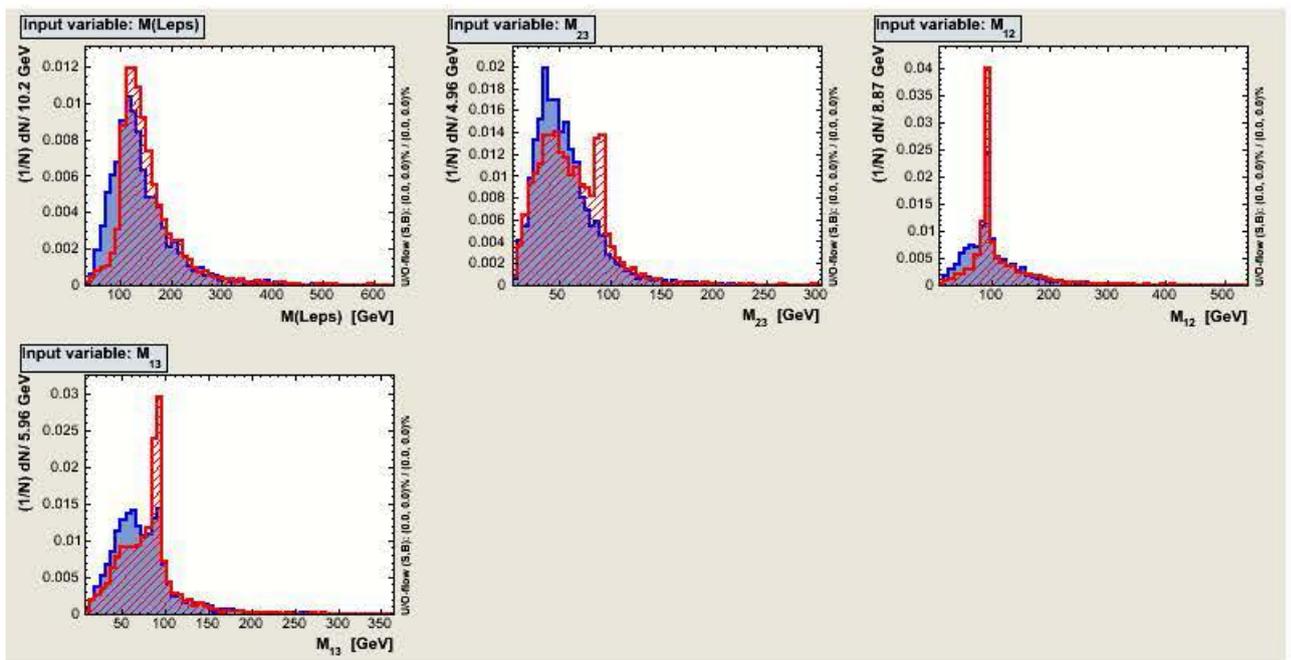
Figure 4.10:  Input Variable Distributions for $f^{DB0}$ (PART 2).
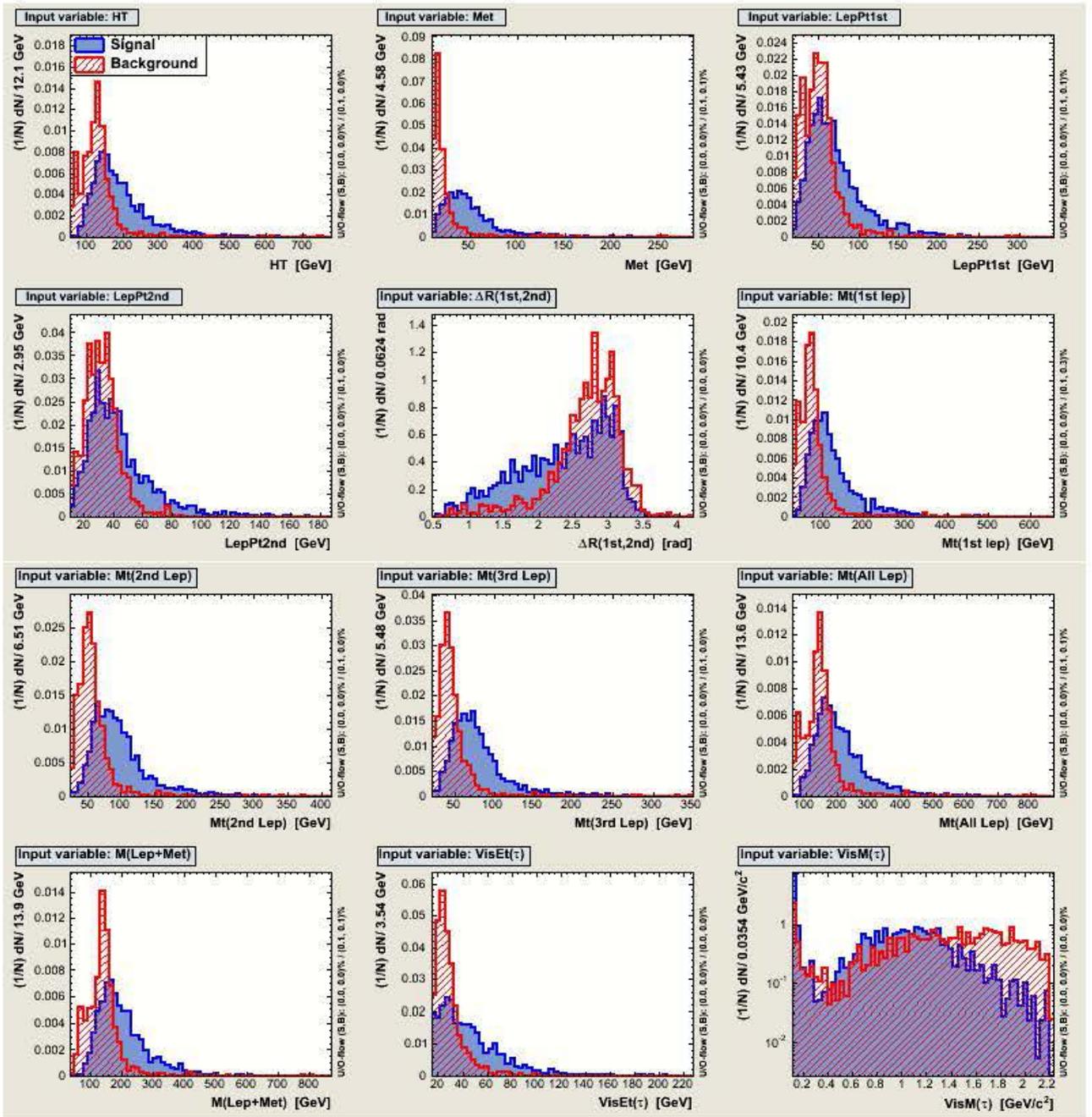
Figure 4.11: Input Variable Distributions for $f^{DY1}$ (PART 1).
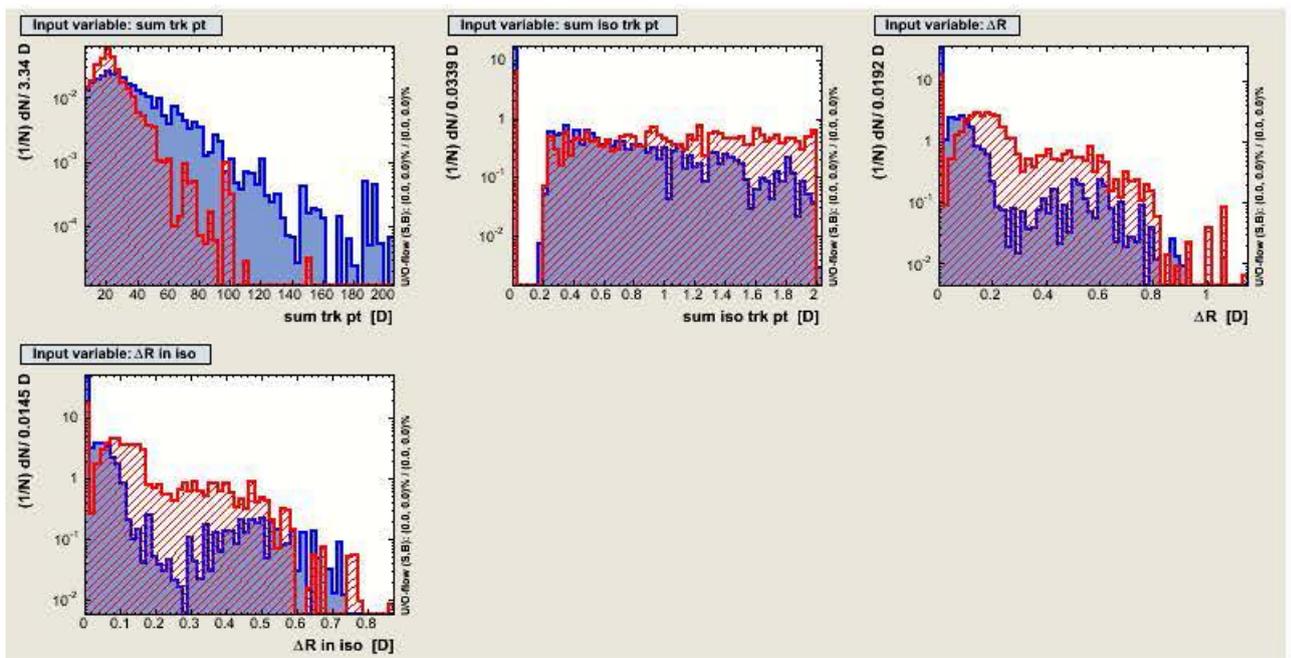
Figure 4.12: Input Variable Distributions for $f^{DY1}$ (PART 2).
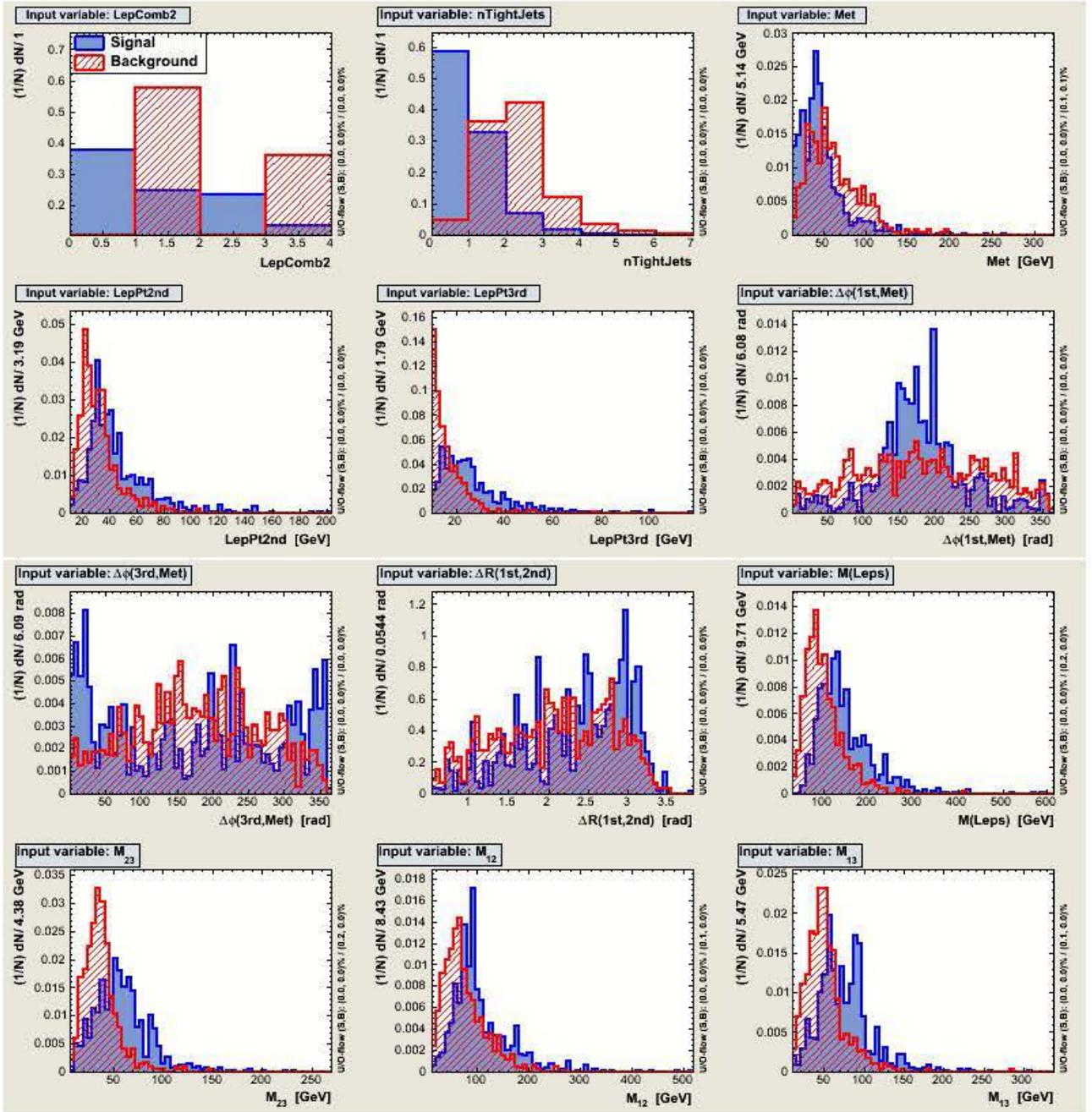
Figure 4.13: Input Variable Distributions for $f^{TT1}$ (PART 1).
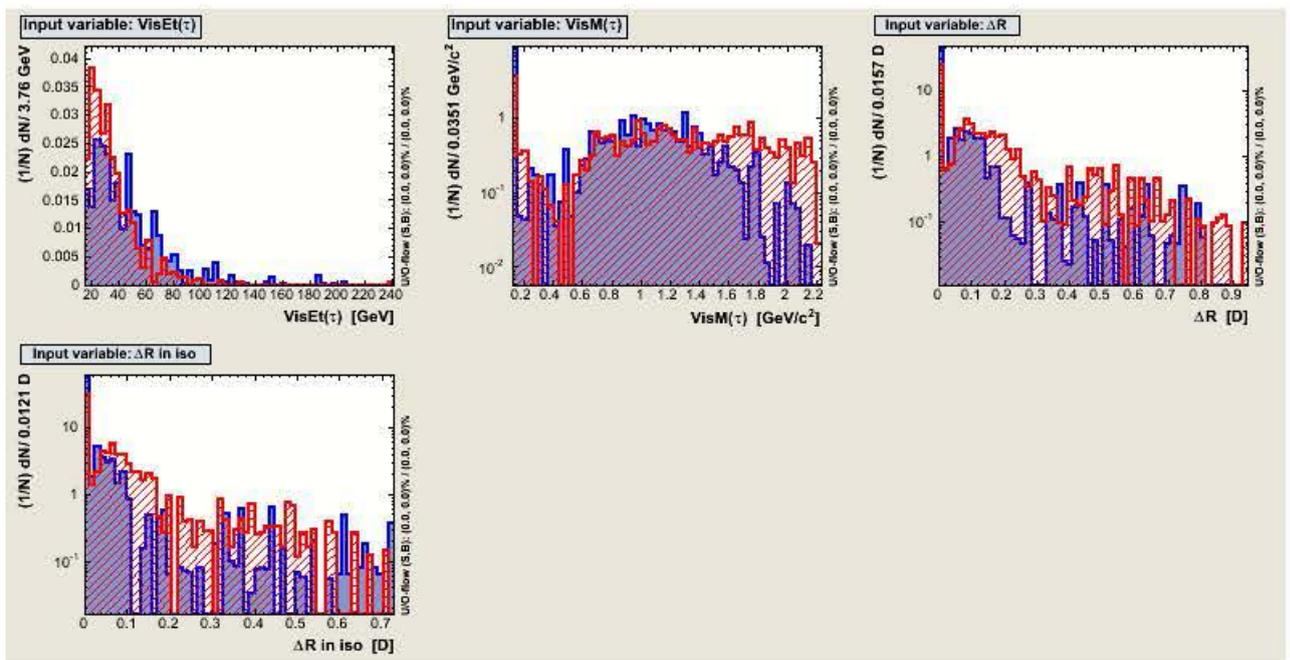
Figure 4.14:  Input Variable Distributions for $f^{TT1}$ (PART 2).
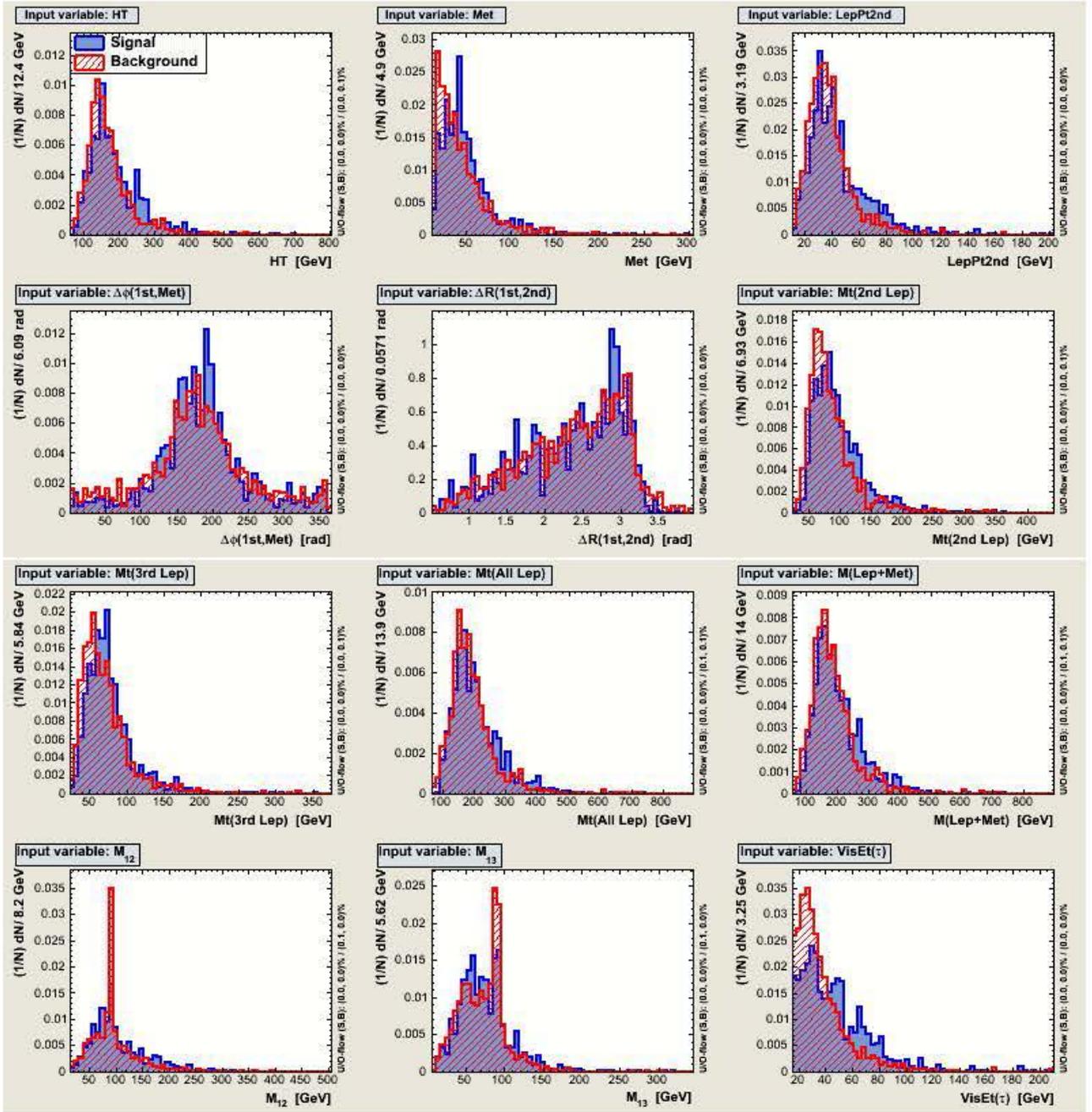
Figure 4.15: Input Variable Distributions for $f^{DB1}$ (PART 1).
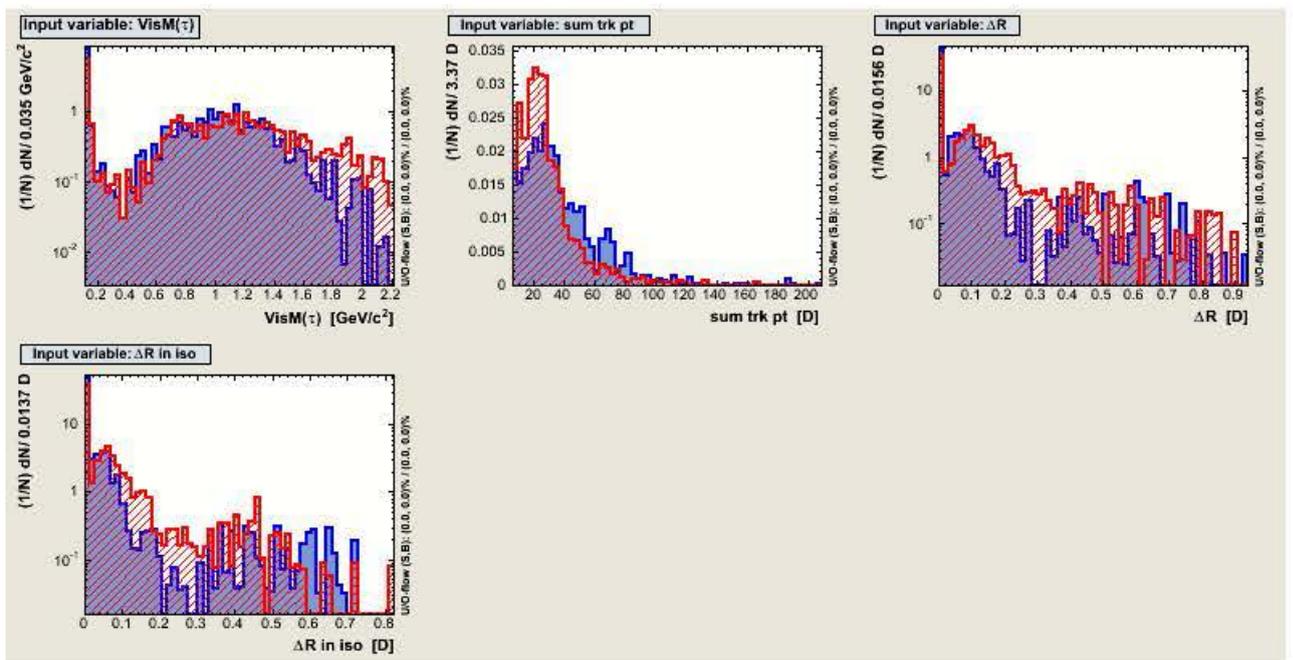
Figure 4.16: Input Variable Distributions for $f^{DB1}$ (PART 2).
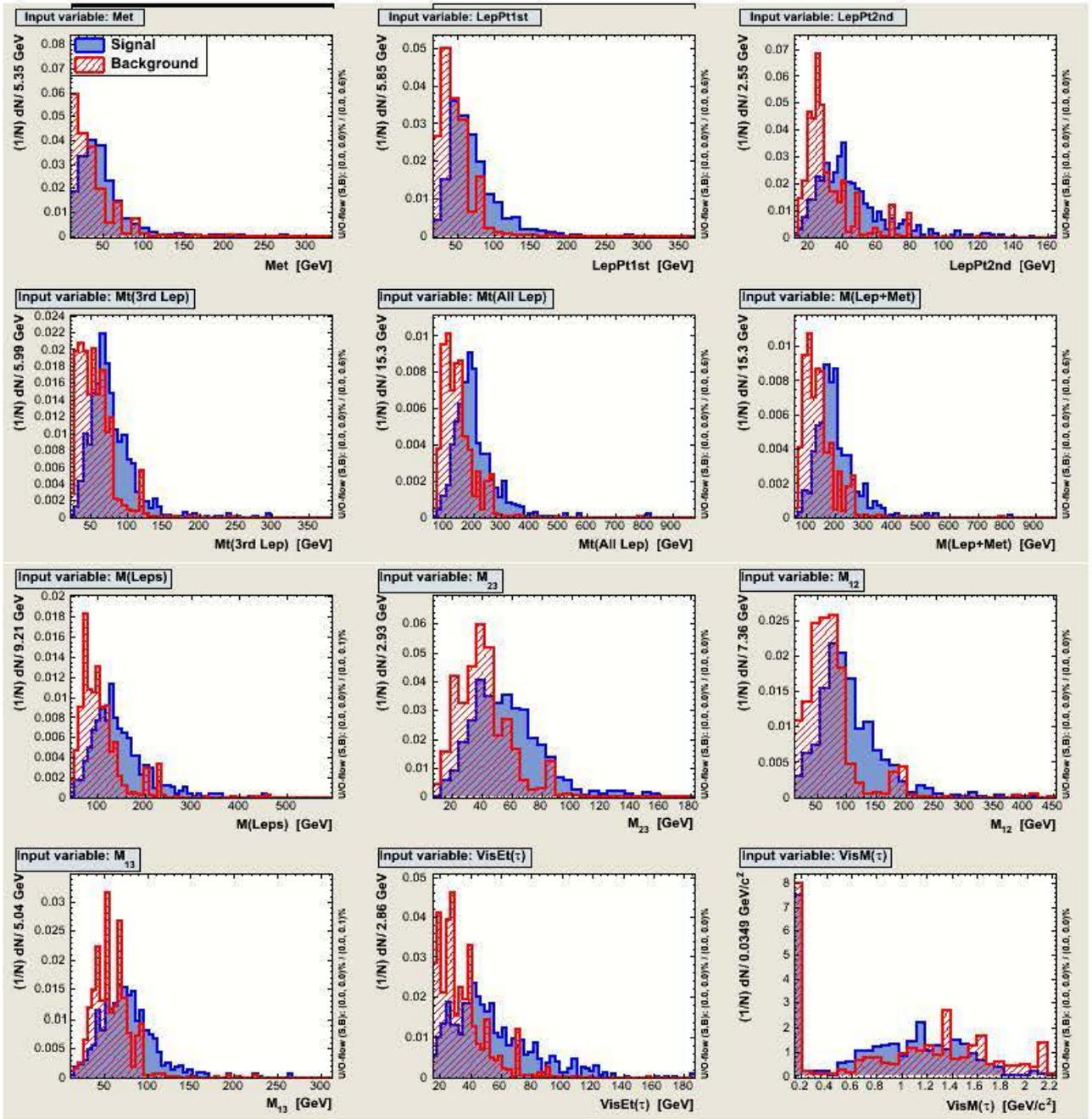
Figure 4.17: Input Variable Distributions for $f^{AL0}$.
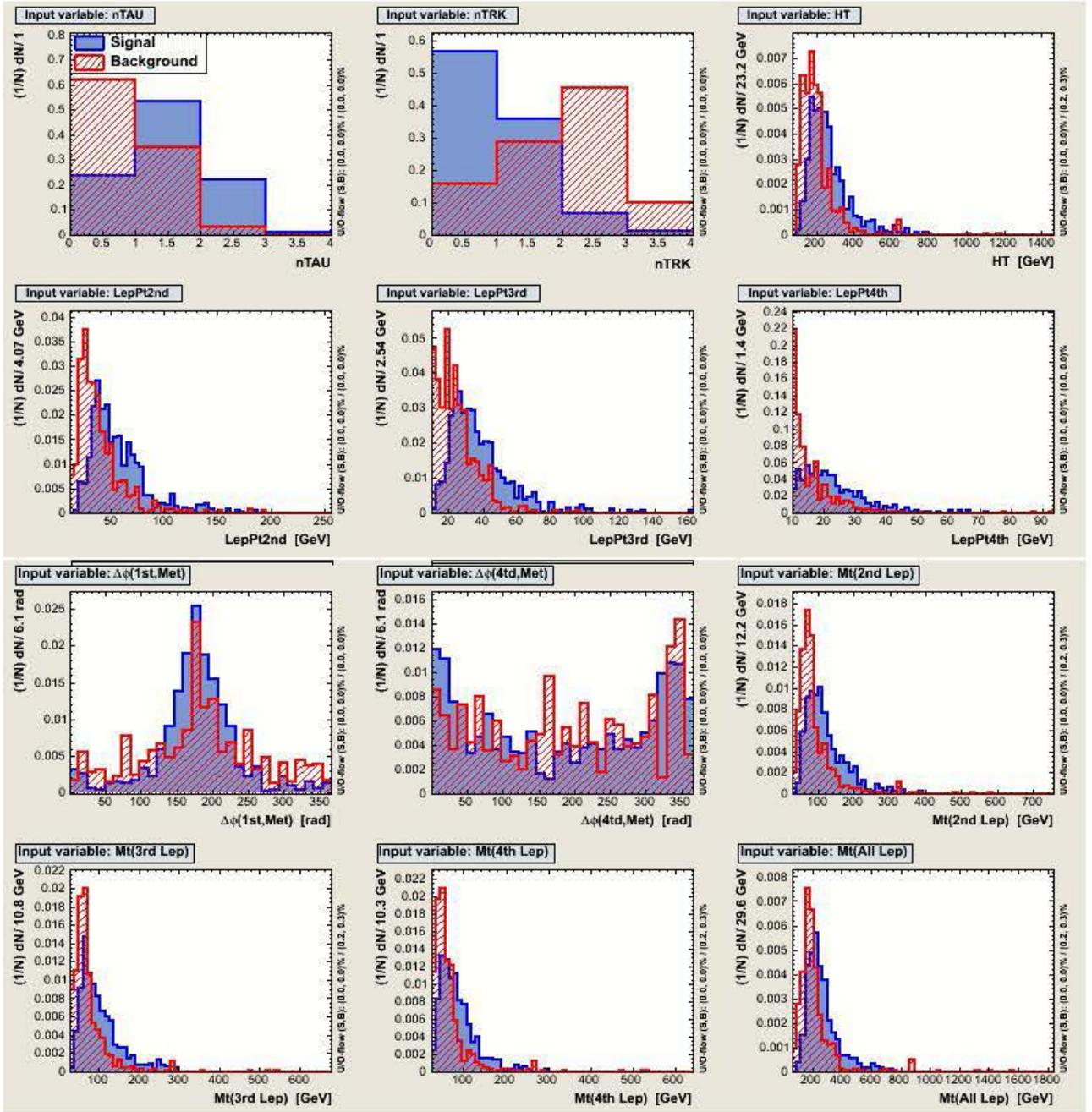
Figure 4.18: Input Variable Distributions for $f^{AL1}$ (PART 1).
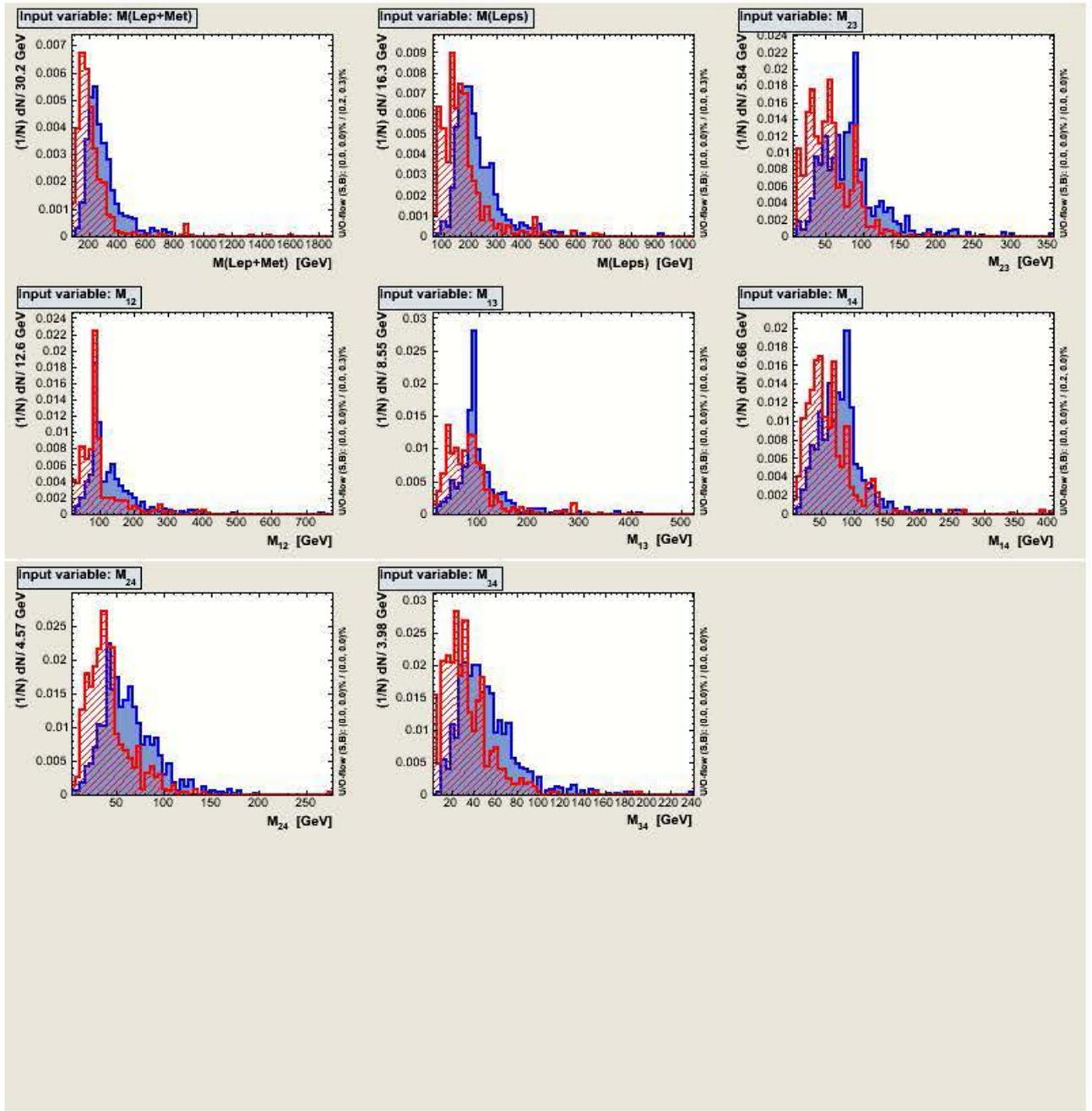
Figure 4.19: Input Variable Distributions for $f^{AL1}$ (PART 2).
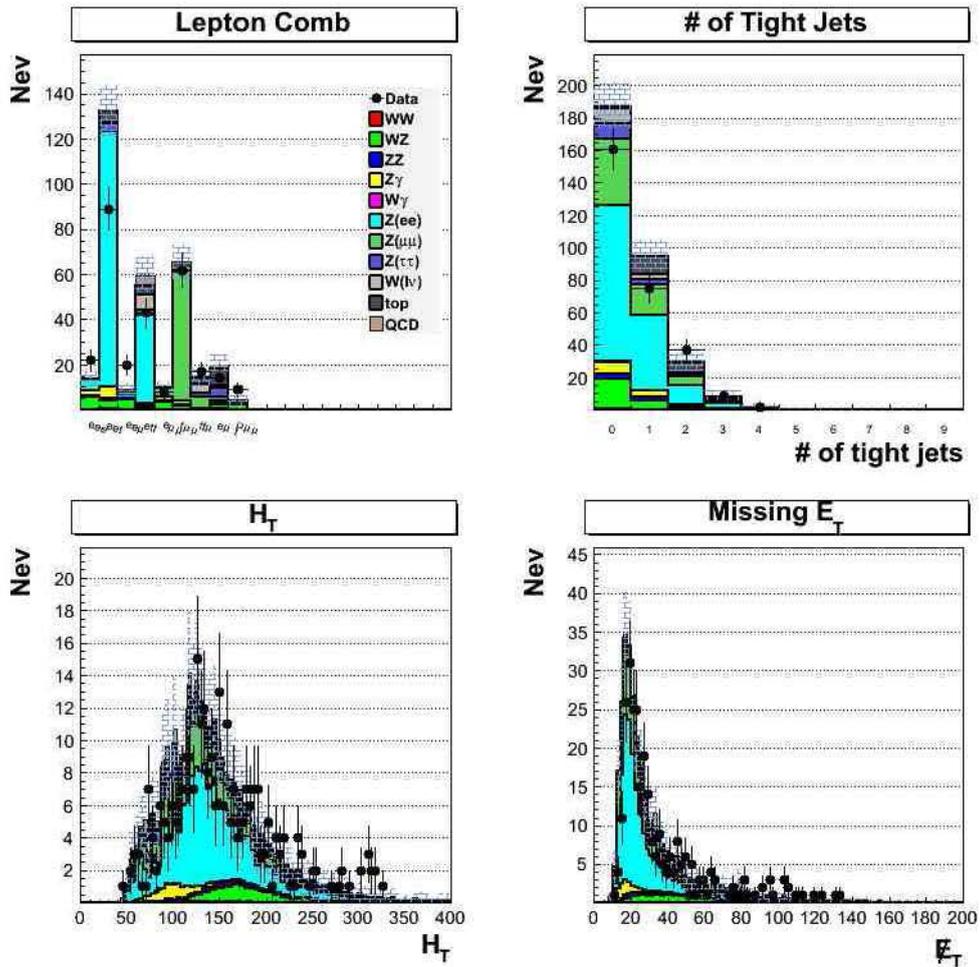
Figure 4.20: Input variables of full background to data comparison for *lll* case.
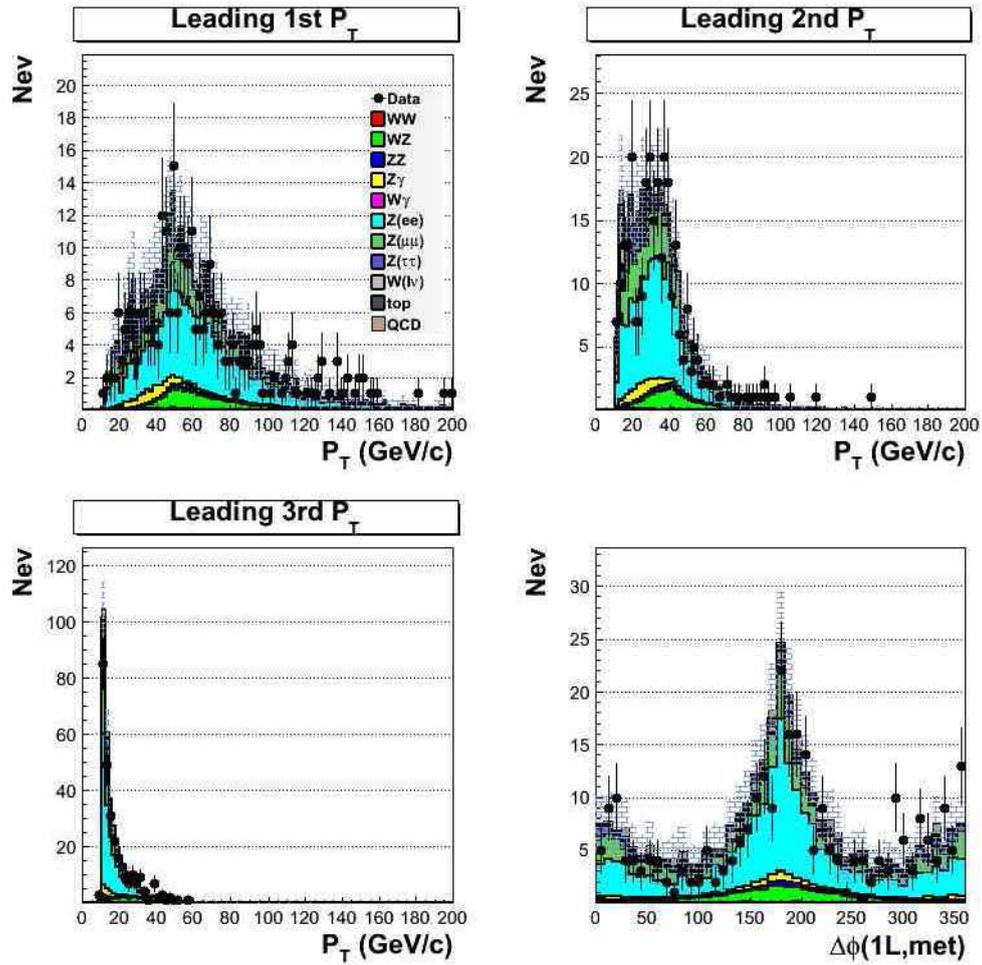
Figure 4.21: Input variables of full background to data comparison for *lll* case.
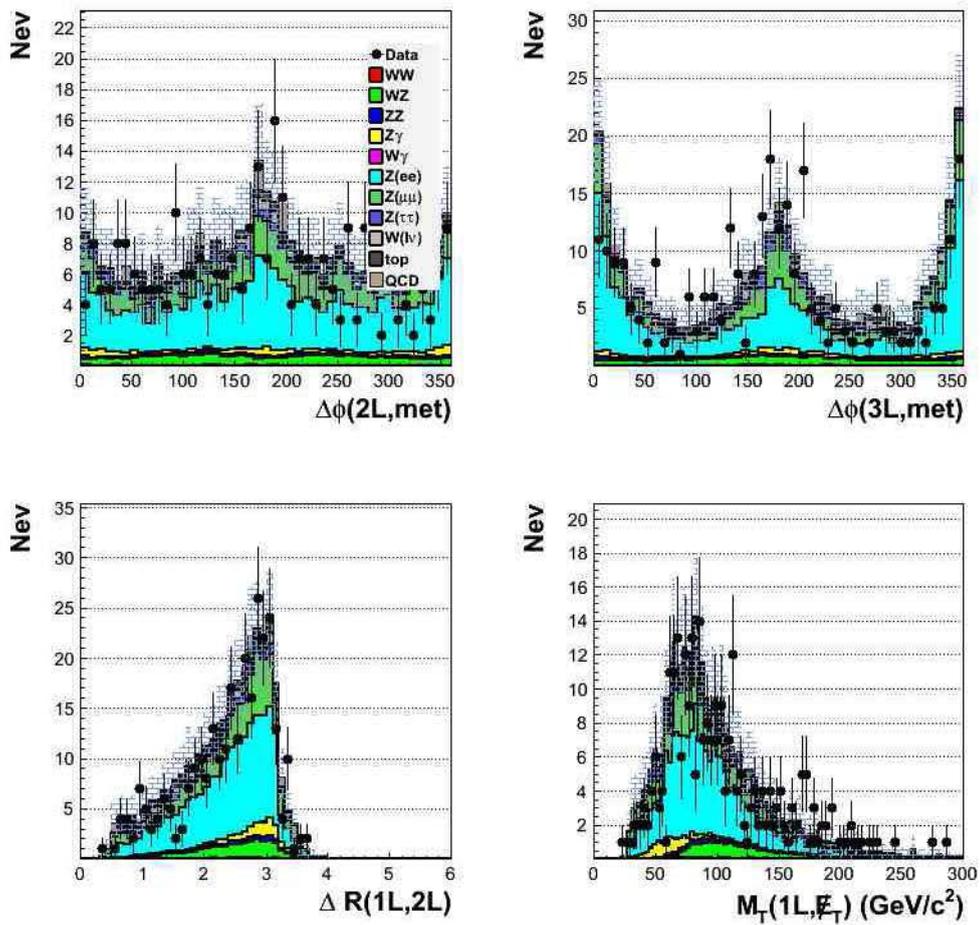
Figure 4.22: Input variables of full background to data comparison for *lll* case.
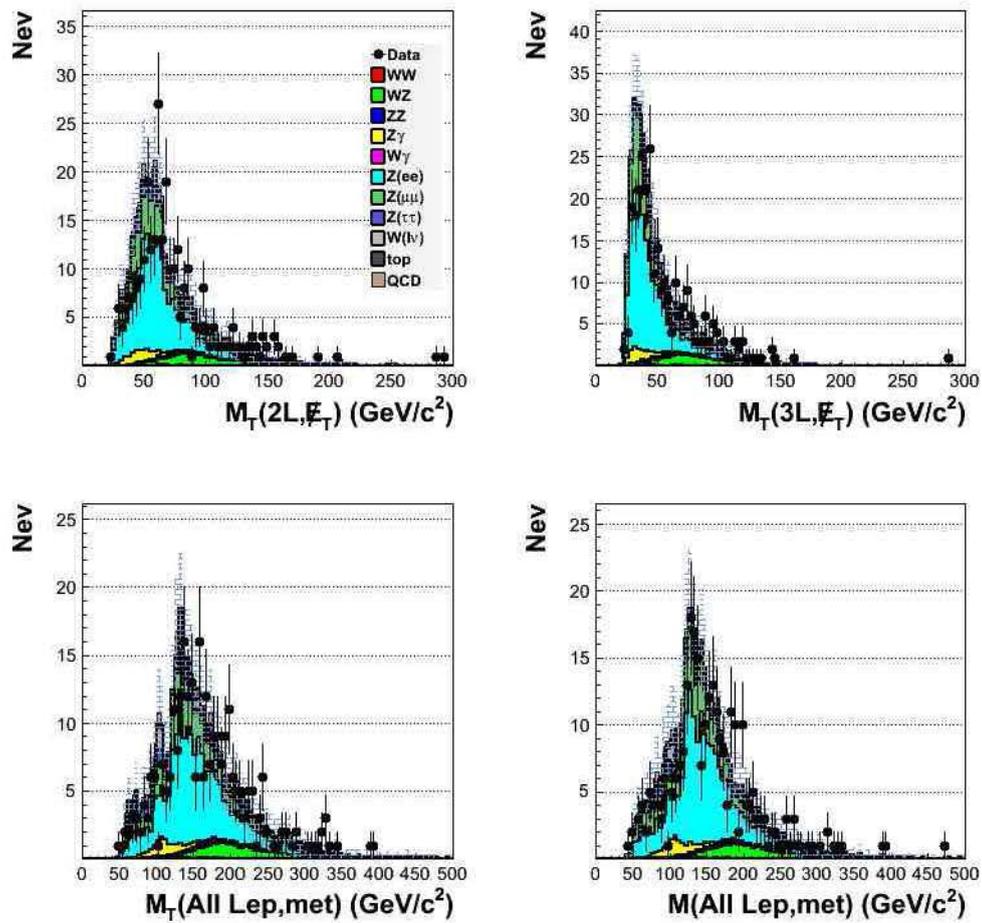
Figure 4.23: Input variables of full background to data comparison for *lll* case.
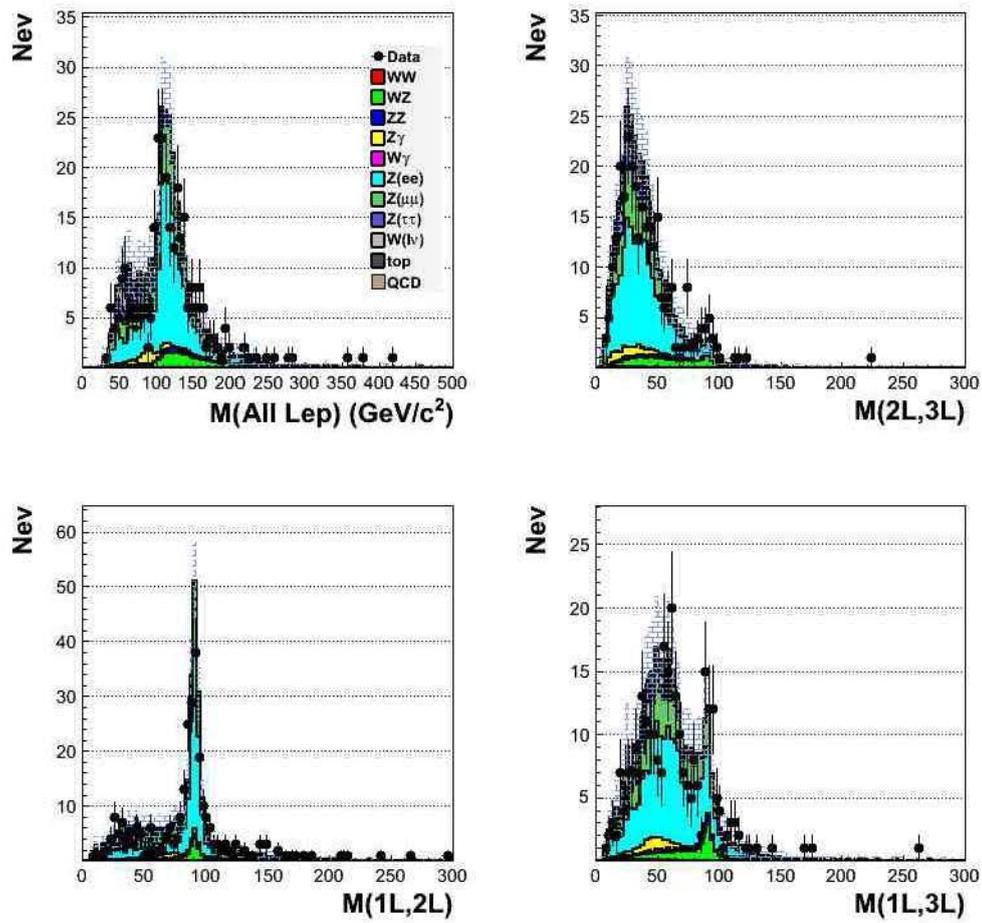
Figure 4.24: Input variables of full background to data comparison for *lll* case.
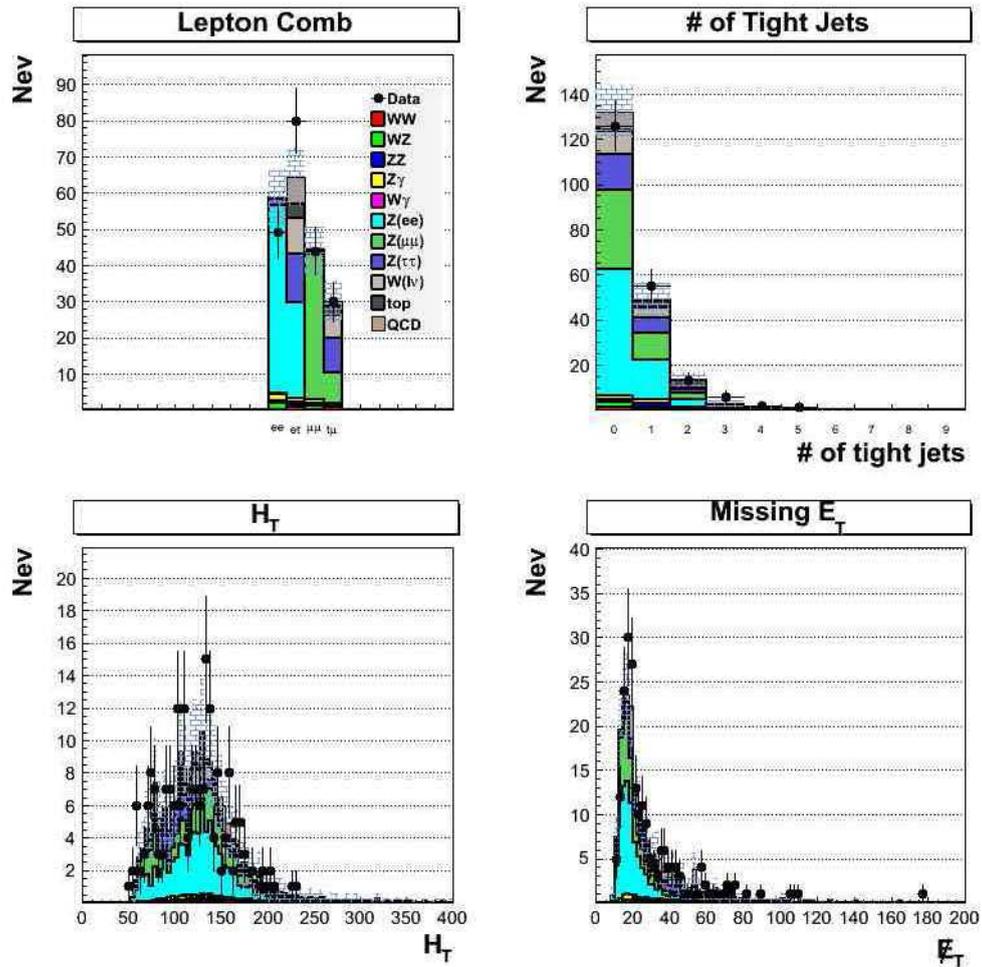
Figure 4.25: Input variables of full background to data comparison for $ll\tau$ case.
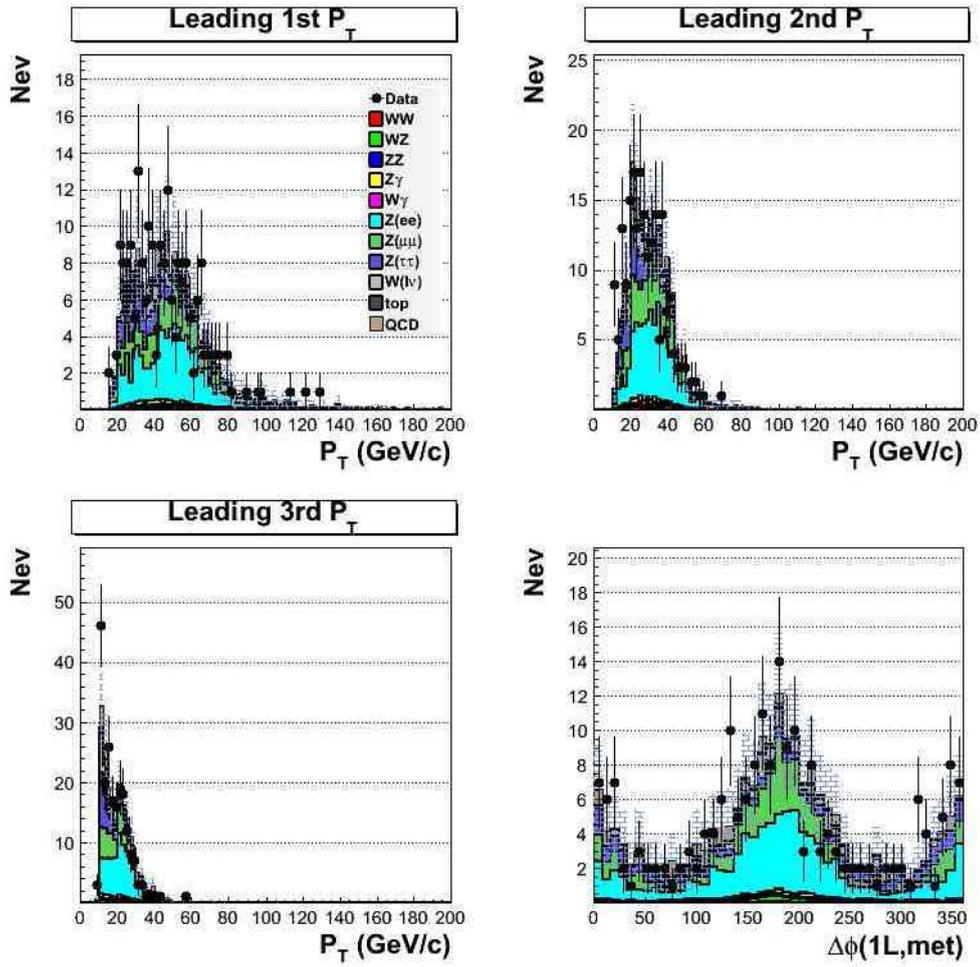
Figure 4.26: Input variables of full background to data comparison for $ll\tau$ case.
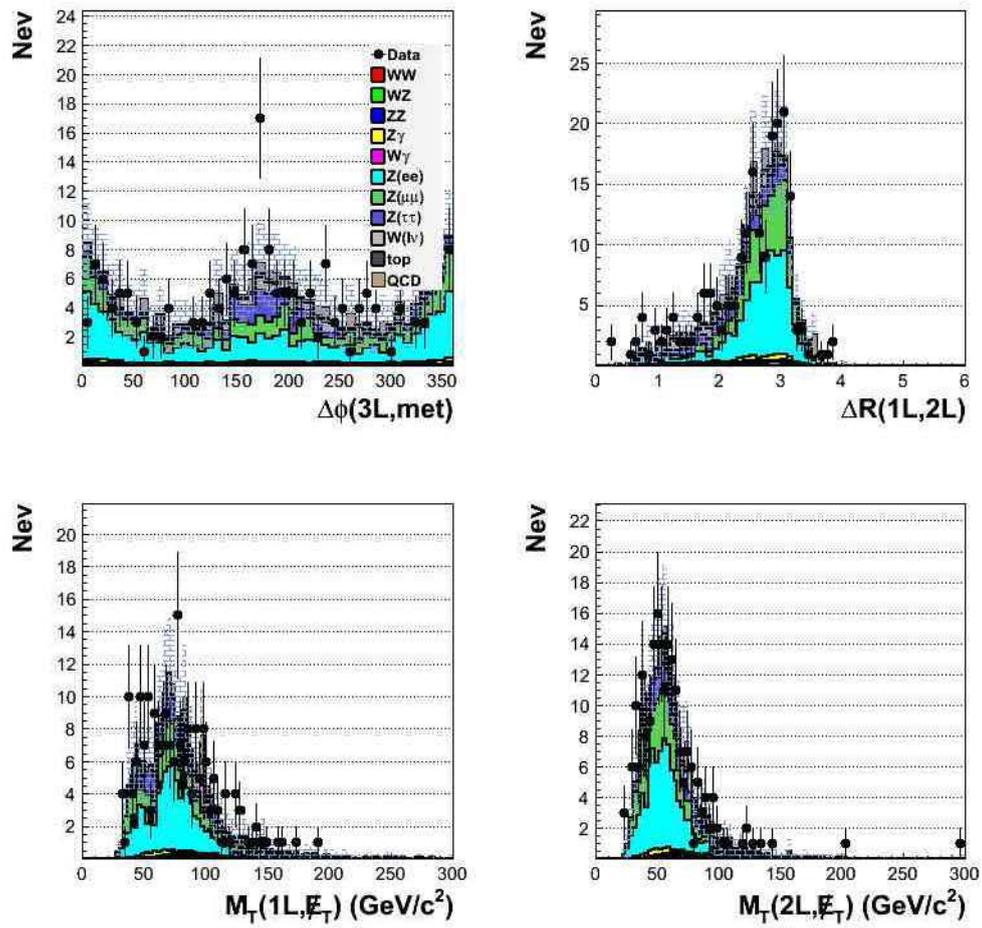
Figure 4.27:  Input variables of full background to data comparison for $ll\tau$ case.
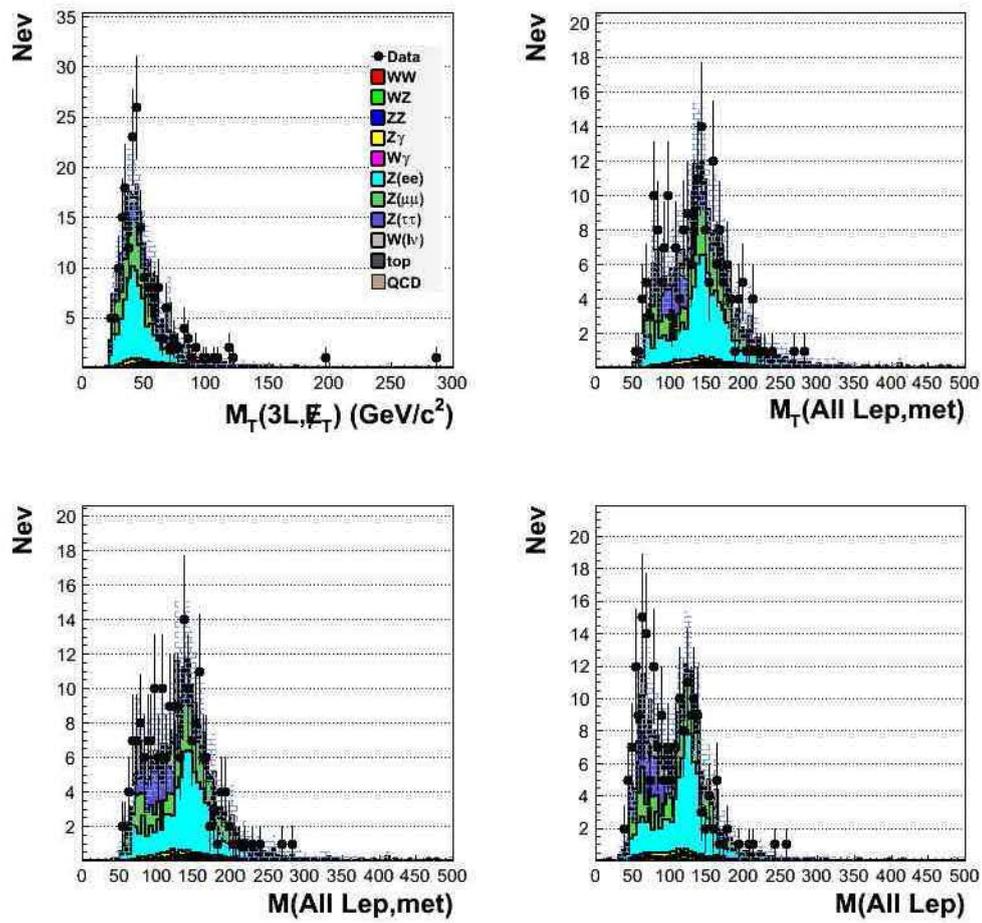
Figure 4.28: Input variables of full background to data comparison for $ll\tau$ case.
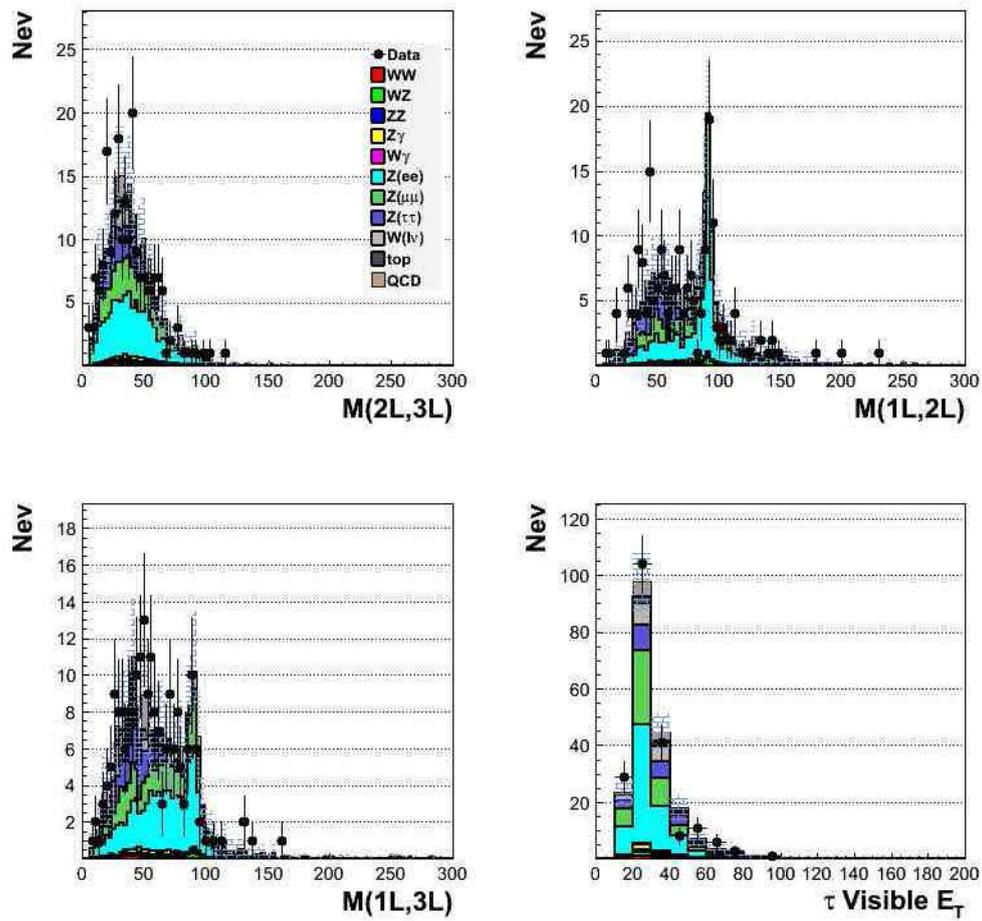
Figure 4.29: Input variables of full background to data comparison for $ll\tau$ case.
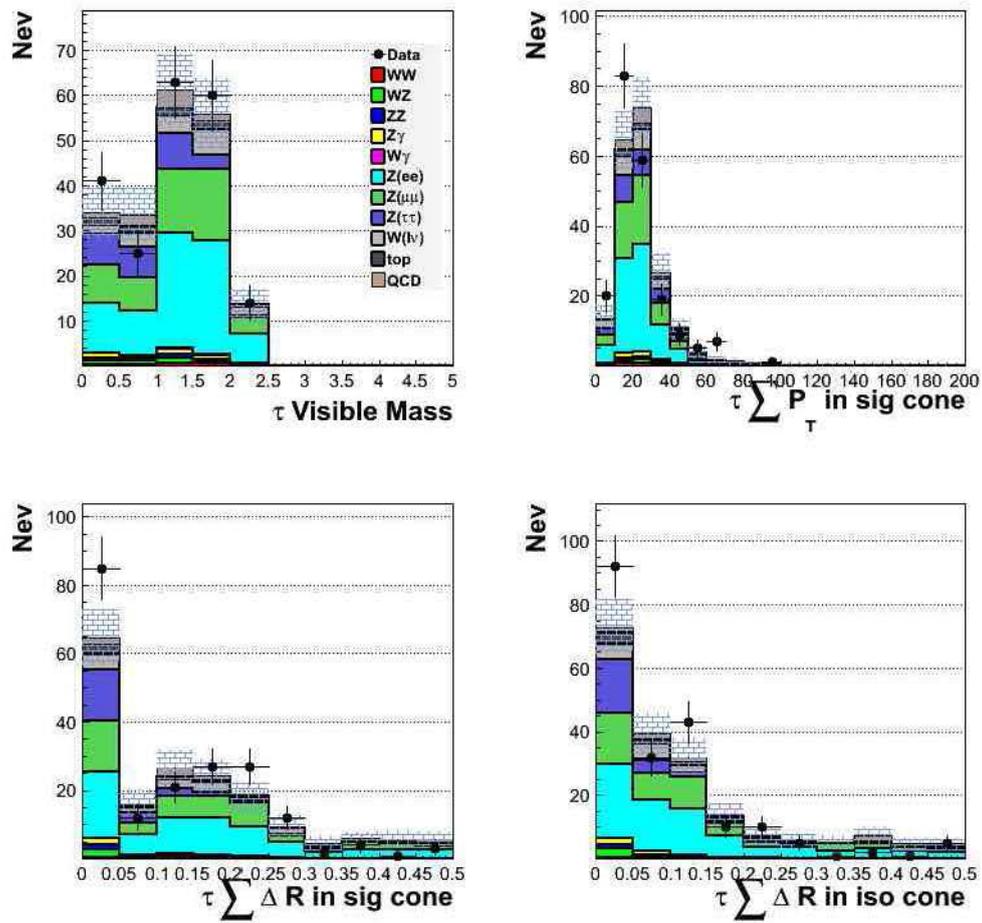
Figure 4.30: Input variables of full background to data comparison for $ll\tau$ case.
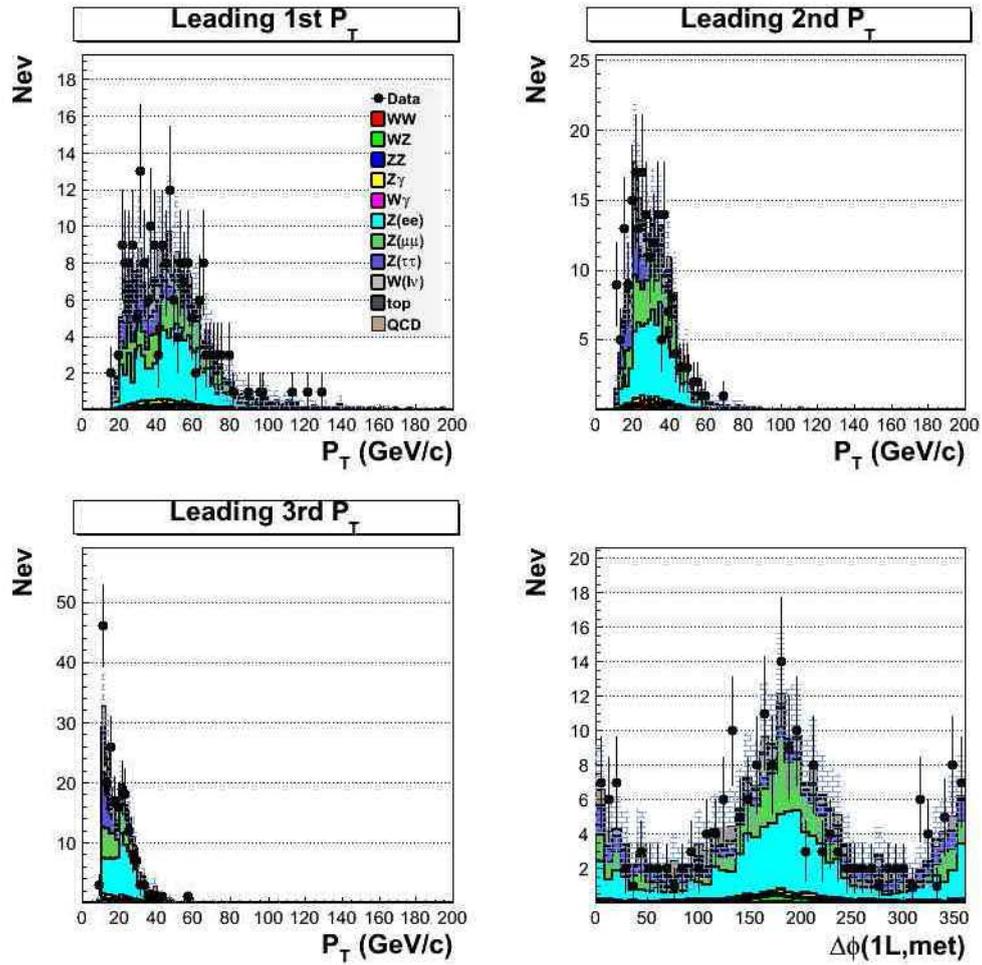
Figure 4.31: Input variables of full background to data comparison for $e\mu\tau$ case.
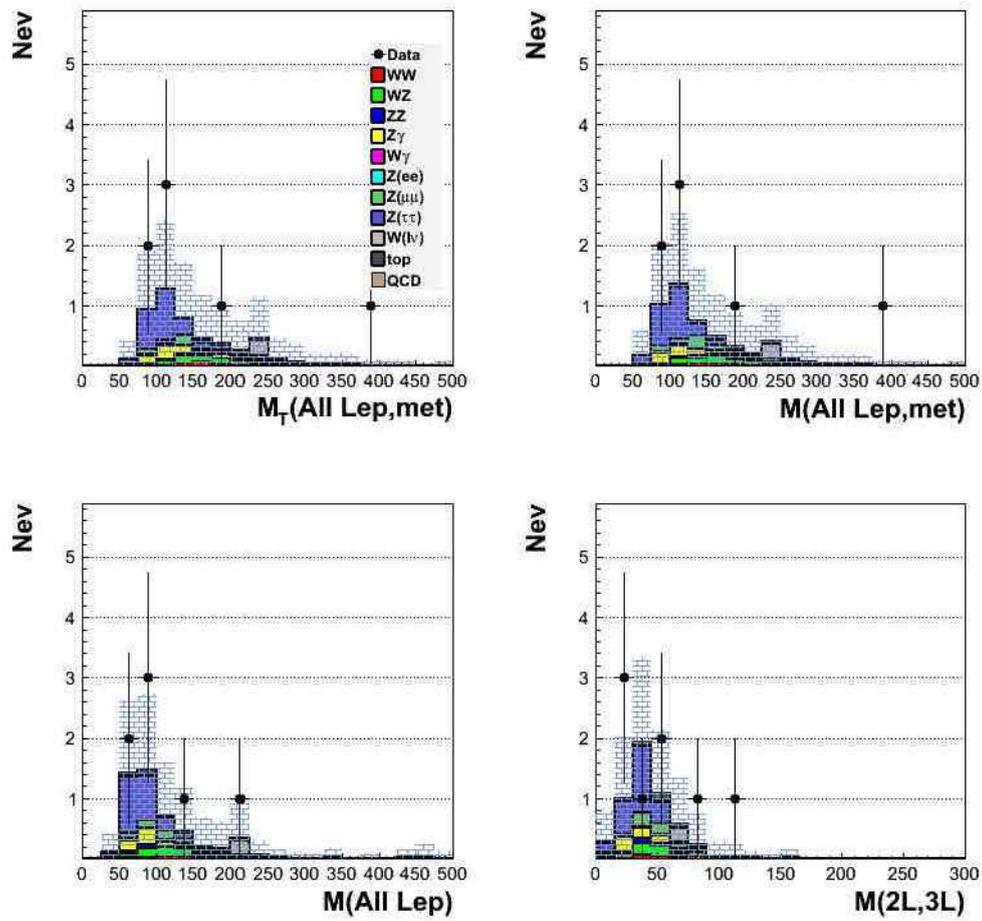
Figure 4.32: Input variables of full background to data comparison for $e\mu\tau$ case.
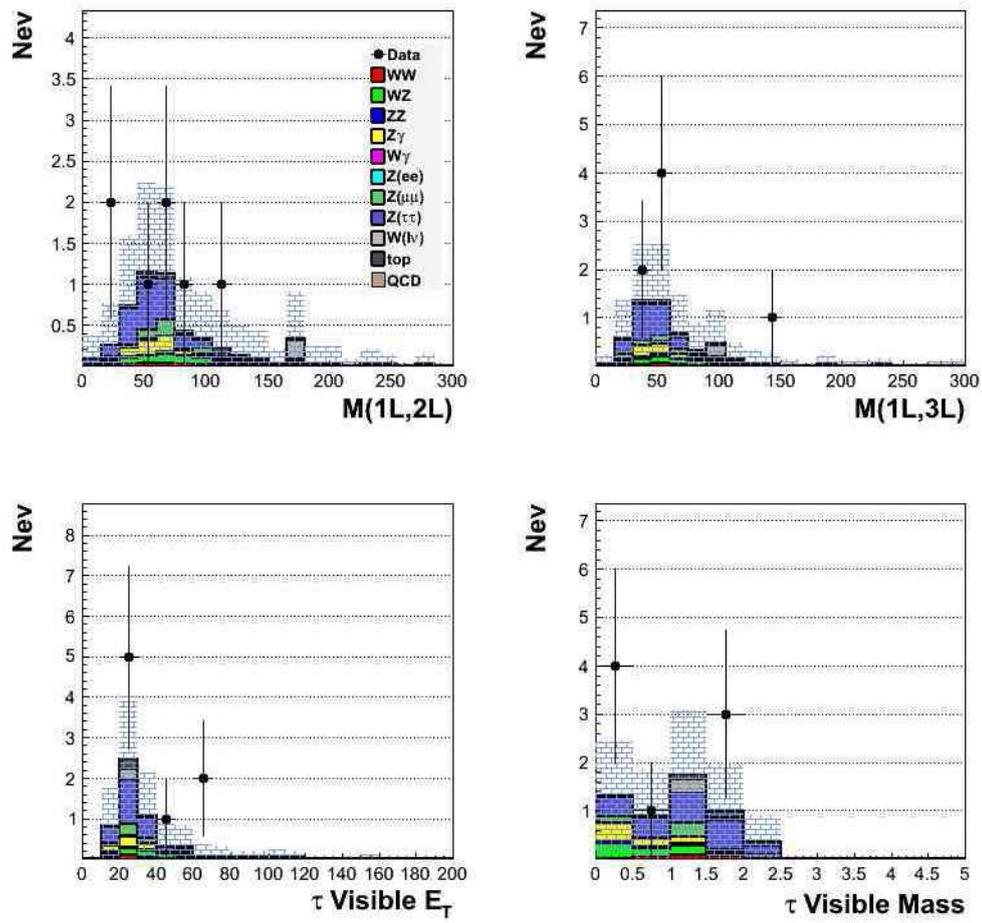
Figure 4.33: Input variables of full background to data comparison for $e\mu\tau$ case.
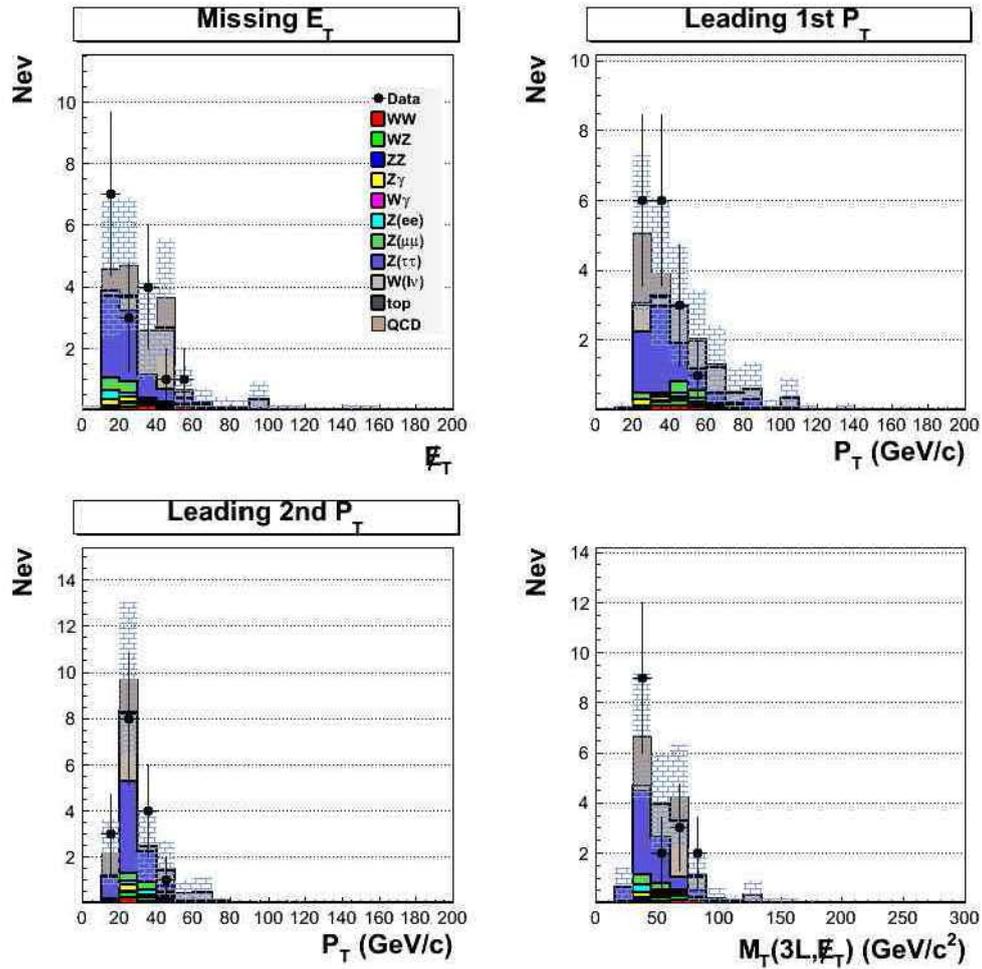
Figure 4.34: Input variables of full background to data comparison for $l\tau\tau$ case.
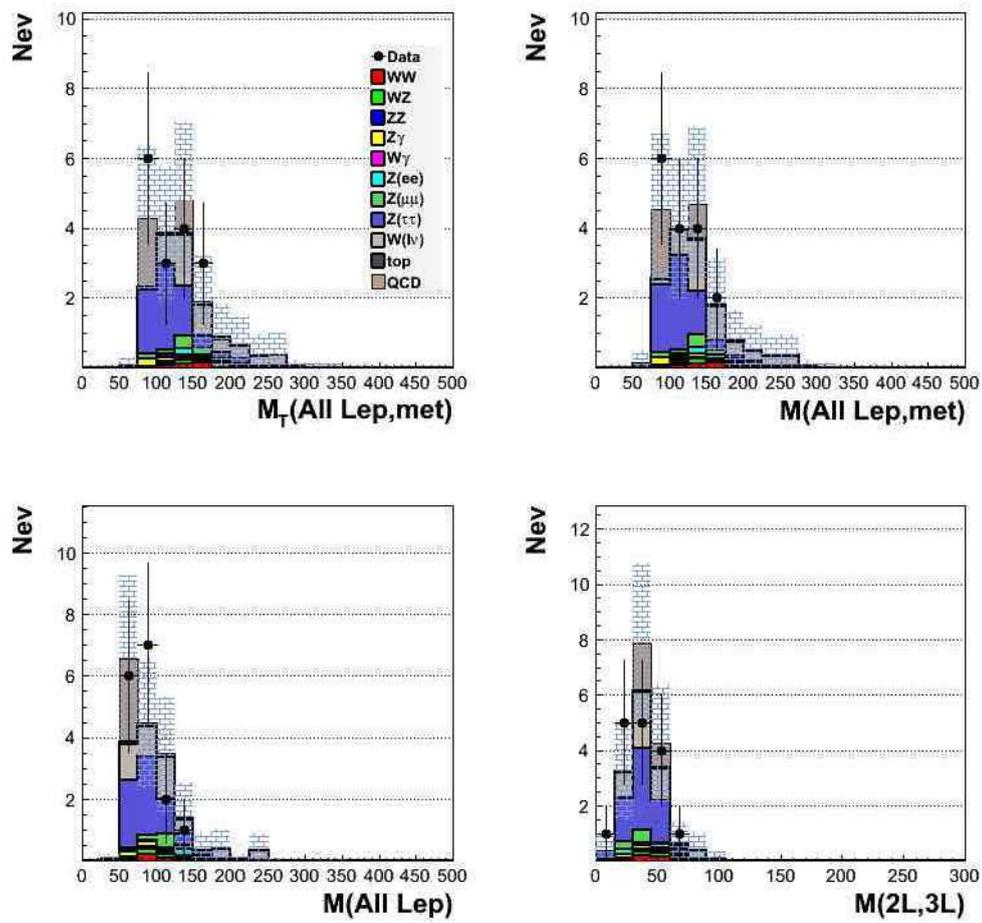
Figure 4.35: Input variables of full background to data comparison for $l\tau\tau$ case.
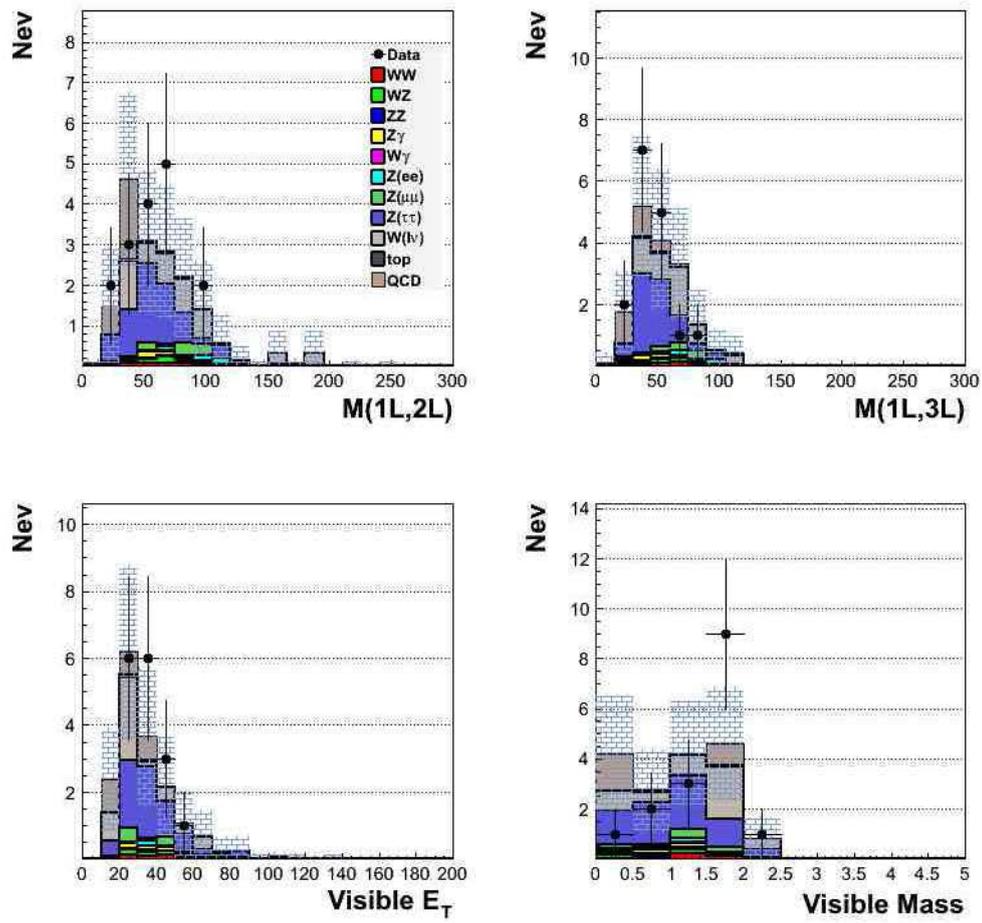
Figure 4.36: Input variables of full background to data comparison for $l\tau\tau$ case.
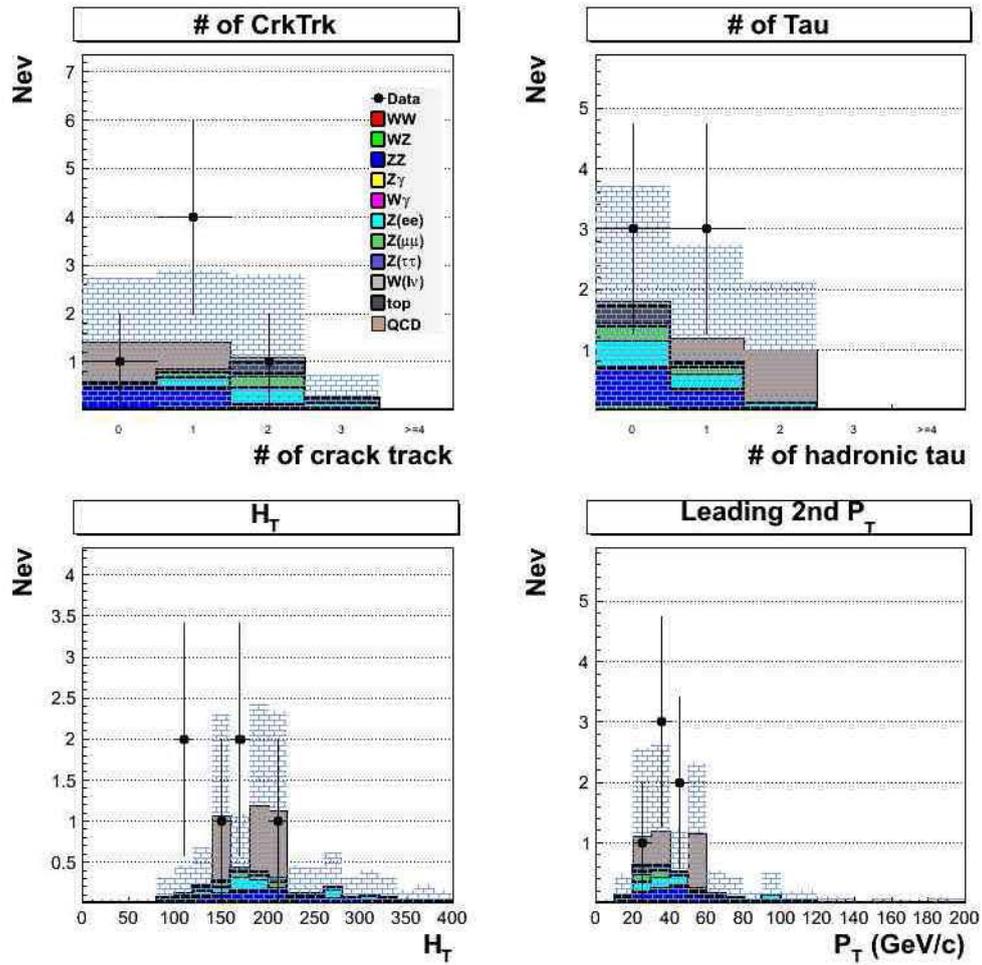
Figure 4.37: Input variables of full background to data comparison for 4 lepton case.
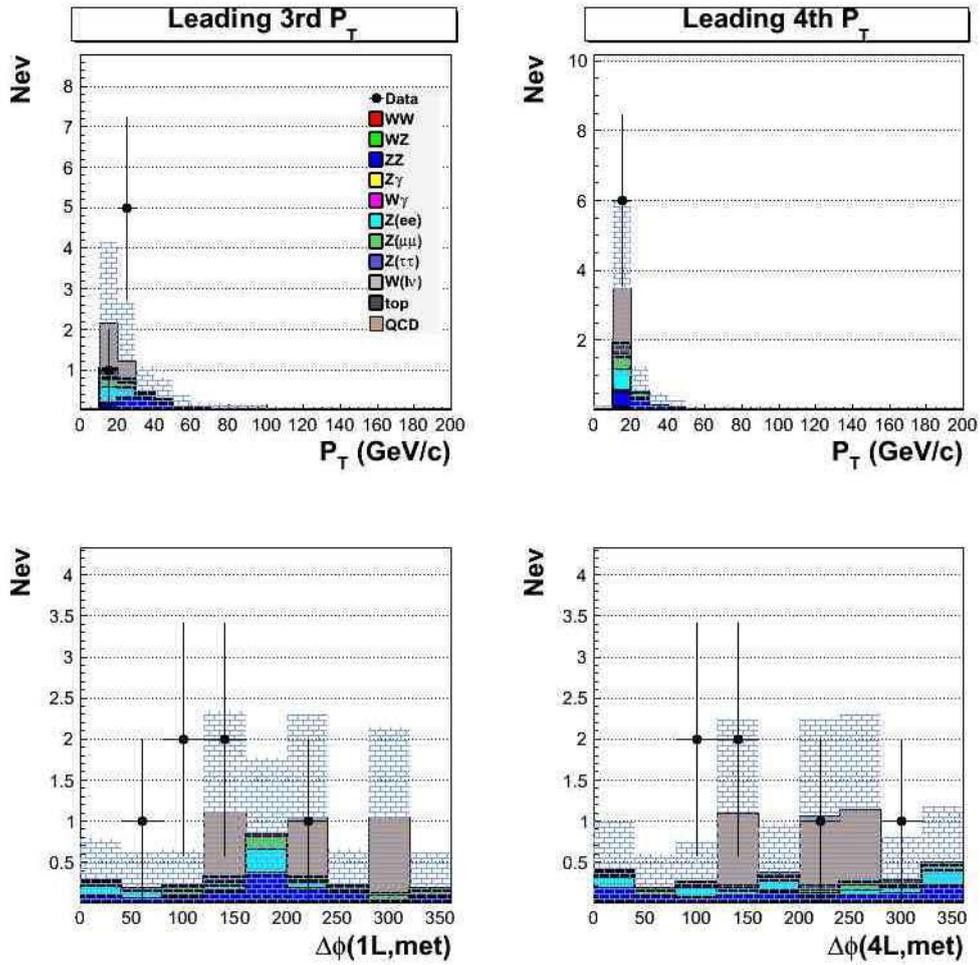
Figure 4.38: Input variables of full background to data comparison for 4 lepton case.
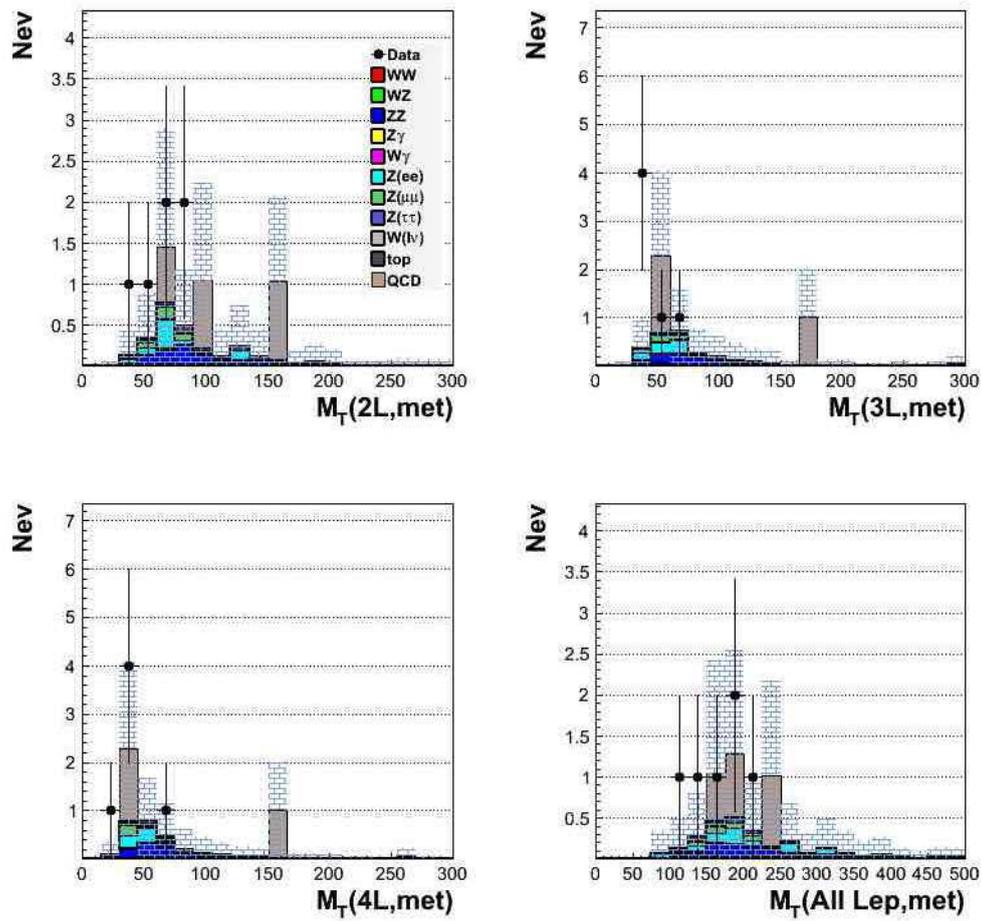
Figure 4.39:  Input variables of full background to data comparison for 4 lepton case.
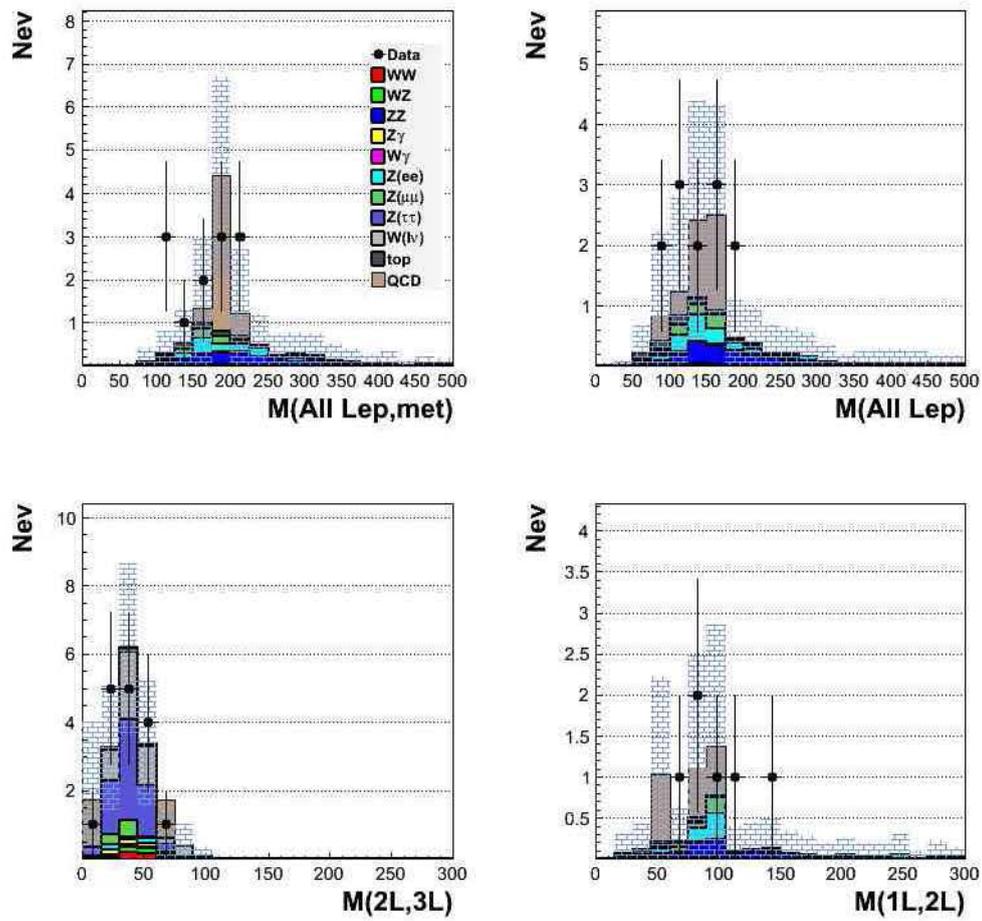
Figure 4.40:  Input variables of full background to data comparison for 4 lepton case.
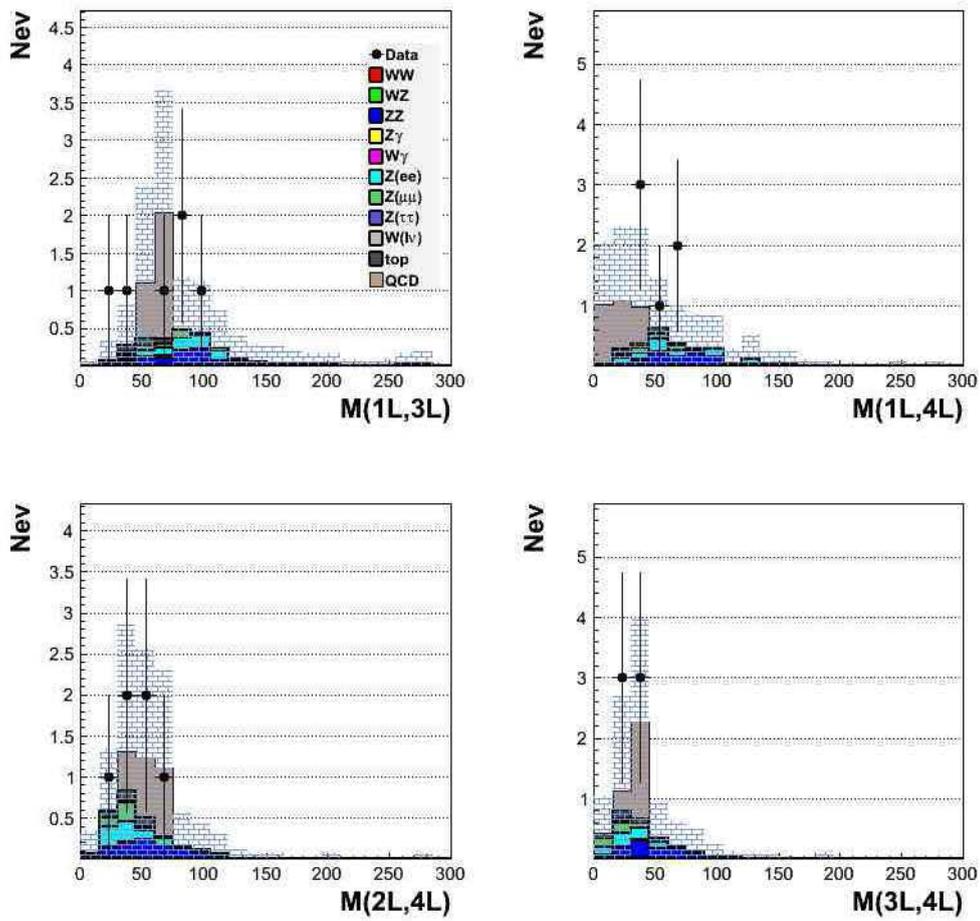
Figure 4.41: Input variables of full background to data comparison for 4 lepton case.

### 4.4.4 Training Results

Input variables that is used to train the training category are defined in previous section.
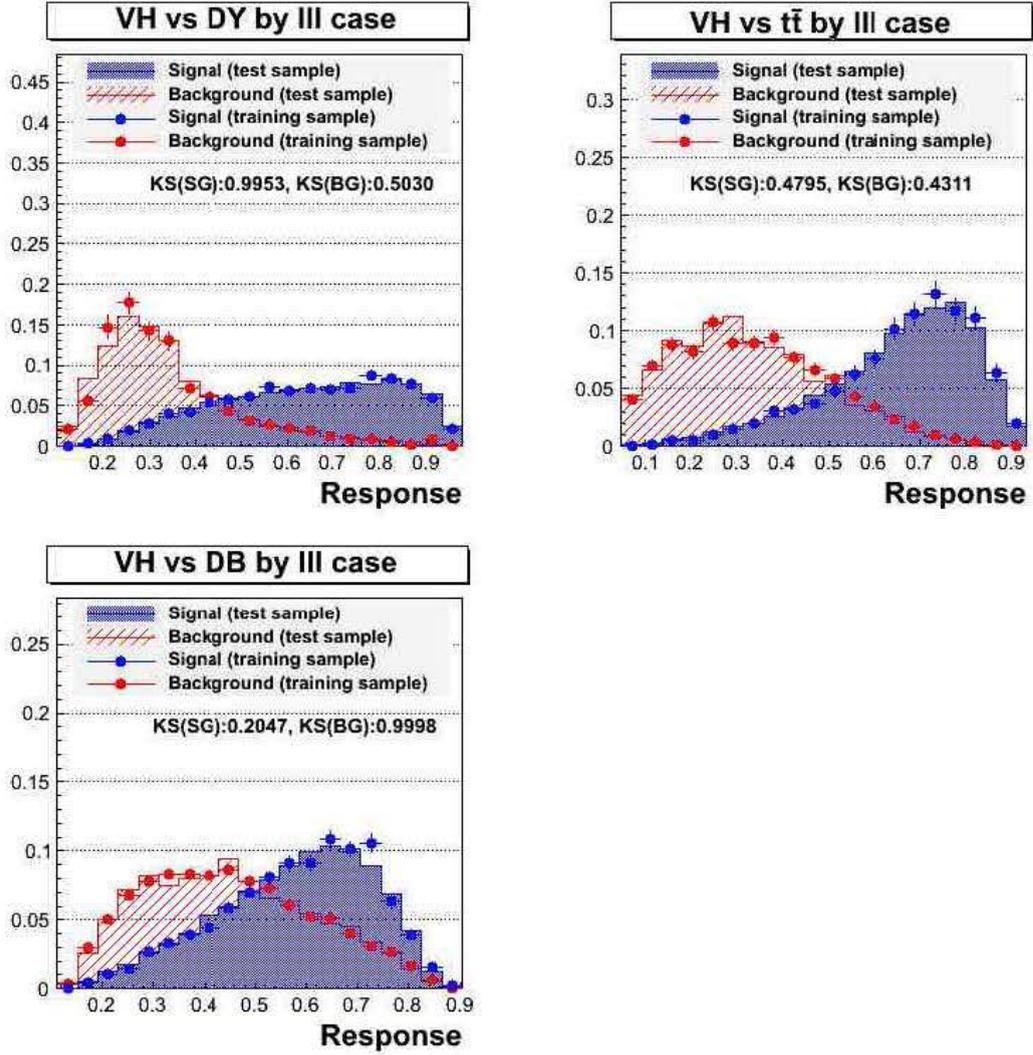


Figure 4.42: Training Results of 3 classifiers in *lll* case. Red-like histogram shows background process and blue-like histogram shows signal process. Left-top shows response distribution of the classifier $f^{DY0}$ trained by "$VH$ and Drell-Yan $(ee,\mu\mu)$". Right-top shows response distribution of the classifier $f^{TT0}$ trained by "$VH$ and $t\bar{t}$". Left-bottom shows response distribution of the classifier $f^{DB0}$ trained by "$VH$ and Diboson $(WZ/ZZ)$".
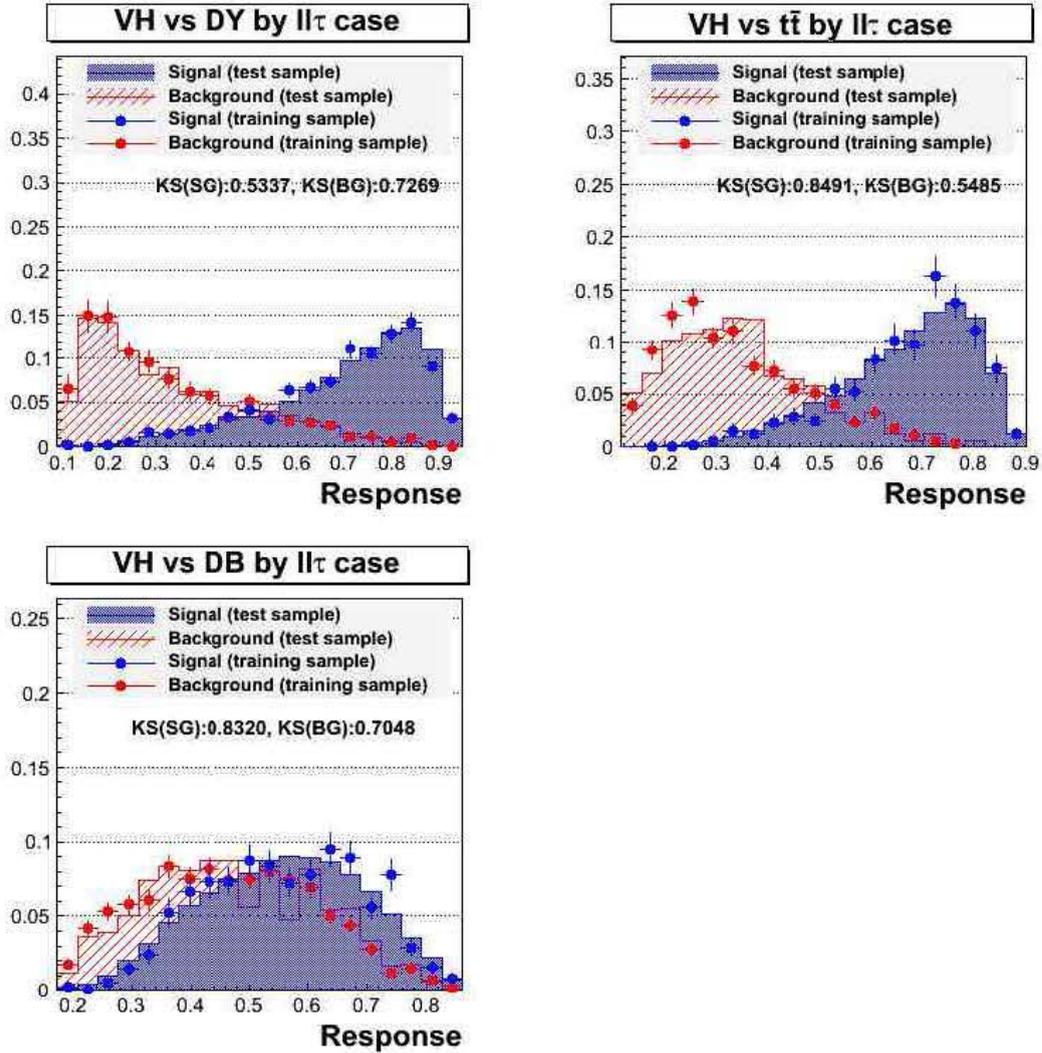
Figure 4.43: Training Results of 3 classifiers in $ll\tau$ case. Red-like histogram shows background process and blue-like histogram shows signal process. Left-top shows response distribution of the classifier $f^{DY1}$ trained by "$VH$ and Drell-Yan $(ee,\mu\mu)$". Right-top shows response distribution of the classifier $f^{TT1}$ trained by "$VH$ and $t\bar{t}$". Left-bottom shows response distribution of the classifier $f^{DB1}$ trained by "$VH$ and Diboson $(WZ/ZZ)$".
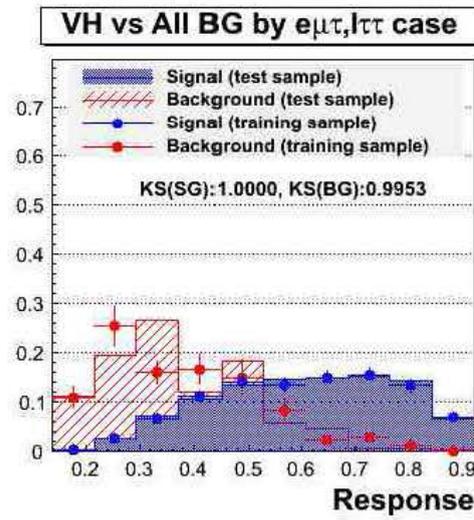
Figure 4.44: Training Result of 1 classifier $f^{AL0}$ for $e\mu\tau$ and $l\tau\tau$. Red-like histogram shows background process and blue-like histogram shows signal process.
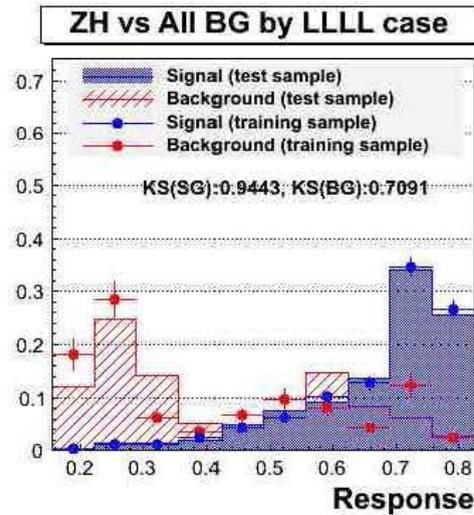


Figure 4.45: Training Result of 1 classifier $f^{AL1}$ for $LLLL$. Red-like histogram shows background process and blue-like histogram shows signal process. Here signal process $ZH$ is only used.

## 4.4.5   Response Distribution

Using 8 trained classifier and function $g(x_1, x_2, x_3) = (x_1 \cdot x_2 + x_2 \cdot x_3 + x_3 \cdot x_1)/3.$ to convolute 3 responses into 1 response, we get 5 response in total for all lepton categories.

At first, we check the response from control region to simply confirm how well our background models real data in terms of kinematics and also correlations. Then afterwards, we finally look at signal region.

**Check Response of Control Region** $\displaystyle{\not{E}_T / \sum E_T \leq 1.0}$

We choose a control region $\not{E}_T / \sum E_T \leq 1.0$ to confirm our background modeling. This control region has Drell-Yan process that is dominant background of this analysis and also almost negligible signal events is expected in this region. Figure 4.46 shows counting ratio between data and background estimation. These is a good agreement for each lepton category.

From response distributions shown in Figure 4.47 for *lll* case, Figure 4.48 for *llτ* case, Figure 4.49 for *eμτ* case, Figure 4.50 for *lττ* case and Figure 4.51 for 4 lepton case, we conclude that our modeling is reasonably well even though statistics is not enough for *lll* and *llτ* cases. Therefore at this time we do not assign systematic uncertainty on methodology itself.
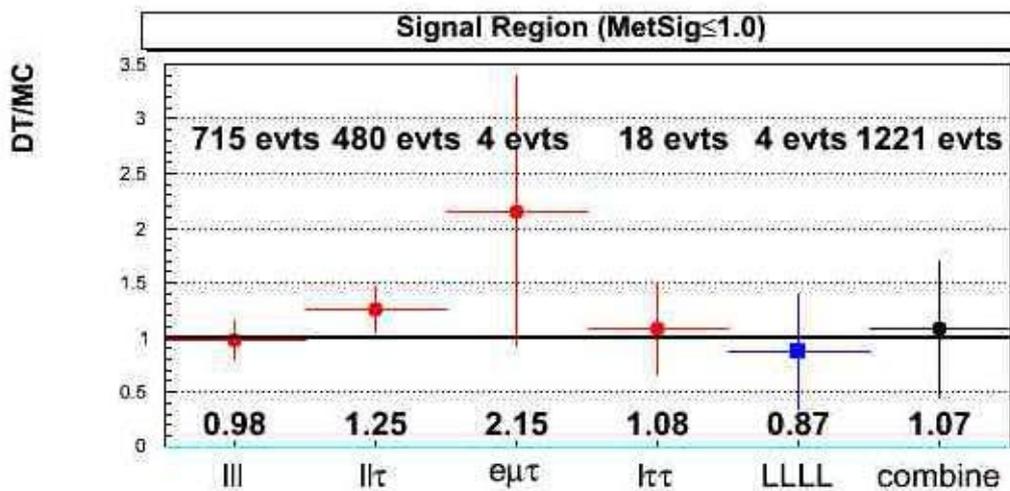


Figure 4.46:  Data to our background estimation ratio in Control Region ($\not{E}_T / \sum E_T \leq 1.0$).
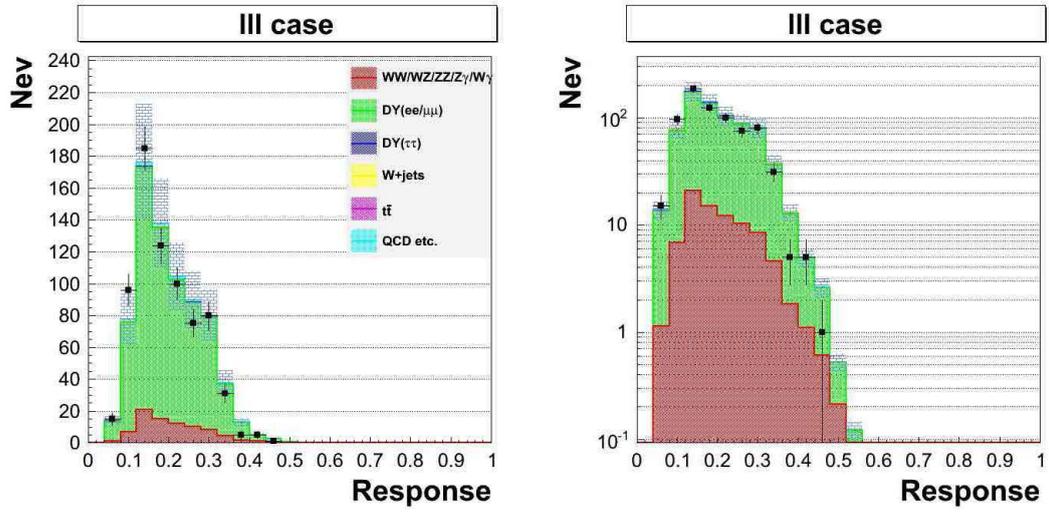
Figure 4.47: Response distributions of control region in *lll* case. Marker shows data. Histogram show our background estimation. Right plot shows log scale of left plot.
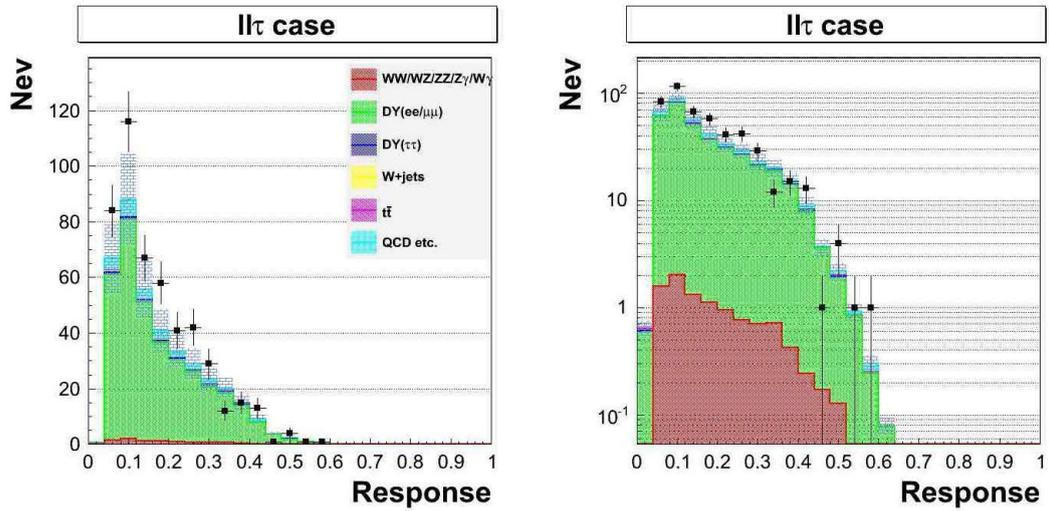


Figure 4.48: Response distributions of control region in *llτ* case. Marker shows data. Histogram show our background estimation. Right plot shows log scale of left plot.
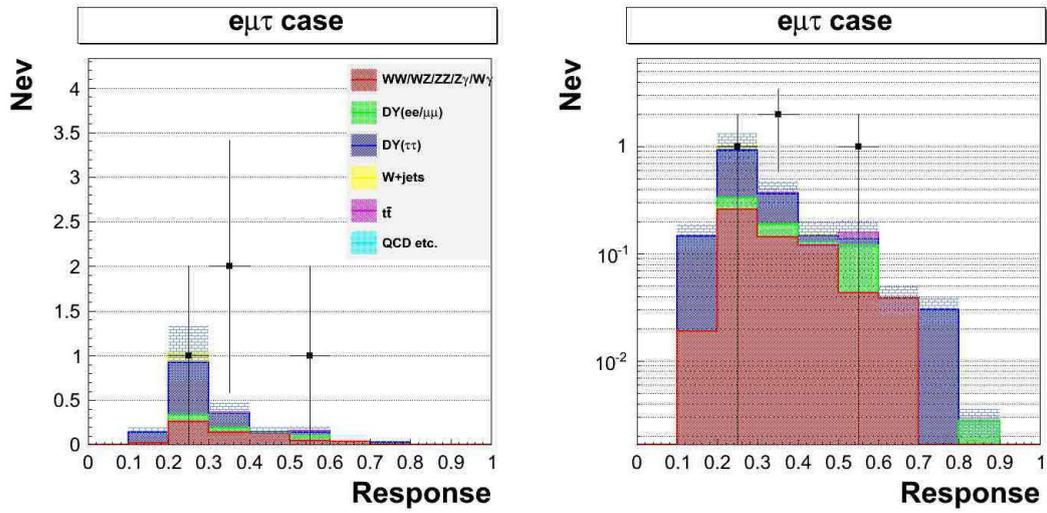
Figure 4.49: Response distributions of control region in $e\mu\tau$ case. Marker shows data. Histogram show our background estimation. Right plot shows log scale of left plot.
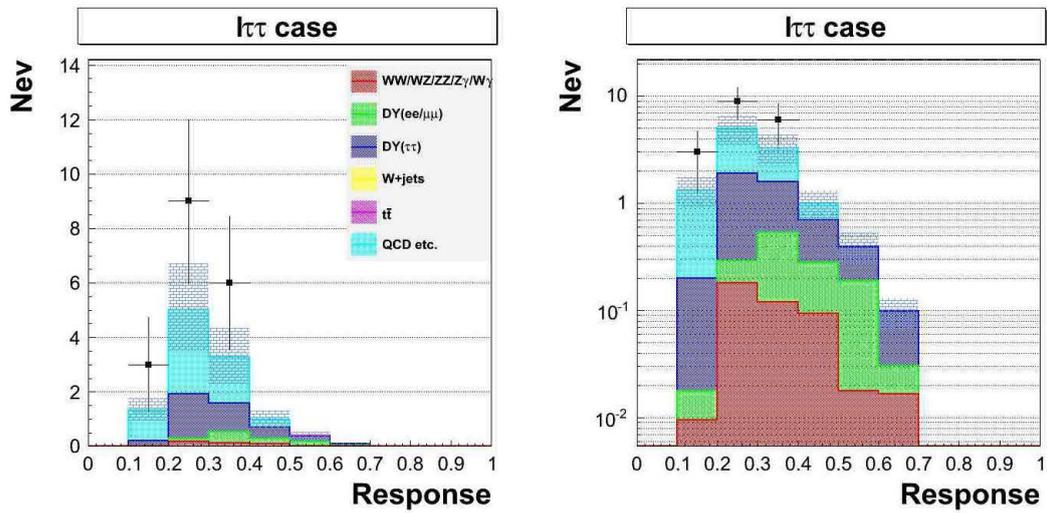


Figure 4.50: Response distributions of control region in $l\tau\tau$ case. Marker shows data. Histogram show our background estimation. Right plot shows log scale of left plot.
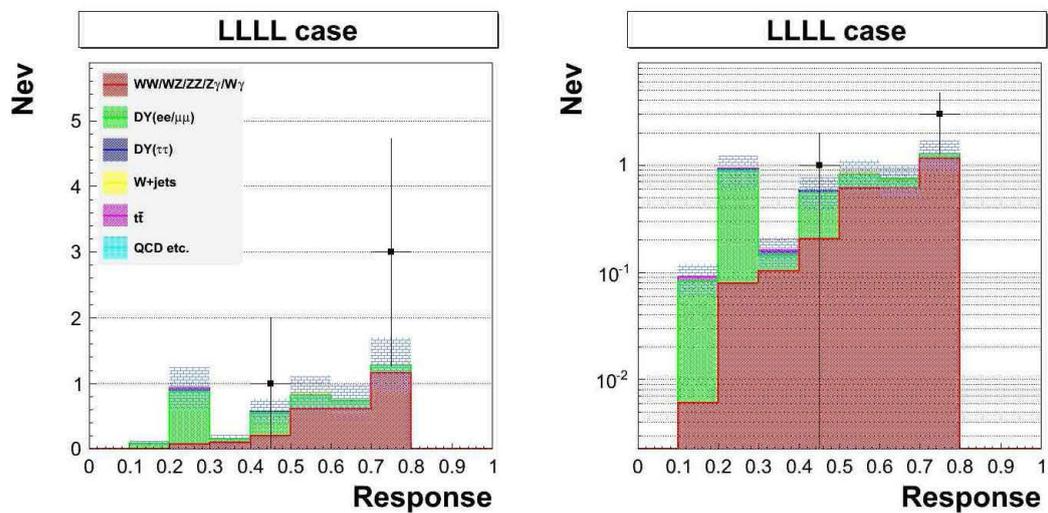
Figure 4.51:   Response distributions of control region in 4 lepton case. Marker shows data. Histogram show our background estimation. Right plot shows log scale of left plot.

## Response of Signal Region

We show the response distribution of each category. In figures we show here, black line shows signals $(VH)$ and colored histograms shows backgrounds. Signal histogram area is normalized by each total background area.

Figure 4.53 shows the response distribution in $lll$ case. This case has more events than any other categories. As in Table 4.3, dominant background process is Drell-Yan $(ee,\mu\mu)$ and a fake $e/\mu$. Figure 4.54 shows the response distribution in $ll\tau$ case. As mentioned before, we unify 3 responses to 1 response in these case ($lll$ and $ll\tau$) by using function $g(x_1, x_2, x_3) = (x_1 \cdot x_2 + x_2 \cdot x_3 + x_3 \cdot x_1)/3.$. In this case, dominant background process is that Drell-Yan $(ee,\mu\mu)$ and a fake tau. Figure 4.55 shows the response distribution in $e\mu\tau$ case. Figure 4.56 shows the response distribution in $l\tau\tau$ case. Figure 4.57 shows the response distribution in $LLLL$ case.

These distributions are used for discriminant templates.
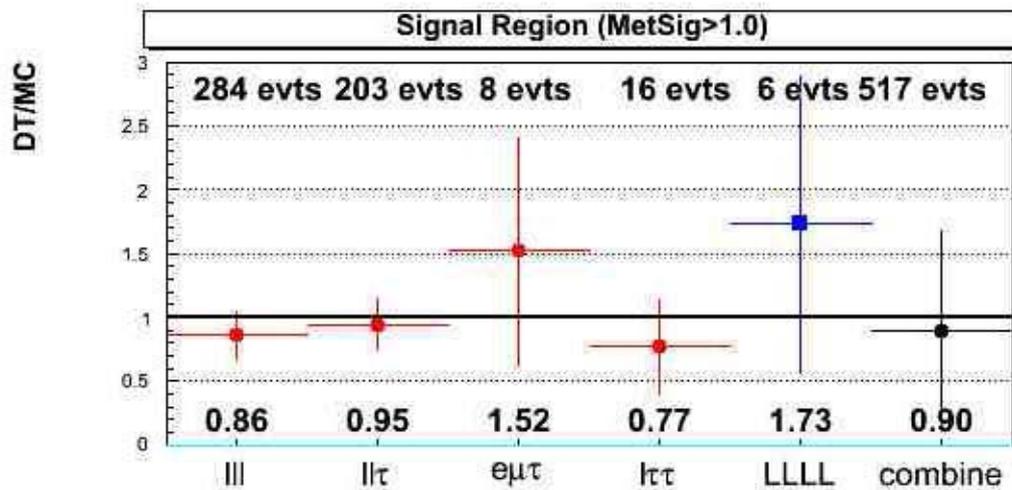


Figure 4.52:  Data to our background estimation ratio in Signal Region ($\not{E}_T/\sum E_T > 1.0$).
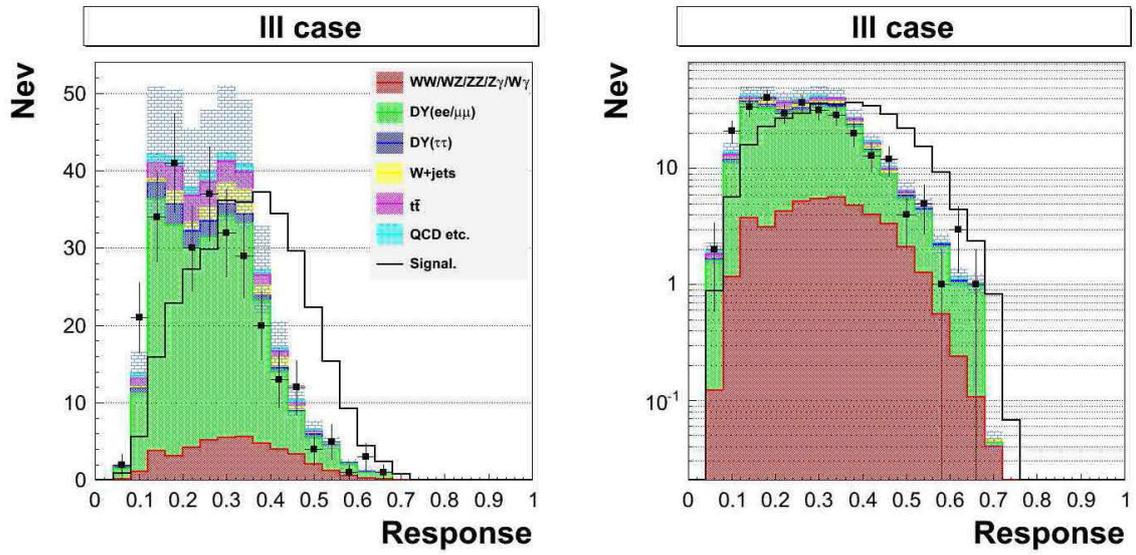
Figure 4.53:   Response Distribution of in *lll* case.  Right plot shows log scale of left plot.
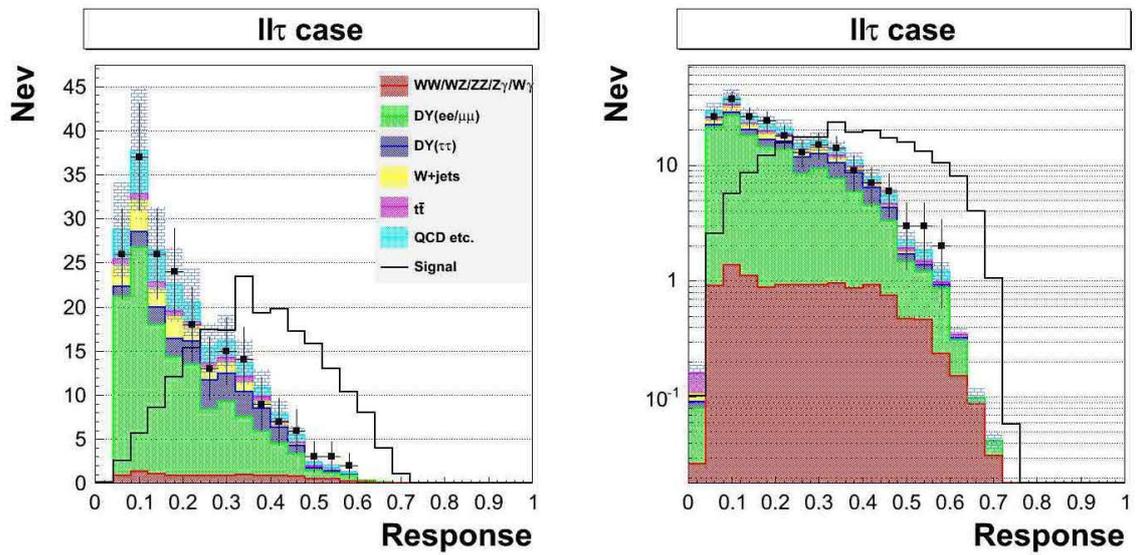


Figure 4.54:   Response Distribution of in *llτ* case.  Right plot shows log scale of left plot.
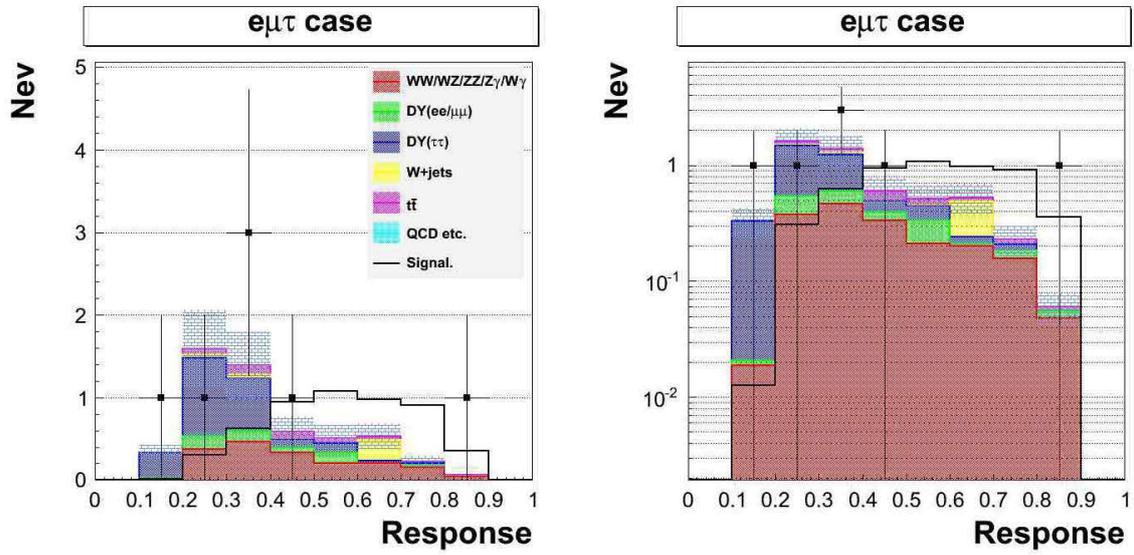
Figure 4.55:   Response Distribution of in $e\mu\tau$ case.  Right plot shows log scale of left plot.
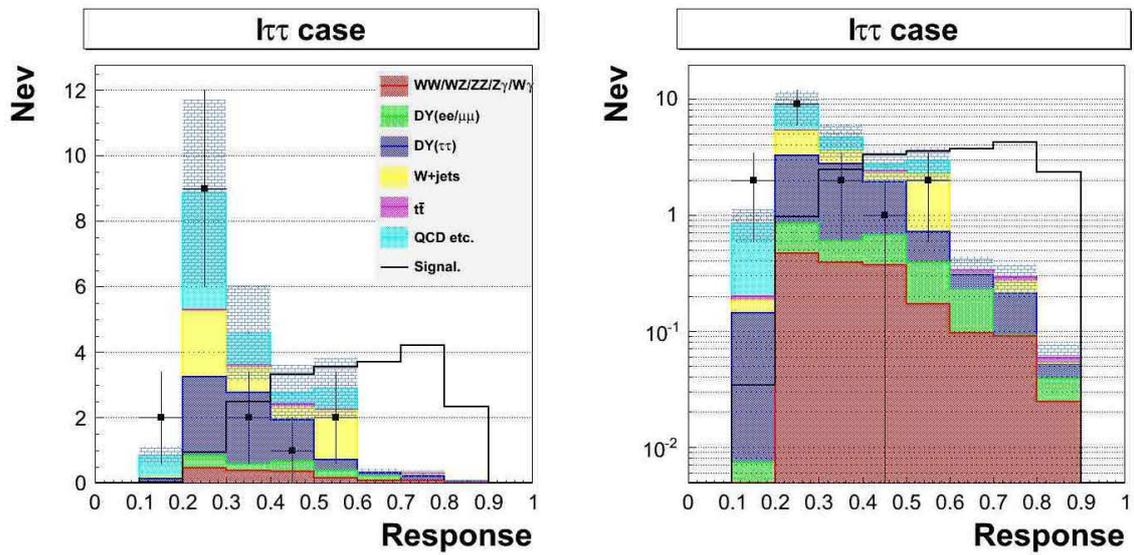


Figure 4.56:   Response Distribution of in $l\tau\tau$ case.  Right plot shows log scale of left plot.
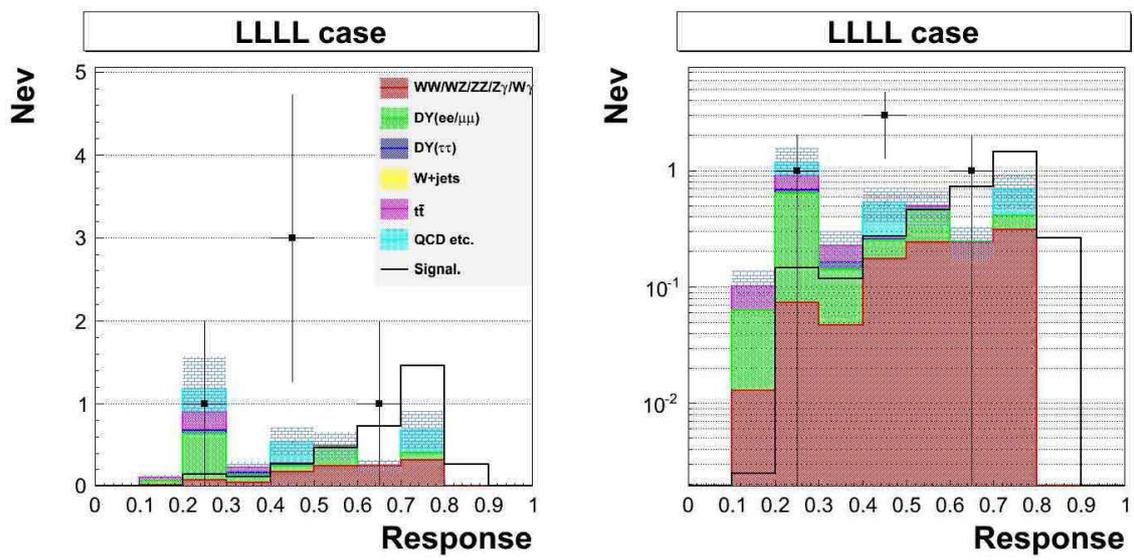
Figure 4.57: Response Distribution in 4 lepton case. Right plot shows log scale of left plot.

# 4.5 Systematic Uncertainty

Here we describe all the systematic uncertainties. It is categorized into luminosity, theoretical cross section and acceptance terms. Furthermore, we categorize uncertainty on acceptance to 5 lepton combinations.

## 4.5.1 Systematic Uncertainty on Luminosity

We assign 5.9% systematic uncertainty on luminosity for all MC based estimate.

## 4.5.2 Systematic Uncertainty on Theoretical Cross Section

We take the uncertainties on theoretical cross sections of MC process.

| Source | $WW$ | $WZ$ | $ZZ$ | $t\bar{t}$ | $W\gamma/Z\gamma$ | $Z/\gamma^*$ | $W$ |
|---|---|---|---|---|---|---|---|
| $\sigma$ | 6.0% | 6.0% | 6.0% | 10.0% | 5.0% | 5.0% | 5.0% |
| Higher Order Diagrams | 10.0% | 10.0% | 10.0% | 10.0% | 11.0% | - | - |

Table 4.9: Systematic uncertainty on background cross section

| Source | $WH$ | $ZH$ | $VBF$ | $ggH$ |
|---|---|---|---|---|
| $\sigma$ | 5.0% | 5.0% | 10.0% | 10.0% |

Table 4.10: Systematic uncertainty on signal cross section

## 4.5.3 Systematic Uncertainty on Acceptance

We distinguish 5 categories of lepton combinations, which are $lll$, $ll\tau$, $e\mu\tau$, $l\tau\tau$ and $LLLL$. The notation of "$l$" represent electron, muon and crack track and the notation of "$L$" represent electron, muon, crack track and hadronic tau. We assign systematic uncertainties on each acceptance as below.

1. Z vertex cut ($|z_{vertex}| < 60cm$): 0.5% is assigned for all Monte Carlo samples. This is common uncertainty for each category.

2. Trigger Efficiencies: This depends on lepton type, CEM/CMUP/CMX. This also depends on $N_{track}$ of isolated track. We estimate this uncertainty in each category.

3. Lepton ID scale factor: We estimate this uncertainty in each category.

4. Jet Energy Scale: Systematic uncertainty of jet energy scale effect on missing energy significance cut. We take a half of the difference between the acceptance results of $+\sigma$ and $-\sigma$. This value is evaluated by applying to all MC samples.

5. MC statistics: We estimate this uncertainty in each category.

6. Jet Fake Rate: We evaluate systematic uncertainties $(< r_{fake}^{JET} > - r_{fake}^{MC})/r_{fake}^{MC}$ from jet data and Monte Carlo samples. We evaluate it for each lepton (electron, muon and hadronic tau), $-34\%$, $-38\%$ and $+23\%$. For the time being, we take the biggest one. Then, we assign this uncertainties for $WZ$, $WW$, Drell-Yan and $W$ MC samples.

7. Parton Distribution Function (PDF): This is considered for higgs signal process. This uncertainty does not depend on lepton combination category.

8. ISR/FSR: This is considered for higgs signal process using MC samples.

| Source | Systematic Uncertainties (%) | | | | | | | | | |
|---|---|---|---|---|---|---|---|---|---|---|
| | $ZZ$ | $WZ$ | $WW$ | $DY(ee)$ | $DY(\mu\mu)$ | $DY(\tau\tau)$ | $Z\gamma$ | $t\bar{t}$ | $W\gamma$ | $W$ |
| $|Z_{vertex}|$ | 0.5 | 0.5 | 0.5 | 0.5 | 0.5 | 0.5 | 0.5 | 0.5 | 0.5 | 0.5 |
| $\epsilon^{trigger}$ | 1.5 | 1.4 | 1.5 | 1.3 | 1.5 | 1.4 | 1.4 | 1.4 | 1.4 | 1.5 |
| $s^{leptonID}$ | 0.6 | 0.5 | 0.6 | 0.5 | 0.7 | 0.6 | 0.5 | 0.6 | 0.5 | 0.6 |
| JES | 1.7 | 0.0 | 0.3 | 0.7 | 2.2 | 0.3 | 5.1 | 0.2 | 1.9 | 0.2 |
| MC stat | 2.2 | 1.2 | 7.4 | 0.8 | 1.1 | 2.9 | 2.4 | 1.7 | 19.6 | 3.4 |
| Jet Fake Rate | - | - | 37.6 | 37.6 | 37.6 | 37.6 | - | 37.6 | - | 53.2 |

Table 4.11: Systematic Uncertainties on acceptance for $lll$ case of MC process

| Source | Systematic Uncertainties (%) | | | | | | | | | |
|---|---|---|---|---|---|---|---|---|---|---|
| | $ZZ$ | $WZ$ | $WW$ | $DY(ee)$ | $DY(\mu\mu)$ | $DY(\tau\tau)$ | $Z\gamma$ | $t\bar{t}$ | $W\gamma$ | $W$ |
| $|Z_{vertex}|$ | 0.5 | 0.5 | 0.5 | 0.5 | 0.5 | 0.5 | 0.5 | 0.5 | 0.5 | 0.5 |
| $\epsilon^{trigger}$ | 1.1 | 1.1 | 1.0 | 1.0 | 1.0 | 1.1 | 1.1 | 1.0 | 0.8 | 1.0 |
| $s^{leptonID}$ | 2.4 | 2.3 | 2.4 | 2.3 | 2.4 | 2.4 | 2.3 | 2.4 | 2.3 | 2.4 |
| JES | 1.3 | 1.1 | 0.0 | 3.2 | 5.1 | 0.6 | 6.6 | 0.1 | 2.0 | 0.2 |
| MC stat | 3.7 | 2.9 | 7.6 | 1.5 | 1.7 | 2.2 | 4.1 | 3.1 | 20.0 | 3.1 |
| Jet Fake Rate | - | - | 37.6 | 37.6 | 37.6 | 37.6 | - | 37.6 | - | 53.2 |

Table 4.12: Systematic Uncertainties on acceptance for $ll\tau$ case of MC process

| Source | Systematic Uncertainties (%) | | | | | | | | | |
|---|---|---|---|---|---|---|---|---|---|---|
| | $ZZ$ | $WZ$ | $WW$ | $DY(ee)$ | $DY(\mu\mu)$ | $DY(\tau\tau)$ | $Z\gamma$ | $t\bar{t}$ | $W\gamma$ | $W$ |
| $|Z_{vertex}|$ | 0.5 | 0.5 | 0.5 | 0.5 | 0.5 | 0.5 | 0.5 | 0.5 | 0.5 | 0.5 |
| $\epsilon^{trigger}$ | 1.4 | 1.4 | 1.1 | 1.1 | 1.3 | 1.1 | 1.4 | 1.1 | 1.0 | 0.7 |
| $s^{leptonID}$ | 2.4 | 2.4 | 2.4 | 2.5 | 2.4 | 2.4 | 2.4 | 2.4 | 2.4 | 2.5 |
| JES | 0.0 | 0.3 | 2.2 | 0.0 | 0.8 | 1.5 | 0.5 | 0.8 | 0.0 | 0.0 |
| MC stat | 12.9 | 7.2 | 20.9 | 57.7 | 12.6 | 7.7 | 10.2 | 12.4 | 35.4 | 25.8 |
| Jet Fake Rate | - | - | 37.6 | 37.6 | 37.6 | 37.6 | - | 37.6 | - | 53.2 |

Table 4.13: Systematic Uncertainties on acceptance for $e\mu\tau$ case of MC process

| Source | Systematic Uncertainties (%) | | | | | | | | | |
|---|---|---|---|---|---|---|---|---|---|---|
| | $ZZ$ | $WZ$ | $WW$ | $DY(ee)$ | $DY(\mu\mu)$ | $DY(\tau\tau)$ | $Z\gamma$ | $t\bar{t}$ | $W\gamma$ | $W$ |
| $|Z_{vertex}|$ | 0.5 | 0.5 | 0.5 | 0.5 | 0.5 | 0.5 | 0.5 | 0.5 | 0.5 | 0.5 |
| $\epsilon^{trigger}$ | 1.0 | 1.1 | 0.9 | 1.0 | 1.1 | 1.1 | 1.1 | 1.0 | 0.7 | 0.9 |
| $s^{leptonID}$ | 3.3 | 3.3 | 3.3 | 3.2 | 3.3 | 3.3 | 3.3 | 3.3 | 3.3 | 3.3 |
| JES | 5.5 | 0.0 | 0.0 | 3.3 | 1.6 | 1.2 | 1.6 | 0.0 | 0.0 | 1.1 |
| MC stat | 12.5 | 8.1 | 16.9 | 18.3 | 12.5 | 4.9 | 12.6 | 14.7 | 70.7 | 8.7 |
| Jet Fake Rate | - | - | 37.6 | 37.6 | 37.6 | 37.6 | - | 37.6 | - | 53.2 |

Table 4.14: Systematic Uncertainties on acceptance for $l\tau\tau$ case of MC process

| Source | Systematic Uncertainties (%) | | | | | | | | | |
|---|---|---|---|---|---|---|---|---|---|---|
| | $ZZ$ | $WZ$ | $WW$ | $DY(ee)$ | $DY(\mu\mu)$ | $DY(\tau\tau)$ | $Z\gamma$ | $t\bar{t}$ | $W\gamma$ | $W$ |
| $|Z_{vertex}|$ | 0.5 | 0.5 | 0.5 | 0.5 | 0.5 | 0.5 | 0.5 | 0.5 | - | - |
| $\epsilon^{trigger}$ | 1.5 | 1.4 | 0.7 | 1.3 | 1.4 | 1.2 | 1.5 | 1.4 | - | - |
| $s^{leptonID}$ | 1.4 | 1.2 | 2.4 | 1.2 | 1.5 | 2.0 | 2.0 | 1.0 | - | - |
| JES | 0.3 | 0.0 | 0.0 | 1.9 | 0.7 | 0.0 | 4.6 | 0.0 | - | - |
| MC stat | 5.8 | 17.1 | 100 | 6.9 | 8.3 | 23.6 | 30.2 | 12.5 | - | - |
| Jet Fake Rate | - | 37.6 | 53.2 | 53.2 | 53.2 | 53.2 | - | 53.2 | - | - |

Table 4.15: Systematic Uncertainties on acceptance for $LLLL$ case of MC process

| Source | Systematic Uncertainties (%) | | | |
|---|---|---|---|---|
| | $WH$ | $ZH$ | $VBF$ | $H$ |
| $|Z_{vertex}|$ | 0.5 | 0.5 | 0.5 | 0.5 |
| $\epsilon^{trigger}$ | 1.4 | 1.5 | 1.4 | 1.4 |
| $s^{leptonID}$ | 0.6 | 0.6 | 0.6 | 0.6 |
| JES | 0.1 | 0.02 | 1.4 | 0.9 |
| MC stat | 1.7 | 1.4 | 5.7 | 13.0 |
| PDF | 1.2 | 0.9 | 2.2 | 4.9 |
| ISR/FSR | 0.1 | 0.3 | 0.3 | 0.02 |

Table 4.16: Systematic Uncertainties on acceptance for $lll$ case of Higgs MC process

| Source | Systematic Uncertainties (%) | | | |
|---|---|---|---|---|
| | $WH$ | $ZH$ | $VBF$ | $H$ |
| $|Z_{vertex}|$ | 0.5 | 0.5 | 0.5 | 0.5 |
| $\epsilon^{trigger}$ | 1.2 | 1.2 | 1.2 | 1.1 |
| $s^{leptonID}$ | 2.4 | 2.4 | 2.4 | 2.4 |
| JES | 0.1 | 0.03 | 0.6 | 0.4 |
| MC stat | 1.5 | 1.4 | 3.8 | 9.4 |
| PDF | 1.2 | 0.9 | 2.2 | 4.9 |
| ISR/FSR | 1.3 | 2.1 | 0.6 | 0.2 |

Table 4.17: Systematic Uncertainties on acceptance for $ll\tau$ case of Higgs MC process

| Source | Systematic Uncertainties (%) | | | |
|---|---|---|---|---|
| | $WH$ | $ZH$ | $VBF$ | $H$ |
| $|Z_{vertex}|$ | 0.5 | 0.5 | 0.5 | 0.5 |
| $\epsilon^{trigger}$ | 1.3 | 1.3 | 1.2 | 1.2 |
| $s^{leptonID}$ | 2.4 | 2.4 | 2.4 | 2.4 |
| JES | 0.2 | 0.1 | 1.7 | 0.0 |
| MC stat | 2.1 | 3.9 | 13.0 | 45.0 |
| PDF | 1.2 | 0.9 | 2.2 | 4.9 |
| ISR/FSR | 0.6 | 0.2 | 0.1 | $\ll 1$ |

Table 4.18: Systematic Uncertainties on acceptance for $e\mu\tau$ case of Higgs MC process

| Source | Systematic Uncertainties (%) | | | |
|--------|------|------|------|------|
|        | $WH$ | $ZH$ | $VBF$ | $H$ |
| $|Z_{vertex}|$ | 0.5 | 0.5 | 0.5 | 0.5 |
| $\epsilon^{trigger}$ | 1.1 | 1.1 | 1.1 | 1.1 |
| $s^{leptonID}$ | 3.3 | 3.3 | 3.3 | 3.3 |
| JES | 0.1 | 0.6 | 1.8 | 1.7 |
| MC stat | 2.0 | 3.3 | 9.4 | 18.0 |
| PDF | 1.2 | 0.9 | 2.2 | 4.9 |
| ISR/FSR | 1.2 | 0.5 | 0.4 | 0.04 |

Table 4.19: Systematic Uncertainties on acceptance for $l\tau\tau$ case of Higgs MC process

| Source | Systematic Uncertainties (%) | | | |
|--------|------|------|------|------|
|        | $WH$ | $ZH$ | $VBF$ | $H$ |
| $|Z_{vertex}|$ | 0.5 | 0.5 | 0.5 | - |
| $\epsilon^{trigger}$ | 1.3 | 1.4 | 1.0 | - |
| $s^{leptonID}$ | 2.0 | 2.2 | 2.0 | - |
| JES | 0.0 | 0.0 | 0.0 | - |
| MC stat | 15 | 2.1 | 40.8 | - |
| PDF | 1.2 | 0.9 | 2.2 | - |
| ISR/FSR | 0.01 | 0.4 | 0.02 | - |

Table 4.20: Systematic Uncertainties on acceptance for $LLLL$ case of Higgs MC process

### 4.5.4   Systematic Uncertainty on QCD estimation

We assume that pure QCD events do not have charge correlation between final state leptons. Namely, a lepton charge from jet is randomly plus(or minus) at 50% and there is no charge correlations between jets. Under this assumption, for instance, $(+ + +)$, $(+ - +)$, $(- - -)$, $(- + -)$,,, all appear at the same rate.

Here, we define "same sign" events (SS) as $|\sum Q| == 3$ for 3 lepton case, and as $|\sum Q| == 2$ or $|\sum Q| == 4$ for 4 lepton case. To evaluate the number of pure QCD events, we use SS data and SS Monte Carlo samples. Table 4.21 shows same sign events with $\not{E}_T / \sum E_T \leq 1.0$ from Monte Carlo samples. Table 4.22 shows same sign events with $\not{E}_T / \sum E_T > 1.0$ from Monte Carlo samples.

|  | 3L | | | | 4L |
|---|---|---|---|---|---|
|  | $lll$ | $ll\tau$ | $e\mu\tau$ | $l\tau\tau$ | $LLLL$ |
| $ZZ$ | $0.10 \pm 0.01$ | $0.03 \pm 0.01$ | $0.00 \pm 0.00$ | $0.00 \pm 0.00$ | $0.05 \pm 0.01$ |
| $WZ$ | $0.06 \pm 0.02$ | $0.02 \pm 0.01$ | $0.00 \pm 0.00$ | $0.00 \pm 0.00$ | $0.21 \pm 0.04$ |
| $WW$ | $0.02 \pm 0.01$ | $0.01 \pm 0.01$ | $0.00 \pm 0.00$ | $0.00 \pm 0.00$ | $0.00 \pm 0.00$ |
| $DY(ee)$ | $3.19 \pm 1.24$ | $5.83 \pm 2.27$ | $0.00 \pm 0.00$ | $0.01 \pm 0.01$ | $1.00 \pm 0.39$ |
| $DY(\mu\mu)$ | $0.17 \pm 0.07$ | $0.01 \pm 0.01$ | $0.00 \pm 0.00$ | $0.00 \pm 0.00$ | $1.02 \pm 0.40$ |
| $DY(\tau\tau)$ | $0.21 \pm 0.10$ | $0.09 \pm 0.04$ | $0.02 \pm 0.02$ | $0.00 \pm 0.00$ | $0.01 \pm 0.01$ |
| $Z\gamma$ | $0.56 \pm 0.10$ | $0.12 \pm 0.03$ | $0.00 \pm 0.00$ | $0.01 \pm 0.01$ | $0.12 \pm 0.03$ |
| $t\bar{t}$ | $0.12 \pm 0.03$ | $0.07 \pm 0.02$ | $0.00 \pm 0.00$ | $0.00 \pm 0.00$ | $0.02 \pm 0.01$ |
| $W\gamma$ | $0.00 \pm 0.00$ | $0.00 \pm 0.00$ | $0.00 \pm 0.00$ | $0.00 \pm 0.00$ | $0.00 \pm 0.00$ |
| $W + Jets$ | $0.31 \pm 0.17$ | $0.39 \pm 0.22$ | $0.05 \pm 0.04$ | $0.08 \pm 0.06$ | $0.01 \pm 0.01$ |
| total | $4.75 \pm 1.26$ | $6.56 \pm 2.28$ | $0.08 \pm 0.05$ | $0.10 \pm 0.06$ | $2.45 \pm 0.56$ |

Table 4.21: Same Sign MC events with $\not{E}_T / \sum E_T \leq 1.0$. Errors are as same as ones of signal region except for MC stat.

| | 3L | | | | 4L |
|---|---|---|---|---|---|
| | $lll$ | $ll\tau$ | $e\mu\tau$ | $l\tau\tau$ | $LLLL$ |
| $ZZ$ | $0.07 \pm 0.02$ | $0.04 \pm 0.01$ | $0.01 \pm 0.01$ | $0.00 \pm 0.00$ | $0.10 \pm 0.02$ |
| $WZ$ | $0.34 \pm 0.06$ | $0.12 \pm 0.02$ | $0.01 \pm 0.01$ | $0.01 \pm 0.01$ | $0.09 \pm 0.02$ |
| $WW$ | $0.10 \pm 0.05$ | $0.16 \pm 0.08$ | $0.00 \pm 0.00$ | $0.01 \pm 0.01$ | $0.03 \pm 0.02$ |
| $DY(ee)$ | $1.05 \pm 0.42$ | $1.24 \pm 0.50$ | $0.01 \pm 0.01$ | $0.03 \pm 0.02$ | $0.48 \pm 0.19$ |
| $DY(\mu\mu)$ | $0.11 \pm 0.05$ | $0.31 \pm 0.13$ | $0.05 \pm 0.03$ | $0.00 \pm 0.00$ | $0.26 \pm 0.10$ |
| $DY(\tau\tau)$ | $0.15 \pm 0.07$ | $0.26 \pm 0.12$ | $0.00 \pm 0.00$ | $0.00 \pm 0.00$ | $0.15 \pm 0.07$ |
| $Z\gamma$ | $0.10 \pm 0.03$ | $0.02 \pm 0.01$ | $0.03 \pm 0.02$ | $0.01 \pm 0.01$ | $0.05 \pm 0.02$ |
| $t\bar{t}$ | $1.01 \pm 0.29$ | $0.52 \pm 0.15$ | $0.28 \pm 0.15$ | $0.01 \pm 0.01$ | $0.40 \pm 0.12$ |
| $W\gamma$ | $0.05 \pm 0.02$ | $0.05 \pm 0.02$ | $0.06 \pm 0.03$ | $0.14 \pm 0.14$ | $0.00 \pm 0.00$ |
| $W + Jets$ | $2.86 \pm 1.58$ | $2.59 \pm 1.45$ | $0.02 \pm 0.02$ | $0.72 \pm 0.57$ | $0.08 \pm 0.06$ |
| total | $5.84 \pm 1.66$ | $5.31 \pm 1.56$ | $0.47 \pm 0.15$ | $0.94 \pm 0.58$ | $1.63 \pm 0.26$ |

Table 4.22: Same Sign MC events with $\displaystyle{\not}E_T / \sum E_T > 1.0$. Errors are as same as ones of signal region except for MC stat.

### 3 Lepton Case

In 3 lepton case, same sign ($|\Sigma Q| = 3$) data include several physical process, for example, $W + jets \to l + 2fakes$, $Z + jets \to l\!\!\!/ + 2fakes$ and so on. Except for pure QCD, we can estimate from Monte Carlo samples. So, to evaluate the number of pure QCD events, we subtract the number of same sign Monte Carlo events from same sign data as below.

$$N^{QCD}(SS) = N^{DATA}(SS) - N^{MC}(SS) \qquad (4.2)$$

In considering combination of 3 lepton charge sum (Table 4.23), the number of OS combinations is equal to the number of SS combinations times 3.

| $L1$ | $L2$ | $L3$ | $\Sigma Q$ | |
|------|------|------|------------|------|
| + | + | + | +3 | SS |
| + | + | - | +1 | OS |
| + | - | + | +1 | OS |
| + | - | - | -1 | OS |
| - | + | + | +1 | OS |
| - | + | - | -1 | OS |
| - | - | + | -1 | OS |
| - | - | - | -3 | SS |

Table 4.23: Lepton charge combination in 3 lepton case. $N(OS) = 3 \times N(SS)$

We evaluate the number of pure QCD events in OS data under pure QCD assumption as below.

$$N^{QCD}(OS) = 3 \times N^{QCD}(SS) \qquad (4.3)$$

We apply the above way to events with $\not{E}_T / \sum E_T \leq 1.0$ and $\not{E}_T / \sum E_T > 1.0$. The result is in Table 4.24 and Table 4.25. In $e\mu\tau$ case, we have no SS data event. We assign 0 event as QCD event in $e\mu\tau$ case. For 0 event, we assign error as $\approx 0.4$ which is the mean of Poisson distribution $P(0) = e^{-\lambda} = 0.68$.

|                        | $lll$              | $ll\tau$          | $e\mu\tau$       | $l\tau\tau$      |
| ---------------------- | ------------------ | ----------------- | ---------------- | ---------------- |
| $N^{DATA}(SS)$         | 8                  | 14                | 0                | 4                |
| $N^{MC}(SS)$           | $4.75 \pm 1.26$    | $6.56 \pm 2.28$   | $0.08 \pm 0.05$  | $0.10 \pm 0.06$  |
| $N^{QCD}(SS)$          | $3.25 \pm 3.10$    | $7.44 \pm 4.38$   | 0 (negative)     | $3.90 \pm 2.00$  |
| $N^{QCD}(OS)$          | $9.75 \pm 9.29$    | $22.31 \pm 13.14$ | $0.00 \pm 1.21$  | $11.70 \pm 6.00$ |
| $N^{MC}(OS)$           | $723.00 \pm 151.73$ | $360.40 \pm 74.22$ | $1.86 \pm 0.33$  | $4.96 \pm 1.23$  |
| $N(OS)$                | $732.75 \pm 152.01$ | $382.71 \pm 74.22$ | $1.86 \pm 1.25$  | $16.66 \pm 6.13$ |
| $N^{DATA}(OS)$         | 715                | 480               | 4                | 18               |
| $N^{DATA}(OS)/N(OS)$   | $0.98 \pm 0.21$    | $1.25 \pm 0.25$   | $2.15 \pm 1.63$  | $1.08 \pm 0.47$  |

Table 4.24: Evaluate pure QCD events with $\not{E}_T / \sum E_T \leq 1.0$ in 3 lepton case.

|                        | $lll$              | $ll\tau$          | $e\mu\tau$       | $l\tau\tau$      |
| ---------------------- | ------------------ | ----------------- | ---------------- | ---------------- |
| $N^{DATA}(SS)$         | 9                  | 14                | 0                | 3                |
| $N^{MC}(SS)$           | $5.84 \pm 1.66$    | $5.31 \pm 1.56$   | $0.47 \pm 0.15$  | $0.94 \pm 0.58$  |
| $N^{QCD}(SS)$          | $3.16 \pm 3.43$    | $8.69 \pm 4.05$   | 0 (negative)     | $2.06 \pm 1.83$  |
| $N^{QCD}(OS)$          | $9.48 \pm 10.29$   | $26.06 \pm 12.16$ | $0.00 \pm 1.29$  | $6.19 \pm 5.48$  |
| $N^{MC}(OS)$           | $320.91 \pm 67.35$ | $188.26 \pm 38.16$ | $5.26 \pm 0.93$  | $14.24 \pm 3.54$ |
| $N(OS)$                | $330.40 \pm 68.13$ | $214.32 \pm 40.05$ | $5.26 \pm 1.59$  | $20.44 \pm 6.53$ |
| $N^{DATA}(OS)$         | 284                | 203               | 8                | 16               |
| $N^{DATA}(OS)/N(OS)$   | $0.86 \pm 0.18$    | $0.95 \pm 0.19$   | $1.52 \pm 0.71$  | $0.78 \pm 0.32$  |

Table 4.25: Evaluate pure QCD events with $\not{E}_T / \sum E_T > 1.0$ in 3 lepton case.

**4 Lepton Case**

We apply the same method for 3 lepton case to 4 lepton case as well.

$$N^{QCD}(SS) = N^{DATA}(SS) - N^{MC}(SS) \qquad (4.4)$$

| L1 | L2 | L3 | L4 | $\Sigma Q$ | |
|----|----|----|----|----|----|
| + | + | + | + | +4 | SS |
| + | + | + | - | +2 | SS |
| + | + | - | + | +2 | SS |
| + | - | + | + | +2 | SS |
| + | + | - | - | 0 | OS |
| + | - | - | + | 0 | OS |
| + | - | + | - | 0 | OS |
| + | - | - | - | -2 | SS |
| - | + | + | + | +2 | SS |
| - | + | - | + | 0 | OS |
| - | + | + | - | 0 | OS |
| - | - | + | + | 0 | OS |
| - | + | - | - | -2 | SS |
| - | - | + | - | -2 | SS |
| - | - | - | + | -2 | SS |
| - | - | - | - | -4 | SS |

Table 4.26: Lepton charge combination in 4 lepton case. $N(OS) = 0.6 \times N(SS)$

As shown in Table 4.26, the ratio is different from 3 lepton case. The number of OS events is equal to the number of SS events times 0.6 in this case.

$$N^{QCD}(OS) = 0.6 \times N^{QCD}(SS) \qquad (4.5)$$

We apply the above way to events with $\not{E}_T/\sum E_T \leq 1.0$ and $\not{E}_T/\sum E_T > 1.0$. The result is in Table 4.27 and Table 4.28. In $e\mu\tau$ case, we have no SS data event. We assign 0 event as QCD event in $e\mu\tau$ case. For 0 event, we assign error as $\approx 0.4$ which is the mean of Poisson distribution $P(0) = e^{-\lambda} = 0.68$.

|  | $LLLL$ |
|---|---|
| $N^{DATA}(SS)$ | 0 |
| $N^{MC}(SS)$ | $2.45 \pm 0.56$ |
| $N^{QCD}(SS)$ | 0 (negative) |
| $N^{QCD}(OS)$ | $0.00 + 0.41$ |
| $N^{MC}(OS)$ | $4.60 \pm 0.85$ |
| $N(OS)$ | $4.60 \pm 0.94$ |
| $N^{DATA}(OS)$ | 4 |
| $N^{DATA}(OS)/N(OS)$ | $0.87 \pm 0.50$ |

Table 4.27: Evaluate pure QCD events with $\not{E}_T / \sum E_T \leq 1.0$ in 4 lepton case.

|  | $LLLL$ |
|---|---|
| $N^{DATA}(SS)$ | 3 |
| $N^{MC}(SS)$ | $1.63 \pm 0.26$ |
| $N^{QCD}(SS)$ | $1.37 \pm 1.75$ |
| $N^{QCD}(OS)$ | $0.82 \pm 1.05$ |
| $N^{MC}(OS)$ | $2.62 \pm 0.48$ |
| $N(OS)$ | $3.44 \pm 1.16$ |
| $N^{DATA}(OS)$ | 6 |
| $N^{DATA}(OS)/N(OS)$ | $1.74 \pm 0.92$ |

Table 4.28: Evaluate pure QCD events with $\not{E}_T / \sum E_T > 1.0$ in 4 lepton case.

## 4.5.5 Summary of Systematic Uncertainties

We summarize systematic uncertainties as Table 4.29 and Table 4.30.

| | Total Systematic Uncertainties (%) | | | | |
|---|---|---|---|---|---|
| | 3L | | | | 4L |
| | $lll$ | $ll\tau$ | $e\mu\tau$ | $l\tau\tau$ | $LLLL$ |
| $ZZ$ | 13.5 | 13.9 | 18.6 | 19.2 | 14.4 |
| $WZ$ | 13.2 | 13.7 | 15.2 | 15.7 | 43.4 |
| $WW$ | 40.5 | 40.6 | 45.1 | 43.4 | 100 |
| $DY(ee)$ | 38.4 | 38.6 | 69.3 | 42.6 | 54.2 |
| $DY(\mu\mu)$ | 38.5 | 38.8 | 40.4 | 40.5 | 54.4 |
| $DY(\tau\tau)$ | 38.5 | 38.5 | 39.2 | 38.8 | 58.7 |
| $Z\gamma$ | 14.7 | 15.8 | 17.1 | 18.8 | 33.4 |
| $t\bar{t}$ | 40.7 | 40.8 | 42.5 | 43.3 | 56.7 |
| $W\gamma$ | 23.9 | 24.3 | 37.9 | 72.1 | - |
| $W + jets$ | 53.6 | 53.6 | 59.4 | 54.2 | - |

Table 4.29: Total Systematic Uncertainties on acceptance

| | Total Systematic Uncertainties (%) | | | | |
|---|---|---|---|---|---|
| | 3L | | | | 4L |
| | $lll$ | $ll\tau$ | $e\mu\tau$ | $l\tau\tau$ | $LLLL$ |
| $WH$ | 8.2 | 8.5 | 8.6 | 8.9 | 17.2 |
| $ZH$ | 8.1 | 8.3 | 9.1 | 9.2 | 8.5 |
| $VBF$ | 13.3 | 12.7 | 17.9 | 15.6 | 42.6 |
| $H$ | 18.3 | 16.0 | 46.5 | 22.5 | - |

Table 4.30: Total Systematic Uncertainties on acceptance of Higgs MC process

## 4.6 Summary

We do not figure out any clear excess from out background estimation in the final response distributions of 5 categories, which distributions are within $\pm\sigma$ of error, comparing with our background estimations. Therefore, we conclude that it is no indications of the Standard Model Higgs existence using only $l\nu + \tau\tau$ and $ll + \tau\tau$ final states. We try to extract cross section upper limit in next section.

# Chapter 5

# Summary of the Standard Model Higgs Search

As mentioned, we do not clearly see any discrepancies between data and background estimation. To summarize the results of search for the Standard Model Higgs using $l\nu + \tau\tau$ and $ll + \tau\tau$ final states, we extract the cross section of upper limit of $VH \rightarrow l\nu(l) + \tau\tau$ at 95 % confidence level.

## 5.1    Expected and Observed Limit @ 95 % C.L.

At first, we define the likelihood function from the response distributions, here.

For $i$ th bin of responses, the expected number of events ($\mu_i$) including signals is evaluated as below.

$$\mu_i = \sum_k^{N_B} f_i^k N^k + \sum_l^{N_S} f_i^l \cdot (\epsilon^l \cdot \sigma^l \cdot \int Ldt),$$

where the notation of $k$ and $l$ represents kinds of backgrounds ($WZ$, $ZZ$, $Z$+fake and so on) and signals, and $N_B$ and $N_S$ shows the number of kinds of backgrounds and signals, and $f$ represent the expected fraction in bin, and $\epsilon^l$ is the detection efficiency including acceptance, trigger efficiency and so on, and $\int Ldt$) is the integrated luminosity, and $\sigma^l$ is the cross section of signals, which are $WH$, $ZH$, $VBF$ and $ggH$.

Then, we define the likelihood function for each lepton category as below.

$$L(\frac{\sigma}{\sigma_{SM}}) = \int \cdots \int \prod_{i=1}^{N_{bin}} \frac{\mu_i^{N_i}}{N_i!} e^{-\mu_i} \prod_{k=1}^{N_B} G(N^k, \Delta^k) dN_k \prod_{l=1}^{N_S} G(\frac{\sigma^l}{\sigma_{SM}} N^l, \Delta^l) dN_l$$

$\Delta^k$ and $\Delta^l$ show the uncertainties of each source correlation under consideration. The function $G$ shows Gaussian function; we fluctuate by the expected uncertainties ($\Delta^k$ for each background and $\Delta^l$ for each signal). $N_i$ shows the number of observed events for $i$ th bin. About signal cross section ($\sigma^l$), we assume these are 100% correlated. So,

we use the same ratio $(\frac{\sigma}{\sigma_{SM}})$ for signal processes, which means $\frac{\sigma^l}{\sigma_{SM}} = \frac{\sigma}{\sigma_{SM}}$ in above equation.

As above, we define 5 likelihoods ($L_0, L_1, L_2, L_3$ and $L_4$) from each response distribution. Then, we simultaneously fit for likelihoods of 5 categories into global likelihood ($L_g$).

$$L_g = L_0 \times L_1 \times L_2 \times L_3 \times L_4$$

We extract the expected 95% confidence level limit from binned likelihood ($L_g$) by pseudo experiments. In pseudo experiment, we evaluate the expected number of events by adding the expected number of events for each background source, which is fluctuated with Gaussian function by uncertainties, then the total number of events ($N_i$) in each bin for one pseudo experiment is determined within Poisson fluctuations.

The upper expected and observed limits for each category are listed in Table 5.1 for $L_0$, Table 5.2 for $L_1$, Table 5.3 for $L_2$, Table 5.4 for $L_3$ and Table 5.5 for $L_4$. And Figure 5.1 shows limits for each category.

We summarized the expected and observed upper limit from $L_g$ in Table 5.6 and Figure 5.2.

| $M_H$ | Expected limit/$\sigma$(SM) | | | | | Observed limit/$\sigma$(SM) |
|---|---|---|---|---|---|---|
| $(GeV/c^2)$ | $-2\sigma$ | $-1\sigma$ | median | $+1\sigma$ | $+2\sigma$ | |
| 100 | 44.65 | 62.75 | 90.95 | 136.45 | 211.65 | 98.05 |
| 105 | 48.45 | 67.95 | 98.25 | 147.55 | 225.75 | 104.05 |
| 110 | 55.25 | 76.95 | 111.35 | 166.65 | 256.65 | 123.35 |
| 115 | 61.25 | 86.05 | 124.55 | 185.95 | 287.05 | 135.65 |
| 120 | 72.45 | 101.15 | 146.35 | 218.55 | 331.85 | 163.25 |
| 125 | 87.25 | 120.95 | 175.25 | 259.35 | 385.35 | 199.15 |
| 130 | 108.35 | 150.05 | 217.35 | 322.95 | 478.05 | 243.05 |
| 135 | 139.65 | 193.65 | 280.15 | 411.55 | 601.65 | 322.65 |
| 140 | 190.15 | 261.45 | 374.95 | 537.15 | 752.55 | 431.65 |
| 145 | 283.85 | 387.25 | 541.45 | 745.25 | 1002.15 | 645.35 |
| 150 | 431.25 | 566.65 | 751.85 | 977.95 | 1221.85 | 992.25 |

Table 5.1:  Expected and Observed limit @ 95% C.L. for *lll* case.

| $M_H$ | Expected limit/$\sigma$(SM) | | | | | Observed limit/$\sigma$(SM) |
|---|---|---|---|---|---|---|
| $(GeV/c^2)$ | $-2\sigma$ | $-1\sigma$ | median | $+1\sigma$ | $+2\sigma$ | |
| 100 | 14.45 | 19.95 | 28.55 | 41.25 | 59.15 | 47.45 |
| 105 | 16.05 | 21.95 | 31.55 | 45.45 | 64.85 | 52.05 |
| 110 | 16.95 | 23.35 | 33.25 | 47.95 | 68.65 | 54.95 |
| 115 | 19.95 | 27.45 | 39.15 | 56.35 | 80.35 | 64.05 |
| 120 | 23.75 | 32.15 | 45.65 | 66.05 | 93.25 | 75.55 |
| 125 | 27.15 | 36.85 | 52.35 | 75.65 | 106.75 | 86.55 |
| 130 | 33.85 | 45.65 | 64.65 | 93.35 | 131.55 | 106.25 |
| 135 | 43.55 | 58.65 | 83.15 | 120.15 | 170.15 | 136.45 |
| 140 | 59.75 | 79.95 | 114.05 | 164.55 | 231.15 | 185.15 |
| 145 | 85.55 | 114.05 | 161.65 | 232.95 | 324.65 | 261.45 |
| 150 | 134.85 | 179.65 | 254.65 | 365.95 | 504.25 | 412.45 |

Table 5.2: Expected and Observed limit @ 95% C.L. for $ll\tau$ case.

| $M_H$ | Expected limit/$\sigma$(SM) | | | | | Observed limit/$\sigma$(SM) |
|---|---|---|---|---|---|---|
| $(GeV/c^2)$ | $-2\sigma$ | $-1\sigma$ | median | $+1\sigma$ | $+2\sigma$ | |
| 100 | 16.05 | 20.65 | 29.55 | 43.25 | 60.65 | 38.55 |
| 105 | 17.85 | 22.85 | 32.55 | 47.35 | 66.45 | 41.75 |
| 110 | 20.25 | 25.95 | 36.45 | 53.15 | 74.55 | 47.35 |
| 115 | 23.05 | 29.25 | 41.05 | 59.45 | 84.05 | 52.45 |
| 120 | 27.15 | 34.45 | 48.15 | 70.55 | 99.65 | 62.45 |
| 125 | 32.55 | 41.05 | 57.45 | 83.95 | 118.75 | 73.25 |
| 130 | 42.55 | 53.15 | 73.75 | 107.35 | 151.95 | 94.65 |
| 135 | 54.75 | 68.45 | 94.95 | 138.05 | 195.75 | 123.15 |
| 140 | 75.35 | 93.65 | 129.45 | 186.35 | 259.65 | 162.65 |
| 145 | 115.05 | 142.35 | 195.15 | 280.65 | 388.85 | 247.85 |
| 150 | 186.35 | 228.45 | 311.75 | 442.15 | 596.95 | 397.85 |

Table 5.3: Expected and Observed limit @ 95% C.L. for $e\mu\tau$ case.

| $M_H$ | Expected limit/$\sigma$(SM) | | | | | Observed limit/$\sigma$(SM) |
|---|---|---|---|---|---|---|
| $(GeV/c^2)$ | $-2\sigma$ | $-1\sigma$ | median | $+1\sigma$ | $+2\sigma$ | |
| 100 | 16.25 | 21.75 | 31.35 | 46.65 | 67.45 | 21.15 |
| 105 | 17.15 | 22.55 | 32.05 | 47.15 | 68.05 | 22.15 |
| 110 | 18.85 | 24.65 | 34.85 | 51.25 | 73.85 | 24.05 |
| 115 | 21.95 | 28.25 | 39.15 | 57.15 | 81.95 | 27.35 |
| 120 | 26.15 | 33.25 | 45.35 | 65.95 | 94.25 | 32.55 |
| 125 | 32.25 | 40.15 | 54.15 | 78.25 | 111.85 | 39.55 |
| 130 | 39.55 | 49.05 | 65.85 | 94.85 | 135.65 | 48.45 |
| 135 | 53.95 | 66.55 | 89.05 | 127.85 | 183.15 | 65.35 |
| 140 | 72.25 | 88.25 | 117.55 | 166.55 | 238.85 | 86.55 |
| 145 | 107.65 | 130.85 | 173.05 | 244.15 | 346.55 | 127.25 |
| 150 | 172.25 | 207.05 | 272.15 | 380.65 | 529.55 | 204.45 |

Table 5.4:   Expected and Observed limit @ 95% C.L. for $l\tau\tau$ case.

| $M_H$ | Expected limit/$\sigma$(SM) | | | | | Observed limit/$\sigma$(SM) |
|---|---|---|---|---|---|---|
| $(GeV/c^2)$ | $-2\sigma$ | $-1\sigma$ | median | $+1\sigma$ | $+2\sigma$ | |
| 100 | 31.75 | 36.05 | 52.35 | 75.65 | 106.95 | 71.85 |
| 105 | 36.05 | 40.65 | 58.35 | 84.45 | 119.15 | 75.75 |
| 110 | 40.35 | 44.55 | 65.45 | 94.45 | 132.65 | 83.75 |
| 115 | 46.45 | 53.05 | 75.15 | 109.35 | 154.25 | 97.85 |
| 120 | 51.85 | 58.15 | 82.75 | 120.95 | 169.55 | 107.75 |
| 125 | 63.85 | 71.35 | 102.25 | 147.75 | 207.15 | 129.05 |
| 130 | 81.35 | 90.05 | 130.05 | 188.25 | 262.85 | 159.65 |
| 135 | 110.05 | 124.15 | 177.45 | 255.35 | 357.45 | 227.25 |
| 140 | 151.05 | 171.15 | 239.85 | 342.05 | 470.45 | 291.45 |
| 145 | 221.95 | 245.35 | 344.75 | 484.65 | 649.95 | 401.05 |
| 150 | 344.15 | 377.65 | 524.45 | 700.65 | 900.95 | 676.95 |

Table 5.5:   Expected and Observed limit @ 95% C.L. for 4 lepton case.
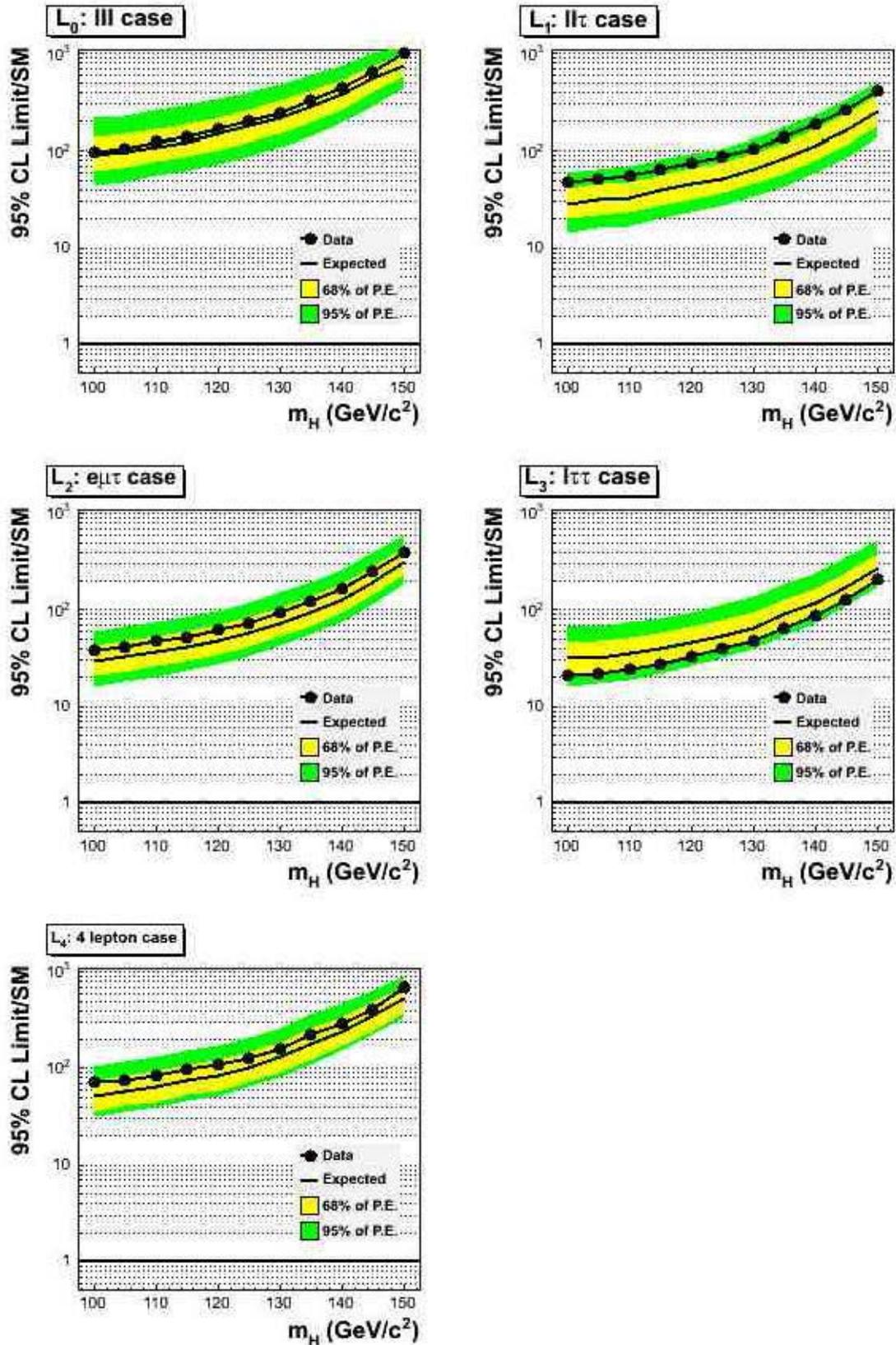
Figure 5.1: Expected and Observed limit @ 95% C.L. for each category.

| $M_H$ | Expected limit/$\sigma$(SM) | | | | | Observed limit/$\sigma$(SM) |
|---|---|---|---|---|---|---|
| $(GeV/c^2)$ | $-2\sigma$ | $-1\sigma$ | median | $+1\sigma$ | $+2\sigma$ | |
| 100 | 6.55 | 9.15 | 13.05 | 18.65 | 26.35 | 19.75 |
| 105 | 7.05 | 9.85 | 13.95 | 19.95 | 28.25 | 20.35 |
| 110 | 7.65 | 10.75 | 15.15 | 21.75 | 30.75 | 22.25 |
| 115 | 8.85 | 12.15 | 17.25 | 24.75 | 34.95 | 25.05 |
| 120 | 10.35 | 13.95 | 19.95 | 28.85 | 40.15 | 29.55 |
| 125 | 12.15 | 16.55 | 23.55 | 34.05 | 47.45 | 34.85 |
| 130 | 15.25 | 20.65 | 29.25 | 42.15 | 58.95 | 42.25 |
| 135 | 20.15 | 27.05 | 38.25 | 55.25 | 77.05 | 57.55 |
| 140 | 27.45 | 36.25 | 51.35 | 73.55 | 103.25 | 73.95 |
| 145 | 39.95 | 52.75 | 74.45 | 106.85 | 149.55 | 105.75 |
| 150 | 63.25 | 83.65 | 117.95 | 169.55 | 236.15 | 172.85 |

Table 5.6:  Expected and Observed limit @ 95% C.L.
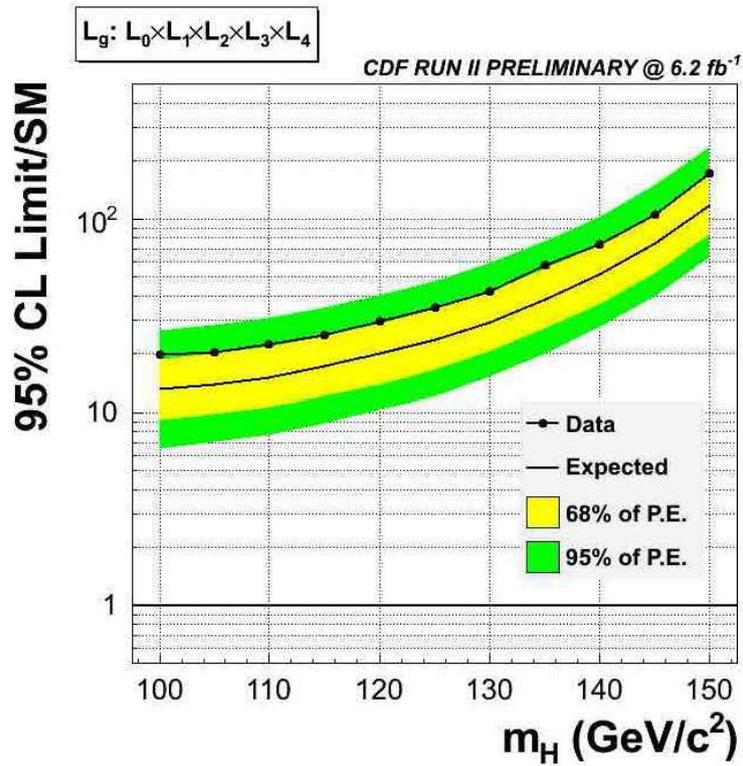


Figure 5.2:  Expected and Observed limit @ 95% C.L.

## 5.2 Conclusion

The main purpose of this paper is to search for the Standard Model Higgs boson. We however measure top quark properties first, especially the pair production cross section and the mass. Because top quark and W boson mass can give a constraint on Higgs boson mass through the radiative correction. Given the fact that a relation between measured top cross section and mass is well explained in the Standard Model, there is no strong indication on physics beyond the Standard Model from those experimental results.

As of July 2010, the top quark mass is measured to be by $m_{top} = 173.3 \pm 1.1 GeV/c^2$ from Tevatron combination, including results summarized in Chapter 3. This latest result gives constraints of $M_H = 89^{+35}_{-26} GeV/c^2$ (68% confidence level). As mentioned in Section 1.2.2, experimental results excluded $M_H < 114.4 GeV/c^2$ at 95% confidence level by LEP experiments and $158 GeV/c^2 < M_H < 175 GeV/c^2$ at 95% confidence level by Tevatron combination as of July 2010. Therefore, these mass of the Standard Model Higgs boson is likely to range $114.4 GeV/c^2 < M_H < 158 GeV/c^2$ if exists.

Finally with more statistics, we performed a direct search for the Standard Model Higgs boson. This analysis is the first challenge to look for the Higgs boson in $l\nu + \tau\tau$ and $ll + \tau\tau$ final state. To maximize the sensitivity, we used Support Vector Machine. Since there is not significant discrepancy between data and our background estimation, we extracted the expected and observed cross section limit of 95% confidence level. In consequence, the expected upper limit of the Standard Model cross section times branching ratio ($\sigma(SM) \times B(H \to \tau\tau)$) is from 13.1 to 118.0 in search range of $M_H \in [100, 150]$. Using approximately $6fb^{-1}$ data, The observed limit is from 19.8 to 172.9 in the same range for the expected limit.

Though it is regrettable that CDF II experiment will be finished on September 2011, by then CDF will accumulate $\sim 10fb^{-1}$ of an integrated luminosity for analysis use. Thus the signal events are increased by $\sim 1.6$, resulted in an upper limit improvement by $\sim 0.79$ even if there is no improvement of analysis sensitivity.

The final goal at Tevatron would be to exclude the Higgs boson in all possible mass range or 3 sigma evidence for a certain mass. It depends on the truth of Nature.

# Chapter 6

# Appendix

## 6.1  Privious Collider Run

| Period | Run |
|--------|-----|
| 1988-1989 | Collider Run |
| 1992-1993 | Collider Run Ia |
| 1994-1995 | Collider Run Ib |

Table 6.1:  Privious Run Period.
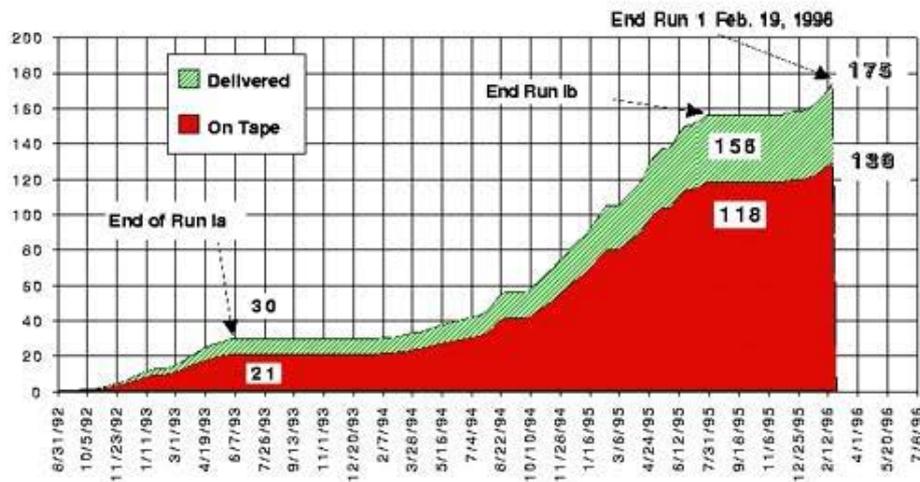


Figure 6.1:  Integrated Luminosity in Rin I.

# Bibliography

[1] Kodama K et al. (DONUT Collaboration), "Observation of tau neutrino interactions", Phy. Lett. B 504, Number 3, pp. 218-224(7), 2001/04/12

[2] P.W.Higgs, Phys. Rev. Lett 12, 132(1964);
*idem*, Phys. Rev. 145, 1156 (1966);
F.Englert and R. Brout, Phys. Rev. Lett. 13, 321 (1964);
G.S.Guranlnik, C.R.Hagen, and T.W.Kibble, Phys. Rev. Lett. 13, 585 (1964)

[3] D.J.Gross and F.Wilczek, "Asympotically free gauge theories", Rev D 8,3633 (1973)

[4] H.D.Politzer, "Asymptotic freedom: An approach to strong interactions", Phys. Rept., 14, 129 (1974).

[5] S.L.Glashow, Nucl. Phys. 20, 579 (1961);
S.Weinberg, Phys. Rev. Lett. 19, 1264 (1967);
A. Salam, "Elementary Particle Theory", eds.: Svartholm, Almquist, and Wiksells, Stockholm, 1968;
S.Glashow, J.Iliopoulos, and L. Maiani, Phys. Rev. D2, 1285 (1970)

[6] A.Salam and J.C.Ward, "Electromagnetic and weak interactions", Phys. Lett., 13, 168 (1964).

[7] D. Acosta et al., "The Performance of the CDF Luminosity Monitor", Nucl.Instrum.Meth.A494:57-62,2002

[8] D. Acosta et al., "The CDF Luminosity Monitor", Nucl.Instrum.Meth.A461:540-544,2001

[9] C. S. Hill et al., "L00: Operational Experience and Performance of the CDFII Silicon Detector", Nucl. Instrum. Meth. A530:1-6, 2004

[10] A. Sill et al., "SVX-II: CDF Run II Silicon Tracking Projects", Nucl. Instrum. Meth. A447:1-8, 2000

[11] A. Affolder et al., "ISL: Intermediate Silicon Layers Detector for the CDF Experiment", Nucl. Instrum. Meth. A453:84-88, 2000

[12] T. Affolder et al., "COT Central Outer Tracker", Nucl. Instrum. Meth. A526: 249, 2004

[13] L. Breccia et al., "Test of 2000 Phototubes for the CDF Endplug Calorimeter Upgrade", Nucl. Instrum. Meth. A532:575-610, 2004
G. Apollinari et al., "Shower Maximum Detector for the CDF Plug Upgrade Calorimeter", Nucl. Instrum. Meth. A412:515-526, 1998.
K. Goulianos et al., "The CDF Miniplug Calorimeters at the Tevatron", Nucl. Instrum. Meth. A518:42-44, 2004
K. Goulianos et al., "The CDF Miniplug Calorimeters", Nucl. Instrum. Meth. A496:333-346, 2003
Michele Gallinaro, "Performance of the CDF Miniplug Calorimeters", Nucl. Phys. B 125C:128-132, 2003
Konstantin Goulianos et al., "Performance of a Prototype Position Sensitive Towerless Calorimeter", Nucl. Instrum. Meth. A430:34-47, 1999
M. Albrow et al., "The CDF plug upgrade electromagnetic calorimeter: test beam results", Nucl. Instrum. Meth. A480:524-546, 2002

[14] M. Albrow et al., "Intercalibration of the longitudinal segments of a calorimeter system", Nucl. Instrum. Meth. A487:381-395, 2002

[15] M. Albrow et al., "A preshower detector for the CDF Plug Upgrade: test beam results", Nucl. Instrum. Meth. A431:101-111, 1999

[16] O. Pukhov et al., "Automatization of the Monitoring and Control of the Muon Scintillation Counters at CDF II", Part. Nucl. Lett. 5:72-81, 2002

[17] A. Artikov et al., "The Miniskirt Counter Array at CDF-II", Part. Nucl. Lett. 114:25-39, 2002

[18] W. Koska et al., "Evaluation of candidate photomultiplier tubes for the upgrade of the CDF End Plug calorimeter", Nucl. Inst. and Meth. A406:103, 1998.

[19] A. Artikov et al., "Design and construction of new central and forward muon counters for CDF II", Nucl. Instrum. Meth. A538:358-371, 2005

[20] S. Cabrera et al., "Making the most of aging scintillator", Nucl. Instrum. Meth. A453:245-248, 2000

[21] G. Ascoli, et al., "The CDF Central Muon Detector", Nucl. Instrum. Meth. A268:33-40, 1988

[22] S. Cabrera et al., "Making the most of aging scintillator", Nucl. Instrum. Meth. A453:245-248, 2000

[23] Robert Downing et al., "Track Extrapolation and Distribution for the CDF-II Trigger System", Nucl.Instum.Meth. A570:36-50, 2007

[24] A. Annovi et al., "A VLSI Processor for Fast Track Finding Based on Content Addressable Memories", IEEE Trans. on Nucl. Science, 53, 2428, 2006

[25] E.J. Thomson et al., "Online Track Processor for the CDF Upgrade", IEEE Trans. on Nucl. Science, 49, 1063, 2003

[26] G. Gomez-Ceballos et al., "Event Builder and Level 3 at the CDF Experiment", Nucl. Instrum. Meth. A518:522-524, 2004

[27] S. Baroiant et al., "Selection of Tau Leptons with the CDF II Trigger System", Nucl. Instrum. Meth. A518: 609, 2004

[28] T. Sjostrand et al., Comput. Phys. Commun. 135, 238 (2001).

[29] F.Abe et al., "Observation of top quark production in $p\bar{p}$ collisions with the Collider Detector at Fermilab", Phys. Rev. Lett. 74, 2626 (1995).

[30] S.Abachi et al., "Observation of the top quark", Phys. Rev. Lett. 74, 2632 (1995)

[31] The CDF Collaboration, the DZERO Collaboration, the Tevatron Electroweak Working Group, "Combination of CDF and DZERO Results on the Top-Quark Mass", hep-ex/0404010

[32] C.Amsler et al. (Particle Data Group), Phys. Lett. B667,1 (2008)

[33] T.Aaltonen et al. (CDF Collaboration), Phys. Rev. D76, 072009(2007)

[34] A. Bhatti et al., Nucl. Instrum. Methods Phys. Res., Sect. A 506, 375 (2006).

[35] R.Barate et al., "Search for the Standard Model Higgs boson at LEP", Phys. Lett. B 565, 61 (2003)

[36] The LEP Collaboration, The LEP Electroweak Working Group, "Precision Electroweak Measurements and Constraints on the Standard Model", Tech. Report CERN-PH-EP/2007-039, CERN, 2007

[37] A. Hoecker, P. Speckmayer, J. Stelzer, J. Therhaag, E. von Toerne, H. Voss, "TMVA 4 Toolkit for Multivariate Data Analysis with ROOT Users Guide", arXiv:physics/0703039

[38] C. Cortes and V. Vapnik, "Support vector networks", Machine Learning, 20, 273 (1995).

[39] V. Vapnik, "The Nature of Statistical Learning Theory", Springer Verlag, New York, 1995.

[40] C.J.C. Burges, "A Tutorial on Support Vector Machines for Pattern Recognition", Data Mining and Knowledge Discovery, 2, 1 (1998).

# Papers by AUTHOR

1. **"Measurement of the Top Quark Mass and $p\bar{p} \to t\bar{t}$ Cross Section in the All-Hadronic Mode with the CDFII Detector"**
   K. Ebina *et al.* [The CDF Collaboration]
   Phys. Rev. D **81**, 052011 (2010) [arXiv:1002.0365 [hep-ex]]

2. **"Measurement of the t anti-t Production Cross Section in p anti-p Collisions at $\sqrt{s} = 1.96$-TeV"**
   K. Ebina *et al.* [The CDF Collaboration]
   Phys. Rev. Lett. **97**, 202002 (2006) [arXiv:1002.0365 [hep-ex]]

3. **"Measurement of the cross section for t anti-t production in p anti-p collisions using the knematics of lepton + jets events"**
   K. Ebina *et al.* [The CDF Collaboration]
   Phys. Rev. D **72**, 052003 (2005) [arXiv:1002.0365 [hep-ex]]

4. **"Measurement of the t anti-t production cross section in p anti-p collisions at $\sqrt{s} = 1.96$-TeV using lepton + jets events with secondary vertex b-tagging"**
   K. Ebina *et al.* [The CDF Collaboration]
   Phys. Rev. D **71**, 052003 (2005) [arXiv:1002.0365 [hep-ex]]

5. **"Making the most of aging scintillator"**
   K. Ebina *et al.*
   Nucl. Instrum. Meth. A **453**, 245 (2000)
   *Prepared for 7th International Conference on Instrumentation for Colliding Beam Physics (INSTR99), Hamamatsu, Japan, 15-19 Nov 1999*

Other 119 papers with The CDF Collaboration as below.

1. T. Aaltonen *et al.* [ The CDF Collaboration ], [arXiv:1101.6058 [hep-ex]].

2. T. Aaltonen *et al.* [ The CDF Collaboration ], [arXiv:1102.0024 [hep-ex]].

3. T. Aaltonen *et al.* [ The CDF Collaboration ], [arXiv:1101.5728 [hep-ex]].

4. T. Aaltonen *et al.* [ The CDF Collaboration ], [arXiv:1101.4926 [hep-ex]].

5. T. Aaltonen *et al.* [ The CDF Collaboration ], [arXiv:1101.4578 [hep-ex]].

6. T. Aaltonen *et al.* [ CDF Collaboration ], [arXiv:1101.2996 [hep-ex]].

7. T. Aaltonen *et al.* [ CDF Collaboration ], [arXiv:1101.1028 [hep-ex]].

8. T. Aaltonen *et al.* [ CDF Collaboration ], [arXiv:1101.0034 [hep-ex]].

9. T. Aaltonen *et al.* [ CDF and D0 Collaboration ], [arXiv:1005.3216 [hep-ex]].

10. T. Aaltonen *et al.* [ CDF Collaboration ], [arXiv:1012.3093 [hep-ex]].

11. T. Aaltonen *et al.* [ CDF Collaboration ], [arXiv:1012.3138 [hep-ex]].

12. T. Aaltonen *et al.* [ CDF Collaboration ], Phys. Rev. **D83** (2011) 011102. [arXiv:1012.2795 [hep-ex]].

13. T. Aaltonen *et al.* [ CDF Collaboration ], Phys. Rev. Lett. **105** (2010) 252001. [arXiv:1010.4582 [hep-ex]].

14. T. Aaltonen *et al.* [ CDF Collaboration ], Phys. Rev. Lett. **105** (2010) 251802. [arXiv:1009.3047 [hep-ex]].

15. T. Aaltonen *et al.* [ CDF Collaboration ], Phys. Rev. **D82** (2010) 092001. [arXiv:1009.0266 [hep-ex]].

16. T. Aaltonen *et al.* [ CDF Collaboration ], Phys. Rev. **D82** (2010) 091105. [arXiv:1008.5077 [hep-ex]].

17. T. Aaltonen *et al.* [ CDF Collaboration ], Phys. Rev. **D82** (2010) 112001. [arXiv:1008.4404 [hep-ex]].

18. T. Aaltonen *et al.* [ CDF Collaboration ], Phys. Rev. Lett. **105** (2010) 232003. [arXiv:1008.3891 [hep-ex]].

19. T. Aaltonen *et al.* [ CDF Collaboration ], Phys. Rev. **D82** (2010) 112004. [arXiv:1007.5048 [hep-ex]].

20. T. Aaltonen *et al.* [ CDF Collaboration ], [arXiv:1007.4423 [hep-ex]].

21. T. Aaltonen *et al.* [ CDF Collaboration ], Phys. Rev. Lett. **105** (2010) 101801. [arXiv:1006.4597 [hep-ex]].

22. T. A. Aaltonen *et al.* [ CDF Collaboration ], Phys. Lett. **B692** (2010) 232-239. [arXiv:0908.3914 [hep-ex], arXiv:0908.3914 [hep-ex]].

23. T. Aaltonen *et al.* [ CDF Collaboration ], Phys. Rev. Lett. **105** (2010) 081802. [arXiv:1005.3600 [hep-ex]].

24. T. Aaltonen *et al.* [ The CDF Collaboration ], Phys. Rev. Lett. **104** (2010) 241801. [arXiv:1004.4946 [hep-ex]].

25. T. Aaltonen *et al.* [ CDF Collaboration ],

    [arXiv:1004.4855 [hep-ex]].

26. T. Aaltonen *et al.* [ The CDF Collaboration ], Phys. Rev. Lett. **105** (2010) 191801. [arXiv:1004.3042 [hep-ex]].

27. T. Aaltonen *et al.* [ CDF Collaboration ], Phys. Rev. Lett. **105** (2010) 012001. [arXiv:1004.3224 [hep-ex]].

28. T. Aaltonen *et al.* [ CDF Collaboration ], Phys. Rev. **D82** (2010) 112005. [arXiv:1004.1181 [hep-ex]].

29. T. Aaltonen *et al.* [ CDF Collaboration ], Phys. Rev. **D82** (2010) 031103. [arXiv:1004.1140 [hep-ex]].

30. T. Aaltonen *et al.* [ The CDF Collaboration ], Phys. Rev. **D82** (2010) 034001. [arXiv:1003.3146 [Unknown]].

31. T. Aaltonen *et al.* [ The CDF Collaboration ], Phys. Rev. Lett. **105** (2010) 042002. [arXiv:1003.0224 [hep-ex]].

32. T. Aaltonen *et al.* [ The CDF Collaboration ], Phys. Rev. **D82** (2010) 052002. [arXiv:1002.2919 [hep-ex]].

33. T. Aaltonen *et al.* [ CDF and D0 Collaboration ], Phys. Rev. Lett. **104** (2010) 061802. [arXiv:1001.4162 [hep-ex]].

34. T. Aaltonen *et al.* [ The CDF Collaboration ], Phys. Rev. Lett. **104** (2010) 061803. [arXiv:1001.4468 [hep-ex]].

35. T. Aaltonen *et al.* [ The CDF Collaboration ], Phys. Rev. **D81** (2010) 072003. [arXiv:1001.4577 [hep-ex]].

36. T. Aaltonen *et al.* [ CDF Collaboration ], Phys. Rev. Lett. **105** (2010) 131801. [arXiv:0912.4691 [hep-ex]].

37. T. Aaltonen *et al.* [ CDF Collaboration ], Phys. Rev. Lett. **104** (2010) 201801. [arXiv:0912.4500 [hep-ex]].

38. T. Aaltonen *et al.* [ CDF Collaboration ], Phys. Rev. Lett. **104** (2010) 102002. [arXiv:0912.3566 [hep-ex]].

39. T. Aaltonen *et al.* [ CDF Collaboration ], Phys. Rev. **D81** (2010) 052006. [arXiv:0912.3453 [hep-ex]].

40. T. Aaltonen *et al.* [ CDF Collaboration ], Phys. Rev. Lett. **104** (2010) 111802. [arXiv:0912.2059 [hep-ex]].

41. T. Aaltonen *et al.* [ CDF Collaboration ], Phys. Rev. Lett. **104** (2010) 091801. [arXiv:0912.1057 [hep-ex]].

42. T. Aaltonen *et al.* [ CDF Collaboration ], Phys. Rev. Lett. **104** (2010) 101801. [arXiv:0911.4449 [hep-ex]].

43. T. Aaltonen *et al.* [ CDF Collaboration ], Phys. Rev. Lett. **104** (2010) 141801. [arXiv:0911.3935 [hep-ex]].

44. T. Aaltonen *et al.* [ CDF Collaboration ], Phys. Lett. **B691** (2010) 183-190. [arXiv:0911.3112 [hep-ex]].

45. T. Aaltonen *et al.* [ CDF Collaboration ], Phys. Rev. **D81** (2010) 031102. [arXiv:0911.2956 [hep-ex]].

46. T. Aaltonen *et al.* [ CDF Collaboration ], Phys. Rev. **D81** (2010) 031105. [arXiv:0911.0425 [hep-ex]].

47. T. Aaltonen *et al.* [ CDF Collaboration ], Phys. Rev. **D82** (2010) 052005. [arXiv:0910.5170 [hep-ex]].

48. T. Aaltonen *et al.* [ CDF Collaboration ], Phys. Rev. **D80** (2009) 111106. [arXiv:0910.3623 [hep-ex]].

49. T. Aaltonen *et al.* [ CDF Collaboration ], Phys. Rev. Lett. **104** (2010) 011801. [arXiv:0910.3606 [hep-ex]].

50. A. Abulencia *et al.* [ CDF and CDF - Run II Collaborations ], Phys. Rev. **D74**, 072006 (2006). [hep-ex/0607035].

51. A. Abulencia *et al.* [ CDF Collaboration ], Phys. Rev. Lett. **97**, 211802 (2006). [hep-ex/0607021].

52. A. Abulencia *et al.* [ CDF Collaboration ], Phys. Rev. Lett. **97**, 191802 (2006). [hep-ex/0606043].

53. A. Abulencia *et al.* [ CDF - Run II Collaboration ], Phys. Rev. Lett. **97**, 062003 (2006). [hep-ex/0606027].

54. A. Abulencia *et al.* [ CDF Collaboration ], Phys. Rev. Lett. **97**, 082004 (2006). [hep-ex/0606017].

55. A. Abulencia *et al.* [ CDF Collaboration ], Phys. Rev. Lett. **97**, 081802 (2006). [hep-ex/0605124].

56. A. Abulencia *et al.* [ CDF Collaboration ], Phys. Rev. **D74**, 032009 (2006). [hep-ex/0605118].

57. A. Abulencia *et al.* [ CDF Collaboration ], Phys. Rev. **D74**, 032008 (2006). [hep-ex/0605099].

58. A. Abulencia *et al.* [ CDF Collaboration ], Phys. Rev. Lett. **97**, 031801 (2006). [hep-ex/0605097].

59. A. Abulencia *et al.* [ CDF Collaboration ], Phys. Rev. **D74**, 031109 (2006). [hep-ex/0605027].

60. A. Abulencia *et al.* [ CDF Collaboration ], Phys. Rev. Lett. **97**, 171802 (2006). [hep-ex/0605101].

61. A. Abulencia *et al.* [ CDF Collaboration ], Phys. Rev. Lett. **97**, 012002 (2006). [hep-ex/0603027].

62. A. Abulencia *et al.* [ CDF Collaboration ], Phys. Rev. Lett. **96**, 211802 (2006). [hep-ex/0603006].

63. A. Abulencia *et al.* [ CDF Collaboration ], Phys. Rev. Lett. **96**, 211801 (2006). [hep-ex/0602045].

64. A. Abulencia *et al.* [ CDF Collaboration ], Phys. Rev. **D73**, 112006 (2006). [hep-ex/0602008].

65. A. Abulencia *et al.* [ CDF Collaboration ], Phys. Rev. Lett. **96**, 231801 (2006). [hep-ex/0602005].

66. A. Abulencia *et al.* [ CDF Collaboration ], Phys. Rev. Lett. **96**, 102002 (2006). [hep-ex/0512074].

67. A. Abulencia *et al.* [ CDF Collaboration ], Phys. Rev. Lett. **96**, 171802 (2006). [hep-ex/0512072].

68. A. Abulencia *et al.* [ CDF Collaboration ], Phys. Rev. Lett. **96**, 152002 (2006). [hep-ex/0512070].

69. A. Abulencia *et al.* [ CDF Collaboration ], Phys. Rev. **D73**, 051104 (2006). [hep-ex/0512069].

70. A. Abulencia *et al.* [ CDF Collaboration ], Phys. Rev. **D73**, 051101 (2006). [hep-ex/0512065].

71. A. Abulencia *et al.* [ CDF II Collaboration ], Phys. Rev. Lett. **96**, 122001 (2006). [hep-ex/0512062].

72. A. Abulencia *et al.* [ CDF Collaboration ], Phys. Rev. Lett. **96**, 081803 (2006). [hep-ex/0512051].

73. A. Abulencia *et al.* [ CDF Collaboration ], Phys. Rev. **D73**, 051102 (2006). [hep-ex/0512055].

74. A. Abulencia *et al.* [ CDF Collaboration ], Phys. Rev. **D74**, 071103 (2006). [hep-ex/0512020].

75. A. Abulencia *et al.* [ CDF Collaboration ], Phys. Rev. **D73**, 092002 (2006). [hep-ex/0512009].

76. A. Abulencia *et al.* [ CDF Collaboration ], Phys. Rev. **D73**, 111103 (2006). [hep-ex/0511023].

77. A. Abulencia *et al.* [ CDF Collaboration ], Phys. Rev. Lett. **96**, 042003 (2006). [hep-ex/0510065].

78. A. Abulencia *et al.* [ CDF Collaboration ], Phys. Lett. **B639**, 172-178 (2006). [hep-ex/0510063].

79. A. Abulencia *et al.* [ CDF Collaboration ], Phys. Rev. Lett. **96**, 022004 (2006). [hep-ex/0510049].

80. A. Abulencia *et al.* [ CDF Collaboration ], Phys. Rev. **D73**, 032003 (2006). [hep-ex/0510048].

81. A. Abulencia *et al.* [ CDF Collaboration ], Phys. Rev. Lett. **96**, 201801 (2006). [hep-ex/0509015].

82. A. Abulencia *et al.* [ CDF Collaboration ], Phys. Rev. Lett. **96**, 011802 (2006). [hep-ex/0508051].

83. A. Abulencia *et al.* [ CDF Collaboration ], Phys. Rev. Lett. **95**, 221805 (2005). [hep-ex/0508036].

84. A. Abulencia *et al.* [ CDF Collaboration ], J. Phys. G **G34**, 2457-2544 (2007). [hep-ex/0508029].

85. D. E. Acosta *et al.* [ CDF Collaboration ], Phys. Rev. Lett. **96**, 202001 (2006). [hep-ex/0508022].

86. D. E. Acosta *et al.* [ CDF Collaboration ], Phys. Rev. **D72**, 051104 (2005). [hep-ex/0507067].

87. D. E. Acosta *et al.* [ CDF Collaboration ], Phys. Rev. **D72**, 051107 (2005). [hep-ex/0506074].

88. D. E. Acosta *et al.* [ CDF Collaboration ], Phys. Rev. **D72**, 032002 (2005). [hep-ex/0506001].

89. D. E. Acosta *et al.* [ CDF Collaboration ], Phys. Rev. Lett. **95**, 102002 (2005). [hep-ex/0505091].

90. A. Abulencia *et al.* [ CDF Collaboration ], Phys. Rev. Lett. **96**, 082002 (2006). [hep-ex/0505076].

91. A. Abulencia *et al.* [ CDF Collaboration ], Phys. Rev. Lett. **96** (2006) 191801. [hep-ex/0508014].

92. A. Abulencia *et al.* [ CDF Collaboration ], Phys. Rev. Lett. **95** (2005) 252001. [hep-ex/0507104].

93. D. Acosta *et al.* [ CDF Collaboration ], Phys. Rev. **D71** (2005) 032001. [hep-ex/0412071].

94. D. Acosta *et al.* [ CDF II Collaboration ], Phys. Rev. Lett. **94** (2005) 091803. [hep-ex/0406078].

95. D. E. Acosta *et al.* [ CDF Collaboration ], Phys. Rev. **D71**, 112002 (2005). [hep-ex/0505013].

96. D. E. Acosta *et al.* [ CDF Collaboration ], Phys. Rev. Lett. **95**, 071801 (2005). [hep-ex/0503004].

97. D. E. Acosta *et al.* [ CDF Collaboration ], Phys. Rev. Lett. **95**, 031801 (2005). [hep-ex/0502044].

98. D. E. Acosta *et al.* [ CDF Collaboration ], Phys. Rev. **D71**, 051103 (2005). [hep-ex/0502003].

99. D. E. Acosta *et al.* [ CDF Collaboration ], Phys. Rev. Lett. **94**, 211801 (2005). [hep-ex/0501050].

100. D. E. Acosta *et al.* [ CDF Collaboration ], Phys. Rev. **D71**, 051104 (2005). [hep-ex/0501023].

101. D. E. Acosta *et al.* [ CDF Collaboration ], Phys. Rev. **D71**, 091105 (2005). [hep-ex/0501021].

102. D. E. Acosta *et al.* [ CDF Collaboration ], Phys. Rev. Lett. **94**, 101803 (2005). [hep-ex/0412057].

103. D. E. Acosta *et al.* [ CDF Collaboration ], Phys. Rev. Lett. **95**, 022003 (2005). [hep-ex/0412050].

104. D. E. Acosta *et al.* [ CDF Collaboration ], Phys. Rev. Lett. **95**, 022001 (2005). [hep-ex/0412042].

105. D. E. Acosta *et al.* [ CDF Collaboration ], Phys. Rev. **D71**, 052002 (2005). [hep-ex/0411059].

106. D. E. Acosta *et al.* [ CDF Collaboration ], Phys. Rev. **D71**, 112001 (2005). [hep-ex/0410076].

107. D. E. Acosta *et al.* [ CDF Collaboration ], Phys. Rev. **D71**, 012005 (2005). [hep-ex/0410058].

108. D. E. Acosta *et al.* [ CDF Collaboration ], Phys. Rev. **D71**, 031104 (2005). [hep-ex/0410053].

109. D. E. Acosta *et al.* [ CDF Collaboration ], Phys. Rev. Lett. **94**, 122001 (2005). [hep-ex/0504006].

110. D. E. Acosta *et al.* [ CDF Collaboration ], Phys. Rev. Lett. **94**, 101802 (2005). [hep-ex/0410013].

111. D. E. Acosta *et al.* [ CDF II Collaboration ], Phys. Rev. Lett. **94**, 041803 (2005). [hep-ex/0410008].

112. D. E. Acosta *et al.* [ CDF-II Collaboration ], Phys. Rev. **D71**, 072005 (2005). [hep-ex/0409029].

113. D. E. Acosta *et al.* [ CDF Collaboration ], Phys. Rev. Lett. **93**, 221802 (2004). [hep-ex/0406073].

114. D. E. Acosta *et al.* [ CDF Collaboration ], Phys. Rev. Lett. **93**, 142001 (2004). [hep-ex/0404036].

115. D. E. Acosta *et al.* [ CDF Collaboration ], Phys. Rev. Lett. **93**, 032001 (2004). [hep-ex/0403032].

116. D. E. Acosta *et al.* [ CDF II Collaboration ], Phys. Rev. Lett. **93**, 072001 (2004). [hep-ex/0312021].

117. D. E. Acosta *et al.* [ CDF Collaboration ], Phys. Rev. **D68**, 091101 (2003). [hep-ex/0308059].

118. D. E. Acosta *et al.* [ CDF II Collaboration ], Phys. Rev. **D68**, 072004 (2003). [hep-ex/0310043].

119. D. E. Acosta *et al.* [ CDF Collaboration ], Phys. Rev. Lett. **91**, 241804 (2003). [hep-ex/0307080].

# Talks by AUTHOR

1. K. Ebina *et al.*,
   "Search for the Standard Model Higgs Boson in $l\nu + \tau\tau$ and $ll + \tau\tau$",
   JPS, Section Meeting, 2010

2. K. Ebina *et al.*,
   "Top Mass Measurement in all hadronic decay channel by Dynamical Likelihood Method",
   JPS, Section Meeting, 2004

3. K. Ebina *et al.*,
   "Readout of refurbished large scintillation counters by fibers",
   JPS, Section Meeting, 2001